Vrije Universiteit Brussel

Faculty of Engineering
Department of Mechanical Engineering

Flexible Heat Production from a micro Gas Turbine

Design and experimental analysis of humidified air cycles

Thesis submitted in fulfilment of the requirements
of the degree of Doctor in Engineering Sciences

Ward De Paepe

Promoters: em. prof. dr. ir. J. De Ruyck
prof. dr. ir. S. Bram

November 2014

Vrije Universiteit Brussel

Faculty of Engineering
Department of Mechanical Engineering

Flexible Heat Production from a micro Gas Turbine

Design and experimental analysis of humidified air cycles

Thesis submitted in fulfilment of the requirements
of the degree of Doctor in Engineering Sciences

Ward De Paepe

Promoters: em. prof. dr. ir. J. De Ruyck
prof. dr. ir. S. Bram

Jury: prof. dr. ir. P. Lataire (Chairman, VUB)
prof. dr. ir. R. Pintelon (Vice-chairman, VUB)
prof. dr. ir. F. Contino (Secretary, VUB)
prof. dr. ir. M. De Paepe (UGent)
prof. dr. ir. M. Thern (Lund University, Sweden)

November 2014

Print: Silhouet, Maldegem

2014 Uitgeverij VUBPRESS Brussels University Press
VUBPRESS is an imprint of ASP nv (Academic and Scientific Publishers nv)
Ravensteingalerij 28
B-1000 Brussels
Tel. +32 (0)2 289 26 50
Fax +32 (0)2 289 26 59
E-mail: info@vubpress.be
www.vubpress.be

ISBN 978 90 5718 183 2
NUR 950/961
Legal deposit D/2014/11.161/86

To Ellen

Acknowledgements

First of all, I would like to express my sincere gratitude to Jacques De Ruyck, my supervisor, for letting me participate in this project and his many helpful suggestions during this research. He provided me the flexibility and freedom I needed to find my way in independent research and development. I feel honoured to be your last PhD-student.

I am also very thankful to Svend Bram. Despite his very tight schedule, he always had time to answer my questions and take the time to read my papers.

I would like to thank Frank Delattin for guiding me during the first two years. Your jokes and laughters were a relief as well as our regular *Steak Pizzaiola* moments. The emptiness you left in the office could not be filled.

A special word of gratitude goes to Francesco Contino, who accepted the difficult task of guiding me during the past two years. Without being an expert in the field, your suggestions and comments were very valuable to me. Additionally, I would like to thank you for taking the time to listen to me and to take care of all additional *stuff* so that I could focus on my work.

I am also very grateful to Jens Klingmann, Parisa Sayad, Alessandro Schönborn, Marcus Thern and Magnus Genrup and all the other people of the Thermal Power Engineering division of Lund University for the environment they created during the experiments in Lund.

I am very thankful to everyone involved with the construction and maintenance of the Turbec T100 mGT test rig. Our technicians, Marc, Marnix and André, thank you for your immediate and professional support. Francies and Bram, thank you for helping designing the test rig. I would also like to thank Jan Magnusson for providing valuable assistance whenever technical problems occurred with the Turbec T100.

Thanks to all my colleagues at the department of Mechanical Engineering for making the everyday work at the department more interesting and fun. A special thanks goes to Stefanie and Marina for sharing the office with me everyday.

I would like to thank my friends, family and family-in-law for all the love and support I received in the past and especially during these long four years. Moeke and Vake, thank you for giving me all opportunities to fully develop myself and all unconditional love and support, making this work possible. A special thanks goes to my young nephews, Simon and Mathis, and niece, Séraphine, who showed that a simple smile can turn a bad day into a good one. Finally, I would like to thank my wonderful wife, Ellen. Without your support, understanding, guidance and patience, this work would never have been written. Words cannot describe how lucky I am that you are my wife. Marrying you while writing this thesis was not the easiest thing to do, but it was the best I ever did.

Brussels — Ward De Paepe
November 2014

Abstract

Micro Gas Turbines (mGTs) offer several advantages for small-scale Combined Heat and Power (CHP) production compared to Internal Combustion Engines (ICEs) such as low vibration level, cleaner exhaust and lower maintenance. The major drawback is their heat-driven use. In periods with no or low heat demand, part of the heat should be discarded to keep the mGT operated at high electric load. Compared to ICEs, the lower electric efficiency of mGTs makes them less attractive in this case and economic constraints could even lead to complete shutdown. In addition, the specific capital cost of the mGT is still high, which involves any shutdown having a severe negative effect on the economic performance of the mGT.

In order to increase the flexibility of the mGT and shift its use towards various heat and power demand profiles, the waste heat in the exhaust gases can be used to generate auto-raised steam or hot liquid water, which is then re-injected in the cycle. Humidifying the mGT working fluid will increase the electric performance, resulting in higher profitability during periods with no or low heat demand.

The scope of this thesis is the development of such a humidified mGT cycle for flexible heat production. This thesis covers the entire development process of a micro Humid Air Turbine (mHAT) cycle based on a Turbec T100 mGT, including the dry and wet characterisation, the development of the optimal cycle layout and water injection system and finally the test rig construction and experimental evaluation.

For the development of a humidified mGT, the dry and wet operation of the available Turbec T100 mGT needed to be fully characterized. For accurate wet simulations of the mGT, correct compressor maps are essential. The compressor map was reconstructed by performing dry and wet (with steam injection) mGT tests. Additional steam injection experiments were

performed to characterize the behaviour of the mGT in wet conditions. Steam injection experiments resulted in stable mGT operation at reduced rotational speed and pressure ratio, and increased electric efficiency. Finally, the effect of water on the combustion of natural gas (Lean Blowout (LBO) limit) was experimentally studied in an atmospheric, premixed, variable-swirl burner.

In the next step towards the humidified mGT, the optimal cycle for water introduction in the mGT could be determined by using black box analysis in combination with composite curves. Direct injection of heated water was identified as the optimal cycle, resulting in an absolute efficiency increase of 4.4 %. Transforming the existing T100 mGT into a mHAT results in a lower electric efficiency increase of 2 % absolute, but requires less changes to the T100 mGT. Therefore, the mHAT was selected as final humidified mGT layout.

Transforming the T100 mGT into a mHAT requires the development of a saturation tower. To reduce the pressure drop, a new type of saturation tower, a spray saturation tower, was developed, using two-phase flow theory. Cross-current injection was identified as the optimal injection method for a spray saturation tower for mHAT applications. Based on these simulations, a cross-current spray saturation tower was developed and integrated in the T100 mGT cycle.

Experiments on the modified Turbec T100 mGT were performed to evaluate the test rig and identify its shortcomings. Using a specific developed wet start-up and shutdown procedure, the effect of humidifying the compressed air on the mGT performances was studied experimentally. These tests resulted in stable operation at constant power output and reduced fuel flow rate, resulting in absolute electric efficiency increase of 1.0 ± 1.8 %, 1.1 ± 1.8 % and 0.8 ± 1.8 % at power levels of 80, 85 and 90 kW_e. These changes are however in the range of the accuracy on the measurements. Additionally, the electric efficiency was below the predictions from the simulations results (2 %), which indicated that the compressed air was not yet fully saturated. These experiments however indicated the beneficial effect of compressed air humidification on the mGT performance. Further optimizing the mHAT test rig operation will heighten the final electric efficiency increase.

To conclude, the proposed route for waste heat recovery through water injection in a mGT cycle offers high potential for electric efficiency increase without major changes to the mGT cycle.

Contents

List of Figures

List of Tables

Nomenclature

Acronyms

ABL	Atmospheric Boundary Layer
AF	Air-Fuel ratio
AHAT	Advanced Humid Air Turbine
ANN	Artificial Neural Network
BB	Black Box
CAF	Corrected Air Flow
CCHP	Combined Cooling, Heating and Power
CHAT	Cascaded Humidified Advanced Turbine
CHP	Combined Heat and Power
CIT	Combustor Inlet Temperature
CTA	Constant Temperature Anemometer
EEA	European Environment Agency
EFGT	Externally Fired Gas Turbine
EGR	Exhaust Gas Recirculation
ETS	Emissions Trading System
EU	European Union
EvGT	Evaporative Gas Turbine
GT	Gas Turbine
HAT	Humid Air Turbine
HRSG	Heat Recovery Steam Generator
ICE	Internal Combustion Engine
IEA	International Energy Agency
LBO	Lean Blowout
LDA	Laser Doppler Anemometry
LHV	Lower Heating Value

LMTD	Logarithmic Mean Temperature Difference
MCFC	Molten Carbonate Fuel Cell
mGT	micro Gas Turbine
mHAT	micro Humid Air Turbine
MPPT	Maximum Power Point Tracking
NGCC	Natural Gas-fuelled Combined Cycle
NPV	Net Present Value
NTU	Non-Thermal Unit
ODE	Ordinary Differential Equation
ORC	Organic Rankine Cycle
PIT	Pressure Inlet Turbine
POT	Pressure Outlet Turbine
RBMD	Roughness, Barrier and Mixing Device
REVAP®	REgenerative EVAPoration
S1	Scenario 1
S2	Scenario 2
SM	Surge Margin
SOFC	Solide Oxide Fuel Cell
TIT	Turbine Inlet Temperature
TOPHAT®	TOP Humid Air Turbine
TOT	Turbine Outlet Temperature
UHC	Unburned Hydrocarbons
VUB	Vrije Universiteit Brussel
WAC	Water Atomizing inlet air Cooling

Roman Symbols

A	cross section area	m^2
a	speed of sound	m/s
b	frontal base of Irwin spire	m
C	velocity	m/s
C_f	friction coefficient	
C_p	heat capacity	$\mathrm{kJ/(kg\,K)}$
D	spacing between roughness elements	m
D	diameter	m
d	zero plane displacement	m
d	droplet diameter	m
d_s	Sauter mean diameter	m

$\dot{E}x$	exergy flow	kW
F	force	N
f	frequency	Hz
f_L	reduced frequency	
Fr	Froude number	
g	gravitation constant	$9.81\,\mathrm{m/s^2}$
G_a	axial flux of axial momentum	$\mathrm{kg\,m/s^2}$
G_t	axial flux of tangential momentum	$\mathrm{kg\,m^2/s^2}$
H	height	m
h	specific enthalpy	J/kg
h	height of the Irwin spire	m
I_u	turbulence intensity in the x-direction relating to u' fluctuating velocity component	
I_v	turbulence intensity in the v-direction relating to v' fluctuating velocity component	
I_w	turbulence intensity in the w-direction relating to w' fluctuating velocity component	
k	size of roughness elements	m
k	heat capacity ratio	C_p/C_v
L	length	m
L	characteristic length	m
Le	Lewis number	
${}^xL_u$	integral length scales of turbulence in the x-direction relating to u' fluctuating velocity component	m
${}^xL_v$	integral length scales of turbulence in the x-direction relating to v' fluctuating velocity component	m
${}^xL_w$	integral length scales of turbulence in the x-direction relating to w' fluctuating velocity component	m
$\dot{M}$	molar flow rate	kmol/s
$\dot{m}$	mass flow rate	kg/s
Ma	Mach number	
N	rotational speed	rpm
n	amount of droplets	
P	power	kW
p	pressure	Pa
$\dot{Q}$	heat flux, heat exchange rate	kW

R	universal gas constant	$8.3144\,\mathrm{J/(K\,mol)}$
Re	Reynolds number	
R_S	radius of the swirler	m
r	radius of the swirler exit	m
$R_{u,x}$	autocorrelation function	
S	Swirl number	
S	small-scale turbulence parameter	
$S_u\,(f)$	power spectral density of longitudinal velocity component	
T	total record time	s
T	temperature	°C
t	time	s
U	axial velocity combustion air	m/s
u	absolute velocity component in the x-direction	m/s
$\bar{u}$	mean velocity component in the x-direction	m/s
u'	fluctuating velocity component in the x-direction	m/s
u_δ	wind velocity above the boundary layer	m/s
u_τ	friction velocity	m/s
W	tangential velocity combustion air	m/s
W	width	m
w'	fluctuating velocity component in the z-direction	m/s
x	distance in the direction of the flow (longitudinal direction)	m
x	position along the axis of the saturation tower parallel to the flow direction of the compressed air	m
y	spanwise distance from the test section centerplane (lateral direction)	m
z	vertical distance from the wind tunnel floor (vertical direction)	m
z_0	roughness length	m

Greek Symbols

α	exponent of power law profile
Δ	accuracy

δ	boundary layer thickness	m
δ	perturbation of a parameter	
Φ	equivalence ratio	
κ	von Karman constant	0.41
μ	dynamic viscosity	kg/(m s)
η	efficiency	
Ω	steam fraction	
π	pressure ratio	
ρ	density	kg/m^3
σ_u	standard deviation of u	m/s
τ	turbulent Reynolds shear stress	Pa
ψ	parameter in perturbation analysis	

Subscripts

abs	absolute
adapted	adapted state
air	properties of air
cold	cold side of the heat exchanger
comp	compressor
condens	condens
cooler	cooler
droplet	droplet
dry	dry condition
el	electric
filt	filter
fluegas	condition of the fluegases
fuel	fuel
gain	flow gaining exergy
gas	partially humidified compressed air
heater	heater
hot	hot side of the heat exchanger
i	component (film, droplets or gas core)
in	inlet condition
out	outlet condition
init	initial condition
inj	condition of the injected steam
is	isentropic conditions

lose	flow loosing exergy
loss	loss
mech	mechanical
mix	condition of the mixing point
natgas	natural gas
net	netto
powel	power electronics
rec	recuperator
ref	reference
rel	relative
req	requested
s	source
sat	properties of the saturation tower
stack	conditions at the stack
steam	properties of steam
surge	condition at the surge limit
th	thermal
turb	turbine
water	properties of water
working	condition at the working point

Superscripts

dest	destruction
eff	efficiency
$'$	per unit of length
$*$	properties of standard air composition

List of publications

Journal publications

[1] W. De Paepe, F. Delattin, S. Bram, J. De Ruyck, Steam injection experiments in a microturbine – A thermodynamic performance analysis, Applied Energy 97 (2012) 569 – 576.

[2] W. De Paepe, F. Delattin, S. Bram, J. De Ruyck, Discussion of the effects of recirculating exhaust air on performance and efficiency of a typical microturbine, Energy 45 (2012) 456–463.

[3] W. De Paepe, F. Delattin, S. Bram, J. De Ruyck, Water injection in a micro gas turbine – Assessment of the performance using a black box method, Applied Energy 112 (2013) 1291–1302.

[4] W. De Paepe, F. Contino, F. Delattin, S. Bram, J. De Ruyck, New concept of spray saturation tower for micro humid air turbine applications, Applied Energy 130 (2014) 723–737.

[5] W. De Paepe, F. Contino, F. Delattin, S. Bram, J. De Ruyck, Optimal waste heat recovery in micro gas turbine cycles through liquid water injection, Applied Thermal Engineering 70 (2014) 846–856.

[6] W. De Paepe, M. Montero Carrero, S. Bram, A. Parente, F. Contino, Experimental characterization of a T100 micro gas turbine converted to full humid air operation, Energy Procedia (2014) (Accepted for publication).

[7] M. Montero Carrero, W. De Paepe, A. Parente, J. Blondeau, H. Laget, F. Contino, Economic analysis of a micro humid air turbine for combined heat and power based on experimental data, Energy Procedia (2014) (Accepted for publication).

Conference publications

[1] W. De Paepe, F. Delattin, S. Bram, J. De Ruyck, Steam injection experiments in a microturbine – A thermodynamic performance analysis, in: U. Desideri, J. Yan (Eds.), Third International Conference on Applied Energy (ICAE 2011), 2011, pp. 2045–2056.

[2] W. De Paepe, F. Delattin, S. Bram, J. De Ruyck, Discussion of the effects of recirculating exhaust air on performance and efficiency of a typical microturbine, in: Proceedings of the 24th International conference on Efficiency, Cost, Optimization, Simulation and Environmental Impact of Energy Systems (ECOS 2011), 2011, pp. 745–756.

[3] W. De Paepe, F. Delattin, S. Bram, J. De Ruyck, Water injection in a microgasturbine – Assessment of the performance using a black box method, in: J. Yan (Ed.), Fourth International Conference on Applied Energy (ICAE 2012), 2012, pp. 1756–1766.

[4] W. De Paepe, F. Contino, F. Delattin, S. Bram, J. De Ruyck, A new route for water introduction in a micro gas turbine cycle, in: The 3rd International Conference on Mircogeneration and Related Technologies, 2013, p. 10 pages.

[5] W. De Paepe, F. Delattin, S. Bram, F. Contino, J. De Ruyck, A study on the performance of steam injection in a typical micro Gas Turbine, in: ASME Conference Proceedings, 2013, ASME paper GT2013-94569, p. 10 pages.

[6] W. De Paepe, F. Contino, F. Delattin, S. Bram, J. De Ruyck, Saturation tower design for micro Humid Air Turbine applications, in: J. Yan (Ed.), Fifth International Conference on Applied Energy (ICAE 2013), 2013, p. 14 pages.

[7] I. Herrera Moya, J. De Ruyck, R. Zanzi, W. De Paepe, V. Nùñez, V. S. Ocaña, Environmental impact assessment of decentralized power generation based on heavy fuel oil in Santa Clara City, Cuba, in: J. Yan (Ed.), Fifth International Conference on Applied Energy (ICAE 2013), 2013, p. 10 pages.

[8] W. De Paepe, M. Montero Carrero, S. Bram, F. Contino, T100 micro gas turbine converted to full humid air operation: Test rig evaluation,

in: ASME Conference Proceedings, 2014, ASME paper GT2014-26123, p. 11 pages.

[9] W. De Paepe, M. Montero Carrero, S. Bram, A. Parente, F. Contino, Experimental characterization of a T100 micro gas turbine converted to full humid air operation, in: J. Yan (Ed.), Sixth International Conference on Applied Energy (ICAE 2014), 2014, p. 6 pages.

[10] M. Montero Carrero, W. De Paepe, A. Parente, J. Blondeau, H. Laget, F. Contino, Economic analysis of a micro humid air turbine for combined heat and power based on experimental data, in: J. Yan (Ed.), Sixth International Conference on Applied Energy (ICAE 2014), 2014, p. 7 pages.

Chapter 1

Introduction

This chapter aims to set the scene for this PhD thesis. First, the research question is raised. In the second section, the solution is elaborated on, i.e. converting the micro Gas Turbine (mGT) into a micro Humid Air Turbine (mHAT). Finally, the possible route towards the development and implementation of flexible heat production from a mGT is discussed.

1.1 Problem statement

In this section, the main motivation for the development of flexible heat production from a mGT – the relative low attraction of mGT for small-scale Combined Heat and Power (CHP) production – is presented. The first subsection discusses the potential of CHP for energy use and greenhouse gas emissions reduction. After showing this potential, the second part introduces the current position of CHP in the total energy market on a worldwide, European and regional level. Finally, the main problem is discussed: the relatively low interest in mGTs for small-scale CHP production, despite the potential and advantages compared to other techniques.

1.1.1 CHP: A measure to reduce greenhouse gas emissions

All major economies need to make deep emission reductions to keep global warming below 2 °C compared to the temperature in pre-industrial times. The European Union (EU) has set an ambitious target, called the 2020 *climate and energy package* [1], to address the climate change. The climate and energy package is a set of binding rules which aims to ensure the EU meeting its ambitious targets for 2020. These targets, known as the 20-20-20 targets, compromise of following three objectives [1]:

- a reduction of 20 % in EU greenhouse gas emissions, compared to the 1990 levels;
- achieving a total share of 20 % of the total energy production by renewable energy sources;
- improving energy efficiency by 20 %.

The European Commission has presented a framework on the 22$^{\text{nd}}$ of January 2014, the 2030 *framework for climate and energy policies* [2]. This framework aims to make the EU's economy and energy system more competitive, secure and sustainable. The 2030 framework sets forth the continued progress towards a low-carbon economy. The objective is to reduce greenhouse gas emissions by 40 % and to increase the share of renewable energy to at least 28 % of the total energy production. Finally, the EU has set a roadmap for moving to a low-carbon economy in 2050 [3]. The idea is to cut most of the greenhouse gases in the EU. The roadmap suggests that, by 2050 ,

the EU should cut its emissions to 80 % below 1990 levels through domestic reductions alone. The roadmap sets out cost-effective milestones to this goal: reductions of the order of 40 % by 2030 and 60 % by 2040 [3].

To achieve the ambitious 20-20-20 targets, the 2020 *climate and energy package* includes four major measures [1]:

- reforming the EU Emissions Trading System (ETS);
- setting national targets for non-EU ETS emissions;
- setting national renewable energy targets;
- creating a framework for carbon capture and storage.

Since the 2020 *climate and energy package* does not directly addresses the energy efficiency target, an additional *energy efficiency plan* [4] and *energy efficiency directive* [5] have been published by the EU in 2011. In these directives, the EU suggests that the efficiency of energy and heat production needs to be improved. Increasing the installed Combined Heat and Power (CHP) capacity is a possible measure to improve the energy efficiency of the heat and power production.

CHP systems use one single primary fuel to simultaneously produce electric and thermal power. By doing so, they realize significant energy savings compared to conventional schemes of separated production (Figure 1.1). To produce the same amount of thermal (Q) and electric power (E), 20 % more primary fuel is used in this case for the separate production compared to the simultaneous CHP production.

CHP production has been identified by the European Commission as a measure with high energy-saving potential but which is presently underused [6]. From an energy and environmental perspective, benefits of CHP include: primary energy savings, reduction of the need for investment in energy infrastructure, avoidance of network losses and reduction of emissions, particularly greenhouse gases. From an economic point of view, CHP positively contributes to security of energy supply as well as for the competitiveness of the country and of the EU as a whole.

1.1.2 CHP – Current situation

An overview on the current situation for CHP production is given. The position of CHP production in the worldwide electricity production is

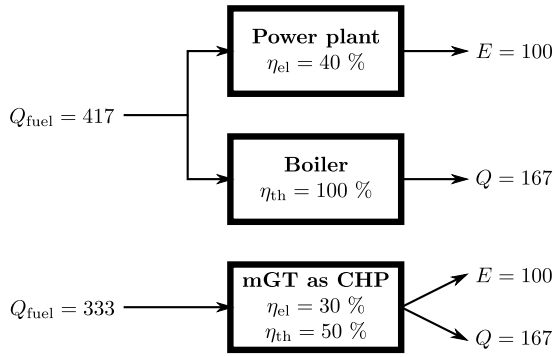

Figure 1.1: By simultaneously producing heat (Q) and electric power (E), CHP units achieve considerable (20 % here) energy savings compared to separate power and heat production.

discussed, as well as the situation in Europe and in Flanders. For Belgium, the current installed CHP capacity from Flanders is discussed, since part of the energy policy, including CHP, is controlled by the regions. In addition, an outlook for future CHP development is given.

CHP worldwide

The International Energy Agency (IEA) calculated the total share of CHP production in the total share of electricity production of the G13 countries, showing that the share is still rather small (Figure 1.2 [7]).

The IEA expects a small increase in CHP installed capacity for the G13 by 2015 and a larger growth by 2030 (Figure 1.3). The IEA has established the potential of CHP in the G13 countries to show the policy makers what can be achieved under the right conditions. To analyse the potential, the IEA used a simple *top-bottom* approach. The level of CHP development depends on the different heating and cooling demand in the different sectors (residential, industrial and commercial). These demands were taken as basis for the analysis of the CHP potential. The final results of the analysis indicate that significant growth opportunities in the CHP sector are available.

In addition to the calculation of the potential for CHP in the G13, the IEA also calculated the benefits that would be achieved when this CHP potential would be reached. The outputs of the benefits assessment were:

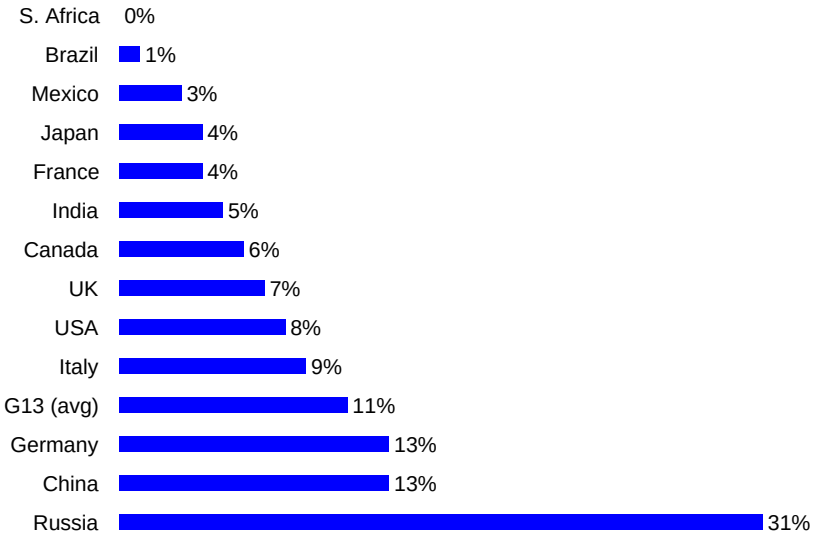

Figure 1.2: The total share of CHP production in the electricity production of the G13 countries [7].

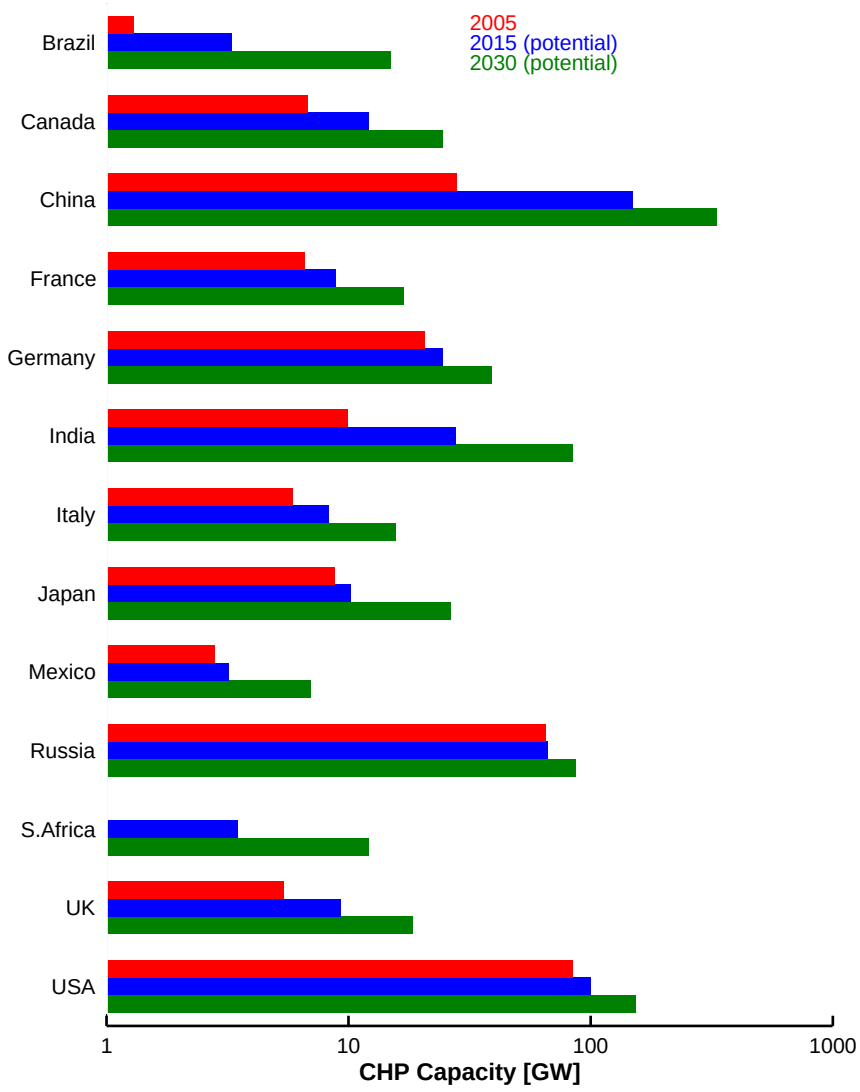

Figure 1.3: The IEA expects a potential large growth of CHP in the G13 countries by 2030 [7].

- **Capital Investment Costs**: To meet the future electricity demand, substantial investments are necessary. By increasing the share of CHP in the electric power production, overall costs can be reduced by 3 % by 2015 and 7 % by 2030. These savings are achieved by lower transport and investment costs.

- **Delivered Electricity Costs**: The delivered costs to the end consumers will slightly reduce. So increasing the CHP production will not lead to increased electricity prices.

- **CO_2 Emissions and Fuel Consumption**: Due to the higher generating efficiency compared to conventional separate production (see Figure 1.1), CO_2 emissions and fuel consumption can be reduced. By 2015, exhaust of greenhouse gases can be reduced by 4 %. By 2030, savings will increase to more than 10 %.

CHP in Europe

The different EU member states still have a limited share of CHP in their total electric power production (Figure 1.4). The share of electricity from CHP production in the total electricity production in the EU-27 was 11.4 % in 2009. Compared to 2008, this share has grown by 0.4 % absolute, while the rise in share between 2005 and 2009 is just 0.3 % (Figure 1.5). This indicates that CHP has only a modest progress in increasing the share of CHP in the electric power production. According to the European Environment Agency (EEA), high gas prices, inconsistent energy policies and relatively low electricity prices have kept the competitiveness of gas-fired CHP plants marginal, despite the strong policy support to promote the technology in many member states. More recently, the agency noted indicators of the opposite direction [8].

The new member states have a significantly higher share of CHP production in the total electricity production (15.6 % of total gross electricity production) in 2009, compared to the EU-15, where the share was only 11.0 % (Figure 1.4). The countries with the highest market penetration of CHP in electricity production are however members of EU-15: Denmark (45.3 %), Finland (35.8 %) and the Netherlands (32.5 %). The main reason is the strong government support for CHP. In Denmark, CHP received support by providing tax incentives and subsidies. In addition, the growth was

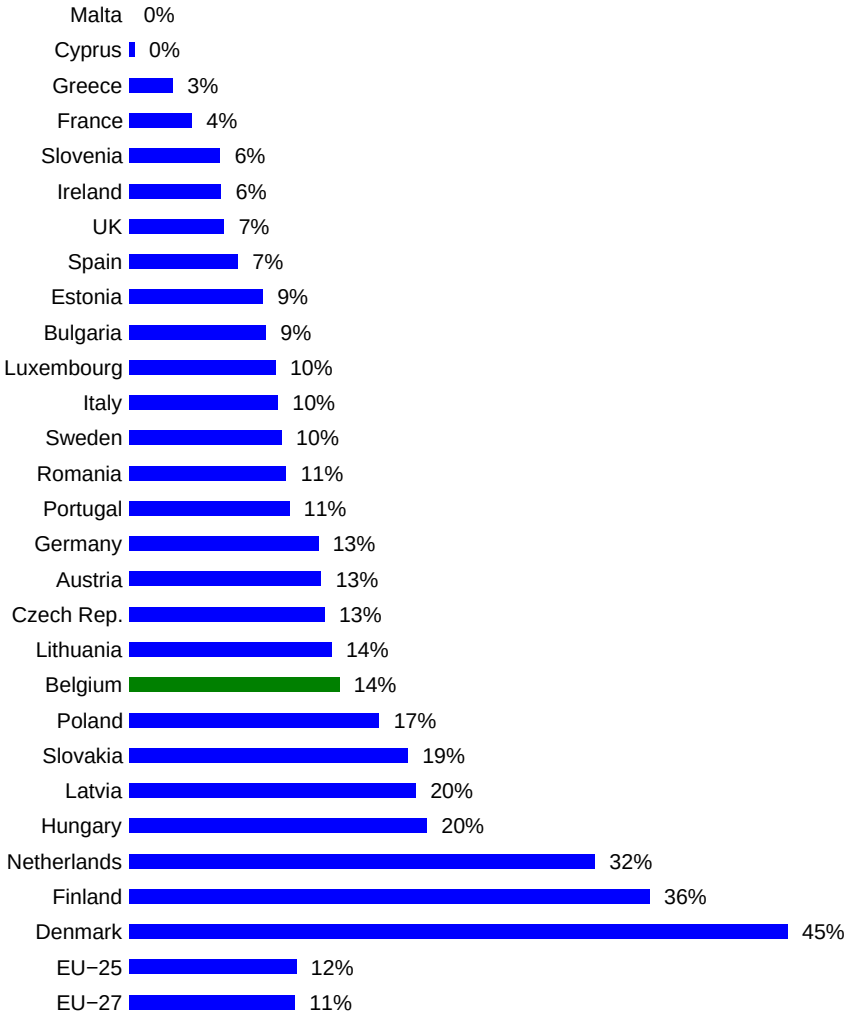

Figure 1.4: CHP production is responsible for 11 % of the total electricity production in the EU. Depending on the EU country, a different share of electric power is produced using CHP [8].

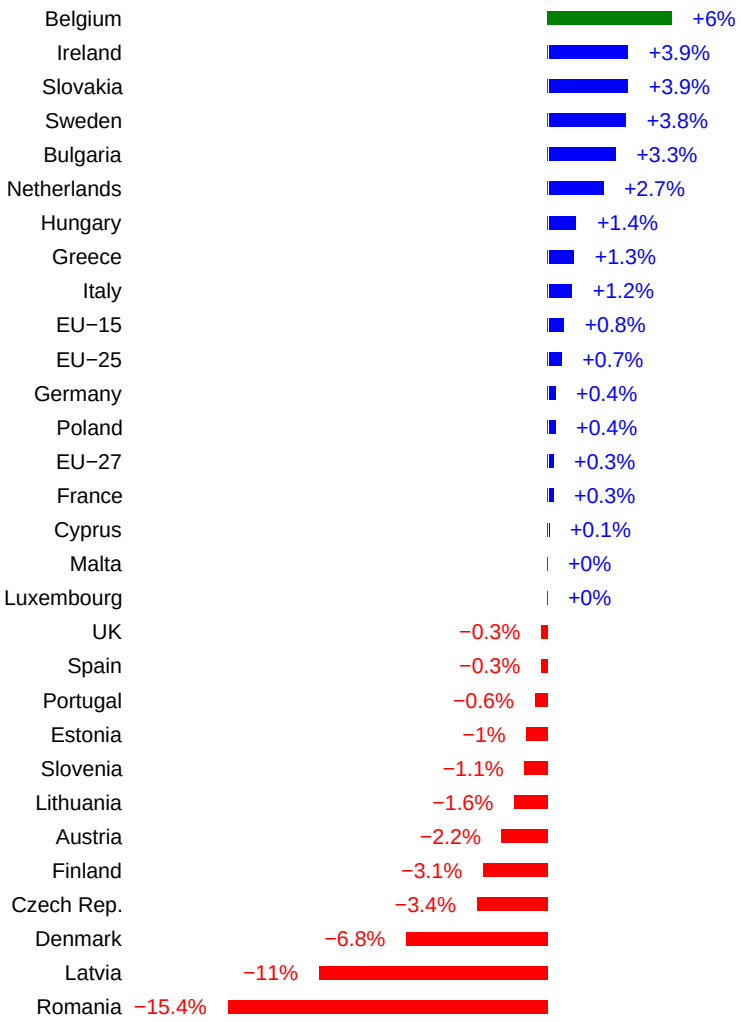

Figure 1.5: Absolute progress of the electricity share in the EU (2005 to 2009) indicates that major differences exist between the different member states [8].

highest in public supply because of investments in district heating infrastructure. Next to the government support, the availability of natural gas in the Netherlands resulted in a higher CHP share. The high level of CHP production in Finland is a result of the cold climate, which facilitates the use of heat through district heating combined with electricity production in CHP. A general trend is that a strong demand for heat and electricity, coupled with a well developed district heating network helps stimulating investment in CHP. A poor infrastructure for natural gas supply and a lower heat demand, like in Greece, will hinder the CHP development, leading to a low share in electricity production. Trigeneration, Combined Cooling, Heating and Power (CCHP) systems, offers a solution in warmer countries, like Greece or Portugal. The surplus heat production can be used for cooling applications. The share in Romania has drastically reduced from 26.2 % in 2005 to 9.6 % in 2007, which was due to restructuring. More recently, the share has increased again to 10.8 % 2009 [8].

CHP provided 15.2 % of the total heat supplied in the EU-27 in 2009 (Figure 1.6). The figures of 2008 and 2009 cannot be compared, since the EEA has adjusted the methodology for calculating the heat production. The countries with a high market penetration are Finland (37.5 %), Denmark (32.0 %) and Sweden (29.4 %). Finland, Denmark and Sweden are countries with a high share of district heating, while Finland also has strong intensive industries which use CHP extensively [8].

The preferred fuel for new CHP plants is natural gas (Figure 1.7). The EEA identified the flexibility of changing the heat to power ratio as well as the better environmental performance compared to liquid fossil fuels as the main reasons for the large natural gas driven CHP. In recent years, CHP has suffered from increasing natural gas prices and falling electricity prices, a development which diminished the cost competitiveness of these plants. Other barriers included high costs for grid connection to sell surplus electricity, relatively high start-up costs and the design of the policy framework in some cases [8].

Natural gas accounts for 39 % of the fuel input in CHP plants in the EU. There is however a big difference between the EU-15 (53.6 %) and the new member states (22.6 %). The new member states still use a very large portion of solid fossil fuels like coal and lignite (74.2 % compared to 14.6 %). Compared to Belgium, the difference is even bigger with 77 % of the total fuel consumption being natural gas. The use of renewable energies (biomass) in combined heat and power provides an opportunity to further improve

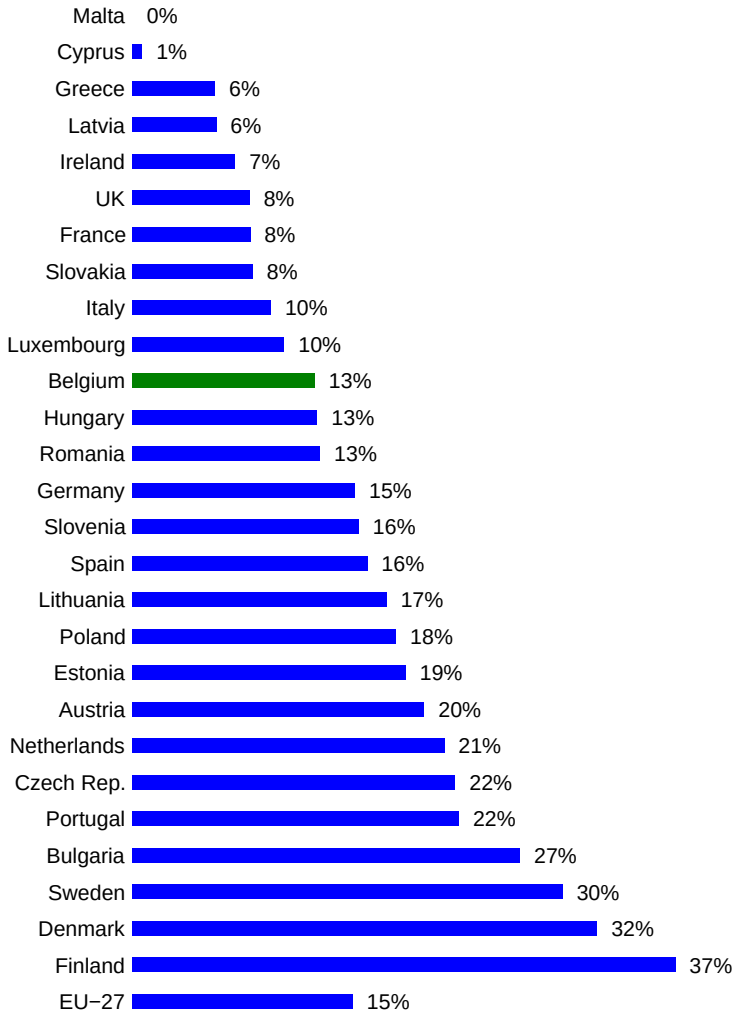

Figure 1.6: The share of CHP in the total heat production in the EU showing that countries with a high share of district heating have a high CHP market penetration [8].

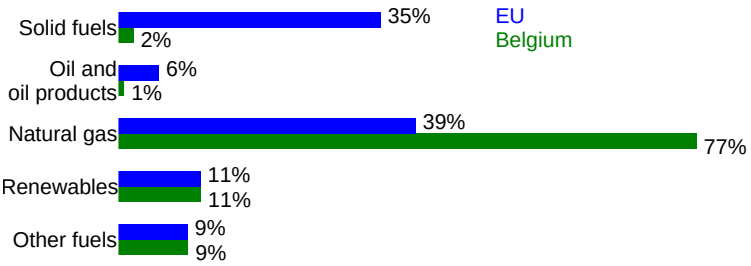

Figure 1.7: Natural gas has the largest share for CHP production both in Europe (EU-27, 39 %) and in Belgium (77 %) [8].

the environmental performance of CHP, while simultaneously increasing renewable electricity production. However, renewables provided only 11.0 % of the fuel input in CHP plants in the EU-27 and in Belgium [8].

The overall picture for CHP in Europe is mixed [9]. The current situation and prospects are good in some regions (like the Flemish region in Belgium) and some sectors. In most countries, a large uncertainty exists around CHP leading to a stagnation or decline of the CHP development. Most experts predict micro (below 50 kW_e) and small CHP (50 kW_e to 500 kW_e) for the domestic and commercial service sector to experience growth, together with renewable CHP. Larger CHP production, primarily used in industry or for district heating, and particularly gas fired CHP was identified as declining due to the crisis and increasing gas prices. Factors that determine the success of CHP are: economic downturn and poor financing opportunities for investments, political instability and unfavourable fuel prices versus the electricity prices [9].

CHP in Flanders

For the past twenty years, the total installed capacity of CHP units in Flanders has increased continuously (Figure 1.8). More recently, the installation of additional CHP units has slowed down due to the crisis. On the 31st of December 2013, a total of 1553 MW_e electric CHP capacity was installed in Flanders [10]. Gas Turbine (GT) based CHP accounts for 54 % of the total installed capacity (Table 1.1). This capacity is however divided

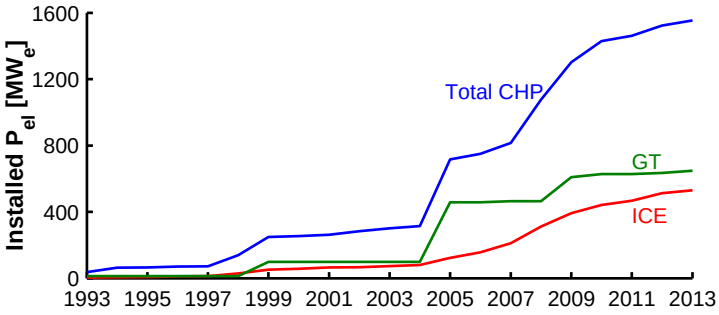

Figure 1.8: The total installed CHP capacity in Flanders has increased over the past twenty years [10].

Table 1.1: The installed electric CHP power in Flanders at 31/12/2013 of which the CHP certificates have been approved [10].

CHP primary mover	**Installed P_{el}**	**units**	**share**	**Power per unit**
Gas Turbine with heat recuperation	648 MW_e	12	41.7 %	54.0 MW_e
Internal Combustion Engine	531 MW_e	355	34.2 %	1.49 MW_e
Natural Gas-fuelled Combined Cycle	191 MW_e	2	12.3 %	95.7 MW_e
Counter pressure steam turbine	150 MW_e	10	9.7 %	15.0 MW_e
Drain condensation steam turbine	33.3 MW_e	2	2.1 %	16.7 MW_e
Stirling Engine	93 kW_e	24	0 %	3.8 kW_e
Other technologies	55 kW_e	1	0 %	55 kW_e
Total	1553 MW_e	406	100 %	3.83 MW_e

over a small number of units (14). CHP using an Internal Combustion Engine (ICE) as primary mover accounts for 34 % of the installed capacity divided over 355 different units. This indicates that on average, a GT based CHP unit has a capacity of 59.9 MW_e, while for the ICE, an average capacity of 1.49 MW_e is used. For small-scale CHP applications, consumers tend more towards ICEs.

1.1.3 mGT applications for small-scale CHP

mGTs offered new perspectives in small-scale (up to 500 kW_e) CHP production. mGTs in CHP mode are very cost effective: using mGTs in trigeneration can reduce the annual primary energy consumption by 3 to 5 % for office buildings and 6 to 10 % for hospitals [11] while the annual costs can be reduced by 4 to 18 % [12]. Using a non-recuperated cycle can even attain higher profit flows, but higher heat demands are necessary [13]. Additionally mGTs offer several advantages for small-scale CHP production compared to ICEs: reduced maintenance and engineering costs, a small amount of moving parts, lower noise and vibration level, multi-fuel capabilities and opportunities for lower emissions and cleaner exhaust [14]. The optimal power and number of installed mGT units depend on the specific CHP system and need to be determined on a case-by-case basis [15], as well as the optimal operating strategy [16, 17]. The economic incentives, provided by national politics, are very important to make mGT CHP production attractive [18]. Finally, the cogeneration planning suffers from this uncertainty, mainly depending on the evolution of energy loads and prices [19, 20].

Despite the advantages and the market potential for mGT CHP production, the installed capacity is still rather limited. mGT has a very low market share compared to ICE worldwide, in the EU and in Flanders (subsection 1.1.2). For instance in the United States, only a limited fraction, 6.5 %, uses a mGT as primary mover, while 48.0 % of the electricity is produced by ICE [21]. The major drawback of the mGTs is their heat-driven use. In periods with no or low heat demand, part of the heat should be discarded to keep the mGT operating at high electric load (Figure 1.9). For an equal power output, the mGT has a lower efficiency than the ICE [22]. Compared to ICEs, the lower electric efficiency of mGTs makes them less attractive in this case and economic constraints could even lead to complete shutdown. In addition, like the ICE, the efficiency decreases at part load, resulting in

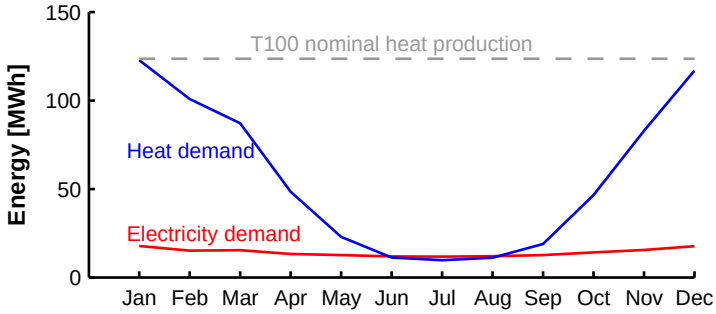

Figure 1.9: The monthly thermal demand of the user will determine the mean heat output of the mGT and therefore the operational settings (Data representative for the heat load of 61 EU dwellings [29]).

lower total efficiency [23]. The specific capital cost of mGTs is still high [24]. Due to this high capital cost, any shutdown has a severe negative effect on the economic performance of the mGT [25]. The mGT can be operated at variable thermal loads by bypassing part of the air over the recuperator, but this leads to a significant efficiency reduction of 50 % when bypassing 80 % of the compressed air [26]. In addition, mGT systems are currently not suitable for single-family residential applications ($< 10\,\mathrm{kW_e}$). Current mGTs are suitable for multi-family residential, commercial and institutional applications [27]. For mGTs in the 5 to $25\,\mathrm{kW_e}$ range, state of the art reaches efficiencies of 22.5 to 27 %. To increase the efficiency, ceramic mGT parts are necessary. The challenge for the success of the domestic mGT is to obtain low cost mGT manufacturing techniques [28]. All these different reasons make the mGT less attractive than the ICE for small-scale CHP.

1.2 Water injection to recover waste heat in mGT applications

A way to improve the overall economic performance of a mGT CHP unit is to improve the electric efficiency of the mGT during periods with low heat demand. Increasing the electric efficiency will make the mGT more competitive against the ICE. A possible route to improve the electric efficiency of the mGT is introducing water (vapour/liquid) in the cycle.

Water injection is considered a successful way to increase electric efficiency of GT cycles [30]. In periods with a low heat demand, the lost thermal power can be recovered by introducing auto-raised steam/heated water inside the mGT cycle, resulting in a more profitable investment [25]. The beneficial effect of steam/water introduction in a mGT on its performance has already been studied several times [31–40]. Lee et al. showed by means of simulations the beneficial effect of steam injection on the performance of a recuperated mGT cycle [31]. Dodo et al. equipped a 150 kW_e mGT with a Humid Air Turbine (HAT) and Water Atomizing inlet air Cooling (WAC) line. Experiments showed stable runs at 32 % electric efficiency and reduced NO_x exhaust [32]. Mochizuki et al. performed steam injections experiments on a Capstone C60 mGT. At 60 kW_e and injection up to 6 wt% steam/air ratio, thermal efficiency could be improved by 3 to 4 % absolute [33]. Parente et al. studied the thermodynamic [34] and the thermo-economic performance of a mHAT [35]. Zhang and Xiao studied the effect of the humid air on the performance of the different mGT components [36]. Wan et al. showed that the efficiency of the mHAT can be improved further by integrating an inverted Brayton cycle with the mHAT. The exhaust gases from the mHAT cycle are directly expanded to a pressure below ambient. For an optimal pressure ratio of 9 to 10, electric efficiency can be increased by 20 % relative [37]. Ferrari et al. injected steam in a hybrid system test rig to study the effect of a steam rich mass flow on engine behaviour. Test results showed that the mGT accepted the injected steam mass flow rate without surge problems [38]. More recently, Wei and Zang experimentally investigated the off-design behaviour of a small-sized (25 kW_e) HAT. Test results at constant fuel flow rate and constant Turbine Inlet Temperature (TIT) indicated significant power output increases of 3 and 9.5 kW_e [39]. Finally, most recently, in parallel with this work, Nikpey et al. simulated the effect of transforming a mGT into a HAT cycle on the plant performance. A final absolute electric efficiency increase of 1.7 % was predicted [40], which is the same order of magnitude as the results presented later in this thesis (section 5.2).

The optimal route for waste heat recovery in a mGT through water injection was found to be the conversion of the mGT into a mHAT (as will be described in section 5.1). The mHAT cycle was selected based on the high electric efficiency achievable, the relative low changes to the mGT CHP cycle resulting in low additional capital cost and the ability to operate with lower water quality. The conversion of the mGT into a mHAT still allows the production of heat, which makes the cycle the perfect candidate for

flexible heat production from a mGT.

Converting the mGT into a mHAT is economically feasible, in case the difference between the electricity prices and gas prices is large enough [29]. Montero Carrero et al. performed an economic feasibility analysis of a Turbec T100 mGT based mHAT facility for domestic applications. 25 natural gas and electricity price combinations have been taken into account. The analysis has been performed for two types of domestic customers: a *reference* consumer with a heat demand that requires 4118 h of dry operation (i.e. mGT operating as a CHP unit) and a *low-heat demand* consumer which only requires 2500 h of yearly dry operation. The CHP facilities were assumed to run only during the above-mentioned hours of dry operation whereas the mHATs run the remaining number of hours per year (up to 8040 h) with water injection (i.e. in wet mode) at elevated electric efficiency (3.8 % absolute efficiency increase). The results of this analysis show that the economic feasibility of the T100 mGT working as a CHP and as a mHAT strongly depends on the natural gas and electricity prices and on the relationship between these two variables. Higher Net Present Values (NPVs) are obtained with higher electricity and lower natural gas prices. For a given number of dry running hours and natural gas price, there is a threshold for the electricity price above which the mHAT becomes more profitable than the mGT working as a CHP unit. This threshold is very close to the limit of positive NPV, especially for the low-heat demand consumer. As expected, the profitability of the mHAT with respect to the CHP case becomes more interesting for consumers with a reduced number of running hours [29].

1.3 Motivation for the proposed research

The route towards flexible heat production from a mGT is unknown and requires additional research. Several studies have been performed on introducing water (steam/liquid) in the mGT, showing the beneficial effect of water injection in a mGT cycle. A general framework to develop a humidified mGT cycle for flexible heat production is however still missing. In this thesis, I developed such a framework for the optimal humidified mGT cycle. This framework consists of four major steps: cycle identification, cycle development, cycle construction and validation. First, dry and wet operation are simulated and experimentally validated to predict the correct mGT behaviour under humidified conditions. Afterwards, these models are used in the development phase to identify the optimal cycle layout using a

two-step method. As will be shown in section 5.1, this optimal cycle layout turns out to be the mHAT cycle. In the development process, this ideal model is converted in a model for the considered Turbec T100 mGT. At this stage, a proper water injection system for this cycle also had to be developed. The next step is the conversion of the mGT into a mHAT. The developed water injection system is constructed and integrated in the cycle, converting the Turbec T100 mGT into a mHAT. Finally, experiments are conducted on the constructed test rig. The experimental results are used to evaluate the mHAT performance and validate the developed model of this mHAT cycle.

1.4 Scope of the thesis

The scope of this thesis is the development of a humidified mGT cycle for flexible heat production (Figure 1.10). This thesis covers the entire development process of a Turbec T100 mGT based mHAT cycle, including the dry and wet characterisation, optimal cycle layout development, water injection system development and finally the test rig construction and experimental evaluation. As the overview in Figure 1.10 suggests, this thesis consists of seven different chapters to cover the entire route towards flexible heat production from a mGT.

In **chapter 2**, a literature review on the mGT and humidified GT cycles is conducted. Different methods to improve mGT performance are discussed. In a second section, the different types of existing humidified GTs cycles are briefly discussed, since similar effects are expected in the humidified mGT cycle. Finally, a literature study on the Turbec T100 mGT is presented. The aim of this literature review is to show the potential of the Turbec T100 as a candidate for the mHAT development.

The dry characterisation of the Turbec T100 mGT is discussed in **chapter 3**. For the design of the optimal humidified mGT cycle, it is crucial to have a correct simulation model of the dry mGT performance. Aspen® simulation results are validated against measurements. In addition, the recurrent problem of unwanted Exhaust Gas Recirculation (EGR) is analysed and discussed. A solution, the heightening of the stack, is found by performing wind tunnel experiments, using a simulated Atmospheric Boundary Layer (ABL) in the wind tunnel.

Next to the dry behaviour, it is also necessary to predict the mGT behaviour under steam injection conditions for humidified mGT cycle development. In **chapter 4**, steam injection experiments in the mGT cycle are discussed. Special focus was placed on the prediction of the mGT performance and the surge margin reduction. In addition, steam injection experiments were performed on a atmospheric, variable-swirl, premixed burner to quantify the effect of water on the combustion stability.

The humidified mGT cycle development is discussed in **chapter 5**. Optimal cycle layout is identified using a two-step method. First a black box analysis is performed to find the thermodynamic limit for water injection. Then using composite curve theory, the corresponding heat exchanger network design is found. Additionally, the effect of non-idealities on the final cycle performance is discussed. Finally, a spray saturation tower to humidify the air is developed using a two-phase flow model.

Chapter 6 gives an overview of the experiments conducted on the mHAT test rig. The developed test rig is discussed, focusing on the surge margin control, spray saturation tower and injection nozzle selection. In addition, specific start-up and shutdown procedures for the mHAT test rig are developed and analysed. Finally, experimental results are evaluated to determine the effect of air humidification on mGT performance and evaluate the test rig.

Finally, in **chapter 7**, the general conclusions are formulated. The final route towards flexible heat production from the mGT is evaluated. The developed mHAT test rig is discussed together with possible future improvements. In addition, a perspective is given. Necessary future developments for the fully flexible heat production of the mGT are discussed, since the current prototype is not yet ready for market entry.

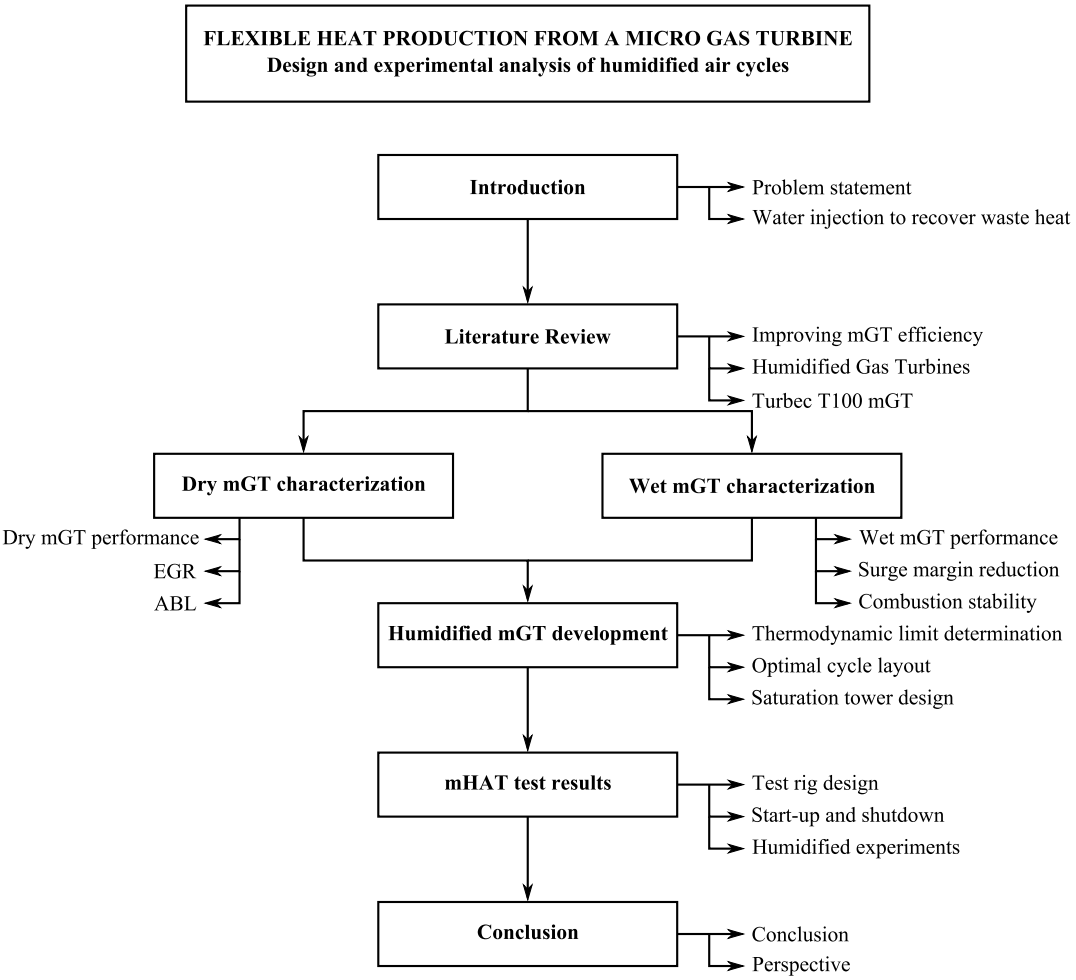

Figure 1.10: Overview – Scope of this thesis.

Chapter 2

Literature Review

In this chapter, a literature review on the mGT and humidified GT cycles is conducted. First, the different options to improve mGT performance – mGT components optimization and cycle innovations – are discussed. In a second section, the different types of existing humidified GT cycles are briefly elaborated on. In particular, the optimal humidified GT, the Humid Air Turbine (HAT) cycle, is studied in more detail. The different HAT pilot plants are analysed to find the major points of attention for humidified GT plant development. Finally, a literature study on the Turbec T100 mGT is presented. The aim of this literature review is to show the potential of the Turbec T100 mGT as a candidate for the mHAT development due to its potential to operate in off-design conditions or even with an adapted cycle layout.

2.1 Towards higher mGT efficiency

With state-of-the-art components, at nominal load and a recuperator inlet temperature of 700 °C, the expected maximal thermal efficiency is close to 30 % for a 50 kW_e mGT [41]. In his study, Rodgers identified the open recuperated mGT cycle as the cycle with the lowest relative costs and weight with near maximal thermal efficiency. In addition, he revealed the key parameters that have an impact on the mGT efficiency: TIT (maximal 1050 °C), recuperator inlet temperature (maximal 700 °C), pressure ratio (at least 3), component efficiency and limited parasitic losses (2 %) [41]. The two parameters that have the most potential for efficiency increase are increased TIT and higher recuperator effectiveness [42]. Since cooling of the small radial flow turbine is difficult, the TIT can only be increased if thermal resistant – ceramic – materials are introduced in the mGT. The use of these ceramic materials allows for a higher TIT, resulting in considerable energy savings [43]. McDonald and Rodgers indicated that a ceramic recuperator and ceramic radial turbine are necessary to achieve 40 % efficiency in a 200 kW_e mGT, since the thermal efficiency limit of an all-metallic mGT is 35 % [44], and provided a development approach for such a 7.5 kW_e ceramic mGT [45]. Campanari and Macchi showed that the high electric efficiency levels achievable with these future advanced ceramic mGTs would dramatically improve the economic competitiveness of the application, as well as the primary energy savings and environmental benefits [46]. By using a heat resistant coating technology, Kim and Lee were able to increase the TIT of their home made mGT by 100 °C, resulting in 20 % more power output and 6 % absolute increase in electric efficiency [47]. Increasing the recuperator efficiency is very straight-forward, but will however result in a significant increase in recuperator size, weight and cost [42]. Pressure drop over the recuperator should be limited, since a decrease of 1 % unit of pressure loss will increase the turbine efficiency by 0.33 % absolute [48]. McDonald proposes a basic concept for better heat exchanger design [49]. Traverso and Massardo showed that the use of a primary surface recuperator can decrease the volume and material weight by 50 % [50]. Finally, Galanti and Massardo indicated that increasing turbine and compressor efficiency by two percentage points would increase the global mGT efficiency by 2 % absolute without affecting costs in a significant manner [24].

An alternative for increasing the mGT performance by improving the component efficiency is modifying the original recuperated Brayton cycle. Introducing water in the mGT cycle has a positive effect on the cycle perfor-

mance (section 1.2). This option will be applied and studied in this thesis. Next to the introduction of water in the mGT cycle, other techniques exist to improve the thermodynamic efficiency. The most promising technique is the integration of a fuel cell with a GT: the so-called hybrid cycle [51]. The hybrid cycle achieves efficiencies up to 60 % [52]. Since the development of fuel cells is still ongoing, no hybrid cycles have been built so far. However several emulator test rigs are constructed and tested [53, 54]. In these test rigs, the coupling of the mGT to the fuel cell is experimentally studied. An alternative route is the use of biomass in the mGT cycle [55]. Two possible routes exist: the use of biofuels (gas/liquid) directly in the combustion chamber [56] or using an external combustion, the Externally Fired Gas Turbine (EFGT) [57]. The advantage of the EFGT is the use of solid or low grade biofuels [58]. External combustion requires lower fuel quality since the hot exhaust gases do not enter the turbine. The EFGT however requires a very expensive heat exchanger, resulting in higher capital cost [59], and the lower TIT results in a lower efficiency [58]. The direct use of biofuels achieves a higher efficiency due to a higher TIT. Using biofuels in the combustion chamber requires however higher fuel quality, combustion chamber redesign to cover the higher necessary fuel mass flow rate [56] and will result in higher emissions [60, 61]. Recovering the remaining waste heat in the exhaust gases improves the total efficiency. The waste heat can be recovered by coupling the mGT to an Organic Rankine Cycle (ORC), obtaining additional electric power resulting in an increased electric efficiency up to 40 % [62]. This requires however the installation of an additional cycle, which increases the capital cost [62]. Introducing solar energy in the mGT cycle reduces the fuel consumption and increases the efficiency [63]. This solution can however only be applied in regions with high solar energy and requires also the modification of the cycle, again resulting in higher capital costs [63]. Finally, chemical recuperation offers some perspective. The chemically recuperated mGT may be effective for improving the power generation efficiency and lowering the NO_x emissions [64], however many research still needs to be performed before this cycle can be built.

2.2 Humidified Gas Turbine

In the past, researchers have been looking for possibilities to improve the performance of GTs by recovering heat from the exhaust gases [65]. Heppenstall analysed different cycle layouts; including the combined, Kalina, gas/gas

recuperation, steam injection, evaporation and chemical recuperation cycles. He predicted that the dominance of the combined cycle will continue in the medium term for large-scale production. He also indicated that the combined cycle may however be mechanically too complex for small-scale operations and that for these applications, other schemes will help to meet specific application requirements [65].

GTs with mixed air/water as working fluid promise high electrical efficiency, high specific power output, low NO_x exhaust and are applicable on a wide power range [30]. Jonsson and Yan divided these mixed air/water GTs into three categories [30]:

- GTs with injection of water that fully evaporates (Figure 2.1(a));
- GTs with injection of steam (Figure 2.1(b));
- GTs with injection of water in a humidification tower, with a recirculation water loop (Figure 2.1(c)).

These different cycles have been studied by different researchers. Some examples: Alhazmy and Najjar showed that the power of the GT can be enhanced by 1 to 7 % and efficiency by 3 % using a spray to cool the inlet air by 3 to 15 °C [66]. Kang et al. showed that both power and efficiency of a regenerative steam injection GT cycle improved by 45 % and 10 % respectively [67].

Since the possibilities for water introduction in the GT cycle are very wide, several researchers tried to identify the optimal way for water introduction in the cycle [68–72]. Gallo compared the HAT cycle with other GT based cycles [68]. Traverso and Massardo performed a thermoeconomic analysis on mixed gas-steam cycles, comparing them with a Natural Gas-fuelled Combined Cycle (NGCC). The study shows that mixed cycles become extremely competitive for sizes under 10 MW_e, where the thermodynamic performance of the bottoming steam cycle quickly decreases in NGCC applications [69]. Haselbacher studied the effect of applying water/steam injection on existing turbo machines compared to adjusted turbo machines. Final results indicated that no thermal efficiency penalties need to be accepted when using existing turbo machines [70]. Nishida et al. studied the performance characteristics of regenerative steam injection GT systems. They indicated that the thermal efficiency of the system is improved by steam injection through the exergy recuperation from the exhaust gases

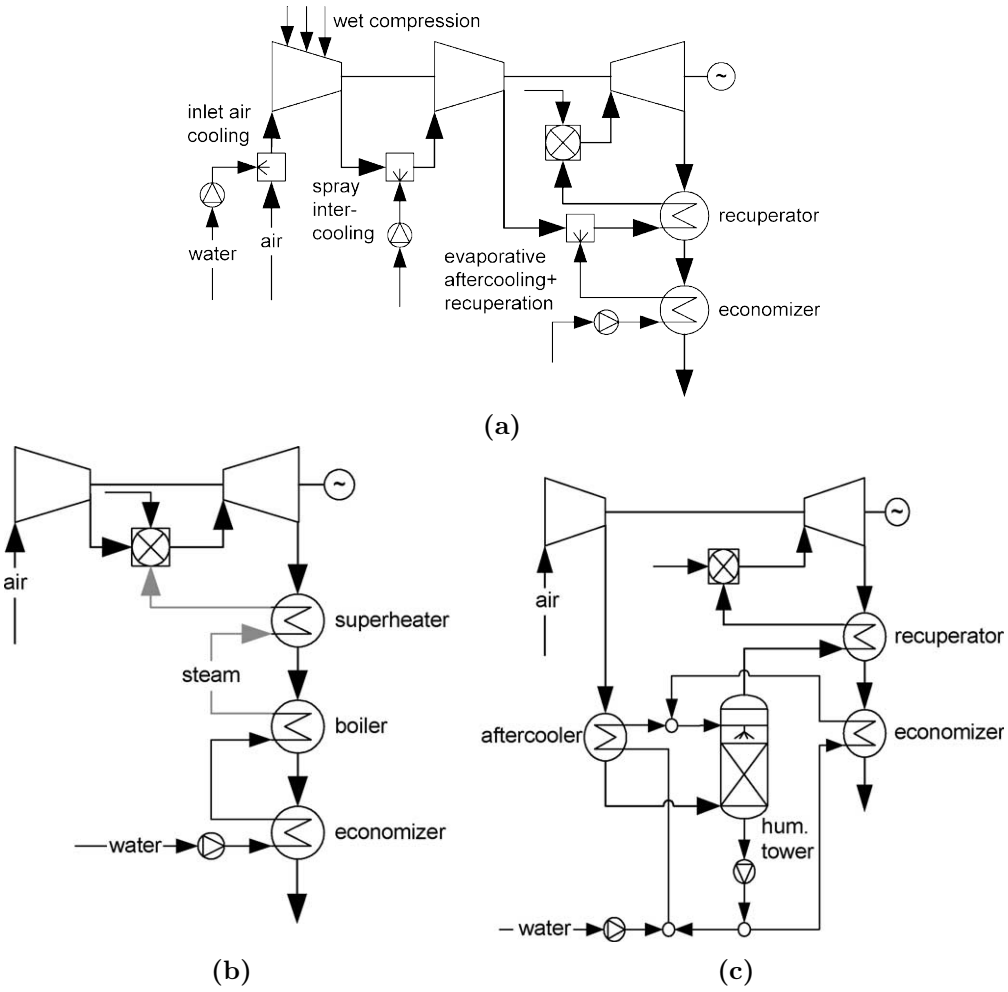

Figure 2.1: Schematic water-injected inlet air cooling system (the water is added as a fog of water droplets or in a media cooler), wet compression system, spray intercooling system and system with evaporative aftercooling and recuperation (a), steam-injection gas turbine (b) and one possible evaporative gas turbine cycle (c) [30].

[71]. Finally, Roumeliotis and Mathioudakis evaluated the water injection at different places in the GT cycle [72]. All of these studies only consider a limited amount of routes to introduce water. Finally, it was De Ruyck et al., who proved that the HAT cycle, as initially proposed by Rao [74, 75], has the highest potential among the mixed air/water GTs. By searching the thermodynamic limit for water introduction in the GT cycle using black box analysis, De Ruyck et al. showed that the HAT cycle approached this limit, identifying this cycle as optimal humidified GT cycle [73].

Since the HAT was first presented in 1989 by Rao [74], several researchers have focused on improving the cycle efficiency [76–81]. Kim et al. studied the influence of ambient conditions on the thermodynamic performance of the HAT cycle. While a higher inlet air temperature results in a lower specific power for GT and NGCC cycles, the specific work of the HAT cycle will increase due to a higher humidifier inlet temperature. This allows more water to evaporate, resulting in increasing power production, compensating for the higher compressor power [76]. Lazzaretto and Segato optimized the original HAT cycle and tried to adapt the heat exchanger network design [77, 78]. The highest efficiency can only be achieved by minimizing the temperature of the compressed air after the aftercooler. In addition, aftercooling is only effective when the heat can be used in the saturation tower [77, 79]. Lazzaretto and Segato also found that for pressure ratios between 10 and 30, maximum efficiency is achieved by using one intercooler, one aftercooler and one economizer [78]. Kavanagh et al. used a different, multi-objective optimisation – the tabu search optimisation algorithm – to optimize the HAT cycle. They identified pressure ratio and recuperator efficiency as key parameters. Depending on the final objective – high efficiency, high specific work or low cost of electricity or a trade-off between both – different optimal pressure ratios and recuperator efficiencies were found [80]. Finally, Nyberg and Thern studied the HAT cycle, indicating that the water temperature in the economizer and the aftercooler should be maximized before maximizing the water mass flow rate. The optimal point for extraction of the turbine cooling flow is after the aftercooler and finally, the make-up water must be injected at the coldest point, being the intercooler. This will reduce the compressor work [81].

In addition to the optimization studies, several other researchers focused on HAT operation [82–89]. Desideri and Di Maria indicated that using the waste heat of the water recovery system to feed an ORC increases the HAT cycle efficiency by 1.6 % [82]. von Heiroth et al. modelled the HAT cycle in CHP operation [83]. When using pre-humidification, the HAT CHP cycle

efficiency can be above 100 % [84]. Ågren and Westermark developed a control strategy for part-load HAT operation. They proposed a strategy where only part of the compressed air is humidified and the exhaust gas is used to produce steam [85, 86]. The economic performance of this cycle was studied by Bartlett and Westermark [87, 88]. Hu et al. indicated that CO_2 capture in the HAT cycle is possible, with a loss in efficiency of 10.5 % or 11.8 %, depending on the absorption mechanism (chemical or oxyfuel). The CO_2 cost and the cost of electricity is however still lower than in the NGCC case [89].

Different variants of the HAT were developed: the Cascaded Humidified Advanced Turbine (CHAT) [90], TOP Humid Air Turbine (TOPHAT®) [91], REgenerative EVAPoration (REVAP®) [92] and the Advanced Humid Air Turbine (AHAT) [93] cycles. The CHAT cycle was developed to overcome the problem of the flow mismatch that exists between compressor and turbine in the original HAT design [90]. In the TOPHAT® cycle, the hot water generated by the economizer is used for spray compression between the different compressor stages, reducing the compressor work [91]. Kavanagh and Parks indicated that the TOPHAT® has thermodynamically a higher performance than the HAT cycle [94]. The cycle is however much more complex and the cost of electricity must be taken into account when optimizing and designing the power plant [95]. The REVAP® cycle, developed by De Ruyck et al., has a performance similar to the HAT cycle, but the saturation tower is removed [92]. The AHAT cycle substitutes the intercooling from the HAT cycle by WAC [93]. An advantage of the AHAT over the HAT cycle is the use of a heavy duty single shaft GT. In addition, the AHAT achieves the same electric efficiency as the HAT at lower pressure ratios. The major advantage of the AHAT compared to the NGCC is the short start-up time, which gives more flexibility to the power plant, and the higher part-load efficiency [96].

Despite the high potential of the HAT cycle and its variants, no commercial power plants have been constructed so far. Only one HAT cycle pilot plant, the Evaporative Gas Turbine (EvGT) project, has been constructed and successfully tested in Lund since the development of the HAT cycle layout. The evaporative cycle without aftercooling achieved a thermal efficiency of approximately 35 % [30, 97]. In addition, Hitachi has constructed a series of AHAT demonstration plants [98].

Since 2004, Hitachi has been participating in a national project to develop a AHAT plant. The final goal of Hitachi is to enter the market with a AHAT

plant of 100 to 200 MW_e [98]. Over a power range from 2 to 200 MW_e, the AHAT is known to have the highest potential (Figure 2.2) [99]. Initially, Hitachi started with the development of a 150 kW_e mGT with 35 % electric efficiency, equipped with a WAC and a HAT line to simulate the effect of inlet air fogging and compressed air humidification. Initial dry test results resulted in 150.3 kW_e electric power output with an electric efficiency of 32 % [32]. This mGT was also equipped with water-lubricated bearings. The heat of the bearings could be re-injected in the cycle [100]. A 3 MW-class AHAT verification plant was built from April 2005 till September 2006. The plant consists of a two-stage radial compressor (pressure ratio of 8), a two-stage axial turbine, a reverse-flow single-can burner, a recuperator, a saturation tower, a water recovery tower, an economizer and auxiliaries. The rated output was 3.6 MW_e with an electric efficiency of 43 % [101]. Special humid air blade cooling was applied on the turbine blades [102]. 30 tests were performed, resulting in an electric power output of 3990 kW_e at 40.02 % electric efficiency. The efficiency was slightly lower than predicted due to sensor losses and a lower TIT to protect these sensors. NO_x levels were slightly reduced [103]. The compressed air was fully saturated, but only 95 % of the water could be recovered. In addition, NO_2^-, NO_3^- and SO_2 ions were found in the water circuit. The SO_2 ions were coming from the inlet air (similar observations were done by Ågren et al. during the EvGT project [97]), indicating the necessity to purify the recovered water [104]. During the tests, no inter-annual changes were observed in the pressure drop, temperature effectiveness and the overall heat transfer coefficient of the recuperator [105]. Finally, the results of the 3 MW-class verification plant were used to develop and construct a 40 MW-class test facility [98]. Tests were started to verify practicalities of the AHAT system for a heavy duty GT. During the tests, the WAC system, the flame stability and control system and the hybrid cooling of the first nozzle were successfully tested [106]. Additional tests showed that the cold start-up time from ignition to rated power was approximately 60 min. In addition, the water recovery exceeded 100 % of the evaporated water [107].

Both the EvGT project in Lund and the AHAT project of Hitachi have shown the potential of humidifying a GT cycle and similar potential is expected for the mHAT cycle. First experiments with water (liquid/steam) injection showed already the potential of the mGT for humidification (see section 1.2). Both projects showed also the necessary steps before building a test rig: full characterisation of the different GT parts, optimisation of the cycle layout and correct simulation of the saturation tower.

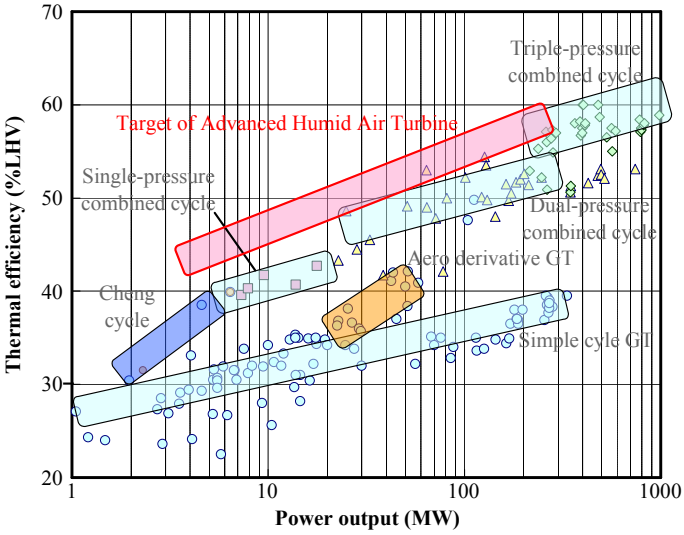

Figure 2.2: The target output of the AHAT cycle is in-between 2 to 200 MW (Figure adapted from [99]).

Humidifying a GT cycle has not only a positive effect on the GT performance, but will affect the surge margin, combustion and requires a specific water quality [30]. Due to the additional mass flow through the turbine, the compressor surge margin will reduce. This can possibly lead to compressor surge. In addition, the water will affect the combustion, leading to possible combustion stability issues: reduced combustion efficiency, unstable combustion and increased CO emissions. Finally, depending on the water introduction method, a different water quality is required. Depending on the requested water quality, more energy is required to provide the make-up water. Throughout my PhD-thesis, at each step of the route towards flexible heat production from a mGT cycle through humidification, I focused on these three critical points.

2.3 Research on the Turbec T100 mGT

The Turbec T100 mGT is widely used by researchers working on mGT applications. This section tries to give an overview of the current conducted research on the T100 mGT. This overview will show that the Turbec T100 mGT is the perfect candidate for a mHAT pilot plant, due to its ability to operate in off-design conditions and with an adapted cycle layout.

Only a small number of mGT providers exists (Table 2.1). The development as well as the production and marketing primarily takes place in the USA and Japan [108]. Turbec is the only European mGT manufacturer. Turbec, previously owned by ABB and Volvo, was purchased by the Italian-based Ansaldo Energia [108]. In all these mGTs, high revolution turbochargers (50 000 to 120 000 rpm) are used and recuperators are necessary to achieve high electric efficiencies [109]. The major difference between the different models is the integration of the recuperator. A first possible design is the annular recuperator. In this case, the recuperator is wrapped around the aero-derivative core. Examples are the Capstone C30 and C60. The major advantages of such an integration is the low heat losses and the very compact size. An alternative design is a separated recuperator, like in the Turbec T100 mGT. The mGT package is larger, but the different parts are much more accessible. An overview of the specifications of the mGTs models can be found in [110].

The steady-state and transient performance of the Turbec T100 mGT engine is well known in literature [112–118]. Colombo et al. performed experiments

Table 2.1: Current mGT (nominal electric power output less than 200 kW_e) manufacturers [111].

Manufacturer	Range of models
Capstone Turbine Corporation	30 and 60 kW_e (next 200 kW_e)
Elliot Energy systems Inc.	80 kW_e
Turbec AB	100 kW_e
Bowman Power Ltd.	50 and 80 kW_e
Ingersoll-Rand Energy Systems	70 kW_e (next 250 kW_e)

on a T100 mGT CHP plant at variable load (50 to 110 kW_e in steps of 10 kW_e) and changing water temperature (from 60 to 80 °C in steps of 5 °C). They indicated that the performance remains constant in the range 80 to 110 kW_e. From 80 to 60 kW_e, a moderate decrease was observed, while a further reduction in power output implies a clear worsening of the performance [112]. Caresana et al. found a similar behaviour, resulting in an electric efficiency reaching 29 % in the 80 to 100 kW_e range [113]. Caresana et al. also showed that increasing the inlet temperature by 1 °C results in a 1.22 % absolute reduction in electric power output [114]. Both Colombo et al. and Caresana et al. saw that the NO_x emissions where low over the whole mGT working range (<6 ppm), while the CO concentration increased substantially at low electric loads (from 4 ppm at 100 kW_e to 600 ppm at 50 kW_e) [112, 113]. Ming et al. also indicated that the lowest emissions are achieved at full-load power output [115]. In addition, Ming et al. saw that emissions are significant higher during start-up. CO emissions are 50 times higher compared to steady-state operation, while NO_x and SO_2 emissions are five times higher. They indicate that start-up transient cannot be neglected and should be considered when comparing techniques on environmental impact [116]. Finally, Ferrari et al. experimentally analysed the primary-surface recuperator, focusing on the thermal transient performance of the component, indicating the effect of temperature and flow steps [117, 118].

Since the performance of the Turbec T100 mGT is well identified, the mGT is a widely used mGT in CHP case study calculations in literature (some examples: [119–122]). Caruso et al. presented a case study were a CCHP system with absorption chiller, driven by a T100 mGT, will be installed. Yearly energy savings of 52 000 Nm^3/y natural gas or 90 $tonCO_2/y$ are expected [119]. Aguiar et al. simulated the use of a T100 mGT as CHP unit in the ceramic industry [120], while Costea et al. used the T100 mGT as basis GT for their optimization of a cogeneration system with various heat

exchanger configurations [121]. Finally, Martirano et al. performed a case study on a microgrid with a T100 mGT for nearly zero-emission buildings [122]. More examples of studies using the T100 mGT in CHP applications can be found in literature. To develop a full mathematical model of the mGT, detailed and exact component characteristics are necessary. As an alternative to these complex mathematical models, Nikpey et al. developed an Artificial Neural Network (ANN) for the CHP T100 mGT. ANNs, in contrast to mathematical models, do not require these detailed and exact component characteristics, which makes them applicable for monitoring in many cases. Their developed ANN model was validated using measurements on their T100 test rig [123, 124].

Next to the simulations and experiments on the existing T100 mGT, researchers try to improve the mGT performance applying the different techniques from section 2.1. The separate recuperator in the Turbec T100 mGT makes the mGT very popular by researchers working in innovative cycles since novel components can easily be integrated in the cycle.

The studies on humidifying the Turbec T100 mGT, except for the work presented in this thesis, presented in literature, are limited [34, 35, 38, 40]. As mentioned in section 1.2, Parente et al. and Nikpey et al. studied the thermodynamic [34, 40] and thermo-economic performance of a T100 mGT converted to HAT cycle [35]. On the experimental work, only Ferrari et al. performed some steam injection experiments in their T100 test rig [118].

In the hybrid cycle, the mGT can be coupled with two types of fuel cells: a Molten Carbonate Fuel Cell (MCFC) or a Solide Oxide Fuel Cell (SOFC). The coupling of a Turbec T100 mGT with both types of fuel cells has been studied in literature [125–129]. Both Orecchini et al. and Leto et al. showed that for a hybrid cycle coupling a T100 mGT in CHP mode with the MCFC high electric efficiencies (up to 60 %) and total efficiencies (over 70 %) can be achieved [125, 126]. Similar efficiencies are expected for the hybrid cycle T100 mGT-SOFC coupling (up to 63 % electric efficiency, depending on the power) [127]. Di Carlo et al. simulated the effect of the use of internal and external reforming MCFC, fuelled with syngas from an atmospheric-pressure biomass gasification. They showed that the MCFC with internal reforming could reach 38 % efficiency [128]. In addition, they also simulated the used of a T100 mGT coupled to a SOFC with enriched air/steam fluidized bed gasifier plant. The system has a total efficiency (including gasification) ranging from 36 to 44 %, which is much higher than the one obtained burning the woodgas in an ICE (up to 30 %) [129].

Two hybrid cycle emulator test rigs with a Turbec T100 mGT have been built and are currently in operation. Both plants simulate the effect of coupling a SOFC to the T100 mGT. A first emulator test rig was constructed at the University of Genova, Italy [53]. The T100 mGT is equipped with a set of external pipes for the connection of the machine with a modular vessel that allows the connection with additional innovative cycle components such as the SOFC [53]. Additionally, an inlet air cooling system was added to the system for inlet air temperature control [130]. The test rig was used to develop a control strategy for the stand-alone hybrid configuration [131] and verified this strategy successfully experimentally [132]. A hardware-in-loop strategy was used for the simultaneous control of the fuel cell temperature and power [133]. Test results showed stable produced power output and temperature. Changing the state takes about 20 s, because faster transitions can lead to instabilities [133]. In addition, an emergency shutdown strategy to avoid the differential pressure between cathode and anode of the fuel cell exceeding maximum acceptable levels was developed. Hazardous conditions could be avoided by adjusting the bleed valve and cold air bypass valve and especially, the anode fuel mass flow rate [134]. Finally, the cathode-anode interaction was experimentally analysed with this emulator test rig [135]. The second Turbec T100 emulator test rig was constructed at the German Aerospace Centre (DLR) in Stuttgart, Germany [54]. Zanger et al. simulated the effect of the pressure loss on the surge margin. Bleeding air and reducing Turbine Outlet Temperature (TOT) will keep the compressor away from surge, but has a negative effect on the mGT output and performance (increasing the surge margin by 100 % results in an electric power loss of 5.8 and 10.3 kW_e, when using respectively bleeding air or reduced TOT) [136]. More recently, Hohloch et al. studied and characterized the impact of the coupling elements. The transient behaviour during start-up, load change and shutdown was analysed. To avoid critical operating conditions and emergency situations, the bleed-air blow-off was demonstrated as a promising manoeuvre [137].

As discussed in section 2.1, using biomass is an alternative route to enhance the mGT economic performance. Also on the Turbec T100 mGT, researchers performed experiments with direct use [138–143] and indirect use of biomass [144–148]. Nikpey et al. performed experiments combusting various mixtures of natural gas and biogas in a standard T100 mGT. The fuel consumption increased due to the lower Lower Heating Value (LHV) of the biogas, however no significant changes were observed in measured performance parameters and electric efficiency was almost constant. A maximum of

26 % biogas could be mixed with natural gas [138]. The results of this study demonstrate the viability of burning a mixture of natural gas and biogas in a standard mGT. Tests on another T100 mGT with a biogas-methane mixture (58 %) resulted in an electric efficiency of 27.4 % [149]. Cameretti and Tuccillo performed similar experiments with gaseous fuels from biomass treatment and solid waste pyrolysis. They however noticed that when using pure biogas, a sort of off-design operation was induced by the employment of low calorific value fuels in both combustor and in the whole T100 mGT [139]. Leach reported on several T100 mGTs running on landfill and sewage gas [140]. More than 5000 to 7000 operating hours could be achieved without problems and without any signs of corrosion, erosion or deposition in the burner. Flue gases however condensed in the economizer, resulting in corrosion, since the T100 economizer is made of non-stainless steel. In addition, several problems arose with the fuel valves, indicating these valves should be improved. Finally, compressing landfill gas to 6 bar may cause problems in the fuel supply line, since the dew point is at that pressure around 60 to 80 °C [140]. A similar experiment with a landfill gas fuelled T100 mGT was performed in Ylivieska, Finland [141]. Finally, both Delattin et al. and Cadorin et al. performed combustion experiments with syngas in a T100 combustor. No problems regarding auto-ignition and dynamic or static instabilities were observed. Temperature stayed within the limits [142, 143]. Delattin et al. performed a stable run of half an hour at 60 kW_e load. NO_x and CO emissions were lower [142]. Additionally, in the ZECOMIX project, researchers plan to run a T100 mGT on syngas provided from coal gasification [150]. The aim of this project is to produce hydrogen and electricity from coal with zero emissions and very high efficiency. The combustion chamber had to be modified because of the decarbonized syngas fuelling. Therefore, the T100 mGT will be retrofitted with a hydrogen burner ARI100TR developed by Ansaldo Energia [151].

The possibility to transform the Turbec T100 mGT into a EFGT has been studied widely in literature [144–148]. Cocco et al. predicted an electric efficiency of 22 to 33 %. In addition, the hot flue gases allow to dry 3.5 to 4 times the necessary biomass fuel, which indicates that there is still a possibility for CHP [144]. Kautz and Hansen also predicted that the efficiency is close to the high efficiency realised in the mGT with recuperation. The primary objective for the conversion would be the optimization of the recuperator and the heat exchanger [145]. The thermal performance of the EFGT strongly depends on the TIT [146]. Riccio and Chiaramonti simulated that, when using 100 % biomass in a T100 mGT based EFGT, TIT

would drop to 805 °C, resulting in an efficiency of 15 % [146]. Camporeale et al. predicted that for the T100 mGT, a full biomass combustion with TIT of 900 °C would lead to an efficiency of 19.2 % [147]. Cofiring biomass and natural gas offers a solution, since higher TIT (950 °C) can be achieved [146, 147]. In this case, the electric efficiency will increase to 21.9 %, when the biomass contribution to the primary energy feed is 70 % [146], while Camporeale et al. predicted an efficiency of 24.0 % for a biomass fraction of 50 %. Although the natural gas fired T100 mGT has the highest conversion efficiency and achieves the highest energy savings, a 70 % biomass cofired T100 EFGT has a higher profitability due to the lower cost of biomass [148]. Finally, several T100 mGT based EFGT for CHP generation from solid biomass test rigs have been constructed in Italy: two 75 kW_e units running on wood chip, producing a thermal power of 200 kW_{th}, and a 75 kW_e and 50 kW_e plant, running on manufacturing residuals [152]. The plants achieved respectively 1700, 1700, 2000 and 2500 operating hours. By burning wood chips with a 38.8 % moisture content, a total net efficiency of 17.7 % was achieved in the 75 kW_e plant, while the heat exchanger efficiency was 68 % [152]. Finally, Cordiner and Mulone reported on a converted T100 EFGT fuelled by dry pinecone. An electric power output of 70 kW_e was achieved with an electric efficiency of 13 %. The decrease of performance is due to the lower TIT, equal to 850 °C [153].

For the integration of solar power in the mGT cycle, Amsbeck et al. has developed and integrated a tube receiver for the conversion of a Turbec T100 mGT into a solar-hybrid mGT system [154]. This solar-hybrid mGT system was tested at the Plataforma Solar de Amería. The design inlet and outlet temperature of the collector were respectively 600 and 800 °C. The solar receiver was tested for more than 100 h showing that the collector outlet temperature was lower due to a lower mass flow rate, resulting in lower mGT power and efficiency [155]. Buck and Friedmann calculated that this system can reach break even in certain cases. In addition, they also found that, to optimally use the advantages of the high exhaust temperature of the mGT, a double-effect absorption chiller should be integrated [63].

Only one application of the coupling of an ORC with a T100 mGT for waste heat recovery could be found in literature [156]. Clemente et al. used different expanders and working fluids to optimize the ORC cycle for the T100 mGT. R245fa, iso-pentane and iso-butane where found more suitable for this application because of the lower volumetric ratio during the expansion. This allows the use of a smaller single-stage machine. In addition, the study indicated that no specific type of expander was preferred

for this power range, since all machines revealed advantages and drawbacks [156].

Finally, since the Turbec T100 mGT performance is well known, the cycle is also used to calculate more exotique GT cycles, like the mirror heat exchange Brayton cycle, where the recuperated Brayton cycle is coupled with a reversed cycle [157].

2.4 Conclusion

In this literature review, an overview of the existing techniques to improve the mGT economic performance has been presented. A first possible route is the improvement of the thermal efficiency of the cycle by improving the performance of the components. Using ceramic materials in the mGT cycle results in higher energy savings. Secondly, the economic attractiveness of the mGT can be enhanced by modifying the cycle. Possibilities are humidification, hybrid cycles, the use of biomass, waste heat recuperation and chemical recuperated cycles.

In the second part of the literature review, the different types of existing humidified GT cycles were briefly discussed. In particular, the optimal humidified GT, the HAT cycle, is studied in more detail. The two HAT demonstration plants (the EvGT and the AHAT project) were analysed to find the major points of attention for humidified GT plant development: surge margin reduction, combustion stability and water quality. Throughout this thesis, I will focus on these three critical points.

Finally, all existing research on the Turbec T100 mGT was summarized. This overview showed that the Turbec T100 mGT has the possibility to operate in off-design conditions and with an adapted cycle layout without major modifications to the basic mGT. This proves that the T100 mGT is the perfect candidate for mHAT cycle development.

Chapter 3

Dry mGT characterization

In this chapter, I will discuss the different steps towards the full dry characterization of the Turbec T100 mGT. In a first section, the dry modelling of the mGT in the Aspen® software package will be discussed together with the additional experiments performed to validate the dry performance of the T100 mGT. In the second section, I address the issue of the recurrent problem of EGR, responsible for the unsteady performance of the T100 mGT in the past. Both steady-state and dynamic effects of EGR on the mGT performance are discussed. To define the necessary minimal stack height, wind tunnel experiments were performed, including the ABL simulated in the industrial wind tunnel at the Vrije Universiteit Brussel (VUB).

3.1 Dry mGT performance

The Turbec T100 mGT CHP system is based on the recuperated mGT (Figure 3.1). The inlet air enters the compressor (1). The compressed air is preheated in the air recuperator by the hot flue gases (2). In order to obtain the best performance, the compressed air is heated until maximal TIT (950 °C) by burning natural gas in the combustion chamber (3). The hot gases expand over the turbine (4), providing the necessary power to drive the compressor. The remaining power is converted into electric power by the high-speed generator (5). The excess heat, available in the exhaust gas at the outlet of the recuperator, is used to heat water for heating purposes in the economizer (6).

The Turbec T100 mGT CHP package has a nominal electric power production of 100 kW_e at standard conditions defined by the constructor (15 °C and 1.013 bar [158], see Table 3.1). When water with a temperature of

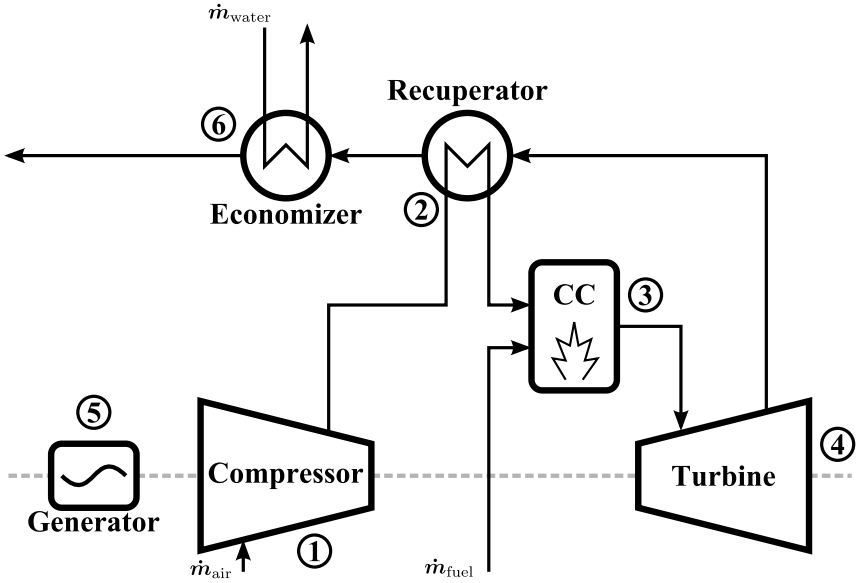

Figure 3.1: The compressed air (1) is preheated by the flue gases in the recuperator (2) and heated in the combustion chamber (3) by burning natural gas. Expanding the hot gases over the turbine (4) provides the power to drive the generator (5). Finally, the residual hot flue gases are used to heat water for domestic heating purposes (6).

Table 3.1: Nominal specifications of the Turbec T100 mGT CHP package, given by the constructor Turbec AB [158].

Nominal electric power	100 kW_e
Nominal thermal power	167 kW_{th}
Nominal electric efficiency	30 %
Nominal thermal efficiency	50 %
Maximal shaft speed	70 000 rpm

50 °C is delivered to the economizer in nominal operating conditions, the water will be heated till 70 °C, resulting in a thermal power production of 167 kW_{th}. In nominal operating conditions, an equivalent of 333 kW of natural gas (LHV) is consumed. This results in an electric and thermal efficiency of 30 and 50 % respectively (LHV-based). The T100 mGT reaches a CHP efficiency of 80 %. The maximal allowed rotational speed by the engine control system is equal to 70 000 rpm.

The T100 mGT is equipped with an engine control system to keep the electric power production constant. By changing the shaft speed (resistive torque), the T100 mGT control system keeps the produced electric power output constant at a user-defined set point (between 60 and 100 kW_e). The compressor and turbine operate thus at the same variable shaft speed, which results in a variable mass flow rate and pressure ratio. The engine control system uses pre-defined tables to track the optimal speed for a given requested power output and inlet air temperature, rather then using a Maximum Power Point Tracking (MPPT) control strategy. In addition, the control system will aim to keep the electric efficiency high. So besides the shaft speed, the fuel flow rate is also controlled in order to maintain TIT at its maximal value of 950 °C. The variable shaft speed and constant TIT allow the T100 mGT to operate at high part-load electric efficiency [158]. Rather than controlling TIT, TOT is controlled. Measuring TIT is technically not possible. Therefore, TIT is calculated out of the measured TOT using fixed built-in correlations. By keeping TOT constant and equal to 645 °C at nominal electric load, TIT will remain constant at 950 °C. Finally, the engine control system will also keep the outlet water temperature constant. The produced thermal power can be controlled by routing part of the exhaust gases directly to the stack and thus bypassing the economizer. This will however lower the thermal efficiency of the mGT, which characterizes again the major problem of the mGT as CHP. Due to the lower part-load thermal efficiency, global mGT operation is mainly heat driven.

3.1.1 Dry Aspen® simulations of the Turbec T100 mGT

The Turbec T100 mGT is fully modelled in the Aspen® plus process simulator (Version 2006.5) [159]. Aspen® plus is a process simulation tool that predicts process behaviour using engineering relationships such as mass and energy balances, phase and chemical equilibrium and reaction kinetics. With the inclusion of extended thermodynamic data, equipment models and the input of realistic operating conditions, the software package is able to simulate actual plant behaviour [159].

The dry Aspen® plus model of the mGT was developed by Delattin et al. [25] and will be briefly explained in this section. The compressor was modelled using the compressor map provided by Turbec (Figure 3.2). Both constant speed lines and efficiency areas were introduced in the compressor model. These constant speed lines are constructed using super-ellipses[1] to fit the points taken from the compressor map provided by the constructor [160]. Super-ellipses were used for two reasons. First, the whole map can be continuously represented, which eliminates variations in the constant speed lines that are inherent to the discretization process. Secondly, fitting the constant speed lines with super-ellipses provides an analytic formula for the compressor map. This analytic representation of the compressor map is necessary for the perturbation analysis (see later: subsection 4.1.2). A total of 15 constant speed lines with each giving 21 points are introduced in Aspen®. The Aspen® plus process simulator will use interpolation between these lines to find the operating point. Additionally, the surge line of the compressor has also been added to the Aspen® model of the compressor (Figure 3.2). Delattin et al. initially also used maps to model the turbine. Turbine efficiency and outlet pressure remained however constant over a large variety of parameters [25]. Therefore, the turbine was defined with a constant turbine outlet pressure and isentropic efficiency. A turbine outlet pressure of 1.05 bar is assumed, which allows the exhaust gases to overcome the head losses in recuperator, economizer and stack. An isentropic efficiency of 85 % is used. In addition, the turbine is assumed to be choked. This means that for a given TIT and Pressure Inlet Turbine (PIT), the mass flow rate is fixed and determined by the section of the turbine and the properties

[1] A super-ellipse is a geometric figure, defined by $\left|\frac{x}{a}\right|^n + \left|\frac{x}{b}\right|^n = 1$, where $n > 0$ and a and b the radius of the oval shape. In case $n = 2$, the formula describes a normal ellipse.

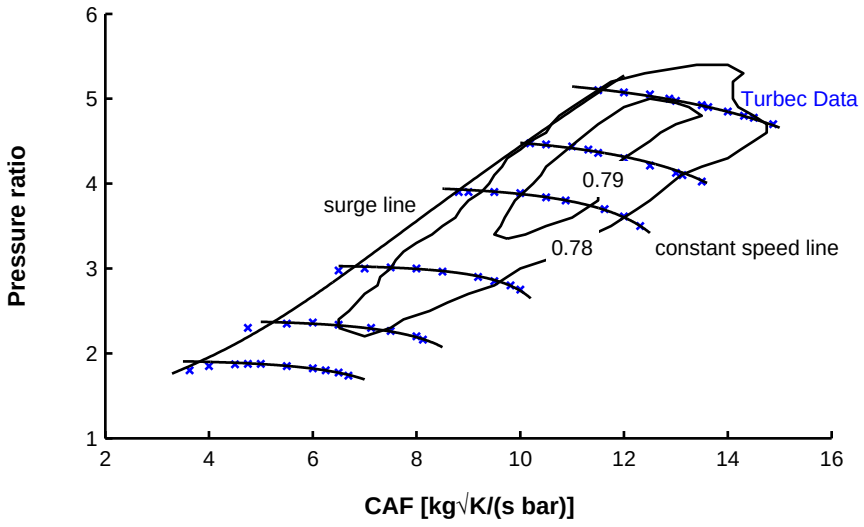

Figure 3.2: The compressor map used for Aspen® simulations is based on the original data provided by Turbec. The constant speed lines are constructed using super-ellipses.

of the fluid, which is expressed as follows [161]:

$$\frac{\dot{m}_{\text{turb}}\sqrt{\text{TIT}}}{\text{PIT}} = A\sqrt{\frac{k_{\text{turb}}}{R}\left(\frac{2}{k_{\text{turb}}+1}\right)^{\frac{k_{\text{turb}}+1}{k_{\text{turb}}-1}}} = cte \tag{3.1}$$

where k_{turb} corresponds to the heat capacity ratio of the turbine working fluid, R is the universal gas constant and A is the cross section area of the turbine. In the dry model, the RHS of Equation 3.1 results in a constant value since the composition of the working fluid remains more or less constant. The choking constant is assumed $6.50\,\text{kg}\sqrt{\text{K}}/\text{s}/\text{bar}$. The recuperator is modelled using the NTU-method and using data from Lagerström and Xie [48]. The recuperator is a combination of cross-flow inlet and outlet areas and a counter-flow main body. The NTU values were corrected for these different layouts. The combustion chamber is modelled as a Gibbs free energy reactor. Pressure losses between compressor exhaust and turbine inlet were concentrated in the combustion chamber for convergence reasons (10 % of compressor exhaust pressure). Since data provided by Turbec AB indicate very low CO and Unburned Hydrocarbons (UHC) emissions (less than 15 and 10 ppm respectively [158]), the combustion is assumed complete (combustion efficiency equal to 100 %). In addition, $10\,\text{kW}_{\text{th}}$ heat loss over the combustion chamber is assumed. This $10\,\text{kW}_{\text{th}}$ heat loss combines all heat losses to the ventilation air.

For each operating point of the compressor, the Surge Margin (SM) is calculated in Aspen®. SM can be defined according to Walsh as follows:

$$\text{SM}\,(\%) = \frac{\pi_{\text{comp,surge}} - \pi_{\text{comp,working}}}{\pi_{\text{comp,working}}} \cdot 100\,\%, \tag{3.2}$$

where $\pi_{\text{comp,surge}}$ is the pressure ratio at the surge line and $\pi_{\text{comp,working}}$ the pressure ratio at the compressor operating point [162]. An alternative method for SM calculation is as follows:

$$\text{SM}\,(\%) = \left.\frac{\dot{m}_{\text{comp,surge}} - \dot{m}_{\text{comp,working}}}{\dot{m}_{\text{comp,working}}}\right|_{N=cte} \cdot 100\,\% \tag{3.3}$$

where $\dot{m}_{\text{comp,working}}$ is the mass flow rate at the current operating point and $\dot{m}_{\text{comp,surge}}$ is the air flow rate through the compressor at the surge limit for the same compressor speed [163]. The definition of SM from Equation 3.2 is more applicable for axial compressors, where the constant speed lines are more vertically towards the surge limit. A small change in compressor mass flow rate results in a large change in pressure ratio close to surge. Since

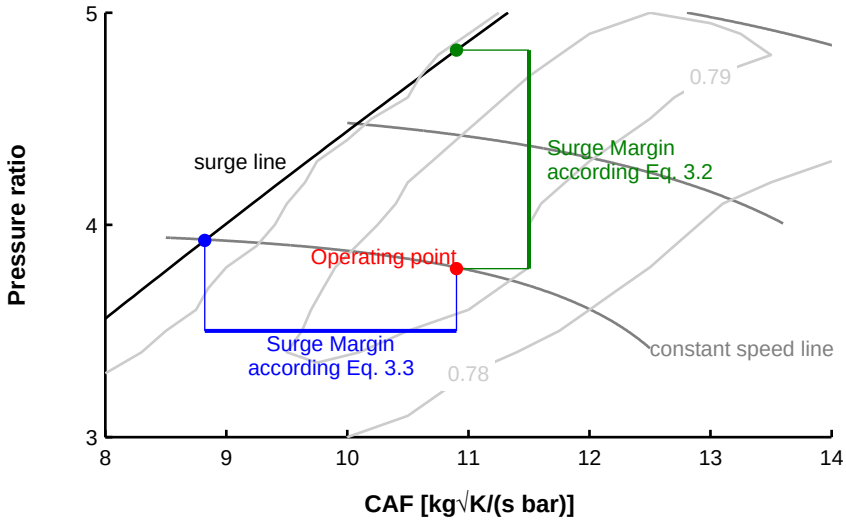

Figure 3.3: Calculating the Surge Margin (SM) using the mass flow rate (Equation 3.3) is more appropriate for radial compressors than using the pressure ratio (Equation 3.2), since for constant rotational speed, a small change in pressure ratio has a huge effect on mass flow rate close to the surge limit.

the T100 mGT has a single-stage radial compressor, it is more appropriate to calculate SM using Equation 3.3. The constant speed lines for a radial compressor are more horizontal towards the surge limit. A small change in pressure ratio results in a large change in compressor mass flow rate for a constant rotational speed. The difference between the two calculation methods for SM is illustrated in Figure 3.3.

The existing controller of the T100 mGT is implemented in the Aspen® model. In the Aspen® model, constant electric power and TOT are thus set as design specifications. The electric power can be calculated taking the difference between turbine and compressor power. The efficiency of the power electronics and the mechanical transmission is 99 %. An additional design specification is given by the turbine choking condition (Equation 3.1). To set these design conditions, the link between the different properties needs to be determined. A first link exists between produced turbine and consumed compressor power. The produced turbine and consumed compressor power

depend on the performance of both components. Since compressor maps were used to simulate the compressor performance, final electric output is a function of the rotational speed ($f(N)$). Secondly, the constant TOT depends on the amount of combustion air and natural gas entering the combustion chamber. Finally, the choking condition depends on the turbine mass flow rate ($\dot{m}_{\text{turb}}$), which is the sum of the compressor air ($\dot{m}_{\text{air}}$) and the natural gas mass flow rate ($\dot{m}_{\text{natgas}}$). Additionally, TIT and PIT also influence the choking constant, but as mentioned before, PIT is function of the rotational speed (N) and TIT can be assumed constant. Following three equations need thus to be solved to get the design specifications [25]:

$$\frac{(\dot{m}_{\text{air}} + \dot{m}_{\text{natgas}})\sqrt{\text{TIT}}}{\text{PIT}} = 6.50\,\text{kg}\sqrt{\text{K}}/\text{s}/\text{bar}; \tag{3.4}$$

$$P_{\text{net}} = \eta_{\text{mech}}\eta_{\text{powel}}(P_{\text{turb}} - P_{\text{comp}}); \tag{3.5}$$

$$\text{TOT} = f(\dot{m}_{\text{air}}, \dot{m}_{\text{natgas}}). \tag{3.6}$$

By varying the shaft speed (N), inlet air ($\dot{m}_{\text{air}}$) and natural gas ($\dot{m}_{\text{natgas}}$) flow rate, the Aspen® solver can converge to a solution, respecting the design specifications.

All three equations are introduced in Aspen® as a design specification. Figure 3.4 shows the implementation of the design specifications in Aspen®. $\dot{m}_{\text{air}}$ is varied to fulfil the choking condition (1). Afterwards, $\dot{m}_{\text{natgas}}$ is varied to obtain a TOT of 645 °C (2). Finally, N is varied to keep $P_{\text{net}} = P_{\text{net}}^{req}$ (3). The different parameters influence each other. These three design specifications are therefore integrated in three iterative loops. By solving these equations, the final solution can be found. Convergence is reached for TOT when the final difference on the temperature is less than $1e^{-8}$. P_{net} is considered converged when differences are smaller than $1e^{-5}$ and $1e^{-4}$ for the choking condition. Final computational time depends on the given initial conditions. Each iterative loop is broken when convergence is not reached after 30 iterations, resulting in a convergence error. Depending on the initial conditions, convergence can be reached or not.

For the calculation, the RKS-BM property method – which is implemented in Aspen® – was used. The RKS-BM method uses the Redlich-Kwong-Soave cubic equation of state with Boston-Mathias alpha function for all thermodynamic properties. This property method is recommended for gas-processing, refinery and petrochemical applications [164]. The Pure 13 database is used as database for the different used components.

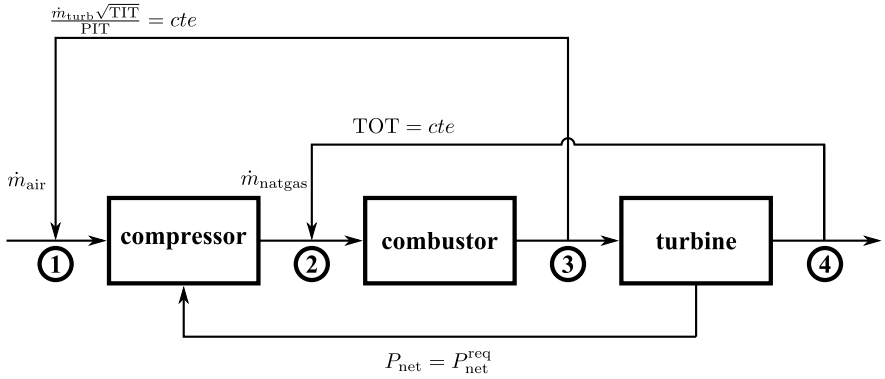

Figure 3.4: The Aspen® model of the mGT contains one iterative loop per design specification. These design specification are: turbine choking condition, constant TOT and constant electric power production.

3.1.2 Experimental dry simulation model validation

A reliable dry mGT model is necessary to be able to predict the performance of the humidified mGT. The dry Aspen® simulation model was validated in the past by Delattin et al. [25]. Due to the recurrent EGR problem, discussed later in this chapter, extra validation of this model was necessary. Therefore additional experiments were performed for model validation. During this validation, I focused on compressor map validation. Water introduction in the mGT cycle will result in a shift of the operating point of the compressor. For correct wet mGT validation, a correct compressor map is necessary.

To measure the mGT performance, the installation was originally equipped with different measuring devices. A first possible data source is the mGT control system. The parameters from the control system can be accessed in two ways: through the Turbec operator's website, where average data over 90 s is displayed, and by logging in directly into the control PLC using WinNap software and a serial cable. Logging into the control PLC allows the visualisation of the different parameters seen by the control system with a higher sample rate. The second data source is the surrounding of the mGT. Different sensors are installed to capture the performance. the signal of these sensors is collected using *Yokogawa* MX110 analog and MX115 digital modules (Figure 3.5).

The produced electric power was measured internally by the mGT control system and externally using the *Socomec Diris Ap* measurement device in combination with measurement coils, with an accuracy of 1 % of the measured value. Externally measured electric power was lower than the values given by the mGT control system. The *Socomec* measuring devices takes into account the consumed power by the auxiliary natural gas scroll compressor. This auxiliary power can vary, depending on the natural gas flow rate and the temperature in the T100 mGT operating room. Therefore, the measured power of the control system was used. The accuracy of this sensor is however not known. A standard error of 1 %, typical for power measurements of International Standard IEC 61053-21 class 1 [165], was used. The inlet air temperature is measured before entering the building, using a K-type thermocouple (±2 K), and inside the T100 casing, using another K-type (±2 K) thermocouple. For the post-processing of the measurements, the temperature measurement inside the T100 mGT casing is used. This sensor is positioned the closest to the compressor inlet, giving the most accurate determination of the compressor inlet air temperature. The natural gas flow rate is measured in front of and behind the natural gas compressor,

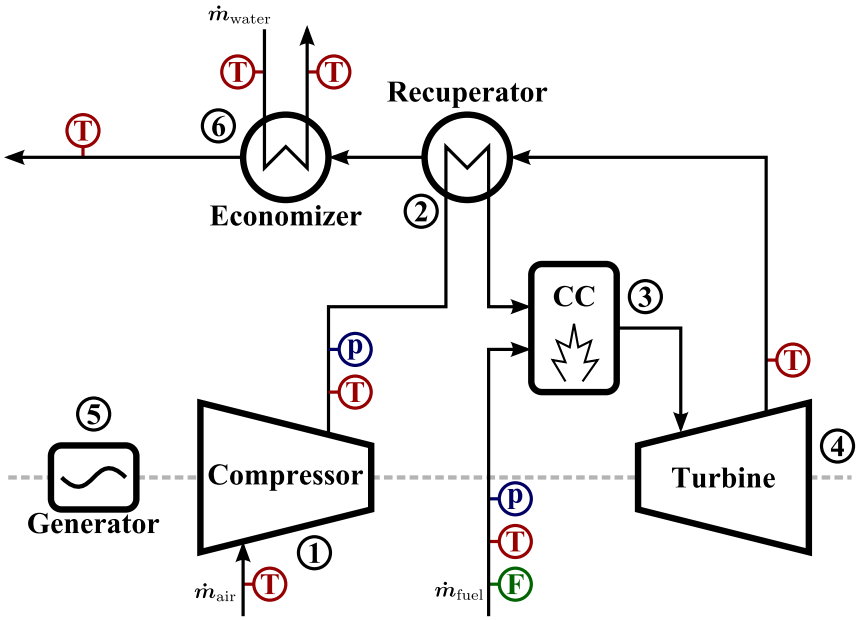

Figure 3.5: To capture the mGT dry performance, the Turbec T100 mGT has been equipped with different sensors.

using respectively an *Actaris* diaphragm meter (accuracy 0.5 %) and a *Yokogawa digitalYEWFLO* vortex flow meter with accuracy 1 % of the reading. Water temperatures are measured using *Siemens QAE170B* Pt100. The rotational speed is measured using an optical rotary encoder. Since the rotational speed is measured in the control system, the error on the measurements is also not known. An error of 0.1 % of the reading is typical for such techniques. The LHV was obtained using data provided by the gas supplier. In the past, the data was available on a daily basis. However, recently, it was no longer possible to obtain these data. Therefore, old data from March 2008 have been used in all simulations and calculations. The standard deviation of this old data was calculated, indicating a standard deviation of 0.84 % on the LHV-value. In addition, based upon the given composition, the LHV has been recalculated in Aspen®, resulting in a difference of 0.17 % with the LHV provided by the supplier. Therefore, an error of 1 % on the LHV has been taken into account.

The electric efficiency η_{el} of the T100 mGT can be calculated using following formula:

$$\eta_{\text{el}} = \frac{P_{\text{el}}}{\dot{m}_{\text{natgas}}\text{LHV}}. \tag{3.7}$$

Using Equation 3.7, the error on the electric efficiency can be determined:

$$\left|\frac{\Delta\eta_{\text{el}}}{\eta_{\text{el}}}\right| \leq \left|\frac{\Delta P_{\text{el}}}{P_{\text{el}}}\right| + \left|\frac{\Delta\dot{m}_{\text{fuel}}}{\dot{m}_{\text{fuel}}}\right| + \left|\frac{\Delta\text{LHV}}{\text{LHV}}\right|. \tag{3.8}$$

Using the accuracy on the electric power and fuel flow rate measurement, together with the accuracy on the LHV, results in a relative accuracy of 3 % on the calculated efficiency.

The error on the measured efficiency could be reduced by using integral electric power and natural gas flow rate measurements. Integral measurement techniques have typically an accuracy of 0.5 % of the reading, which will reduce the relative uncertainty on the calculated efficiency to 2 %. The drawback of these integral measurement techniques is that it is impossible to capture transient behaviour and that as the test needs to be conducted over a longer period to increase the accuracy. Depending on the conducted experiment and especially during wet experiments as will be shown later, it was not possible to keep the mGT operating in steady state conditions for a long period, which would make the use of integral measurement techniques not favourable.

The installation was equipped with additional sensors, allowing the reconstruction of the compressor map. A differential pressure sensor (*Yokogawa EJX*, accuracy 0.015 % of the span) was chosen to measure the outlet pressure of the compressor for pressure ratio determination. An additional Pt100 for compressor outlet temperature measurement (1 % error) was installed between the compressor outlet duct and the recuperator. In the compressor map (Figure 3.2), rather than using the compressor mass flow rate, the Corrected Air Flow (CAF) is used. The compressor operation depends on the inlet temperature and pressure. By using the CAF,

$$\mathrm{CAF} = \frac{\dot{m}_{\mathrm{air}}\sqrt{T_{\mathrm{in}}}}{p_{\mathrm{in}}}, \tag{3.9}$$

compressor performance becomes independent of inlet temperature and pressure. To determine the CAF, the compressor mass flow rate needed to be measured. Direct measurement of the compressor mass flow rate is not possible due to the specific design of the Turbec T100 CHP package. Part of the air entering the casing is used for case cooling purpose. Measuring the air mass flow rate behind the compressor is also not possible since the necessary in- and outlet runs of typical sensors for volumetric flow rate measurements could not be guaranteed. An alternative was proposed by measuring the O_2 content of the exhaust gases without condensing the combustion water. The measurement of the O_2 content in the exhaust gases, in combination with the measurement of the natural gas mass flow rate, allows the calculation of the inlet air mass flow rate by expressing the combustion balances. The O_2 concentration is determined using a Zirconia Oxygen Analyzer (*Yokogawa*) with an accuracy of 1 % on the full-scale reading (25 mol%). Reference for the O_2 content was taken before experiments were started. In the combustion balances, full combustion of the natural gas is assumed, since there is a large air excess (total Air-Fuel ratio (AF) of 90). A lean pre-mix emission type combustion chamber is used, achieving low emissions of NO_x, CO and UHC in the exhaust gases.

The air mass flow rate can be determined through the AF:

$$\mathrm{AF} = \frac{\dot{m}_{\mathrm{air}}}{\dot{m}_{\mathrm{natgas}}}. \tag{3.10}$$

The AF can be determined by expressing the combustion balance:

$$\mathrm{C}_a\mathrm{H}_b\mathrm{O}_c\mathrm{N}_d + e\,(0.21\mathrm{O}_2 + 0.79\mathrm{N}_2) + k\mathrm{H}_2\mathrm{O} \rightarrow f\mathrm{CO}_2 + g\mathrm{H}_2\mathrm{O} + h\mathrm{O}_2 + i\mathrm{N}_2. \tag{3.11}$$

The link between the combustion balance and the AF is given through the coefficient e:

$$e = \mathrm{AF}\frac{\dot{M}_{\mathrm{natgas}}}{\dot{M}_{\mathrm{air}}}. \tag{3.12}$$

Expressing conservation of mass of the different elements gives a set of four equations:

$$f = a; \tag{3.13}$$
$$g = b/2 + k; \tag{3.14}$$
$$h = 0.21e - a - b/4 + c/2 + k/2; \tag{3.15}$$
$$i = d/2 + 0.79e, \tag{3.16}$$

where h is known through the measurement of the O_2 content in the exhaust gases, while k can be calculated taking the injected steam flow rate. Solving Equation 3.16 allows the determination of the different coefficients, AF and air mass flow rate. Final accuracy on the calculated mass flow rate of compressor inlet air amounts to 4 %.

Several tests on the original mGT layout (Figure 3.1) have been performed for Aspen® model validation, resulting in 98 h of dry mGT operation. The different tests were performed at different inlet air temperatures and requested power outputs. After changing the requested power output, the mGT was kept running for at least 1 h. During data post-processing, the initial 20 minutes after mGT start-up or restart after an error were discarded, since initial test results had indicated that the mGT needed approximately 15 minutes before steady-state conditions were achieved. A constant inlet air temperature during the tests is crucial for correct mGT performance analysis. Therefore, the data was divided in blocks of at least 15 minutes, since the inlet temperature is constant over these intervals. Data intervals were cut 2 minutes before an error-provoked, forced or operator-controlled shutdown or a requested change in power output. After changing the requested power output, 2 minutes waiting time for mGT stabilization was taken into account. Figure 3.6 gives an example of a test, performed and post-processed according to the described procedure.

Part-load Aspen® simulations show good correspondence to the experimental results, while nominal load simulations show only moderate correspondence (Figure 3.7 and 3.8). Measurement data at 80 $\mathrm{kW_e}$ validate the Aspen® simulations for different inlet air temperatures (Figure 3.7), except

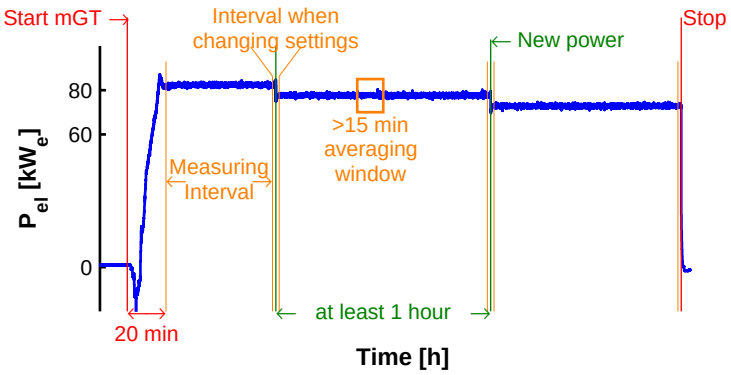

Figure 3.6: During the experiments, each power level was maintained for at least one hour. In the post processing, after removing start-up (first 20 minutes after start-up) and transient behaviour (first 2 minutes after changing the requested power output and last 2 minutes before changing to a new power output or mGT shut down), the measured data divided in blocks of at least 15 minutes and averaged over these intervals.

for very low temperatures (around 0 °C), where the measured efficiency is much higher than the simulated efficiency. This results in a standard deviation for the part load simulations below 1.2 % (not including experiments below 5 °C), which can be considered as a good correspondence. For nominal load, good correspondence exists between experiments and simulations at low temperature (below 15 °C, red diamonds on Figure 3.8). For higher inlet air temperatures, the difference between simulations and experiments is considerably. The lower electric efficiency can be explained by the action of the controller. At high inlet air temperature, more turbine power is consumed by the compressor to reach the necessary compressor outlet pressure. To keep the produced electric power constant and equal to the nominal load (100 kW_e), the compressor has to speed-up. The maximum rotational speed is however limited to 70 000 rpm. Once this speed is reached, the compressor is not allowed to accelerate by the control system. This results in a non-optimal mGT operation at lower produced electric power and electric efficiency (red circles on Figure 3.8), explaining the difference between experiments and simulations.

Most dry experiments were performed at part load (80 kW_e) since the mGT was connected to the VUB heating system [166]. The produced thermal power was injected in this system in the secondary loop. When the temperature outside was not low enough, the thermal load on the heating system was not high enough to compensate for the injection of thermal energy on the system. In this case, the water temperature in the secondary loop of the heating system in building Z started to increase, resulting in a local disturbance in the heating system. Since the boilers of the heating system are installed in the primary loop of the heating system and the effect of the mGT cannot be seen in this loop, there is no compensation for this additional heat injection. Boiling of the water in the secondary circuit needed to be avoided at any time.

For the inlet air temperature measurement, the internal sensor in the T100 mGT has been used. During a mGT run, the room of the T100 starts to heat up due to the heat losses from the T100. Since the air has to travel through several meters of piping before actually entering the T100 casing, the inlet air has already slightly heated, compared to the initial outside air temperature. As indicated in Figure 3.7, increasing the inlet temperature has a negative effect on mGT performance. Therefore, it is of great importance to measure inlet air temperature as close as possible to the actual compressor inlet.

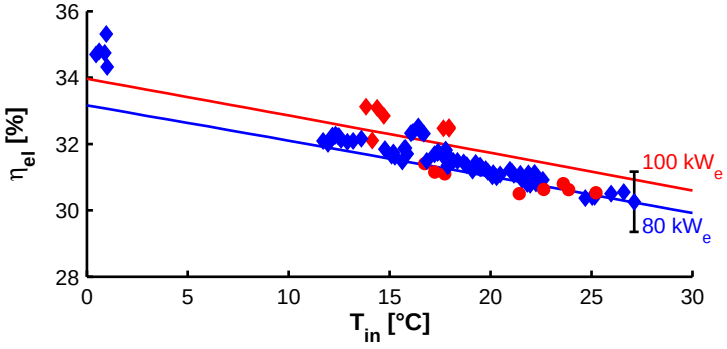

Figure 3.7: Experimental results of T100 mGT at part load (80 kW_e) show good correspondence to the Aspen® simulations over a wide temperature range (standard deviation of 1.2 %), while the experimental results at nominal load (100 kW_e) only show moderate correspondence. The limitation of the control system (mGT operation at maximum rotational speed, red circles) lead to a non-optimal mGT operation and the lower electric efficiency. As expected, electric efficiency increases with decreasing inlet air temperature, due to decreasing compressor work.

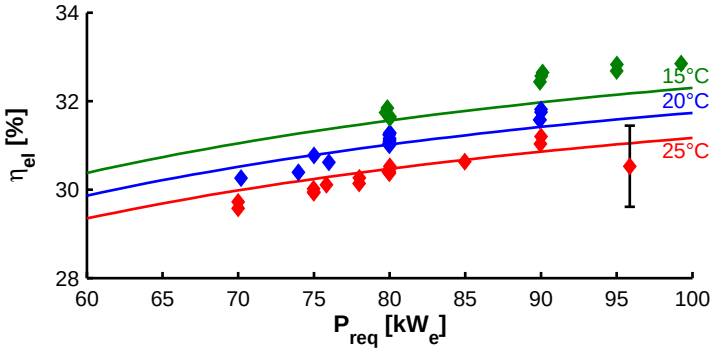

Figure 3.8: Experimental results of T100 mGT at different power output and inlet air temperature between 14.5 and 15.5 °C, 19.5 and 20.5 °C and 24.5 and 25.5 °C show respectively good correspondence to the Aspen® simulations at 15 °C, 20 °C and 25 °C (standard deviation below 1 %). Part-load efficiency is lower than nominal load efficiency.

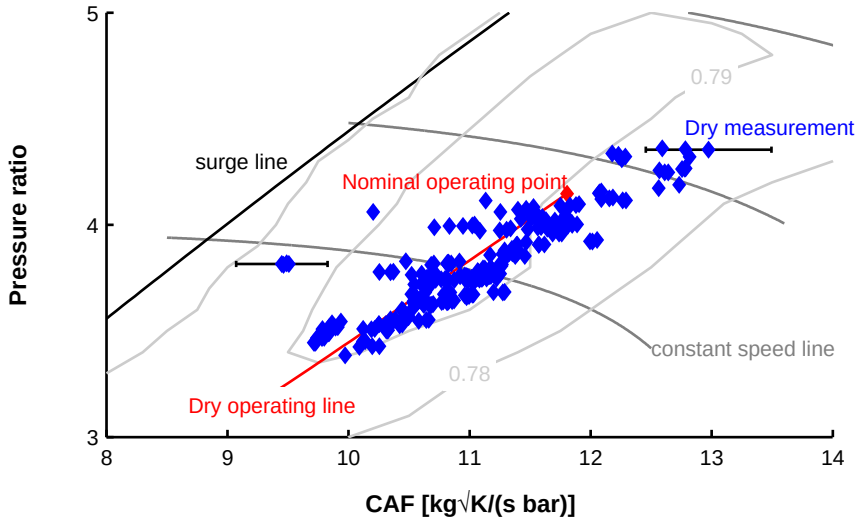

Figure 3.9: The measured dry operating point corresponds well with the predicted dry operating line from Aspen® when taking into account the accuracy on the compressor mass flow rate.

Measurements at different requested power outputs showed good correspondence to the nominal and part-load Aspen® simulations (Figure 3.8, standard deviation below 1 %). This indicates that the Aspen® model is not only able to predict nominal mGT performance, but also part-load performance. For the Aspen® simulations, inlet air temperatures of 15 °C, 20 °C and 25 °C have been used. During experiments, the inlet air temperature cannot be controlled, inlet air temperature depends thus on the weather conditions. Since not enough data at 20 °C was available, all measurements from experiments performed with a compressor inlet air temperatures between 18.5 and 21.5 °C have been used. Aspen® simulations indicate at nominal load an efficiency increase of 0.1 % for every temperature decrease of 1 °C.

Results of dry measurements also show good correspondence to the simulated compressor operating line in Aspen® (Figure 3.9). By performing experiments at nominal and part load of the mGT, the dry operating line could be re-created. As mentioned before, the mGT control system will change the rotational speed to keep the produced power output equal to

the user-defined requested power output. The dry operating line shows the simulated operating point of the mGT compressor for power output ranging from 60 to 100 kW_e. The experimental data are scattered, which can be explained by measurement errors on the results of the CAF calculations (4 % of the measured value). In addition, a systematic error exists between simulations and experiments. Aspen® simulations predict lower pressure ratios and air mass flow rates than measured. Both measurement and simulation results however follow the same trend at changing rotational speed. A second explanation for the scatter is the hot water outlet temperature control system. Next to the requested power output, the operator can also set the requested hot water outlet temperature. Depending on the produced electric power, a different thermal power is available. In order to match thermal load and thermal power production, the T100 control system can bypass part of the hot flue gases, resulting in a different back pressure for the mGT and a different operation point on the compressor map. Experimental results however still correspond well with reference data.

3.2 Exhaust Gas Recirculation (EGR) problem

During the first dry and wet tests on the Turbec T100 mGT, a very unsteady operation of the mGT was observed. This unsteady operation resulted in fast varying produced electric power and several flameouts. This unsteady operation caused some problems characterizing the dry and wet mGT behaviour. Partial EGR was identified to cause the unsteady mGT operation.

In our case, the phenomenon is unwanted and generates problems, but EGR in GT cycles may offers three major advantages: higher CO_2 concentration in the exhaust gases, lower flue gas mass flow rate and lower NO_x emissions. The higher CO_2 concentration in the exhaust gases in combination with a lower flue gas mass flow rate makes post-combustion amine-based carbon capture more economically feasible in NGCC [167]. Therefore EGR on NGCC has been investigated in the past by means of simulations and experiments [167–179]. Li et al. have shown that, compared to a cycle without EGR, a recirculation ratio of 50 % could increase CO_2 concentration from 3.8 to 7.9 mol% and reduce the mass flow rate of flue gases, fed to the absorber, by 51.0 % [168, 169]. With oxygen enrichment, the EGR ratio could principally be increased further [167, 170]. Experiments on a GE Dry Low-NO_x GT combustor at EGR ratios of 30 % [171] and 35 % [172] showed an operation with high efficiency and increased CO_2 levels

of more than 8 vol% and 10 vol%. ElKady et al. predicted that with only minor modifications, the combustor can be operated with EGR levels above 40 % [172]. In addition, ElKady et al. also demonstrated that NO_x emissions decrease with increasing EGR levels, by more than 50 % at an EGR ratio of 35 % [172]. The CO emissions however are a limiting factor for EGR. Although a flame can be sustained at O_2 concentration as low as 14 mol%, the levels of UHC and CO become excessively high when the O_2 concentration reaches 16 mol% [173], which indicates that an EGR ratio exceeding 40 % could be difficult to achieve for the combustor [169, 170]. Based upon the advantages of EGR and the recommendations formulated by different researchers, different novel types of NGCC with post-combustion CO_2 capture using a 40 % EGR ratio have been presented in literature [174–179]. The third positive effect of Dry-EGR, the reduction of NO_x emissions, has recently been studied in mGT combustors by means of CFD simulations [180–182] and experiments [183]. Both experiments and simulations indicated the potential to control NO_x emissions by EGR.

In our specific case however, the EGR is a random, uncontrollable and unwanted phenomenon, which causes an unstable operation of the mGT and should therefore be prevented.

The exhaust and ventilation stack are located directly above the air intake of the mGT (Figure 3.10). It is believed that the flows from these stacks are forced down due to the turbulence caused by the surroundings and the suction generated by the air intake; especially when wind comes from across the building and separates at the end. The surroundings of the building equipped with the T100 mGT (Building Z) can be seen in Figure 3.11.

The aim of this section is to verify the hypothesis of EGR causing the unsteady operation of the mGT and identify the effect of EGR on mGT performance. Direct visualisation of the EGR was too complex. Therefore, measurement results must be used to validate the hypothesis of EGR causing the unsteady mGT operation. In addition to the verification, the effect of EGR on the T100 mGT performance must be studied using simulations to quantify the severity of the EGR problem. If EGR has a major effect on mGT performance, the issue needs to be addressed.

In a first step, the results of dry and wet (steam injection) measurements were examined in order to find proof of the hypothesis of EGR. Correlations between the data were calculated. In a second step, the effect of EGR on the global efficiency in steady-state regime was examined, using the Aspen® plus process simulator. For these simulations, the Aspen® model of the

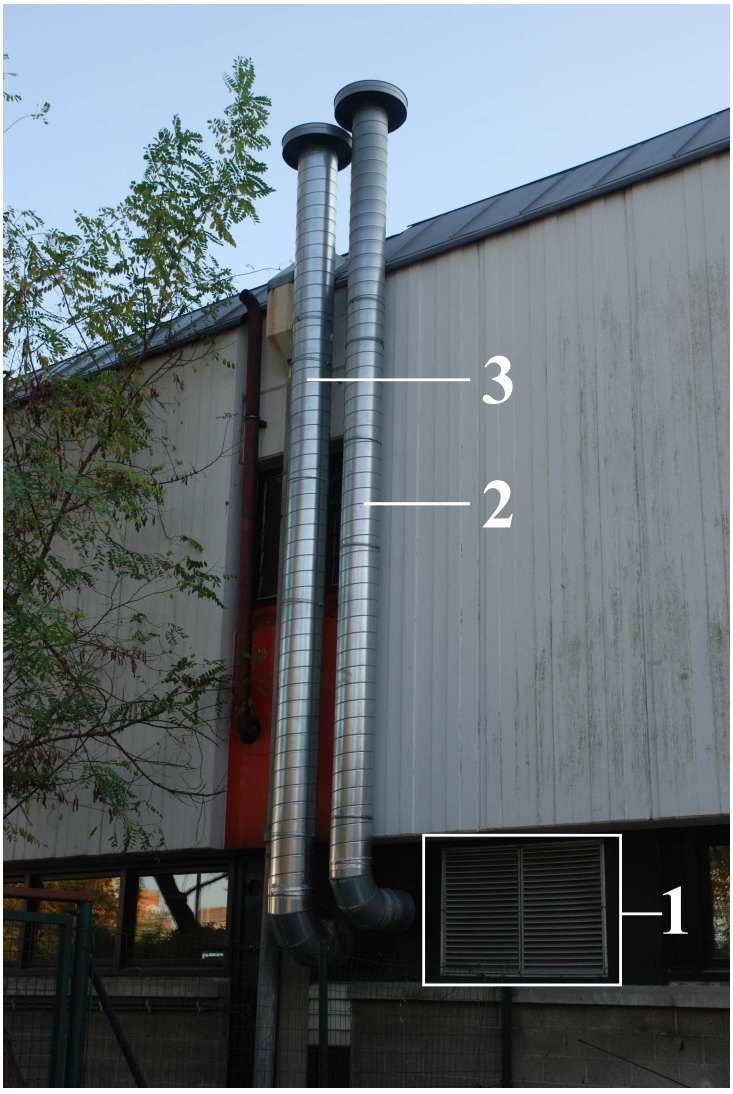

Figure 3.10: Air intake and both stacks of the mGT (1 air intake for the mGT and ventilation, 2 exhaust stack, 3 ventilation stack).

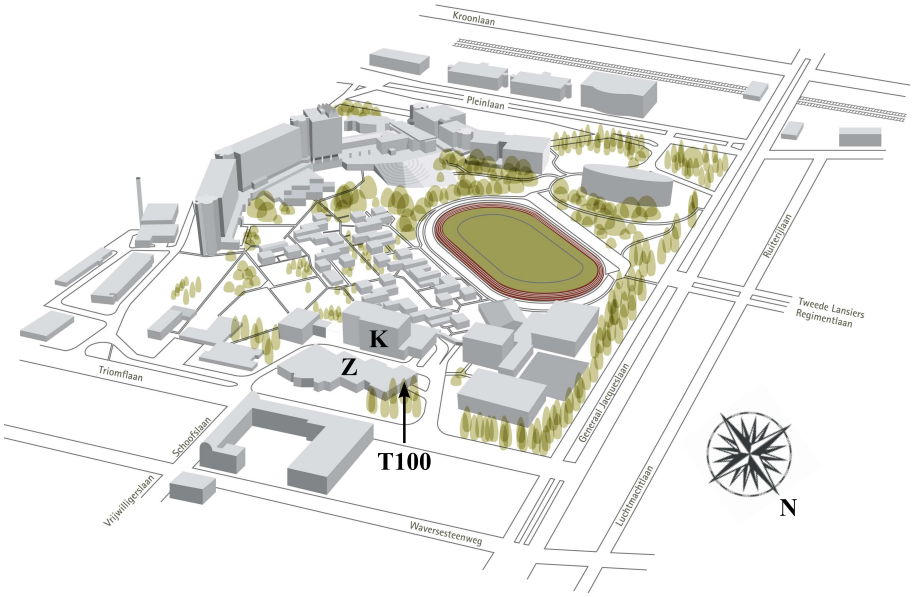

Figure 3.11: Surroundings of building Z, equipped with the Turbec T100 mGT, at the VUB campus.

mGT from previous section (section 3.1) was used. As a third step, the effect of the non-continuous EGR on the T100 mGT was studied using a dynamic simulation model of the T100 in Simulink®[184]. The step response of the engine control unit was simulated in order to study its response on changing inlet conditions. The effect of frequency and amplitude of the recirculation on the overall performance of the T100 was also studied.

3.2.1 EGR problem identification

EGR has an effect on both the dry and wet mGT operation. External EGR is a random, unsteady and turbulent phenomenon, which is very difficult to visualise. Visualisation requires a medium that would make the air stream visible. Using steam was one option, but this could only be applied when outside conditions are favourable for steam visualisation (high relative humidity). A second option is using smoke/fine particles. The smoke needs to be very dense, since the gases are diluted in the air. The particles will however foul the inlet air filter or even enter the mGT. Therefore, by analysing dry and wet experiments, I tried to find indirect proof of the EGR causing the unsteady mGT performance. In this subsection, dry and wet measurements are analysed to find proof of the hypothesis.

Dry operation

The EGR resulted in a fluctuating inlet air temperature that affected the T100 mGT operation. As a result of this non-constant inlet air temperature, the power generated by the mGT changes rapidly and the engine control has to interfere continuously to keep this produced electric power constant (Figure 3.12). The inlet air temperature is measured using the outside thermocouple (Figure 3.5), while the produced electric power is captured using the external power measurement. An increasing inlet temperature results in lower electric power production. To keep the electric power constant, the engine control will speed up the mGT compressor to increase the pressure ratio and restore the constant electric power output. On the other hand, a lower inlet air temperature results in a higher electrical output, so the compressor has to be slowed down. Experimental results were captured before the connection with the T100 mGT control system was established, using WinNap software. The shaft speed was only recorded using the engine monitoring system of Turbec, which averages the shaft

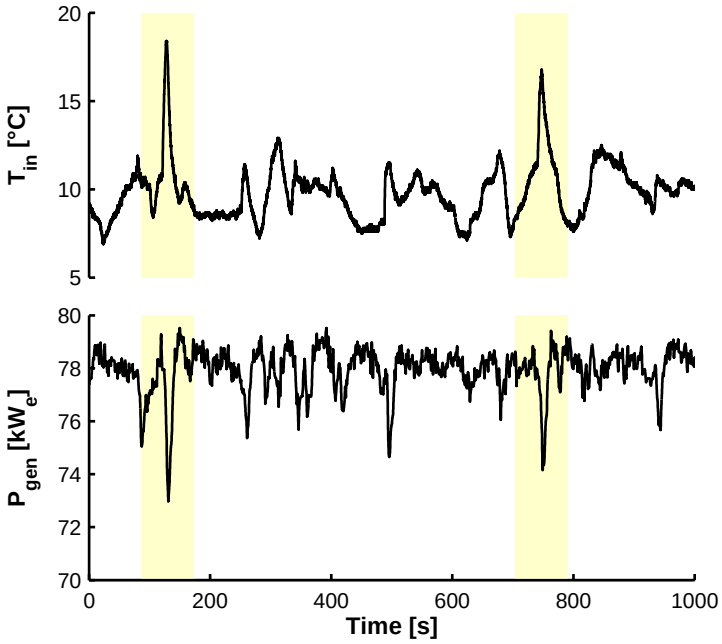

Figure 3.12: Changing inlet air temperature has an effect on produced electric power.

speed over a period of 90 s. Since major temperature changes occur much faster (approximately within 10 s, see Figure 3.12), it is not possible to show these changes and compare them with changing inlet temperature.

The real influence of the inlet air temperature on the produced power can be seen by calculating the correlation between both signals. The correlation between the inlet air temperature and the produced electric power is calculated for different time lag values by shifting one measured parameter in time and using the Matlab® function `corrcoef` (Figure 3.13). The correlation curve is very smooth due to the large number of data points used (10 000 points) to calculated the correlation. As expected, a negative correlation exists: a rise in inlet air temperature has a negative effect on the produced power. The correlation curve shows a minimum for 3 s lag and indicates that there is a strong correlation between both. The probability that this correlation is due to random noise is nearly zero and thus far below the value of 0.05 which indicates that there is, as expected, a real correlation [185]. The strongest correlation at 3 s time lag is due to the

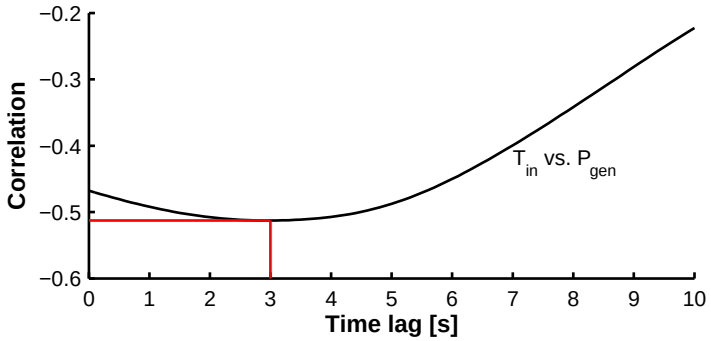

Figure 3.13: The correlation between the inlet air temperature and the produced electric power reaches a minimum at 3 s time lag.

time it takes for the air to travel through the air intake channel and the mGT itself. The inlet air temperature is measured at the entrance of the air intake (at the air filter), but the air still has to flow through 8 m of channel in our particular set-up before it enters the T100 engine.

Wet operation

Due to the changing inlet air temperature, the pressure after the compressor will change, which leads to a non-constant steam flow rate (Figure 3.14). When hotter air enters the compressor, the pressure after the compressor will drop. The steam flow rate from the steam boiler to the compressor outlet duct is governed by the pressure difference between the steam boiler and the compressor exit. The steam generator will produce saturated steam at an operator defined pressure. Pressure in the steam generator is set higher than the pressure behind the compressor. Once the pressure in the steam generator is higher than the pressure behind the compressor, steam will be injected. When the pressure behind the compressor falls, the steam mass flow rate will rise, because of the increase in pressure gradient (the pressure in the steam boiler remains constant).

The higher inlet air temperature and higher amount of injected steam into the mGT counteract on the electric power output. A higher inlet temperature will result in a lower electric power production, while a higher steam injection mass flow rate will result in a higher electric power output. The produced power is still influenced by the changing inlet air temperature,

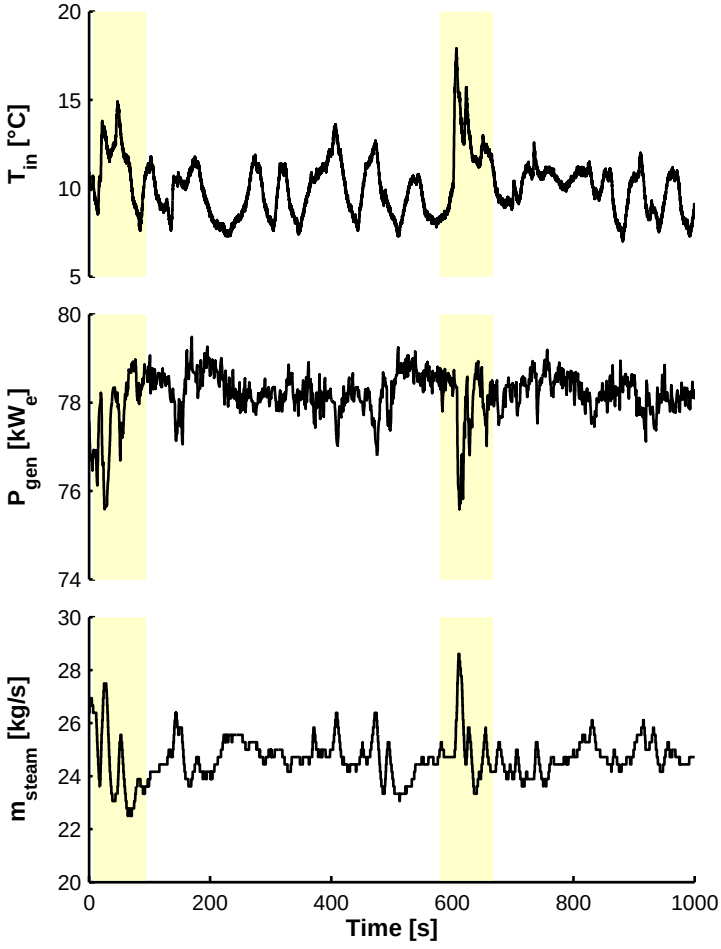

Figure 3.14: Changing steam flow rate and produced electric power due to changing inlet air temperature.

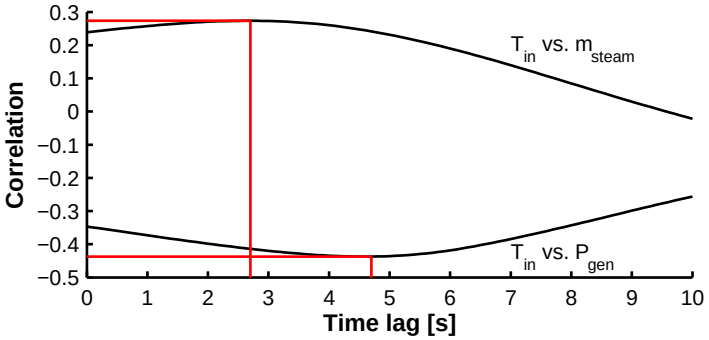

Figure 3.15: Correlation between inlet air temperature, produced electric power and steam injection rate reaches a minimum at 4.7 s and a maximum at 2.7 s time lag .

but the spikes are smaller, due to the compensation through enhanced steam injection (Figure 3.14). This indicates that the higher steam injection ratio cannot fully compensate the loss in electric power production due to the increasing inlet air temperature.

The correlation between the produced power and the inlet air temperature is again negative and reaches a minimum for a 4.7 s time lag, which is a slightly bigger lag than without steam injection. Steam injection has a positive correlation, due to the lower pressure with higher inlet air temperature (Figure 3.15). The correlation reaches a maximum after 2.7 s. The difference between the maximum can be explained as follows: the injected steam mass flow rate is only function of the pressure after the compressor, while the produced power is function of different parameters that are affected by the changing inlet temperature.

3.2.2 Simulations of the EGR

To identify the severity of the EGR problem, both the effect of continuous and varying EGR on mGT performance is simulated using a steady-state and a dynamic simulation model of the T100 mGT.

Steady-state simulations

For the steady-state simulations, the Aspen® model was used (section 3.1). For the simulation of EGR, part of the exhaust gas is first cooled down before it is rerouted to the air intake. Exhaust recirculation had to be simulated in this way, because in reality the exhaust flow is not directly rerouted back to the engine, but has to travel first through the air, where it is cooled down, before reaching the filter inlet duct. Since the correct temperature is not known, as an assumption, an exhaust gas temperature after cooling of 30 °C was taken.

EGR has a severe effect on mGT performance and especially on electric efficiency (Figure 3.16). As expected, EGR has a negative effect on the electric efficiency due to the rising inlet temperature. In addition to the higher inlet air temperature, EGR is also responsible for the presence of combustion products in the inlet air (Figure 3.16). The share of the combustion product in the inlet air increases with increasing inlet air temperature due to the higher fraction of recirculated exhaust gases in the inlet air. To demonstrate the effect of combustion products in the inlet air, the results of EGR simulations are also compared with the results from simulations without recirculation. For this simulation, the same inlet temperature as for the recirculation was used, while the composition of the inlet air was kept constant (21 mol% O_2, 79 mol% N_2 and 0 mol% CO_2 and H_2O). The loss in electric efficiency is not only the result of the rising temperature (Figure 3.16). The presence of combustion products in the inlet air has a non-negligible influence on the mGT performance, which has also been noticed by other researchers during simulations of a NGCC with EGR [175]. The amounts of work and heat to compress and heat these inert components (H_2O and CO_2) have a noticeable part in the electric efficiency loss.

The additional effect of the presence of CO_2 and H_2O in the inlet air, due to the EGR, on electric efficiency illustrates the importance of preventing this EGR. For the characterisation of the wet mGT simulation model, it is important that EGR does not occur. Within this wet model, the composition of the inlet air is kept constant (dry air). Using the wrong inlet air composition will result in an overestimation of the mGT efficiency once recirculation occurs. Changing the composition of the inlet air of the compressor in the simulation is easy; however it is hard to model the recirculation process because it happens randomly and non-continuously. Moreover, it is hard to predict the behaviour of the exhaust flow regarding

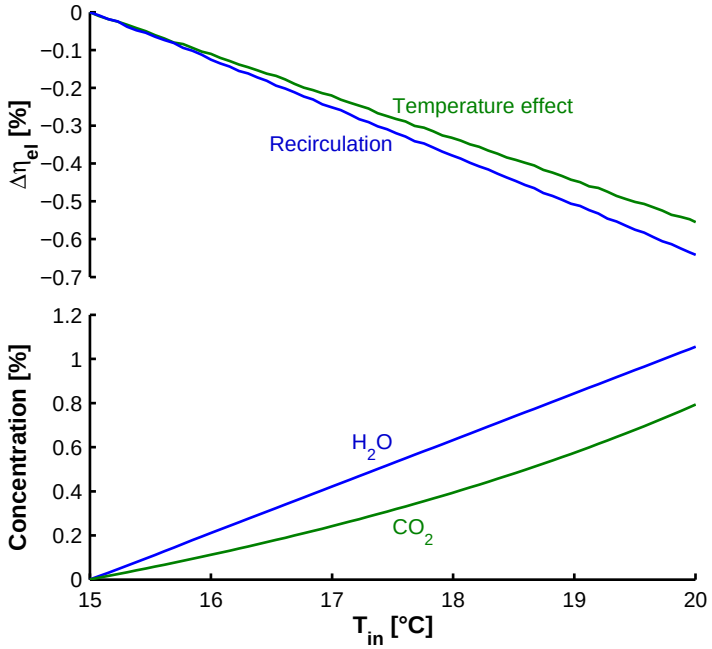

Figure 3.16: The influence of recirculation on mGT performance is not only caused by increasing inlet air temperature, but changing inlet air composition has a major effect on electric efficiency.

cooling and flow pattern. Only by online monitoring the inlet air composition, the right composition can be obtained for the simulations.

Dynamic simulations

Steady-state simulations have shown the influence of the flue gas recirculation on the electric efficiency of the mGT, however the recirculation is not a continuous process. EGR depends on the wind direction and the presence of vortices in the wind. Two series of simulations on the dynamic behaviour of the mGT have been performed. First, the step response of the engine control unit on a change in inlet air temperature and composition was studied using a dynamic model of the mGT in Simulink® [184]. A white box model of the mGT was built in Simulink®. Recuperator, compressor and turbine are considered quasi-static; however the inertia of the axis and the thermal inertia of the mGT are taken into account. For the modulation of the compressor and turbine, constructor maps were used (Figure 3.2).

At the step time (= 500 s), fuel consumption drops, along with the power production and the electric efficiency, due to the sudden change in inlet air temperature and composition (Figure 3.17). The controller will interfere and speed up the machine by giving more fuel to the combustion chamber (Figure 3.17). The produced electric power will increase again until the requested output has been reached. Due to the change in inlet air temperature and composition, the mGT will consume more fuel to produce the same electric power, resulting in a lower electric efficiency. The higher the recirculated part in the inlet air, the lower the efficiency will be after the step, which is in complete agreement with steady-state simulations. Depending on the step height (1, 5 and 10 % recirculated exhaust gases in the inlet air), the controller needs more time to restore the steady-state condition. For a step of 5 % exhaust air in the inlet air, the controller needs 100 s to restore the electric output.

To show the influence of the changing EGR frequency and changing fraction of recirculated exhaust gases in the inlet air on mGT performance and electric efficiency, a second series of dynamic Simulink® simulations was performed. During post-processing of the results of dry and wet mGT tests, different parameters are averaged over a long time period. Steady-state simulations have indicated that the changing inlet air composition has a severe effect on mGT performance. The EGR is however not a continuous process. The amount of recirculated exhaust gases will vary in

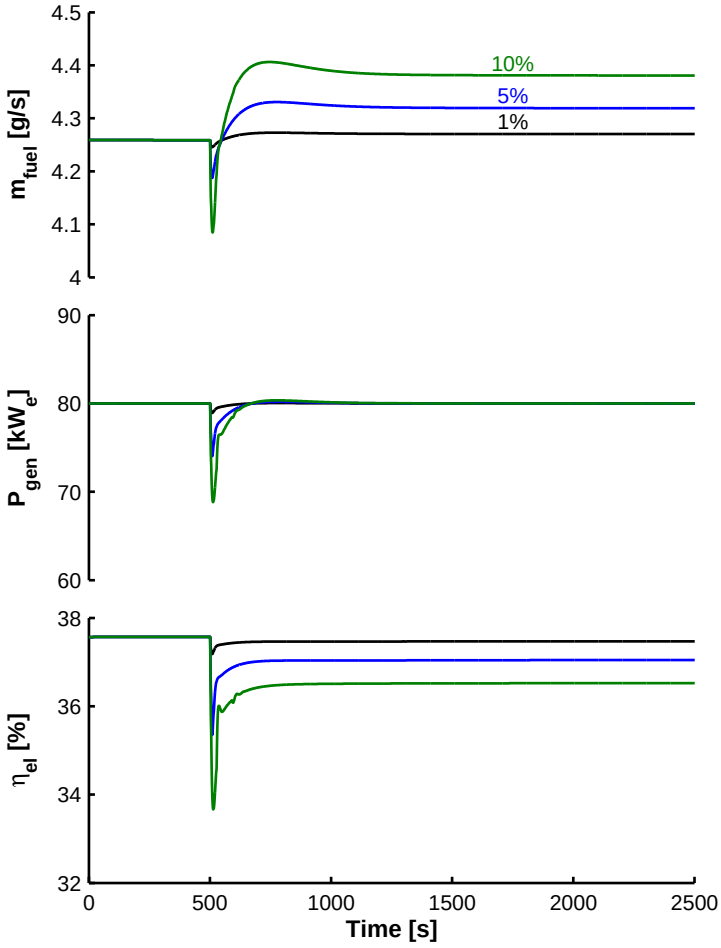

Figure 3.17: Step responses of the fuel flow rate to the combustion chamber, the produced electric power and the electric efficiency of the T100 mGT on a change in inlet composition show that for a higher recirculation fraction, the control system needs more time to stabilize the mGT.

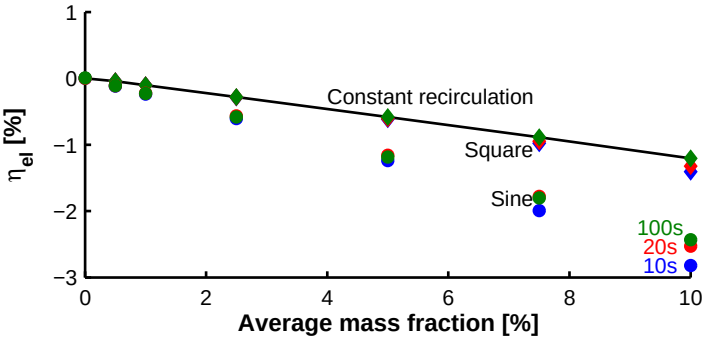

Figure 3.18: Dynamic recirculation simulations show that higher amplitudes, shorter periods and sine waves of the recirculation will result in an additional electric efficiency loss compared to constant recirculation.

time. In addition, the frequency of these variations will also change. With every change in inlet air temperature and composition, the mGT control system will perform an action in order to bring the produced electric power back to the user-defined set point. Depending on the rate of change in recirculated exhaust gases or the amount of recirculated gases, the control system will perform a different action. To show the influence of the engine control unit on the average efficiency, dynamic simulations over long periods were performed. In these simulations, the inlet conditions were changed periodically by changing the amplitude and frequency. In addition, the amount of recirculated air was changed using square and sine waves in order to show the effect of the shape on mGT performance. Simulations of dynamically changing the inlet temperature have shown that there was no difference between a dynamic simulation average and the same steady-state simulation. Possible changes in dynamic and steady-state efficiency for EGR are thus a result of the changing inlet air composition.

Compared to the constant recirculation, there is a small difference between the average efficiency of the square wave (Figure 3.18). The higher the amplitude, the bigger the difference between the average efficiency of the square wave with different periods themselves and between the square waves and the constant recirculation becomes, however these differences are still small. With a shorter period, the controller has to interfere more during a certain fixed period. Every time the inlet air composition and temperature changes (wave front), the controller has to react and speed up or slow down

the mGT to reach the requested output power. During this transition, the mGT is not working at maximal TIT, which results in a lower efficiency. So the shorter the period, the more the mGT has to go through these transitions, the more the mGT is working at a lower instantaneous efficiency, resulting in a lower average efficiency compared to the constant recirculation. When the amplitude of the square wave gets higher, the produced electrical power drops deeper, as can be seen on Figure 3.17. The higher the amplitude, the further the mGT is away from its requested produced power at the step time, so the controller has to speed up or slow down the mGT more quickly. The faster the speed change happens, the further the machine is away from its optimal operating point and the longer it takes to reach this point again, resulting in lower average efficiency, compared to the continuous recirculation.

For the sine wave simulations, the same tendency as for the square wave can be observed, though the difference between non-continuous and continuous recirculation is now very large (Figure 3.18). The different behaviour for the different inlet air compositions and temperatures can be explained by the actions of the controller. For the square wave, the controller only has to act at the leading edge of the square, while with the sine, the controller has to interfere all the time. Because temperature and composition of the inlet air are changing continuously, the controller is aiming for a wrong set point, resulting in a mGT that is not working at its optimal design point, which results in a lower efficiency. When comparing the sine wave efficiency with the efficiency of the constant recirculation, one can remark that the difference between both increases as amplitude increases. This can be explained by the slope of the curves. The more the amplitude of the wave increases, the faster the optimal operation point of the mGT will change and the further the actual operating point will be away from this optimal point, resulting in a larger decrease in efficiency. The same explanation can be used for the increasing difference between the sine and square waves with increasing amplitude. In the case of constant recirculation with the square wave, the inlet conditions change, however the controller only has to act at the fronts of the wave. So most of the time, the inlet conditions are still stable, resulting in a limited controller acting time. Thus the mGT runs most of the time at or close to an optimal working point. This will limit the average efficiency loss, even at higher amplitude, compared to the sine wave were the engine control interferes all the time, resulting in a larger decrease in efficiency with increasing amplitude. When looking to the sine wave only, one can see that with decreasing period at the same amplitude,

the efficiency loss becomes larger. This again, can be explained by the slope of the curves. The more the amplitude of the wave increases, the faster the optimal operating point of the mGT will change, resulting in a lower average efficiency.

Summary of the EGR simulation results

Steady-state and dynamic simulations of the exhaust gas recirculation show the non-negligible influence of the recirculation on the mGT performance. The steady-state simulations showed that – except inlet temperature variations – the changing composition of the flow to the unit also has an impact on the engine efficiency. Dynamic simulations indicated the problem the engine control unit is facing and illustrated the danger of working with average values. The dynamic simulations also indicated that a steady-state model for the recirculation is not sufficient. The modelling of the mGT can only be done correctly when the dynamic recirculation is also modelled, which is practically impossible.

Results of both dynamic and steady-state simulations indicate the need for a solution, especially for validation of simulation models against measurements.

3.3 Atmospheric Boundary Layer (ABL) simulation

To find a solution to prevent EGR, the ABL needed to be simulated in the wind tunnel. By simulating the ABL in the industrial wind tunnel of the VUB, the wind behaviour around the building Z and more in detail around the stack of the mGT could be studied. Wind tunnel experiments with a scale model allow to find a solution for the recurrent problem of EGR. Wind tunnel simulations of the ABL are performed in most wind tunnels using full-depth simulation techniques [186, 187] or part-depth simulation method [188, 189]. In this section, the design and validation of the simulated ABL are presented. In the design phase, the characterising parameters of the ABL are introduced. These parameters have specific values, defined in international standards on turbulent boundary layers, depending on the

roughness of the surrounding. The definition of each parameter is presented together with its specific value for the ABL around building Z. Out of these values, the dimensions of the experimental equipment could be determined. Finally, the simulated ABL is validated by measuring and calculating its characteristic parameters and comparing them with the values given in the standards.

It is generally accepted that allowing the flow to run over a rough surface producing a natural-growth boundary layer is the best method for simulating the ABL in a wind tunnel [190]. Depending on the surroundings of the studied region, a different roughness must be used. When using this technique, the scale of the simulated ABL depends on the length of the roughness fetch. In order to obtain very large scales for the analysis of wind loads on buildings, a specially constructed wind tunnel with a working section that is much longer than its cross-sectional dimension is necessary [191]. The formation of this turbulent boundary layer tunnel can be enhanced by using obstructions upstream that have the ability to absorb energy from the mean flow without introducing large scale disturbance [192]. Many different techniques have been studied since 1960, for instance using spires in combination with roughness elements [191, 193], air jets [194, 195], fences in combination with chains [196] and fences [197] or rods [198]. The Roughness, Barrier and Mixing Device (RBMD) method proposed by Cook has simulated successfully the lower third of the boundary layer using turbulence grid, plane barrier wall and roughness elements [188, 189]. These RBMD techniques are renowned for reproducing mean and fluctuating parameters of the atmospheric boundary layer. The RBMD method, suggested by Counihan, using elliptic wedge generators in combination with a castellated wall and roughness elements [186, 199–202] allows full-depth boundary-layer simulations. This method is widely used for full-depth ABL simulation [203–209]. An alternative for the RBMD method of Counihan is given by Irwin [187]. Irwin uses the flat triangular spires from Standen et al. [191] as a vortex generator and roughness elements to reproduce full-depth boundary layers with a thickness of about 80 % of the spire hight. The major advantage of the techniques of Irwin compared to the technique of Counihan is the use of triangular spires as vortex generators [187]. The construction of triangular spires is much easier compared to quarter ellipses.

For the simulations of the ABL around building Z at the VUB campus, both RBMD methods of Irwin and Counihan were used and verified in order to select the optimal method to use in wind tunnel simulations.

3.3.1 Design of the ABL

The wind tunnel simulations of the ABL were performed in the industrial wind tunnel at the VUB (Table 3.2). The wind tunnel has a working section of 12 m longitude. The cross section is 2 m wide and 1 m high. The wind velocity can be varied from 0 to 20 m/s by changing the rotations speed of the ventilator. In the floor of the wind tunnel, a turn table with diameter 2 m is installed to change the approach of the wind on the scale model. The centre of this turn table is located 10 m behind the end of the contraction. In the past, wind studies have successfully been performed in this wind tunnel [210, 211]. Derdelinckx and Hirsch performed a wind study on the 'Koning Boudewijn Stadion' [210] and also used this set-up to simulate the wind load on the tower of the city hall of Brussels [211].

In following subsections, the design of the vortex generators for the simulation of the ABL using Irwin and Counihan RBMD methods is discussed.

Properties of the ABL at the VUB-site

The ABL is defined by several parameters. In his review paper, Counihan gives an overview of these parameters and the different attempts made by researchers to determine experimentally these parameters [212], for instance by using a captive balloon [213]. These measurements indicated that an inconsistency existed between the parameters defining the ABL, depending on the roughness of the terrain surrounding the measuring position. By defining from the data four distinct terrain types, these issues could be resolved [212]. The most important parameters for ABL simulation in the wind tunnel are:

Table 3.2: Main specifications of the industrial wind tunnel at the Mechanical Engineering Department of the VUB

Type	Open circuit
Total tunnel length	25 m
Testing chamber length	12 m
Testing chamber height	1 m
Testing chamber width	2 m
Turbine power	55 kW
Maximal wind speed	20 m/s

- boundary layer height;
- mean velocity profile;
- roughness length;
- intensity of turbulence;
- length scales of turbulence;
- power spectral densities;
- Reynolds stress.

The roughness of the surrounding of the VUB site will determine the type of boundary layer and the specific value of the different parameters of the ABL. As mentioned by Counihan, four different types of terrain exist: smooth, moderately rough (rural), rough (suburban), very rough (urban) [212]. This classification is used in the Belgian wind standards [214]. For the VUB, the most appropriate, according to the buildings in the neighbourhood, is type III, suburban. This gives the necessary properties of the ABL that should be simulated in the wind tunnel.

Measurements of the ABL showed a boundary layer thickness (δ), depending on the site, of 400 m, up to a maximum of 600 m [212]. Since the maximal height of the wind tunnel at VUB is 1 m, this height will be used as boundary layer thickness.

The mean wind velocity profile can be determined according to the power law [191]:

$$\frac{u}{u_\delta} = \left(\frac{z}{\delta}\right)^\alpha . \tag{3.17}$$

A suburban wind profile (type III) corresponds to an exponent of the power law (α) equal to 0.21 [215]. In this thesis, the mean velocity in the x-direction $\bar{u}$ is calculated as

$$\bar{u} = \frac{1}{T}\int_0^T u\,(t)\,\mathrm{d}t. \tag{3.18}$$

When simulating the ABL in the wind tunnel, a shift appears in the profile. This shift is indicated by the zero plane displacement (d). This zero plane

displacement will slightly change the power law definition from Equation 3.17 into

$$\frac{u}{u_\delta} = \left(\frac{z-d}{\delta}\right)^\alpha. \tag{3.19}$$

Additionally, the roughness length (z_0) of the wind profile is defined as suggested by Thuillier and Lappe [216]:

$$\bar{u} = \frac{u_\tau}{\kappa} \ln\left(\frac{z-d}{z_0}\right). \tag{3.20}$$

Norms indicate a roughness length of 0.3 m for the suburban region [214].

The turbulence intensity (I_u) in the x-direction can be calculated as follows:

$$I_u(z) = \frac{\sqrt{\overline{u'^2(z)}}}{\bar{u}}, \tag{3.21}$$

where

$$u(t) = \bar{u} + u'(t). \tag{3.22}$$

According to Iyengar and Farell, the integral length scale of turbulence (${}^xL_u$) can be determined in three different ways [217]:

- the value of the spectrum at frequency $f = 0$;
- the area under the autocorrelation curve ($R_{u,x}$), which can be calculated using the following formula;

$${}^xL_u = \int_0^\infty R_{u,x}(\Delta t)\,\mathrm{d}t; \tag{3.23}$$

- the location of the central peak.

Out of the integral length scale of turbulence, the scale of the simulated ABL can be determined using Cook's formula [218]:

$$S = 91.3\frac{(z-d)^{0.491}}{{}^xL_u{}^{1.403} z_0{}^{0.088}}. \tag{3.24}$$

Both turbulence intensity (I_u) and integral length scale of turbulence (${}^xL_u$) can be verified using international standards [215, 219, 220]. Kozmar indicated that there is a considerable scatter of recommended values for suburban wind characteristics [221].

Finally, the power spectral density of the longitudinal velocity fluctuations $S_u(f)$, where

$$\overline{u'^2} = \int_0^\infty S_u(f)\,\mathrm{d}f, \tag{3.25}$$

should match a specific profile. Lungu and van Gelder indicate the existence of numerous proposals for the spectral density of along-wind gustiness. In this thesis, the profile of the power spectral density will be validated using the formula given by Kaimal et al. for the lower parts [223], while the ESDU85020, Eurocode1 and von Karman formulas will be used for the entire thickness of the boundary layer [215, 220, 224].

The wind velocity in the ABL was only measured in the x-direction (subsection 3.3.2), making it not possible to calculate the Reynold shear stress

$$\tau = -\rho\overline{u'w'}. \tag{3.26}$$

In addition, the turbulence intensity (${}^xL_v$, ${}^xL_w$) and integral length scale of turbulence (I_v, I_w) in y- and z-direction could also not be calculated.

Design of truncated Counihan ellipses

A series of test was performed using the method of Counihan [202]. As described by Counihan, the height of the elliptic wedges should be equal to the height of the simulated ABL. For large scales (thus large ABLs), this requires a high wind tunnel cross section. Kozmar suggested to install truncated elliptic vortex generators [225]. After further improving this techniques, Kozmar was able to perform successfully part-depth wind tunnel simulations of the urban [226–228], rural and suburban [228] ABL. Analysis of the obtained results indicated the adequacy of redesigned 'Counihan' vortex generators for part-depth ABL simulations [228].

Both elliptic vortex generators (Figure 3.19) and the castellated barrier wall (Figure 3.20), were constructed using the suggestions of Counihan [202]. The elliptic vortex generators were truncated based on recommendations of Kozmar [228]. The angle of the vortex generator is at every height 12°

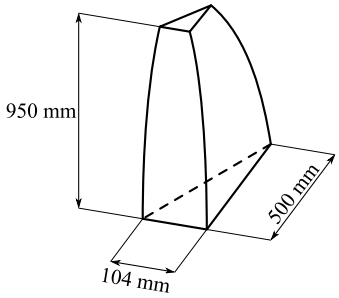

Figure 3.19: Dimensions of the elliptic vortex generators.

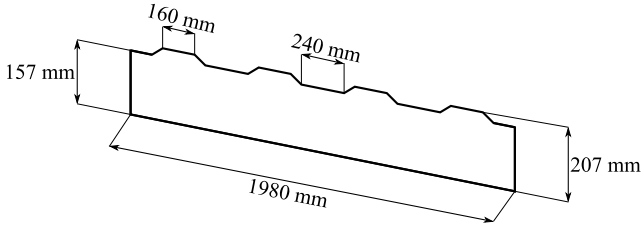

Figure 3.20: Design of the castellated barrier wall for ABL simulation in the wind tunnel.

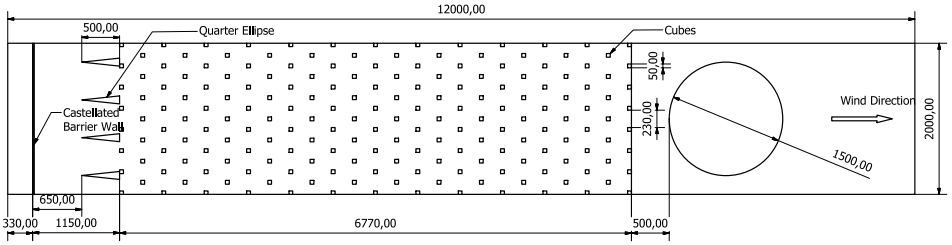

Figure 3.21: Arrangement of the truncated vortex generators according to the recommendations of Kozmar [228].

[202]. The castellated barrier is designed using the properties of the ABL in suburban regions ($\alpha = 0.21$)[215]. For the spacing between the elliptic vortex generators, Counihan suggested a distance of $\delta/2$. For the placement of the barrier wall, a distance of $\delta/3$ between the barrier wall and the intersect of the working section and the contraction of the wind tunnel, is recommended. Test of Counihan also suggested a $5/6\delta$ distance between the barrier wall and the elliptic vortex generators. However the industrial wind tunnel at the VUB is short, so the relative positions of the barrier wall and generators were adapted. For the spacing and the size of the roughness elements, recommendations of Counihan [201], Gartshore and Croos [229] and Fang and Sill [230] were used. The complete adapted experimental set-up is shown in Figure 3.21. Total occupied cross section by the elliptic vortex generators was below 5 % in order to avoid blockage in the wind tunnel.

Design of the Irwin spires

A second series of tests was performed using Irwin spires [187] in combination with roughness elements, according to the recommendations of Wooding et al. [231]. The necessary height of the spires can be calculated, using the formula from Irwin [187]:

$$h = \frac{1.39\delta}{1 + \alpha/2}. \tag{3.27}$$

Using $\alpha = 0.21$ and $\delta = 1\,\text{m}$ for Equation 3.27 results in a spire height of 1.25 m. The working section of the wind tunnel is however only 1 m height. Therefore, it was necessary to truncate the spires at 0.95 m.

The frontal plate base b can be calculated using the formula suggested by Irwin [187]:

$$\frac{b}{h} = 0.5\left[\psi\left(\frac{H}{\delta}\right)(1+\psi)\right]\left(1 + \frac{\alpha}{2}\right), \tag{3.28}$$

with ψ and β from Equation 3.28 equal to

$$\psi = \frac{\beta\dfrac{2}{1+\alpha} + \beta - \dfrac{1.13\alpha}{(1+\alpha)(1+\alpha/2)}}{(1-\beta)^2} \tag{3.29}$$

$$\beta = \frac{\delta}{H}\frac{\alpha}{1+\alpha}. \tag{3.30}$$

and H is equal to the height of the wind tunnel.

Irwin suggests that the boundary layer is fully developed after six times the height of the spires [187]. By reducing the skin friction term $1.13\alpha/[(1+\alpha)(1+\alpha/2)]$ from Equation 3.30, Lopes et al. transformed the formulas for the calculation of the thickness of the spires in order to be able to use Irwin spires in a shorter wind tunnel. Lopes et al. suggested a proportional coefficient to the distance reduction of $x/6$ [232]. By means of an iterative loop, the optimal positioning of the spires and roughness elements in the tunnel was calculated. The goal was to have at least 50 cm between the scale model and the end of the roughness elements on the tunnel floor, but also to have an optimal use of the total tunnel length. Calculations showed an optimal $x = 6$, which results in a frontal plate base $b = 0.182\,\text{m}$. The separated plate (plate perpendicular to the base plane, supporting the base to hold the force of the wind) base is 0.314, a quarter of the spires height (Figure 3.22).

The equations of Irwin for the design of the spires already take into account the existence of roughness elements along the wind tunnel floor. To define the cubes side (k) and the spacing (D) between the cubes, the formula of Wooding et al. must be used [231]:

$$\frac{k}{\delta} = \exp\left[\left(\frac{2}{3}\right)\log_{10}\left(\frac{D}{\delta}\right) - 0.1161\left[\left(\frac{2}{C_f}\right) + 2.05\right]^{0.5}\right], \tag{3.31}$$

where C_f corresponds to the friction coefficient needed to obtain an α-power-law velocity profile and is defined as follows:

$$C_f = 0.136\left(\alpha/(1+\alpha)\right)^2. \tag{3.32}$$

For the 0.05 m side cubes used for the simulations, 0.23 m spacing is necessary.

Spacing between the different spires is equal to $h/2$ from centre-line to centre-line. Initial tests were carried out using four spires with a centre-line distance of 0.5 m. The initial test results however showed that the spires were placed too short to each other, resulting in a too high power law exponent ($\alpha = 0.25$). This value corresponds to urban terrain rather than suburban terrain [215]. For the final experiments, three spires were used with a centre-line distance of 0.67 m. The final set-up used to simulated the ABL in the wind tunnel using Irwin spires is shown in Figure 3.23.

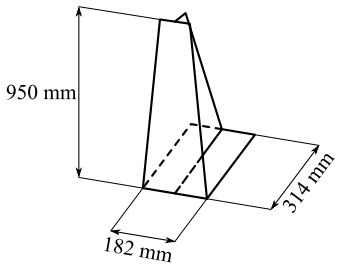

Figure 3.22: Dimensions of the truncated Irwin vortex generators.

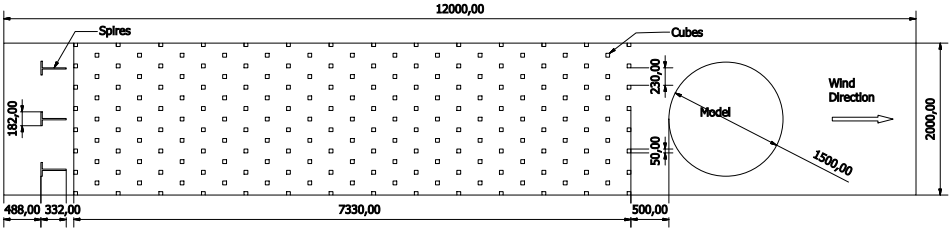

Figure 3.23: Arrangement of the vortex generators according to the recommendations of Irwin [187].

3.3.2 Characterisation of the simulated ABL

A Dantec Mini Constant Temperature Anemometer (CTA) (accuracy ±1 % of the reading above 5 m/s when calibrated in the wind tunnel with a pitot-static tube [233]), with 10 kHz maximal sample rate, was used in the determination of the properties of the ABL. All tests were carried out with a mean free velocity of about 8 m/s. Depending on the application, a different data acquisition rate was used. Used sample rates are specified when discussing the experimental results. The CTA is calibrated using a pitot tube, leading to a fourth-degree calibration curve. Since no temperature compensation was foreseen in the calibration, the CTA was calibrated on a daily basis.

Mean velocity profile

Measurements of the simulated ABL using the truncated ellipses were performed over a measuring period of 20 s, averaged over four periods, using a sample ratio of 10 kHz, while the measurements using truncated spires were performed over a measuring period of 200 s with a sample ratio of 2.5 kHz. For the tests using the truncated spires, measurements were taken every cm, while for the truncated ellipses, in the lower part (below 0.25 m), measurements were also taken every cm, in the upper part every 2.5 cm. The height of the ABL is equal to the height of the tunnel. In the upper part of the ABL, a second boundary layer, due to the ceiling is formed. It is thus not possible to use the free wind velocity as reference for the power law. The reference height is taken at 0.20 m. This height was arbitrary chosen: high enough to eliminate local effects from the roughness elements and low enough since the ABL is there the strongest. Measurement along the entire wind tunnel height indicated that the effect of the upper boundary layer was noticeable from a height of 0.8 m. All measurements above 0.8 m were discarded.

Both methods show good accordance with the power law profile in the lower part of the wind tunnel (Figure 3.24 and 3.25). For the upper part of the ABL, it is clear to see that the profile simulated using truncated Irwin spires keeps following the power law, while measurements with the truncated ellipses of Kozmar start to divert from the profile. The measurement indicate a more linear behaviour of the average wind speed. This indicates that not enough vortices are introduced in the boundary layer due to a too

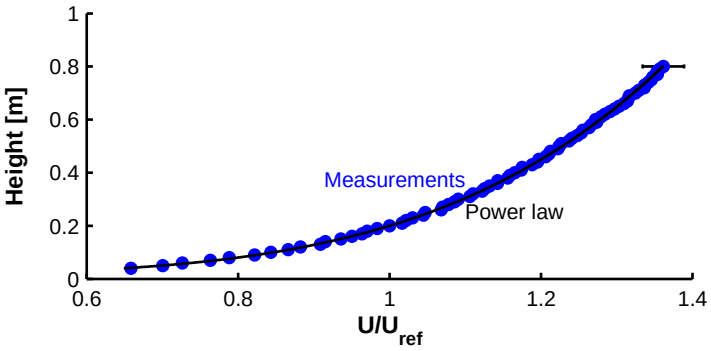

Figure 3.24: Simulations of the ABL using truncated Irwin spires in combinations with roughness elements follow the power law throughout the wind tunnel height. Curve fit indicates a power law exponent α of 0.21.

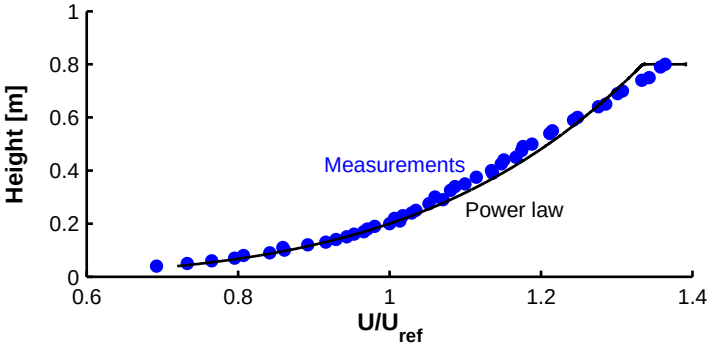

Figure 3.25: Simulations of the ABL using truncated Counihan ellipses in combination with roughness elements indicated a perfect fit with the power law in the lower part of the boundary layer, however a too low energy absorption of the vortex generators results in a more linear behaviour in the upper part of the boundary layer. Curve fit results in a power law exponent α of 0.21.

low energy absorption by the ellipses. To achieve the power law exponent, Equation 3.17 needed to be modified, since u_δ is not known. Modifying the power law results in the formula given by Wang et al. [234]:

$$\frac{u}{u_{\text{ref}}} = \left(\frac{z-d}{z_{\text{ref}}-d}\right)^{\alpha} \tag{3.33}$$

Performing a least square non-linear curve fit of the measurements with the power law, indicated a power law exponent for both methods of $\alpha = 0.21$ and a displacement height of $d = 16\,\text{mm}$ for the Irwin method and $-1\,\text{mm}$ using the truncated ellipses from Kozmar. A power law exponent of $\alpha = 0.21$ corresponds to suburban wind profiles (type III) [214], as was expected.

Fitting the profiles to the logarithmic law allows the determination of the roughness length z_0 (Figure 3.26 and 3.27). Applying a least square non linear fit method results in a roughness length of 1.2 mm for the Irwin method and 1.4 mm for the Kozmar method. When using the scales calculated from the integral length scale (see later), full-scale roughness length for both methods are 0.43 and 0.55 m, which is close to the 0.3 m given in the Eurocode1 for suburban terrain [215]. The friction velocity u_τ in both cases is equal to 0.526 m/s and 0.554 m/s respectively. Both profiles show good accordance to the logarithmic law for the lower part of the simulated boundary layer, as was indicated in literature [188]. For higher values, the measurements start to diverge from the logarithmic law, as was indicated by Cook, since the logarithmic law is only valid in the lower part of the ABL.

Turbulence profile

Next to the correct average wind speed profile, a correct turbulence intensity is necessary to have a correct simulation of the ABL. Using the measurements taken for the velocity profile, the turbulence intensity I_u in the x-direction could be calculated (Figure 3.28 and 3.29). Since a single wire is used to measure the wind velocity, calculating I_v and I_w was not possible. In the international codes (ESDU74031 and ESDU85020), measurement data for the turbulence intensity, depending on the roughness of the surrounding terrain can be found [219, 220]. The measurement results from Figure 3.28 and 3.28 are compared with these results. In both standards, a scatter of 20 % from the given profile is allowed. For the comparison with ESDU74031 and ESDU85020 standards, the measurement data need to be scaled to actual data. The used scaling factor for the Irwin method is 1:363, while

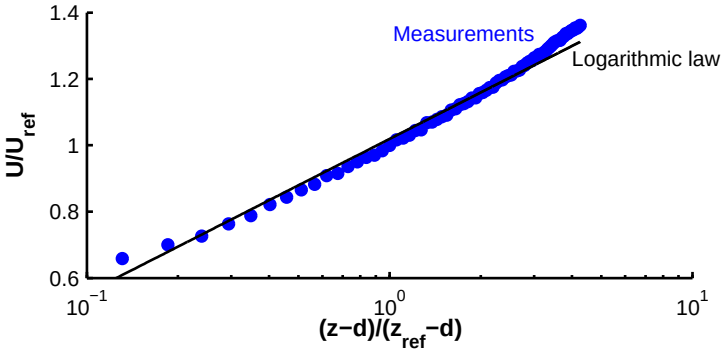

Figure 3.26: Simulations of the ABL using truncated Irwin spires in combinations with roughness elements fit well with the logarithmic law in the lower part of the boundary layer.

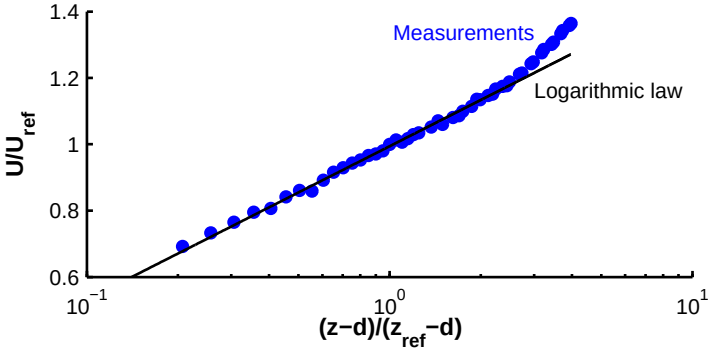

Figure 3.27: Simulations of the ABL using truncated Counihan ellipses in combination with roughness elements indicated a perfect fit with the logarithmic law in the lower part of the boundary layer.

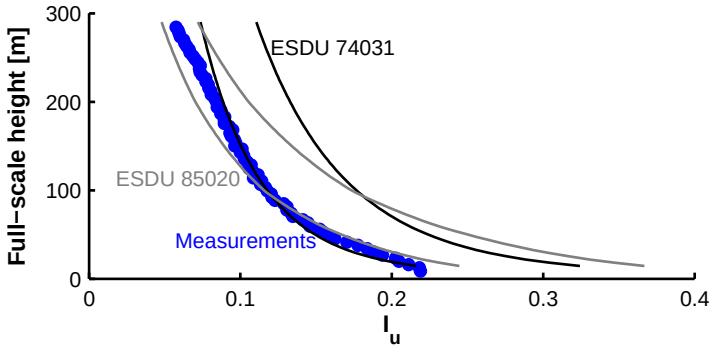

Figure 3.28: Turbulence simulations of the ABL using truncated Irwin spires in combination with roughness elements show good correspondence to the turbulence profile given by ESDU74031 and ESDU85020 data. The results are however close to the lower limit, indicating that a minimum of turbulence is introduced in the simulated boundary layer. The error is within the size of the markers.

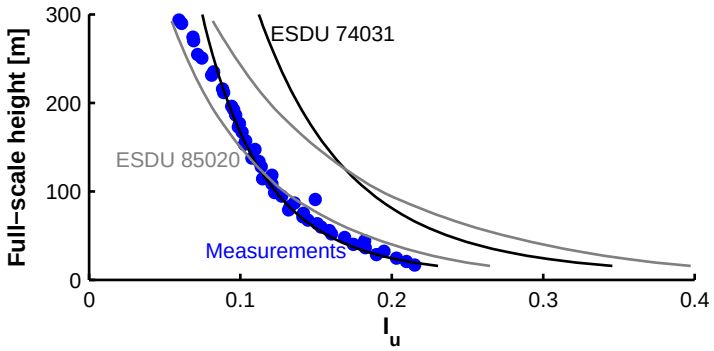

Figure 3.29: Turbulence simulations of the ABL using truncated Counihan quarter ellipses in combinations with roughness elements show good correspondence with the turbulence profile given by ESDU74031 and ESDU85020 data. The results are however close to the lower limit, indicating that a minimum of turbulence is introduced in the simulated boundary layer. The error is within the size of the symbol.

a scale of 1:390 was used for the Counihan method. These scaling factors were obtained from the measurement data. More details about the scale determination can be found in the following subsection. Both measurement data from Figure 3.28 and 3.29 show good correspondence to the standards. Both profiles follow the given trend. Measurements results are however close to the lower limit, indicating that a minimum of turbulence is introduced in the simulated boundary layer.

Integral length scale of turbulence

The integral length scale of turbulence is important to determine the final length scale of the simulated ABL. As mentioned before, the integral length scale of turbulence can be determined in three different ways.

I the value of the spectrum at frequency $f = 0$;

II the area under the autocorrelation curve;

III the location of the central peak.

According to Iyengar and Farell, the errors involved in the determination of the sample spectral values at $f = 0$ (method I) are quite significant unless one has adequate resolution and definition of the spectra at low frequencies [217]. In their measurement, Iyengar and Farell measured the velocity fluctuations over three intervals of 2, 0.2 and 0.05 ms with inline low-pass filters set at frequencies of 0.2, 1 and 5 kHz. Such filters were not available. Therefore, the integral length scale of turbulence was calculated using methods II and III.

The autocorrelation curve (method II) and the location of the central peak (method III) were calculated using Matlab®. The measurement intervals were split in different additional intervals of 2 s, using a Hamming window. The final autocorrelation is calculated using the `pwelch`-function [235]. Ideally, the integral turbulence length scales are calculated taking the complete surface under the autocorrelation curve. This means taking the integral with limits zero and infinity (Equation 3.23). However, since the velocity was measured over a finite period, the autocorrelation curve was cut off after 1000 samples. After 1000 samples, the autocorrelation curve

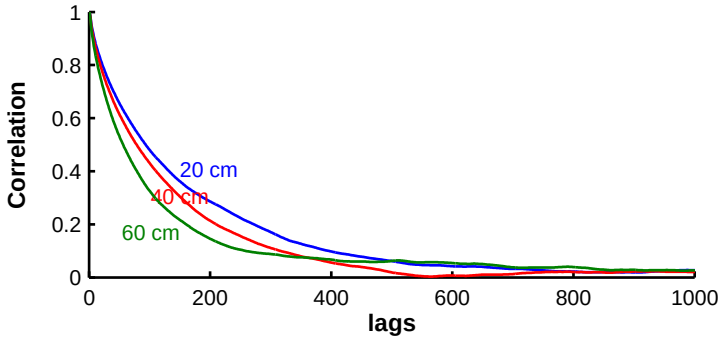

Figure 3.30: Autocorrelation curve of velocity measurements at different heights (20, 40 and 60 cm) indicate that the function has converged after 1000 samples.

has converged (Figure 3.30). For method III, rather than directly taking the central frequency, which introduces errors due to the noise, the frequency was determined by fitting the data to the von Karman-spectrum [224]. This allowed for a more correct determination of the maximum frequency.

The integral lengths scale profiles of the simulated ABLs using Irwin and Counihan method correspond with each other (Figure 3.31 and 3.32). The simulation results agree moderately with the ESDU74031 data, even when taking into account the 30 % spread on the standard data. The experimental results are not compared with ESDU85020 data, since Kozmar indicated that the recommended turbulence length scales are much larger in the ESDU85020 standards, compared to other standards [221]. A linear increase in integral length scales of turbulence with height, similar to full-scale, is however not observed. Experimental results increase strong in the near-ground region, but with further increase in height, the turbulence length scale remains nearly constant. This trend was reported in other wind-tunnel studies as well [217, 221]. The different mechanisms of boundary layer development in wind tunnel simulations and in full-scale is indicated as a possible explanation by Kozmar [227].

Integral length scales from Figure 3.31 and 3.32 are shown on full-scale using the same scales as for Figure 3.28 and Figure 3.29 (1:363 and 1:390). These scales were obtained by using Equation 3.24 to calculate the scale [218], using the integral length scales from Figure 3.31 and 3.32.

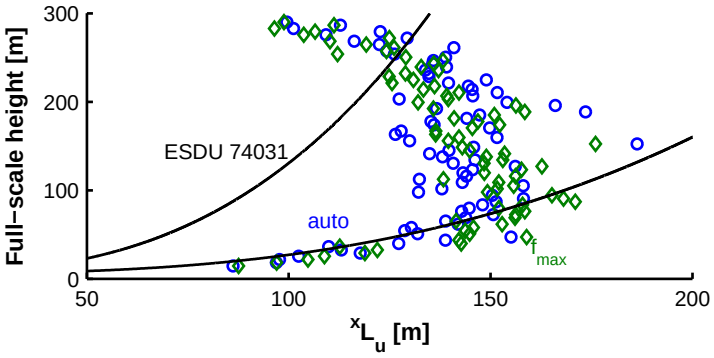

Figure 3.31: The simulated profile of the integral turbulence length scale using truncated Irwin spires in combination with roughness elements show moderate correspondence to the profile given by ESDU74031 data. To calculate the integral turbulence length scale, two techniques have been used: the area under the autocorrelation curve (*auto*, circles) and the location of the central peak (f_{max}, diamonds).

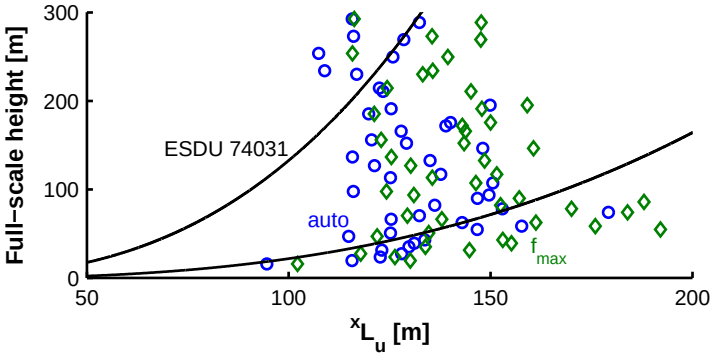

Figure 3.32: The simulated profile of the integral turbulence length scale using truncated Counihan quarter ellipses in combinations with roughness elements show moderate correspondence to the profile given by ESDU74031 data. To calculate the integral turbulence length scale, two techniques have been used: the area under the autocorrelation curve (*auto*, circles) and the location of the central peak (f_{max}, diamonds).

Power spectral density

For the comparison of the power spectral density, several formulas are formulated by different authors in literature [214, 220, 223, 224].

Close to the surface, the power spectral density should correspond to the Kaimal et al. spectrum [223]:

$$\frac{fS_u(f)}{{\sigma_u}^2} = \frac{6.8 f_L}{3\left(1+50 f_L\right)^{5/3}}, \tag{3.34}$$

where f_L, reduced frequency, is defined as $fz/\bar{u}$.

The Kaimal et al. spectrum gives a good approximation of the power spectral density, up to 50 m. For heights above 50 m, it is more appropriate to compare the power spectral density curve with the spectrum given in Eurocode1 [214]:

$$\frac{fS_u(f)}{{\sigma_u}^2} = \frac{6.8 f_L}{\left(1+10.2 f_L^2\right)^{5/3}}, \tag{3.35}$$

where $f_L = f^x L_u/\bar{u}$. This spectrum is similar to the von Karman-spectrum [224]:

$$\frac{fS_u(f)}{{\sigma_u}^2} = \frac{4 f_L}{\left(1+70.8 f_L^2\right) 5/6}. \tag{3.36}$$

The ESDU74031 standard proposes the von Karman-spectrum to be used to match the power spectral density [219], while ESDU85020 proposes the use of the theoretical model of Kolmogorov, where the power spectral density follows a 2/3 slope in the inertial subrange [236].

Power spectral density results of both methods (Figure 3.33 and 3.34) show good corresponce to the norms close the ground (Kaimal et al. [223]) and over the entire boundary layer (Eurocode1 [214], ESDU74031 [219] and ESDU85020 [220]). For the measurement of the power spectral density, 10 series of 200 s, using a sample frequency of 2500 Hz were used. These measurements were taken for different heights (5, 45 and 70 cm). The power spectral densities show maxima between frequencies of 2 and 10 Hz and they follow the Kolmogorov-2/3 slope in the inertial subrange indicating a similar path in turbulent boundary layer structure not dependent on the simulation length scale. With increasing height, the power spectral density maximum shifts to higher frequency. For both simulation method and the different height, the power spectra die-off at the same frequency.

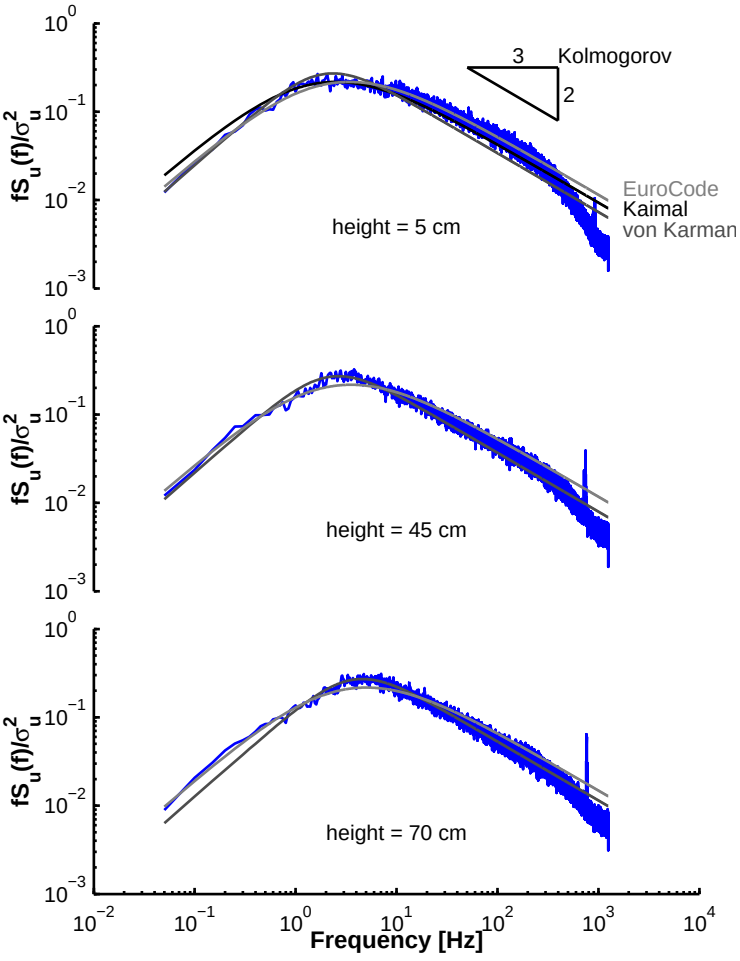

Figure 3.33: Measurements of the power spectral density for the Irwin method show good correspondence to the norms close the ground (Kaimal et al.) and over the entire boundary layer (Eurocode1, ESDU74031 and ESDU85020).

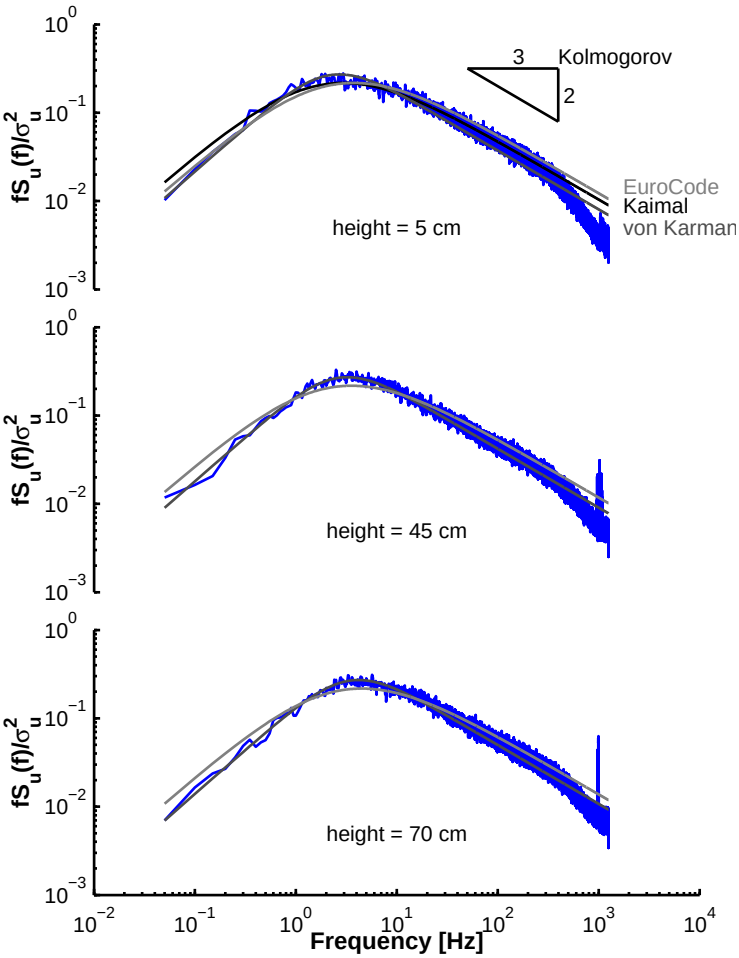

Figure 3.34: Measurements of the power spectral density for the Counihan method show good correspondence to the norms close the ground (Kaimal et al.) and over the entire boundary layer (Eurocode1, ESDU74031 and ESDU85020).

3.3.3 Conclusion of the ABL simulation

To resolve the recurrent EGR problem by performing wind tunnel simulations, the ABL needed to be simulated. In this section, the ABL of the VUB was re-created using well-known techniques. The ABL was identified as suburban (terrain type III). The ABL was simulated in the wind tunnel using two simulations techniques: truncated Irwin-spires in combination with roughness elements and truncated Counihan-ellipses in combination with a castellated barrier wall and roughness elements. Comparison of different characteristics of the ABLs showed good correspondence to the international standards. Both methods showed to be able to simulate a representative boundary layer with scales of 1:363 (Irwin method) and 1:390 (Counihan method). Finally, the Counihan-method was used for ABL simulation in the wind tunnel tests to solve the EGR problem.

3.4 Wind tunnel test with the scale model

In the tunnel, the ABL was re-created at scale using well-known techniques, as mentioned before. After creating this ABL, a scale model of the building where the T100 is installed as well as the surrounding buildings was placed in the tunnel to study the influence of the wind speed and direction on the EGR. The aim of the wind tunnel experiments was to find a solution that would prevent the EGR. The wind tunnel tests demonstrated the required renovations and adaptations to improve the current mGT plant set-up.

3.4.1 Scale model

The T100 is installed in building Z at the VUB campus (Figure 3.35, model scale 1:200). The scaled down stack is indicated on Figure 3.35. For the wind tunnel test, all buildings and vegetation within 300 m distance of building Z were included in the scale model. Figure 3.36 shows the used scale model for the wind tunnel test.

3.4.2 Wind tunnel test conditions

To be able to perform a representative experiment for the real situation, the wind speed should be chosen in a way that the following dimensionless

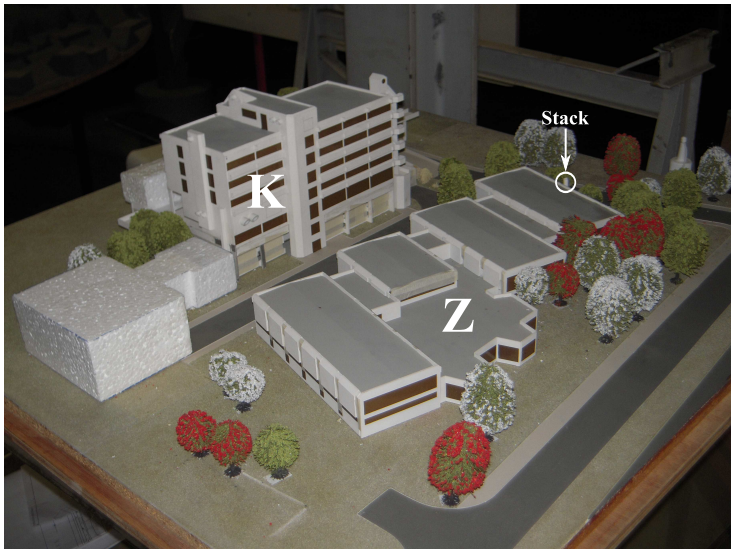

Figure 3.35: 1:200 scale model of buildings Z and K with indicated mGT stack.

Figure 3.36: 1:200 scale model of building Z and surrounding.

numbers remain the same [237]:

$$\mathrm{Re} = \frac{\rho \bar{u} L}{\mu} \tag{3.37}$$

$$\mathrm{Fr} = \frac{\bar{u}^2}{gL} \tag{3.38}$$

$$\mathrm{Ma} = \frac{\bar{u}}{a} \tag{3.39}$$

For experiments in which the model is held stationary during data gathering, the Reynolds number (Re) and Mach number (Ma) are the significant similarity parameters. If a model experiment has the same Re and Ma numbers as the full-scale application, then the model and the full-scale flows will be dynamically similar. For this application, the vortices around the buildings are the most important ones, so the Re number should be kept constant. The characteristic length (L) is scaled down by a factor 200 (scale), which would involve an increase in wind speed by the same factor (Equation 3.37). However, the high intensity turbulence of the ABL and the typical, sharp shape of the buildings reduce the Re number dependency. Barlow et al. stated that if there is no laminar flow due to high free-stream turbulence and the shapes of the buildings are so sharp that all separation locations are geometrically determined, then there will be little dependence on Re number [238]. Therefore during the tests, wind speeds were kept as in reality (2 to 12 m/s). Above this wind speed, for any wind direction, no more recirculation was noticed due to the good diffusion of the smoke.

The same argumentation as used for setting the free wind speed, is used to determine the necessary speed of the exhaust gases and the inlet air flow. The inlet air enters the air filter with an average speed of 2.9 m/s, while the hot exhaust gases leave the stack with an average speed of 15 m/s. The ventilation air speed is a little lower, due to the lower temperature, namely 13 m/s. A smoke generator with changeable flow rate was used for the visualisation of the exhaust gases.

3.4.3 Wind tunnel test results

A first short wind tunnel test was carried out at 0 m/s wind speed. During this run, a problem was already revealed. On top of the stack, a cap is placed, in order to prevent water to enter the stack (Figure 3.10). This

Table 3.3: Results of wind tunnel test on recirculation.

Wind direction	With Cap	Without Cap	Extra height
North	No EGR	No EGR	/
North-East	EGR till 4 m/s	No EGR	/
East	EGR till 8 m/s	No EGR	/
South-East	EGR till 8 m/s	No EGR	/
South	EGR till 8 m/s	EGR till 8 m/s	1 to 1.5 m
South-West	EGR till 12 m/s	EGR till 12 m/s	1 to 1.5 m
West	EGR till 12 m/s	EGR till 12 m/s	2 to 2.5 m
North-West	No EGR	No EGR	/

cap disturbs the natural flow of the exhaust, forces the exhaust gases back down, thus enabling the EGR. By removing this cap, most of the problems for 0 m/s wind speed were solved. Some small recirculation remained, due to the suction at the inlet of the mGT.

During the first series of experiments using the scale model of building Z with the hat on top of the stack, exhaust gases re-enters the mGT for many wind directions, resulting in a lower electric efficiency of the mGT (Table 3.3). For each experiment, wind speed was increased for all wind directions until no recirculation remained. Especially for the wind direction South, West and South-West, recirculation is a huge problem. Even at high wind speed, the exhaust gases still re-enters the engine. A possible explanation is the presence of the building K, which is several times higher than building Z and the stack (see Figure 3.35). Building K probably produces vortices that force the exhaust air down instead of diffusing it.

Once the cap is removed from the stack, EGR seems to solve itself for most of the wind directions (Table 3.3). However for the wind coming across building K (wind direction South, South-West and West, Figure 3.11), recirculation remains a problem, even for high wind speeds. By making the stack 2 m higher, the problem can almost be solved completely.

3.4.4 Applied solution

The two stacks of the T100 mGT have been heightened by 3 m as was found a solution by wind tunnel tests to prevent EGR (Figure 3.37).

New dry and wet experiments were performed to check if the additional height of 3 m was sufficient to prevent EGR. Both the dry (Figure 3.38)

Figure 3.37: The ventilation and exhaust gas stack were heightened to prevent EGR.

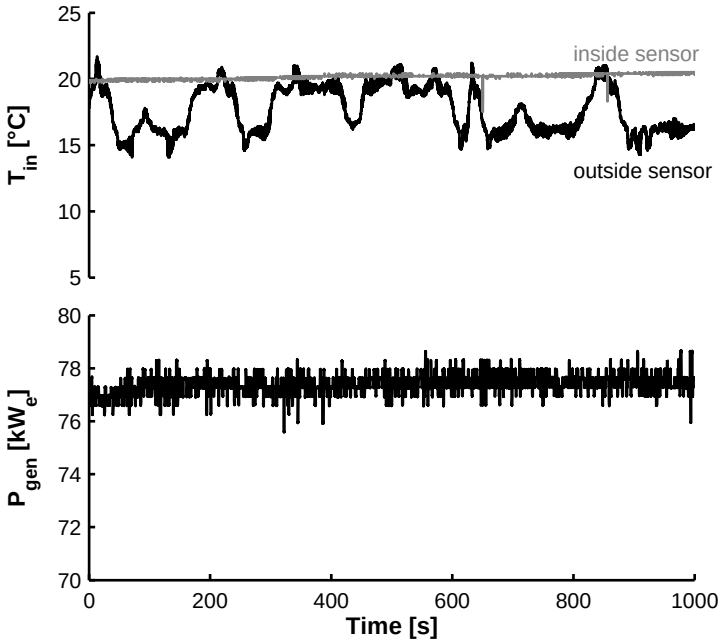

Figure 3.38: Produced electric power remains constant during dry run.

and wet (Figure 3.39) experimental results show a major improvement. Produced electric power and injected steam from rate remain constant during the test run. More noise on the measurements of the produced power and the inlet air temperature can be observed, since in these more recent measurements, no filter was applied on the input signal of the sensors. In addition, inlet air temperature is still varying, but to a lower extent. This variation is a result of the relocation of the sensor. In previous experiments (see Figure 3.12 and Figure 3.14), the thermocouple was installed in front of the inlet air filter. The thermocouple is then relocated in a free accessible position. The variations are due to changing wind speed. Therefore, the second temperature sensor, in the mGT casing was used.

The correlation between the parameters has dropped (Figure 3.40), which shows that heightening the stack prevents EGR. For both the dry and wet experiments, the correlation has dropped significantly. No clear maximum, as in the old measurements, could be observed. This indicates that there is no link between the fluctuations in the inlet air temperature and the fluctuations in produced electric power output and injected steam flow rate.

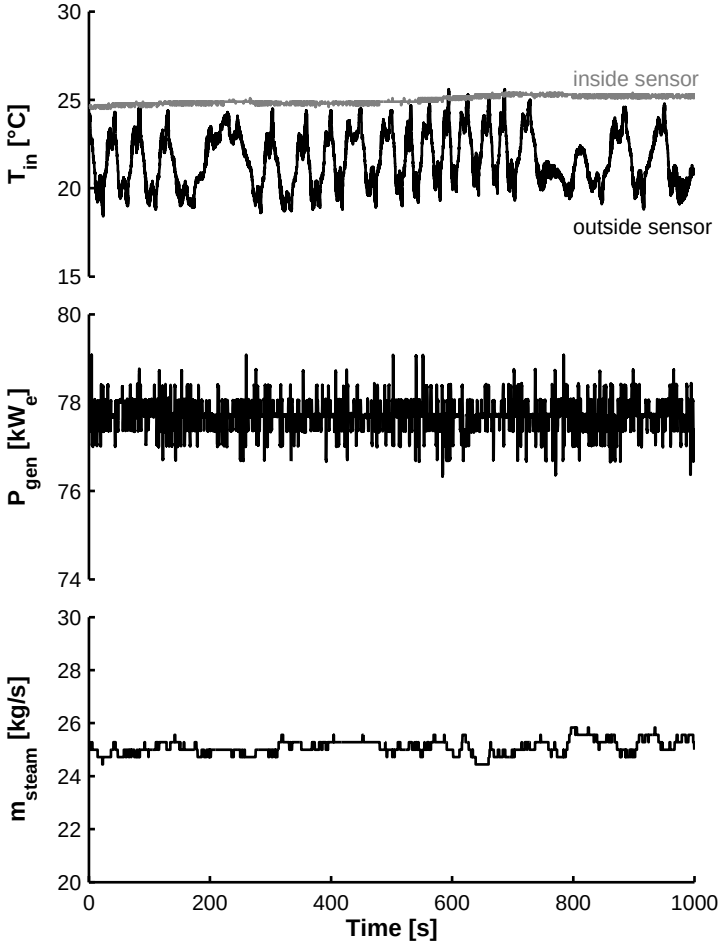

Figure 3.39: Steam injection and power production remain constant during wet run after changing the stacks.

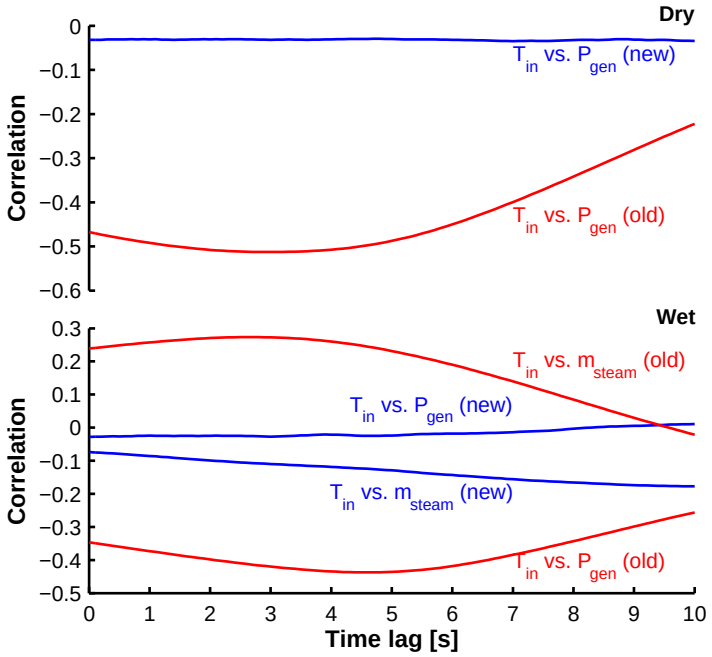

Figure 3.40: Correlation between the different parameters has reduced.

The very small fluctuations in inlet air temperature (measured with the inside sensors) are due to noise on the signal, while the fluctuations in the electric power are a results of the operation of the power electronics and noise on signal. The power electronics are not capable of delivering a perfect constant power output, explaining the fluctuations. Finally, the fluctuations of the steam flow rate can be explained by the operation of the mGT control system that keeps the produced power constant by changing the rotational speed. By changing the rotational speed, the compressor output pressure changes, resulting in a different steam flow rate. The fluctuations are independent of each other, indicating that the problem of EGR has been solved.

3.5 Conclusion

In this chapter, the dry characterization of the mGT is studied. The Aspen® model of the dry performance mGT was validated against measurements. Results indicated that both nominal and part load performance predicted by

the simulation model correspond to the measurement results. In addition, the measurements were able to determine the dry operating line of the compressor in the compressor map.

In a second section, the EGR has been studied on the mGT CHP installation. The exhaust gas recirculation on the T100 mGT was first noticed during experiments with steam injection in the engine. Due to the exhaust recirculation, the composition and temperature of the inlet air varied continuously. These changing inlet air conditions resulted in an unstable operation of the mGT. Analysis of the measured inlet temperature and the produced power showed that the unsteady regime of the mGT was caused by changing inlet conditions. Two sets of simulations, steady-state simulations in Aspen® and dynamic simulations in Simulink® showed the effect of the exhaust recirculation on the overall performance of the mGT. Steady-state simulations indicated that the loss in efficiency was caused by the exhaust gas recirculation. Not only the higher inlet air temperature, but also the changing composition of the inlet air, plays an important role in the loss in efficiency. Dynamic simulations showed the influence of the frequency and amplitude of the recirculation on the average performance. The significant influence of the exhaust recirculation on the global performance of the mGT impedes validation of simulations against measurements. Modelling the recirculation is extremely difficult, due to the complexity of the process. In order to obtain good measurements for validating simulation models, exhaust air recirculation should be avoided in reality.

A solution for the EGR problem was proposed. By simulating the ABL in an industrial wind tunnel, the EGR could be simulated on a scale model. The ABL was simulated using two well-known techniques. Results of ABL simulations were validated against international standards. Wind tunnel tests visualized the recirculating problem and its dependency on wind direction and speed. Above a certain wind speed, no recirculation was observed, due to the good diffusion of the smoke in the air. The results from these wind tunnel tests were used to make adaptations to the T100 installation and certain recommendations were formulated for preventing such EGR. The stack was heightened and test results indicated that there was no more recirculation.

Chapter 4

Wet mGT characterization

It is essential to know the off-design behaviour of the mGT control system and compressor before addressing humidification. Converting a classic recuperated mGT into a humidified mGT cycle requires some additional knowledge of the machine behaviour under wet conditions. In addition, the impact of the humidified working fluid on performance needs to be known to predict the final performance of the humidified mGT. Finally, humidified mGTs also face additional problems like surge margin reduction and combustion stability problems, which requires special attention. To study the effect of humidifying the mGT working fluid, I performed steam injection simulations and experiments on the Turbec T100 mGT. Steam injection was chosen over water injection since it is much easier to accomplish and requires less modifications to the machine. Although the impact of steam on the performance is less profound, the behaviour of the control system and the compressor are similar. In this chapter, I will discuss the characterisation of steam injection in the Turbec T100. This effect was first simulated in Aspen® to predict the potential performance. These simulations were then validated using experimental data. During this validation, I first focused on global performance, but also on the off-design behaviour of the compressor and the surge margin reduction. Finally, steam injection experiments in an atmospheric, variable-swirl, premixed burner were performed to study the effect of water injection on combustion stability.

4.1 Effect of steam injection on the mGT performance

Steam injection is a successful way to improve electric efficiency of GTs [30]. In literature, several studies show the potential for steam injection in mGTs by means of simulations and experiments (see section 1.2).

In the following subsections, I will first discuss the conversion of the dry Aspen® simulation model into a steam injection model of the mGT. Then, the experimental approach for steam injection experiments in the Turbec T100 mGT is discussed. Finally, the simulation model will be validated using the experimental results.

4.1.1 Aspen® simulation model of the steam injection in the Turbec T100 mGT

The steam injection in the Turbec T100 mGT is modelled in the Aspen® plus simulation engine. An adapted version of the previously developed model of the dry mGT cycle (see subsection 3.1.1) is used.

The existing controller of the T100 mGT is implemented in the Aspen® model like in the previous chapter (subsection 3.1.1). The controller keeps the generated electric power and TOT constant by adapting the compressor shaft speed and the natural gas flow rate. In the Aspen® model, constant generated electric power and TOT are set as design specifications. By varying shaft speed and natural gas flow rate, the Aspen® solver can converge to a solution, respecting the design specifications.

For the modelling of the compressor, the same Turbec compressor map, used in previous chapter, was used again (Figure 3.2). When steam is injected in the cycle, the total mass flow rate through the turbine will increase, resulting in a higher turbine and produced electric power. To keep the produced electric power constant, rotational speed is decreased, resulting in a lower compressor mass flow rate (off-design). The operating point of the compressor will thus move away from its optimal dry operating point. This can result in a change in compressor efficiency. The maximum amount of injected steam was however rather low, so the compressor efficiency could be assumed constant (Figure 4.1).

In the Aspen® model, the turbine is still assumed to be choked (Equation 3.1). Due to the injection of steam, the heat capacity ratio (k_{turb})

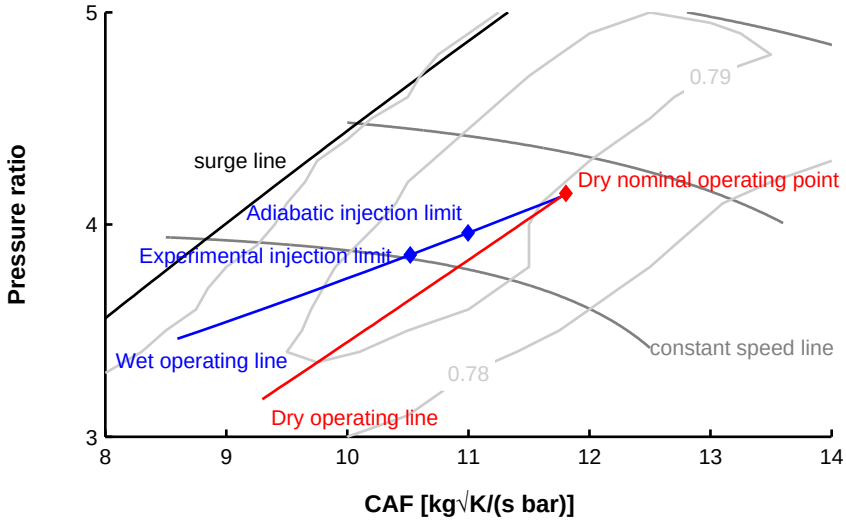

Figure 4.1: Steam injection in the mGT cycle between the compressor outlet and the recuperator inlet will result in a reduced compressor speed and pressure ratio. As a result, the surge margin will reduce. Since only a low amount of steam is injected, compressor efficiency remains constant.

in Equation 3.1 will change (0.1 % per 0.01 kg_{steam}/kg_{air}), resulting in a different choking value. Next to the choking condition, the isentropic efficiency of the turbine will also change due to steam injection. The dry turbine efficiency of 0.85 can be compensated using the following formula (for details, see [34]):

$$\frac{\eta_{is}}{\eta^*_{is}} = \frac{k-1}{k^*-1}\sqrt{\frac{k^*+1}{k+1}\frac{1-1/\pi^{\gamma^*}}{1-1/\pi^{\gamma}}}. \tag{4.1}$$

In Equation 4.1, the apex (*) refers to the properties at standard air composition. γ is defined as $(k-1)/k$. However again, since the amount of injected steam is rather low, the turbine efficiency was assumed constant and equal to the dry efficiency of 0.85 to reduce the calculation time. Simulations using the corrected heat capacity ratio and turbine efficiency showed little effect on the global mGT performance (less than 0.01 % change on final mGT electric efficiency).

The electric steam boiler was modelled as a series of three generic heaters. In the experimental set-up, an electric steam boiler was installed to provide the steam. Normally, an electric boiler can simply be simulated in Aspen® using one generic heater. Aspen® however encounters problems when phase change occurs. Therefore, the boiler was split in three different heaters: a water heater, a boiler and a steam superheater. The first heater will thus heat up the liquid water till the boiling point. This boiling point is determined by the pressure behind the compressor. The Aspen® model is a representation of the experimental set-up. In this experimental set-up, the steam pressure and steam flow rate are determined by the pressure behind the compressor, since there is no control valve in between the steam boiler outlet and the injection point (see later). The second heater will provide the necessary heat to transform the liquid water into steam. Finally the third heater will superheat the steam by 0.1 °C. While in the experimental set-up, the steam flow rate is controlled by the boiler heating power, in the simulations, the steam flow rate is set as a boundary condition, while the heating power is adapted to provide saturated steam.

The Aspen® simulations predict that steam injection will reduce the fuel flow rate by 0.35 g/s when injecting 22 g/s of steam, which results in a higher electric efficiency of 33.92 % (Table 4.1). The mGT control system keeps the produced power constant by reducing the compressor rotational speed (around 1500 rpm). This results in a reduced pressure ratio (0.1 bar), compressor outlet temperature (7 °C) and air mass flow rate (50 g/s). The

slightly lower recuperator inlet temperature in combination with the increased heat capacity due to the steam injection require more heat transfer in the recuperator (3.4 kW_{th}) to achieve a constant cold outlet temperature. TIT reduces slightly by 14 °C since TOT is kept constant while the heat capacity of the working fluid has changed. The remaining thermal power after subtraction of the thermal power necessary to produce the steam amounts 98.3 kW_{th}, resulting in a reduced thermal efficiency of 33.9 %.

4.1.2 Steam injection experimental approach

The mGT electric efficiency is calculated using formula (same as Equation 3.7):

$$\eta_{el} = \frac{P_{el}}{\dot{m}_{natgas} LHV}. \tag{4.2}$$

Although externally produced steam is injected in the mGT, the energy necessary to produce the injected steam is not considered in the efficiency calculations (Equation 4.2). In the final layout of a steam injected mGT, the goal would be to use steam, auto-raised in a low-pressure Heat Recovery Steam Generator (HRSG) with the available heat in the turbine exhaust (Figure 4.2). The amount of injected steam, externally produced with a steam generator, matches the maximum possible amount of steam that can be auto-raised, using a HRSG (which is quite expensive). For the lab set-up however, no HRSG was installed for steam production. Instead, an electric steam generator was used to produce the necessary steam in order to obtain a higher flexibility in the injected steam mass flow rate during the test.

The injected amount of steam is very small (maximum 5 % of the total mass flow rate of air) and the predicted rise in efficiency is limited to 0.44 % absolute per injected steam fraction (1 % steam on total compressor mass flow rate) at nominal load, resulting in a very small change in fuel flow rate (2 % less fuel consumption). The fuel flow rate meters are however not accurate enough to measure this small variation in fuel flow rate (accuracy of 0.5 % and 1 % of the total fuel flow rate measurement). This problem can be solved using an analytical perturbation analysis. In this perturbation model, an analytical model of the mGT is built, in order to accurately calculate the efficiency increase. Starting from a *reference case* (dry case, ψ_{ref}), which is perturbed by steam injection, the new condition (called the *adapted case*, $\psi_{adapted}$) is calculated using only perturbations ($\delta\psi$) of accurate measurable

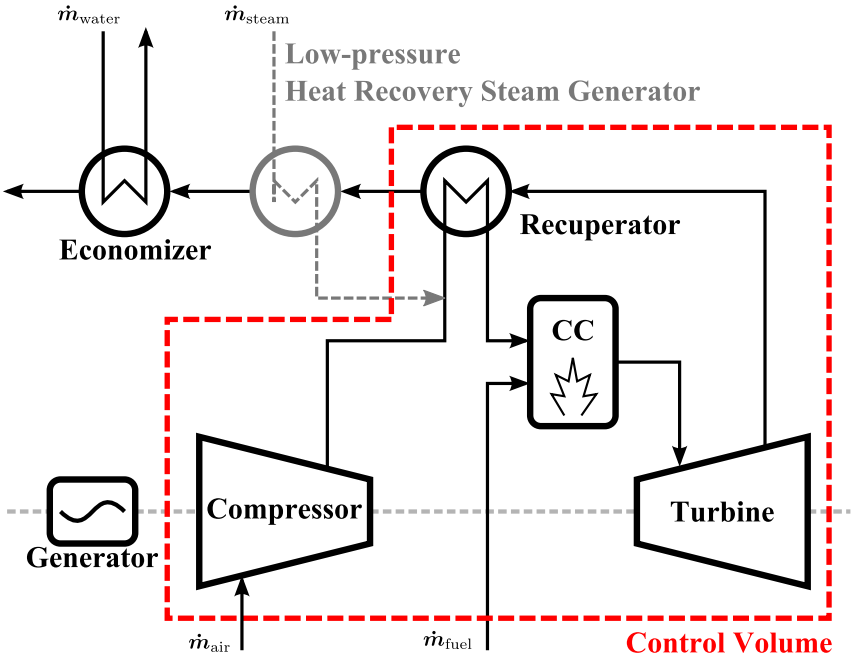

Figure 4.2: Auto-raised steam, produced using the hot exhaust gases, is injected in the mGT cycle between compressor outlet and recuperator inlet. By injecting steam in the cycle, electric efficiency can be improved. For the experiments, the low-pressure Heat Recovery Steam Generator (HRSG) is replaced by an electric boiler.

Table 4.1: Thermodynamic conditions of the T100 mGT at each stage of the cycle using the Aspen® simulation model under normal, dry conditions (Dry mode) and steam injection mode (Wet mode).

	Dry mode[1]	Wet mode[2]
Compressor		
T_{in}	15 °C	15 °C
p_{in}	1.013 bar	1.013 bar
T_{out}	195.7 °C	188.8 °C
p_{out}	4.194 bar	4.008 bar
$\dot{m}_{\text{comp}}$	0.704 kg/s	0.654 kg/s
P_{comp}	129.6 kW	115.8 kW
SM	22.1 %	20.4 %
Recuperator		
$T_{\text{in,cold}}$	195.7 °C	185.9 °C
$T_{\text{in,hot}}$	645 °C	645 °C
$T_{\text{out,cold}}$	574.9 °C	574.1 °C
$T_{\text{out,hot}}$	283.3 °C	274.5 °C
$\dot{Q}_{\text{rec}}$	286.5 kW	289.9 kW
Combustion chamber		
fuel	Natural gas	Natural gas
LHV	40.19 MJ/kg	40.19 MJ/kg
T_{out}	917.1 °C	903.4 °C
p_{out}	3.775 bar	3.607 bar
$\dot{m}_{\text{fuel}}$	7.69 g/s	7.34 g/s
Turbine		
T_{out}	645 °C	645 °C
p_{out}	1.05 bar	1.05 bar
$\dot{m}_{\text{turb}}$	0.711 kg/s	0.684 kg/s
P_{turb}	229.6 kW	215.8 kW
Steam		
$\dot{m}_{\text{steam}}$	–	22.0 g/s
T_{steam}	–	144.9 °C

[1] *Dry mode* corresponds to the normal CHP mode of the mGT, running at nominal electric power.

[2] *Wet mode* corresponds to the steam injected case. The thermodynamic conditions given in the table correspond to the maximal adiabatic steam injection possible (steam fraction of 3.3 %.

Table 4.1: (continued)

	Dry mode	Wet mode
p_{steam}	–	4.008 bar
Steam status	–	Saturated
Global		
P_{el}	100.0 kW_e	100.0 kW_e
η_{el}	32.35 %	33.92 %
N	67 312 rpm	65 751 rpm
$\dot{Q}_{\text{th}}$	170.1 kW_th	98.3 kW_th
η_{th}	55.3 %	33.9 %
T_{stack}	55 °C	55 °C

parameters (in this case rotational speed N and injected steam flow rate $\dot{m}_{\text{steam}}$):

$$\psi_{\text{adapted}} = \psi_{\text{ref}} + \delta\psi. \tag{4.3}$$

In this subsection, first the perturbation analysis is discussed. Secondly, the used steam generator to produce the steam is analysed. In a third part, the specific developed experimental procedure, necessary for the perturbation analysis, is explained. Finally, the effects of steam injection on surge margin and combustion stability is studied.

Perturbation analysis

The electric efficiency of the mGT can be calculated using Equation 4.2. When steam is injected in the mGT, electric power will rise, but the T100 mGT operates under constant power output condition, so the controller will interfere and adjust the injected fuel flow rate in the combustion chamber. Thus, the rise in efficiency caused by steam injection can be found through the following equation (produced electric power remains constant and assuming a constant LHV during the test):

$$\left.\frac{\delta\eta_{\text{el}}}{\eta_{\text{el}}}\right|_{\text{ref}} = -\left.\frac{\delta\dot{m}_{\text{natgas}}}{\dot{m}_{\text{natgas}}}\right|_{\text{ref}}. \tag{4.4}$$

The produced electric power does not appear in Equation 4.4, since the mGT operates under constant power output condition. $\delta\dot{m}_{\text{natgas}}$ has to be

calculated for the aforementioned reasons. The goal of the perturbation analysis is to find an expression:

$$\delta\dot{m}_{\text{natgas}} = f\left(\delta N, \delta\dot{m}_{\text{steam}}\right), \tag{4.5}$$

where $\delta\dot{m}_{\text{natgas}}$ is only a function of the accurately measurable perturbations δN and $\delta\dot{m}_{\text{steam}}$. This means that all parameters of the mGT have to be expressed as a function of the changes in rotational speed (δN) and injected steam flow rate ($\delta\dot{m}_{\text{steam}}$).

In a first step, all perturbations of parameters from the turbine and compressor are expressed as a function of δN and $\delta\dot{m}_{\text{steam}}$. The problem, however, is that all parameters are linked, so a system of equations has to be created and solved. A first set of equations is given by the controller of the mGT. During operation, the controller keeps the electric power output constant. In order to keep the electrical efficiency as high as possible, TIT should be maximal. To do this, TOT is controlled and kept constant.

$$|P_{\text{turb}}| - |P_{\text{comp}}| = |P_{\text{el}}| \tag{4.6}$$

$$\text{TOT} = \text{constant} \tag{4.7}$$

The turbine inlet is assumed to be choked, resulting in the following equation (same as Equation 3.1):

$$\frac{\dot{m}_{\text{turb}}\sqrt{\text{TIT}}}{\text{PIT}} = A\sqrt{\frac{k_{\text{turb}}}{R}\left(\frac{2}{k_{\text{turb}}+1}\right)^{\frac{k_{\text{turb}}+1}{k_{\text{turb}}-1}}} = \text{cte.} \tag{4.8}$$

During steam injection experiments, the composition of the exhaust gas will change significantly, resulting in a changing specific heat ratio, k_{turb} and thus a change in the choking constant. Calculations of this changing condition at maximal steam injection rate showed however a maximal variation of less than 0.01 % of the absolute change in electric efficiency. For further calculations, the value of the choking constant in Equation 4.8 was therefore kept constant, as in the Aspen® simulations. Energy conservation expressed over compressor and turbine gives following equations:

$$|P_{\text{turb}}| = \dot{m}_{\text{turb}} C_{p,\text{turb}} \left(\text{TIT} - \text{TOT}\right); \tag{4.9}$$

$$|P_{\text{comp}}| = \dot{m}_{\text{comp}} C_{p,\text{comp}} \left(T_{\text{comp,out}} - T_{\text{comp,in}}\right). \tag{4.10}$$

Isentropic laws express the relation between in- and outlet of compressor

and turbine resulting in another four equations.

$$\frac{\mathrm{TOT_{is}}}{\mathrm{TIT}} = \left(\frac{\mathrm{POT}}{\mathrm{PIT}}\right)^{\frac{\kappa_{\mathrm{turb}}-1}{\kappa_{\mathrm{turb}}}} \tag{4.11}$$

$$\frac{T_{\mathrm{comp,out,is}}}{T_{\mathrm{comp,in}}} = \left(\frac{p_{\mathrm{comp,out}}}{p_{\mathrm{comp,in}}}\right)^{\frac{\kappa_{\mathrm{comp}}-1}{\kappa_{\mathrm{comp}}}} \tag{4.12}$$

$$\eta_{\mathrm{is,turb}} = \frac{\mathrm{TIT}-\mathrm{TOT}}{\mathrm{TIT}-\mathrm{TOT_{is}}} \tag{4.13}$$

$$\eta_{\mathrm{is,comp}} = \frac{T_{\mathrm{comp,out,is}}-T_{\mathrm{comp,in}}}{T_{\mathrm{comp,out}}-T_{\mathrm{comp,in}}} \tag{4.14}$$

Compressor and turbine efficiency ($\eta_{\mathrm{is,comp}}$ and $\eta_{\mathrm{is,turb}}$) are assumed to be constant. Aspen® simulations of the steam injection showed that with a steam injection ratio of 5 %, the pressure ratio and mass flow rate of the compressor change less than 10 % (Figure 4.1). On the compressor map (Figure 4.1), the efficiency of the compressor changes only little in the zone around the dry operating point (less than the accuracy of the compressor map). Therefore, compressor efficiency was kept constant. The link between the compressor and the turbine is given by the pressure. A small pressure drop (10 %) in the combustion chamber, between compressor and turbine is assumed (see subsection 3.1.1). Pressure Outlet Turbine (POT) is constant and slightly above atmospheric pressure:

$$\mathrm{PIT} = 0.9\ p_{\mathrm{comp,out}}, \tag{4.15}$$

$$\mathrm{POT} = \mathrm{constant}. \tag{4.16}$$

More details about Equations 4.7 to 4.14 can be found in [161]. Differentiating Equations 4.7 to 4.16 results in a set of 11 equations with 12 unknown perturbations δ. To solve this set of equations, a 12^{th} equation is necessary. This 12^{th} equation is given by the ompressor map. This equation expresses the link between shaft speed, air flow rate and pressure ratio of the compressor. The compressor map is made analytical by fitting super ellipses with the constructor's map [160]:

$$\left(\frac{\mathrm{CAF}}{a}\right)^{z} + \left(\frac{\pi-1}{b-1}\right)^{z} = 1, \tag{4.17}$$

where a equals the ingoing mass flow rate when pressure ratio (π) equals 1, just like b is equal to the pressure ratio when the mass flow rate decreases to 0. Both conditions could never be reached, because of the surge and choking

limits of the compressor. The system of equations can now be solved and the perturbation of all turbine and compressor parameters can be expressed as a function of $\delta\dot{m}_{\text{steam}}$ and δN.

In a second step, by expressing and differentiating the energy balance over a control volume (Figure 4.2), an expression for the change in fuel consumption as function of known perturbations, calculated in the previous step, is obtained.

The energy balance over the control volume indicated in Figure 4.2:

$$\begin{aligned}\dot{m}_{\text{comp}}C_{p,\text{air}}\left(T_{\text{comp,in}}-T_{\text{ref}}\right)+\dot{m}_{\text{natgas}}\text{LHV} = \\ P_{\text{el}}+\dot{Q}_{\text{loss}}+\left(\dot{m}_{\text{turb}}-\dot{m}_{\text{steam}}\right)C_{p,\text{fluegas}}\left(T_{\text{rec,out}}-T_{\text{ref}}\right) \\ +\dot{m}_{\text{steam}}C_{p,\text{steam}}\left(T_{\text{rec,out}}-T_{\text{inj}}\right).\end{aligned} \tag{4.18}$$

After differentiating, the energy balance becomes:

$$\begin{aligned}\delta\dot{m}_{\text{comp}}C_{p,\text{air}}\left(T_{\text{comp,in}}-T_{\text{ref}}\right)+\delta\dot{m}_{\text{natgas}}\text{LHV} = \\ \left(\delta\dot{m}_{\text{turb}}-\delta\dot{m}_{\text{steam}}\right)C_{p,\text{fluegas}}\left(T_{\text{rec,out}}-T_{\text{ref}}\right) \\ +\delta\dot{m}_{\text{steam}}C_{p,\text{steam}}\left(T_{\text{rec,out}}-T_{\text{inj}}\right) \\ +\left(\dot{m}_{\text{turb}}-\dot{m}_{\text{steam}}\right)C_{p,\text{fluegas}}\delta T_{\text{rec,out}} \\ +\dot{m}_{\text{steam}}C_{p,\text{fluegas}}\delta T_{\text{rec,out}}.\end{aligned} \tag{4.19}$$

Rearranging Equation 4.19 results in an expression for $\delta\dot{m}_{\text{natgas}}$:

$$\begin{aligned}\delta\dot{m}_{\text{natgas}} = [\left(\delta\dot{m}_{\text{turb}}-\delta\dot{m}_{\text{steam}}\right)C_{p,\text{fluegas}}\left(T_{\text{rec,out}}-T_{\text{ref}}\right) \\ +\delta\dot{m}_{\text{steam}}C_{p,\text{steam}}\left(T_{\text{rec,out}}-T_{\text{inj}}\right) \\ +\left(\dot{m}_{\text{turb}}-\dot{m}_{\text{steam}}\right)C_{p,\text{fluegas}}\delta T_{\text{rec,out}} \\ +\dot{m}_{\text{steam}}C_{p,\text{fluegas}}\delta T_{\text{rec,out}}-\delta\dot{m}_{\text{comp}}C_{p,\text{air}}\left(T_{\text{comp,in}}-T_{\text{ref}}\right)]/\text{LHV}.\end{aligned} \tag{4.20}$$

The only remaining problem is the unknown temperature in between the recuperator and the economizer ($T_{\text{rec,out}}$). Using the Logarithmic Mean Temperature Difference (LMTD) method [239], the specifications of the recuperator given by Lagerström and Xie [48] and the hypotheses from Hahn [240], the temperature of the flue gases at the recuperator outlet can be calculated. Once $\delta T_{\text{rec,out}}$ is known, the change in fuel consumption can be calculated.

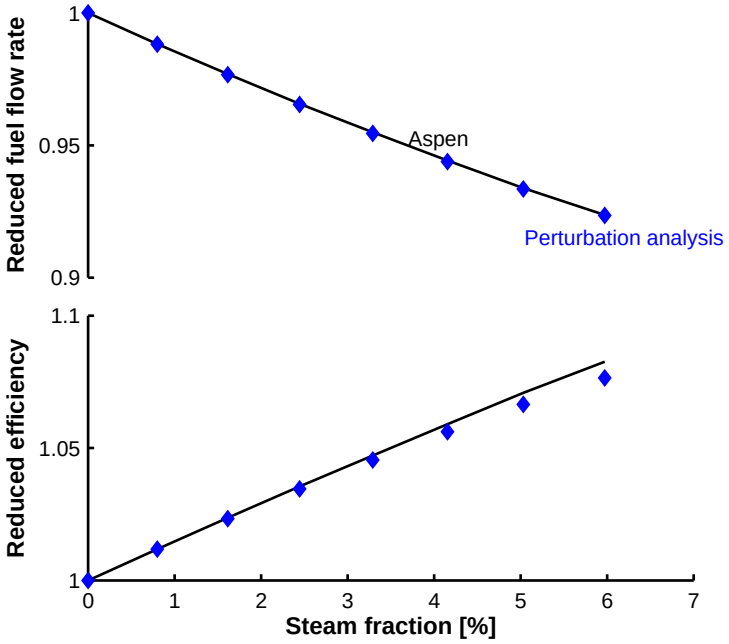

Figure 4.3: Both the reduced efficiency increase and the reduced fuel flow rate decrease through steam injection can be predicted accurately with the perturbation analysis.

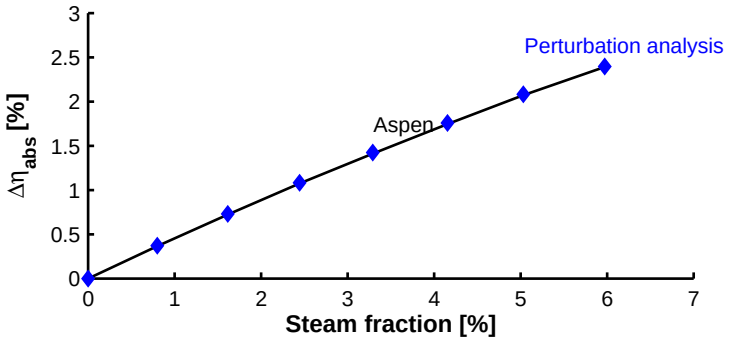

Figure 4.4: The efficiency increase, predicted by the perturbation analysis, agrees well with the simulated absolute efficiency increase using the Aspen® simulation model.

Table 4.2: Results of the *what if*-analysis indicate that the perturbation analysis model is capable of accurately determining the effect of steam injection on the electric efficiency.

$\dot{m}_{\text{steam}}$	Aspen® [1]	δ [2]	*what if* [3]	Δ_{abs} [4]	Δ_{rel} [4]
35 g/s [5]	2.39 %	2.39 %	2.41 %	0.02 %	0.9 %

[1] Simulated electric efficiency increase using Aspen®.

[2] Calculated absolute efficiency increase with the perturbation analysis model, using the exact perturbations from the Aspen® simulations.

[3] Calculated absolute efficiency increase with the perturbation analysis model, by letting the exact perturbations from the Aspen® simulations vary between their limits of uncertainty.

[4] Compared to the Aspen® results.

[5] Maximal steam flow rate injected during reported experiments.

Comparison of the analytic perturbation analysis results with the Aspen® simulations showed good correspondence (Figure 4.3 and 4.4).

The aim of the perturbation analysis is to reduce the error on the change in measured fuel consumption in order to have an accurate estimation of the rise in efficiency. To estimate the error on $\delta\dot{m}_{\text{fuel}}$ in the perturbation analysis, a *what if*-analysis was performed. For this *what if*-analysis, it was necessary to know the relative errors on the measured shaft speed and the mass flow rate of injected steam. By letting the input values of the perturbation model ($\delta N, \delta\dot{m}_{\text{steam}}$) vary between their limits of precision, the maximal and minimal possible efficiency rise can be calculated. Out of these maxima, the uncertainty on the final result can be predicted.

The shaft speed of the compressor is measured through an optical technique (encoder). This technique has typically an accuracy of 0.01 % of the nominal shaft speed. The incoming steam flow rate is measured with a *Yokogawa* flow vortex meter with an accuracy of 1 %.

The *what if*-analysis results in Table 4.2 show that the difference between the rise in efficiency – calculated with the exact *measured* values from the Aspen® simulations – and the maximal rise in efficiency – calculated using values between the uncertainty limits of the input perturbations – is very small. This gives rise to an accuracy around 0.9 % of the absolute increase in efficiency for the perturbation analysis. This will make it possible to calculate the change in efficiency in a very accurate way.

Steam generator

To produce the necessary steam, an *Osbyparca* electric steam boiler is used. This steam boiler has a nominal electric power of 96 kW_e (Table 4.3). This maximum electrical power of the steam boiler was chosen in function of the maximal heat that could be recovered from the hot flue gases in the HRSG. This power was calculated via a pinch analysis, using a pinch of 25 °C and taking into account the changing air flow rate and temperature. Through steam injection, the total air flow rate through the engine will decrease and the temperature of the flue gases after the recuperator will as well decrease because of the additional water in the incoming cold flow [25]. Pinch analysis calculations showed that the adiabatic steam injection limit corresponds to an injection rate of 3.3 %. The electric power can be set over four different, equally distributed, power stages, resulting in different steam flow rates. Finally, the steam boiler produces saturated steam with a pressure corresponding to the set point.

The saturated steam (around 140 °C) from the steam generator is injected in the mGT behind the compressor, but before the recuperator (Figure 4.1) in the compressed air of around 180 °C. The steam boiler does not actively control the injected steam flow rate; the steam flow rate is determined by the pressure difference between the steam boiler and the compressor outlet. Once the pressure in the boiler surpasses the compressor outlet pressure, steam is injected. However, if the pressure after the compressor alters, the injected mass flow rate of steam will immediately adapt itself to the new conditions. A possible solution to avoid this unwanted fluctuation is a higher pressure in the steam boiler, resulting in a choked and constant steam flow rate. To achieve this choking condition, the pressure in the steam boiler needs to be twice as high as the pressure behind the compressor (7 to 9 bar).

The water level inside the boiler is kept constant with an auxiliary pump with adaptable shaft speed and flow rate. Based upon the outgoing steam flow rate, the frequency of the pump can be set. When a constant hot steam flow is leaving the boiler, the pump will inject the same amount of

Table 4.3: Specifications of the electric steam generator.

Voltage	3×400 V
Nominal Power	96 kW_e
Number of power stages	4
Nominal operating pressure	7 bar

cold water. This leads to steady-state operating conditions inside the boiler. In turn, this will keep the temperature and pressure constant, resulting in a constant outgoing steam flow rate. The outgoing steam flow rate is measured with the *Yokogawa* flow vortex meter with an accuracy of 1 %. The measurements of the outgoing steam flow rate of the electric boiler have been checked, using the ingoing electric energy of the boiler.

Experimental procedure for steam injection experiments

The experimental validation of the simulations of the steam injection was done at part and nominal load. The first experiments were performed at part load. After successful injection of steam at part load (70 and 80 kW_e), steam injection experiments at nominal and close to nominal electric power (90 and 100 kW_e) were performed. Because of the unadjusted controller of the T100 mGT, some precautions had to be taken. Therefore, for both series of experiments, two different start-up procedures were developed.

At part load the mGT was started and ran for over half an hour dry, in order to have a dry reference so the electric efficiency rise could be calculated exactly. After this *run in* period, steam was injected. The maximum pressure inside the boiler was raised above the pressure after the compressor. Electric power of the boiler was set to the minimum, in order to minimize the first injection flow rate. After a period, the power input of the boiler was raised and the injected steam flow rate increased. After the injection of the maximal steam flow rate, the flow rate was again gradually reduced. The experiments were finalized by a second dry run, which would serve as a second dry reference. An example of a steam injection test at 80 kW_e can be seen in Figure 4.5.

Initiating the injection of steam in the engine at nominal power was not possible, as predicted by dynamic simulations [184]. The simulations of the dynamic behaviour of the mGT showed that the sudden injection of steam at full load provoked an automatic shutdown by the unadapted control system of the unit. When steam is injected in the mGT, more power will be available at the shaft. This extra power allows the turbine to speed up and generate more electric power. At this point, the controller will interfere and slow down the engine by decreasing the fuel flow rate. At nominal speed however, the safety margin of the controller is narrower. When steam is injected at nominal speed, the sudden increase in rotational speed and produced electric power is seen by the controller as a mGT going

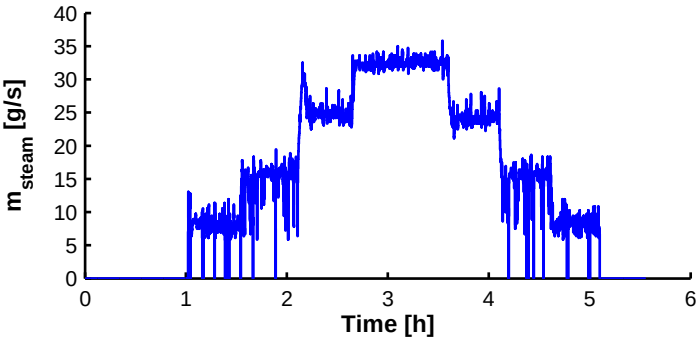

Figure 4.5: After a dry run of over half an hour, steam injection is initiated. By increasing the power of the steam boiler, the steam flow rate can be increased. Steam injection is first gradually increased and afterwards decreased. Each test is closed with a dry run of half an hour as dry reference.

in overspeed and the controller will consequently shut down the engine. Unfortunately, the experiments were performed before the connection with the control PLC through the WinNap software was made. Therefore, the shaft speed was only recorded by the engine monitoring system every 90 s, making it impossible to notice this phenomenon. For the steam injection experiments at nominal load, another steam injection protocol was utilized. From the first experiment, it appeared that the control system of the engine was able to handle the initiation of steam injection at 80 kW_e part load. Therefore, it was decided to start the steam injection at 80 kW_e part-load condition followed by a slow and steady increasing electric power demand towards 100 kW_e. While doing so, steam was injected successfully in this second experiment. After the steam injection was stopped, the engine was kept running for some time in dry mode, this in order to obtain post-run data for dry engine operation at nominal load as dry reference.

Surge margin reduction and combustion stability

Before experiments with steam injection could be started, two potential problems were considered: surge margin reduction and combustion stability.

In industrial GTs, steam injection will lead to an increase of the compressor discharge pressure [241]. This increase causes a surge margin reduction [72]. The maximal surge margin reduction in the mGT compressor is however limited, due to the variable shaft speed (Figure 4.1). In industrial GTs, running at constant rotational speed, the compressor operating point moves towards the surge line, following the constant speed line. Due to the variable rotational speed, the mGT operating point moves also downwards, resulting in a lower surge margin reduction than in the constant speed case.

No surge problems are expected when auto-raised steam is injected in the T100 mGT, since only a limited amount of steam will be injected during experiments in the mGT (maximal steam fraction of 3.3 % or 22.5 g/s). Surge margin drops from 22.1 to 20.3 % when the CHP mode is completely disabled and the adiabatic steam injection limit is reached. For my experiments, steam injection was extended beyond this limit. Therefore, the operating line is extended beyond the adiabatic limit of 3.3 % steam injection by means of adding steam raised through an external heat source. At maximum injected steam flow rate (35 g/s of steam, 5 % steam fraction), the surge margin will drop further till 18.9 % (Figure 4.1) which demonstrates the ability of the mGT to run safely in wet operation. Hohloch et al. and Zanger et al.

however revealed a considerably reduced surge margin for their Turbec T100 mGT, which should be taken into account [54, 136]. This surge margin reduction was however only noticed at their test facility. During steam injection experiments, no problems with surge were encountered.

Combustion instability and a reduction in combustion efficiency may cause augmented emissions of carbon monoxide and UHC. Multiple studies however reported low emission levels of CO [30] except at high humidification levels [242] and a reduction of NO_x emissions [69, 242–245] due to a lower equilibrium temperature and the increasing concentration of OH particles [243]. In the experiments performed for this thesis, the maximal injected steam flow rate, as mentioned before, is limited to 5 % steam of the total compressor mass flow rate. This is below the value of 10 wt%, used in experiments by Chen et al. without major CO emission increase [245] and below the limit of 33 wt%, found to be the limit for combustion, due to high CO levels by Hermann et al. [242]. A more detailed study on the effect of steam addition on the combustion in a mGT combustion chamber can be found in section 4.2.

4.1.3 Experimental results of steam injection tests

In this subsection, the experimental results of two series of steam injection experiments will be discussed. A first series, injecting steam at part load (80 and 90 kW_e) and full load (100 kW_e) was performed from February 2010 till April 2010. The second series, including steam injection experiments at part load of 70, 80 and 90 kW_e was performed in May and September 2012. The first series of experiments was performed before the additional sensors to measure the outlet pressure and temperature of compressor and the O_2 level of the exhaust gases. Therefore it was not possible to determine the compressor mass flow rate. For the second series, the additional sensors were installed as well as the WinNap software to communicate with the control PLC, allowing data recording on a much shorter timescale than before.

First series of steam injection experiments

As predicted by the simulations, the shaft speed reduces by injecting steam (Figure 4.6). At low injection rates, the measured changes in rotational

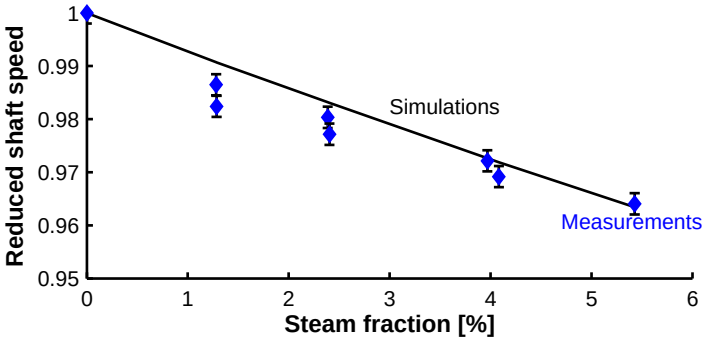

Figure 4.6: The measured change in rotational speed is only slightly larger than the predicted change from the Aspen® simulations for a steam injection experiment at part load (80 kW_e).

speed are larger than predicted in the Aspen® simulations. At maximum injection rate, the changes correspond well with simulations results.

The errors on the directly calculated efficiency values, using Equation 4.2, are very large (Figure 4.7). Therefore, it is of no use to compare simulated values with calculated values because the variance on the calculated efficiency rise is of the same order of magnitude as the rise itself. This illustrates very well the need for the perturbation analysis approach presented in this thesis because the errors on the values obtained via the perturbation analysis are much smaller (0.2 % of the absolute efficiency rise, Table 4.2). On the figures, the simulation results (Simulations), using as inlet air temperature the measured temperature of the air entering the compressor during the reference run of the specific test, are compared to measured results. Results of direct calculation of the efficiency out of the produced electric power and natural gas flow rate measurements (Measurements) are compared to the rise in efficiency, calculated using the analytic perturbation analysis model (Perturbation).

The simulation model of the steam injection in the mGT is too optimistic about the efficiency rise through steam injection (Figure 4.7). In reality, not the predicted 0.44 ± 0.02 % efficiency rise per 1 wt% steam fraction injected at nominal power, but a lower 0.34 ± 0.02 % was observed. Efficiency therefore increases less than expected. Two explanations are possible for the lower efficiency gain:

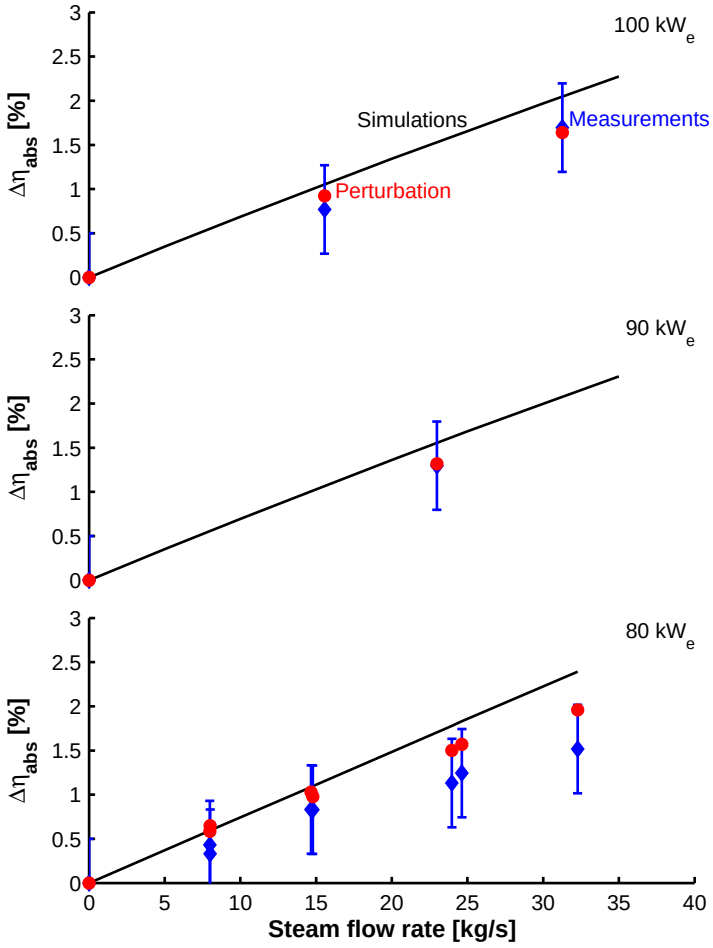

Figure 4.7: Perturbation analysis results indicate a difference between experimental efficiency increase and Aspen® simulation values for steam injection experiments at part load (80 and 90 kW_e) and nominal load (100 kW_e) using different steam flow rates.

- the real mass flow rate through the compressor was not measured during this series of experiments. Therefore, for the calculations in the perturbation analysis, the values obtained from the Aspen® simulation were used. Aspen® underestimates this compressor mass flow rate, as has been indicated in Figure 3.9. Despite the systematic error, the compressor map can still be used for the perturbation analysis, since the trend is the same. In the perturbation analysis, small variations are used rather than the exact mass flow rate and pressure ratio.

- the ingoing air and fuel mass flow rate and the generated power are all derived from the characteristics of the constructor's compressor map. There is a degree of uncertainty to which extent the utilized map is in accordance with the real characteristics of this engine. The dry operating line was already measured (Figure 3.9), but off-design behaviour was unknown at this stage.

The steam injection experiments resulted in stable runs of the engine, a predicted reduction in shaft speed and increasing electrical efficiency. However, the validation of the Aspen® simulations against the experimental data revealed that the simulations were too optimistic. Efficiency increased less than expected with steam injection. This validation revealed the necessity for a more accurate determination of the air and fuel mass flow rate and compressor map validation. Therefore, the second series of steam injection experiments with additional pressure sensor and mass flow rate determination were preformed.

Second series of steam injection experiments

The first validation of the Aspen® model of the steam injection showed a difference between the measured and simulated efficiency increase. More accurate determination of the air mass flow rate and compressor characteristics was thus necessary. In addition, the initial experiments were performed before the stack was heightened. The EGR made the performance of the T100 mGT very unstable, possibly influencing the performance of the mGT under steam injection conditions.

The second series of experiments was performed after the T100 mGT had been equipped with the additional pressure sensor to measure the pressure at compressor outlet. To determine the air mass flow rate, the oxygen level in the exhaust gas has been measured. In addition to the natural gas mass

flow rate and relative humidity of the inlet air, the incoming air mass flow rate could be accurately calculated. In a first step, the wet operating line on the compressor map has been validated by means of extensive experimental data. In a second step, additional steam injection tests have been performed at nominal load and part load.

Adding the steam injection experimental results to the compressor map clearly shows that the dry operating line has a different slope compared to the wet operating lines (Figure 4.8). Simulation results do not perfectly correspond to the experimental results, however the slope of the wet measured operating lines corresponds well with the simulated operating lines. The differences can be explained by the measurement accuracy of the air mass flow rate. Since the perturbation analysis only uses the difference with the dry reference and not the absolute results, the perturbation analysis is still able to give an accurate result for the efficiency increase due to the same slope that can be observed.

The measured efficiency rise corresponds well with the predicted efficiency rise (Figure 4.9 and 4.10). The large error bars, due to the lack of accuracy in the results of the measurement of the natural gas flow rate, illustrated again the need for the analytic perturbation analysis. In Figure 4.9 and 4.10, test results of the first series of steam injection experiments are also included, using as dry reference air mass flow rate $\dot{m}_{\mathrm{air}}$ results from different dry measurements at the same produced electric power and inlet conditions. The results of the perturbation analysis clearly show that for the measurements at 70, 80 and 90 $\mathrm{kW_e}$ perturbation analysis results correspond well with the simulations, however, for the 100 $\mathrm{kW_e}$ measurements, a large difference exists between the results of the perturbation analysis and the predicted rise in efficiency based upon simulations. This can be explained by the fact that for the used reference case of the 100 $\mathrm{kW_e}$ steam injection experiment, produced power was not 100 $\mathrm{kW_e}$, however a limited 96 $\mathrm{kW_e}$. The T100 mGT had some problems reaching nominal speed and power, due to high inlet air temperature and EGR (measurements were taken before the stack was adapted). This clearly emphasizes one of the major problems of perturbation analysis. The accuracy of the results strongly depends on the accuracy of the measurements of the reference case. For the 100 $\mathrm{kW_e}$ case, a new reference – from other dry measurements at 100 $\mathrm{kW_e}$ and the same inlet air temperature – is used. Both measured (Measurements Corrected) and perturbated (Perturbation Corrected) results agree well with simulation results (Figure 4.10). Results of the absolute efficiency increase show good correspondence with the simulation results.

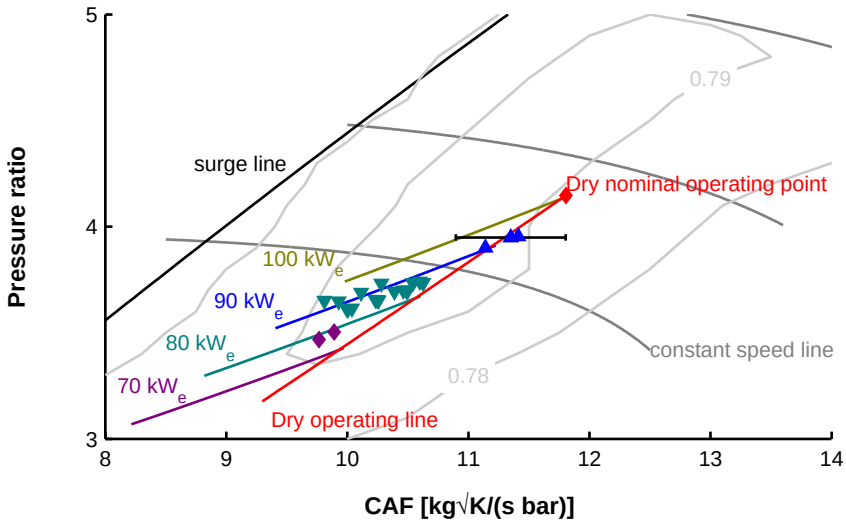

Figure 4.8: Measured compressor operating points under steam injection conditions correspond well with predicted wet operating lines, validating the off-design behaviour.

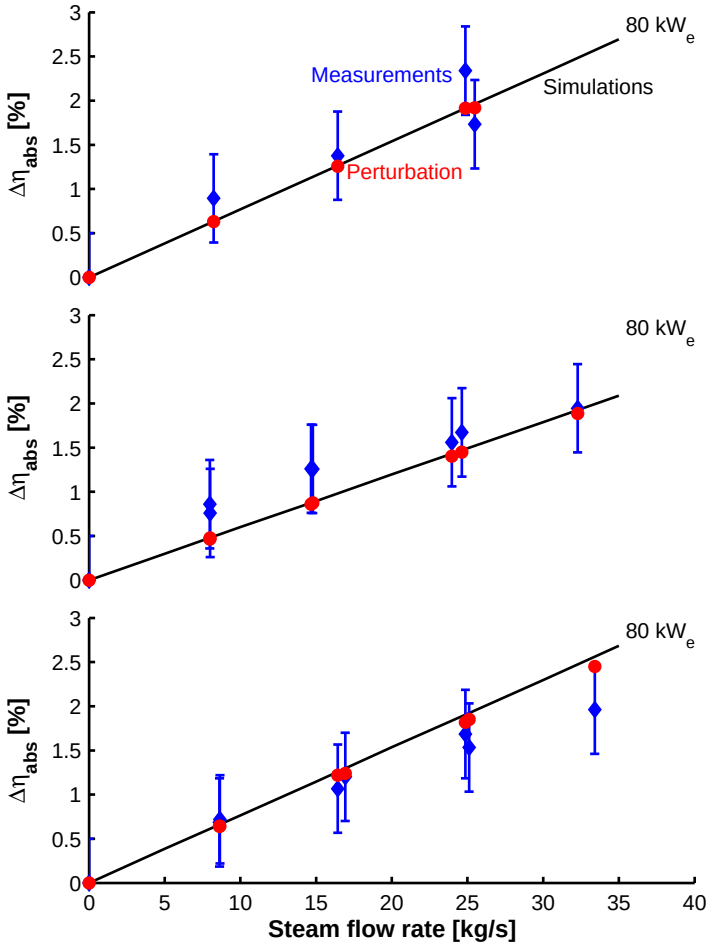

Figure 4.9: Measured and calculated electric efficiency, using the analytic perturbation analysis, correspond well with the simulated efficiency increase during steam injection experiments at part load ($80\,\mathrm{kW_e}$) at different steam flow rates. Relative uncertainty on perturbation analysis results amounts to $0.9\,\%$.

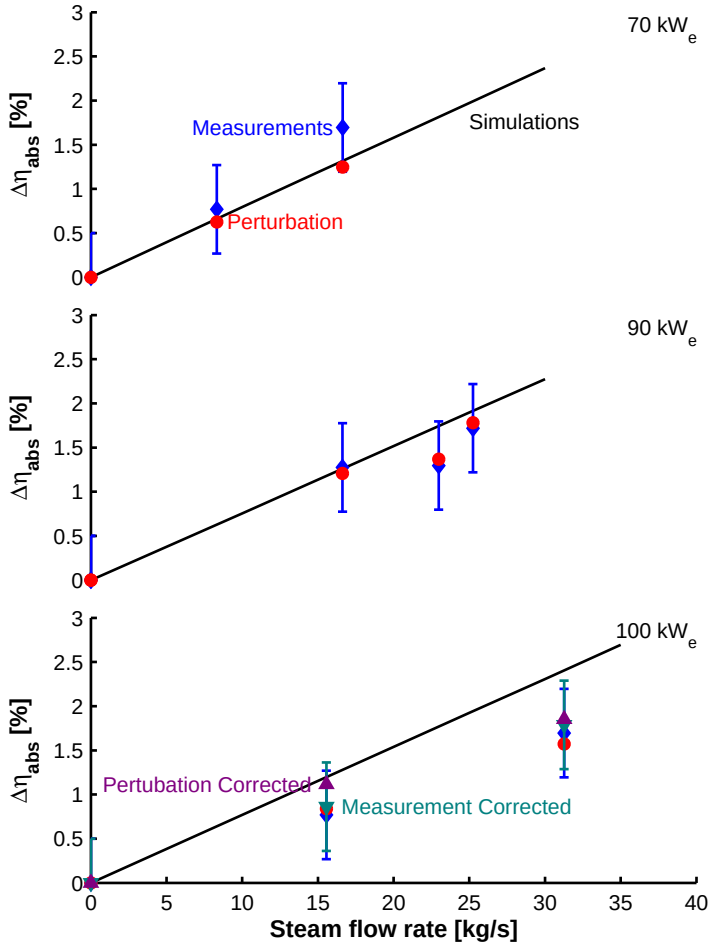

Figure 4.10: The analytic perturbation analysis allows an accurate determination of the efficiency increase at part (70 and 90 kW_e) and nominal load 100 kW_e. Perturbation analysis results validate the steam injection simulations. At full load, the measured results were corrected for the changing inlet air temperature.

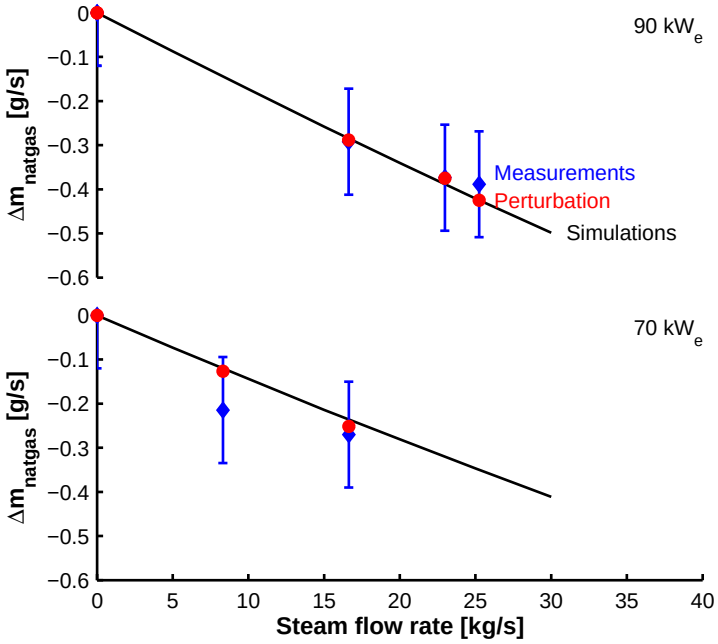

Figure 4.11: Perturbation analysis results for the changing natural gas flow rate correspond well with simulation results, indicating the capability of the Aspen® simulations to predict the change in fuel flow rate under steam injection conditions.

The predicted decrease in natural gas mass flow rate corresponds well with the measured change in natural gas mass flow rate for steam injection experiments at fixed produced electric power output at 70 kW_e and 90 kW_e (Figure 4.11). The size of the error bars on the measurement results illustrates again the problem with the accuracy. As mentioned before, the change in natural gas mass flow rate is of the same order of magnitude as the accuracy of the vortex flow meter.

There is a small difference between measurements and simulations of the rotational speed (Figure 4.12). These small differences can be explained by a slight change in inlet air temperature. During tests, the temperature inside the room of the T100 mGT increases because the inlet air tube is not insulated. As a result, the inlet air heats up (0.25 °C/h). The longer the run, the higher the room temperature and the more the inlet air temperature will increase. Due to the slightly higher inlet air temperature,

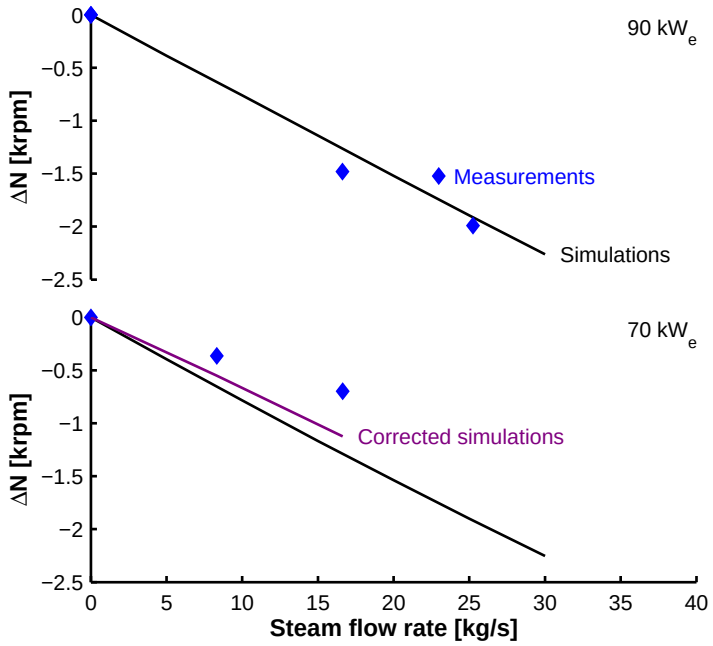

Figure 4.12: Reducing rotational speed during injection experiments at 70 kW_e and 90 kW_e.

rotational speed will reduce less when injecting steam, because the controller of the T100 mGT compensates the lower inlet air mass flow rate (due to a lower density from the higher inlet air temperature). When compensating for this temperature difference, results of simulation and measurements correspond well. This explains the increasing difference between simulations and measurements during the test at 70 kW_e, performed using procedure 1, were the reference state was taken at the beginning of the experiment. For the test performed at 90 kW_e, procedure 2 was used, so the reference is taken after steam injection, which resulted in a more stable inlet air temperature. This explains the better correspondance for the 90 kW_e case. This difference can be compensated in the simulations and the perturbation analysis; however, the results of the efficiency increase and natural gas mass flow rate decrease show that the small change in inlet air temperature has only a minor effect on the performance during steam injection.

The measured decrease in pressure ratio of the 90 kW_e experiments agrees well with the simulation results, but experiments at 70 kW_e differ slightly

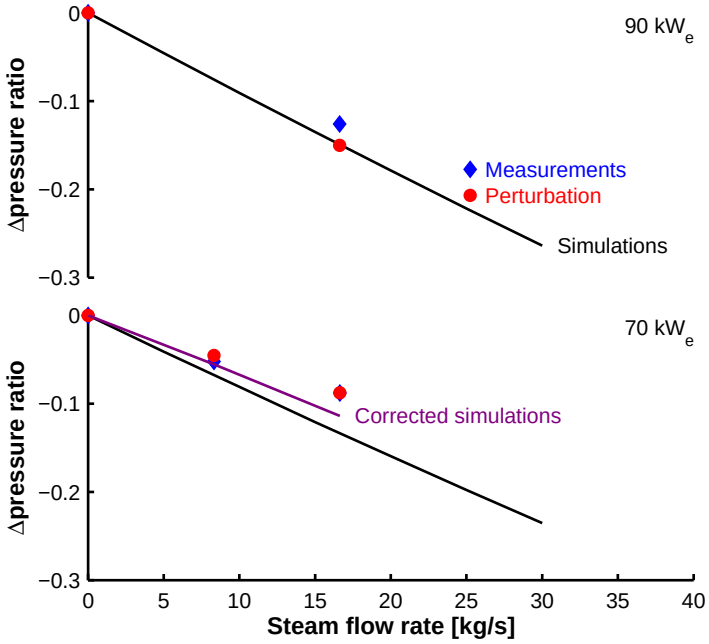

Figure 4.13: Reducing pressure ratio during steam injection experiments at 70 kW_e and 90 kW_e.

from simulations (Figure 4.13). Since pressure ratio and inlet air mass flow rate are determined by the rotational speed, the same explanation given for the difference in reducing rotational speed holds for the different pressure results. Additional to the Aspen® simulation results (Simulations), the results of the corrected simulations (Corrected simulations), using the changing inlet air temperature, are also indicated. The accordance between measurements and simulations can be clearly seen.

Measured changes in air mass flow rates during steam injection experiments slightly differ from the predicted changes in the Aspen® simulations (Figure 4.14). The difference between the measurements and the simulations can again be explained by the changing inlet air temperature. The error on the calculated inlet air mass flow rate is very large (4 %). Since the change is a difference between two calculated results, final error equals 8 % or 0.048 kg/s, which is of the same order of magnitude as the difference in mass flow rate due to the steam injection.

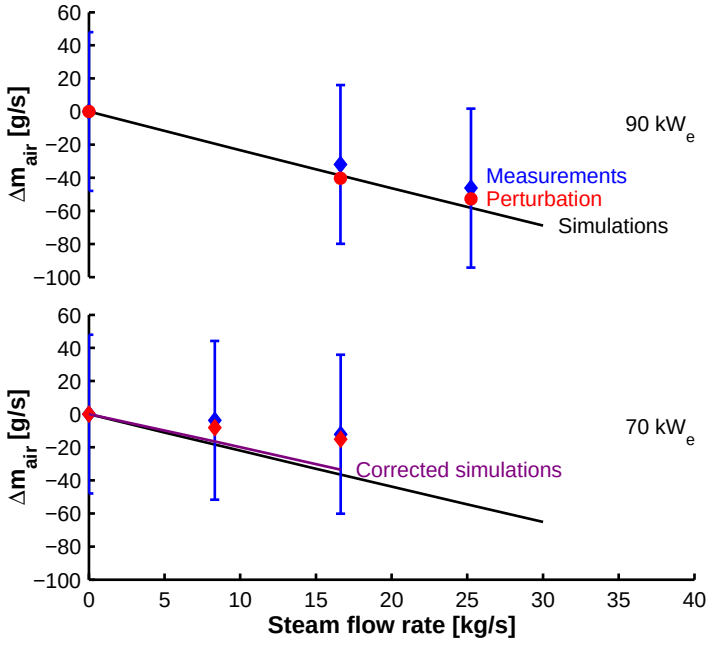

Figure 4.14: Reducing air mass flow rate during steam injection experiments at 70 $\mathrm{kW_e}$ and 90 $\mathrm{kW_e}$.

4.1.4 Conclusion of steam injection experiments

In order to study the effect of humidifying the Turbec T100 mGT, steam injection experiments were performed. The goal of these experiments was to demonstrate the capability of the Turbec T100 mGT to deal with the injected steam and demonstrating the beneficial effect of steam injection on the recuperated mGT performance. The third objective was the validation of the steam injection simulations in Aspen® in order to see the capability of the model to predict correctly the off-design behaviour of the different components. Simulations predicted a 2.2 % absolute efficiency increase when 5 % of the total air mass flow rate was replaced by steam (injection of 35 g/s of steam).

Experiments with steam resulted in a stable operation of the T100 mGT at reduced rotational speed and higher electric efficiency (2 %). Pressure ratio and air mass flow rate measurements showed the effect of steam injection on the mGT compressor operating point. The simulation results were validated by means of a perturbation analysis based upon experimental data. This indicates that the Aspen® simulations correctly describe the T100 mGT off-design behaviour.

The steam injection experiments clearly showed the capability of the T100 mGT to handle humidified air as working fluid, proving that water injection is possible in the mGT.

4.2 Combustion stability

In the previous section, the beneficial effect of steam injection on the Turbec T100 mGT performance in terms of fuel consumption and electric efficiency has been discussed. Additional water in the combustion air will however affect the combustion. Exhaust gas emissions, combustion stability and efficiency will be affected by the steam injection.

Water or steam injection will reduce the NO_x levels. Chen et al. measured a 90% NO_x reduction by adding 10 % humidity to the compressed air compared to the dry gas turbine cycle when using a liquid fuel in a diffusion flame combustor for the HAT [245]. Belokon et al. saw a similar trend for methane combustion in a diffusion flame combustor also for the HAT cycle [246]. For premixed combustion of natural gas, Day et al. also noticed that moisture in the feed stream reduces NO_x emissions [244]. According to

Dryer, the NO_x emissions in natural gas combustion are influenced in two ways [247]: a physical and a chemical way. First, the flame temperature is lower, which will reduce the formation of thermal NO_x. Secondly, the steam addition will change the concentrations of the O, OH and H species [248]. Since these species are also involved in the formation of NO_x, they will influence the final NO_x exhaust. These effects have been studied by different researchers, however the influence of water on NO_x formation has been reported differently. Zhao et al. noticed that for a natural gas diffusion flame, the additional steam leads to higher thermal NO_x emissions. Total NO_x emissions were however lower due to a significantly lower prompt NO_x. This however contradicts with the finding of Göke et al. [250]. According to Bhargava et al., the lower NO_x in humid-air premixed combustion is a result of the higher OH-radical concentration [243]. They however did not investigate the effect of pressure on the NO_x emission. Both Day et al. and Kobayashi et al. showed that the NO_x emissions become higher with increasing pressure [244, 251], but Kobayashi et al. also indicated that this effect becomes weaker with increasing steam fraction [251]. Recently, Göke et al. revealed numerically that reduced NO_x emissions are mainly caused by lower concentrations of atomic oxygen at steam-diluted conditions, constraining the thermal pathway [252].

The different studies in literature on exhaust gas emissions show no clear trend for the CO levels under steam injection conditions. CO levels seem to depend on the operating conditions and the combustor layout. Park et al. indicated that CO is slightly reduced by steam injection [253], while in their studies, Day et al. and Göke et al. indicated no significant effect of steam injection on the CO levels [244, 252]. Both however showed that CO emissions reduce with increasing pressure.

In literature, less studies exist on the combustion efficiency. Belokon et al. developed a method to predict the combustion efficiency and NO_x levels for diffusion flame combustors for HAT applications. Hermann et al. indicated that richer combustion is required to keep the combustion efficiency (thus CO emissions) at a tolerable level using premixed flames. Therefore, although NO_x emissions strongly reduce by the addition of water in a combustion chamber with premixed flame, this decrease will vanish [242].

In this section, I will present the results of the combustion experiments with steam injection I performed in collaboration with the Thermal Power Engineering division of the Department of Energy Sciences of Lund University, Sweden. I performed combustion experiments in their atmospheric,

variable-swirl, premixed combustor. In this study, I focused on the Lean Blowout (LBO) limit and CO emissions of methane combustion, since the effect of steam addition on NO_x emissions is already well known. In addition, mGTs use low-NO_x premixed combustors, resulting in very low emissions (for instance, less then 15 ppm at full load for the Turbec T100 mGT [158]). In the mHAT case, water is added to enhance the performance, not to reduce NO_x levels. By measuring the LBO limit, I tried to see how the fuel control of the mGT needs to be changed in order to get a stable combustion under humid conditions. CO levels were measured to see the influence of steam on the emissions. Out of these results, guidelines for combustion in humidified mGT will be formulated.

The combustion experiments performed for this thesis and discussed in this section are similar to the experiments done by Göke et al. [252]. The major difference between both experiments however is the swirl number. For their experiments, Göke et al. used a swirl number of 0.9. The Turbec T100 mGT combustor has however a lower swirl number of 0.6. Since the swirl number has an impact on LBO limit [254], I decided to perform steam dilution experiments at swirl numbers closer to the T100 mGT swirl number. This allowed for a more accurate discussion on the effect of air humidification on the combustion in the Turbec T100 mGT.

In the following subsections, I will first discuss the experimental approach and provide more details about the atmospheric, variable-swirl, premixed combustor and steam generator. Additional information concerning the experimental procedure, is also given in this section. In the second section, the results of the LBO experiments are shown and discussed together with the CO emission results. The effect of the different variations in the inlet conditions – steam ratio and swirl number – on the results is discussed. Finally, a conclusion about the experiments and guidelines for humidified mGT combustion control are presented.

4.2.1 Experimental approach for combustion experiments

For the combustion experiments an atmospheric, variable-swirl, premixed burner with a circular cross section is used in combination with an electric steam generator. The used burner is a modified version of the burner used to investigate the effect of dilution, mass flow rate and inlet air temperature on methane [254] and different syngas mixtures [255] LBO limits.

In this subsection, the experimental set-up, consisting out of the burner and the steam generator, is discussed. In addition, the used experimental procedures for LBO and CO measurements are given.

Burner

The experiments were carried out in an atmospheric, variable-swirl, premixed burner with circular cross section (Figure 4.15). The burner has a length of 350 mm and an inner diameter of 63 mm. A quartz tube with the same inner diameter as the burner, provides optical access to the first 120 mm of the flame.

A swirling flow of air and methane was supplied to the combustor through a centrally located premixing tube. This tube has a diameter of 15 mm and a total length of 80 mm of which the last 50 mm consists of a quartz tube. This quartz tube allows the detection of possible flashback in the premixing tube.

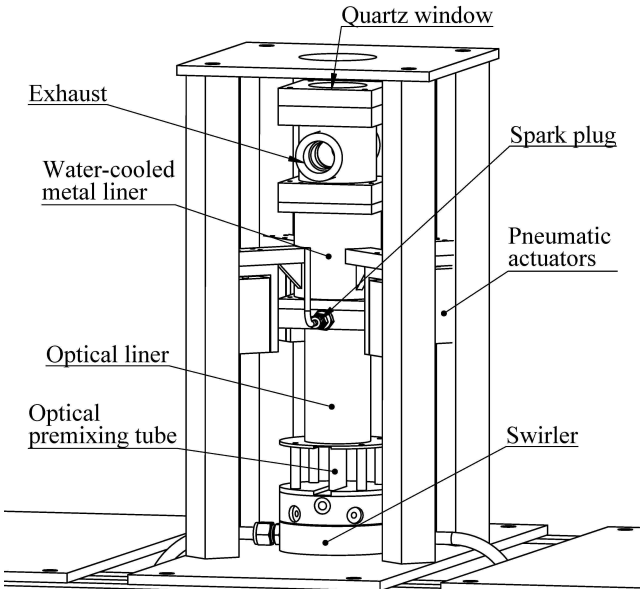

Figure 4.15: The variable-swirl burner, at the labs of the Thermal Power Engineering division of the Department of Energy Sciences of Lund University, Sweden, has an optical access to study the flame [256].

Both axial and tangential air flows are combined in the swirler, located at the entrance of the premixing tube. The swirler allowed for the introduction of air into the premixing tube in axial and tangential directions in varying proportions. Before entering the swirler, the axial flow is passed through a flow straightener, while the tangential flow passes through four channels of 3 mm wide and 10 mm high.

The swirl number of the flow entering the combustor was varied by changing the proportion of tangential to axial flow through the swirler. Axial and tangential flows were measured and preheated individually using two laminar-flow, differential-pressure mass-flow rate controller (Alicat MCR250) and feedback-controlled air heaters (Sylvania Sureheat Jet) of 8 kW power. In order to make sure that the equivalence ratio (Φ) of the fuel-air mixture entering the combustor was the same in both axial and tangential directions, the axial and tangential air flows can be separately premixed with fuel upstream of the swirler. A laminar-flow, differential-pressure mass-flow rate controller (Alicat MCR50) can be used to split and control the fuel flow rate based on the ratio between the tangential and axial air mass flow rates.

Ahead of this splitting mass-flow rate controller, the desired methane fuel rate flow was generated by laminar-flow differential-pressure mass-flow rate controller (Alicat MCR50). Methane (CH_4, purity 99.98 %) was supplied from gas bottles. The exhaust gases from the combustor were discharged into a force-ventilated extractor hood. A scheme of the burner cross section and the details of the geometry are shown in Figure 4.16.

As mentioned before, the mass flow rate of the axial and swirl component of the air can be changed. Depending on the relation between the strength of the two components, different flow patterns will emerge in the combustor. In order to quantify this relation, the swirl number can be defined as [257]:

$$S = \frac{G_\mathrm{t}}{R_\mathrm{S} G_\mathrm{a}}, \tag{4.21}$$

where R_S is the radius of the swirler, G_t the axial flux of the tangential momentum and G_a the axial flux of the axial momentum. These fluxes can be calculated as follows:

$$G_\mathrm{t} = 2\pi \int_0^{R_\mathrm{S}} \rho W U r^2 dr, \tag{4.22}$$

$$G_\mathrm{a} = 2\pi \int_0^{R_\mathrm{S}} \rho W U r dr, \tag{4.23}$$

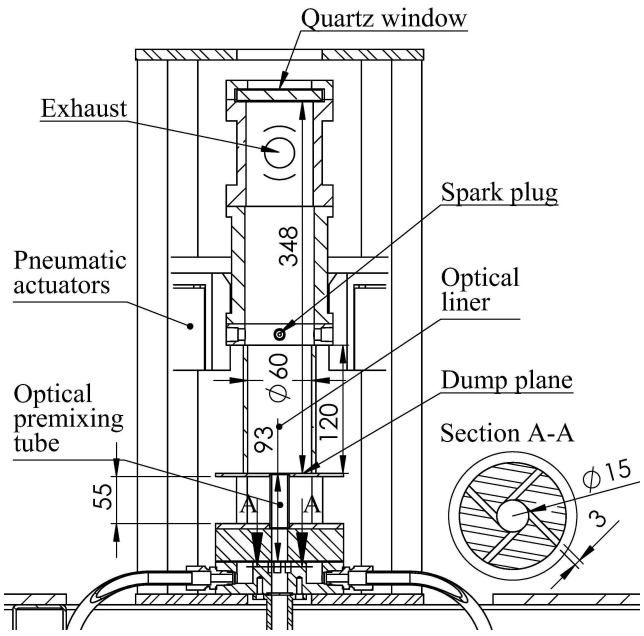

Figure 4.16: Cross section of the swirler [256].

where ρ is the density of the gas, U the axial velocity, W the tangential velocity and r the radius of the swirler exit.

To determine the swirl number for each flow condition, the axial and tangential velocity profiles were measured 1 mm above the dump plane of the combustor using Laser Doppler Anemometry (LDA). A detailed description of the used equipment and measured flow patterns can be found in [256].

Steam boiler

Steam was produced using an electric steam generator. Rather than using a pressurised steam boiler containing a two-phase mixture of boiling water and saturated steam, I opt for a direct-through steam generator in order to avoid safety issues. Water was routed through an electric heated metal block. The metal block was heated by 10 low-density cartridge heaters (*Omega* LDC00261) of each 300 W. By routing the water over multiple passes through the block, the water was heated, converted into steam and superheated. The heat flux was controlled by setting the block temperature rather than controlling the steam temperature. The thermal inertia of the heater block was too large to use a fast changing parameter like the steam temperature to control the heat flux. Once an equilibrium was reached between the ingoing heat flux, the outgoing steam flow rate and the heat losses, the steam temperature would remain constant. This however required a constant steam flow rate. Rather than directly controlling the steam flow rate, I controlled the water flow rate using a precision water flow rate meter and controller (Alicat LC-500-CCM) with a maximum flow rate of 20 kg/h and an accuracy of 2 % of the full scale. I opt for controlling the water flow rate, since it allows much more accurate flow rate control than typical steam flow rate controllers. The steam was mixed upstream of the swirler with the air flows, where the fuel was added. Final injection temperature of the steam varied between 180 °C and 250 °C. This difference in temperature could be compensated by adjusting the feedback-controlled air heaters in order to keep the inlet air temperature constant.

LBO test procedure

The focus of the current work was the investigation of the effect of steam dilution on the LBO limit for methane combustion at different swirl numbers

and steam flow rates. The swirl number was changed from 0.66 to 0.53. Tests were only performed at high swirl numbers, which are representative for mGT combustion chambers. Initially, the total mass flow rate of air was kept constant and equal to 200 slpm for both $S = 0.66$ (200 slpm[1] swirl and 0 slpm axial flow rate) and $S = 0.53$ (150 slpm swirl and 50 slpm axial flow rate). The power of the electric steam boiler was limited, resulting in a maximum possible steam fraction of 18 %. Currently, GT cycle developers are looking towards higher humidity levels (up to 30 %) for ultra-wet combustion. To reach this steam fraction, the air mass flow rate was lowered till 125 slpm to be able to reach 28 % steam fraction at $S = 0.66$. By lowering the air mass flow rate, experiments could be performed at higher steam ratios. Lowering the mass flow rate will however slightly effect the LBO limit, as has been indicated in [254].

For each steam ratio at a certain mass flow rate and swirl number, the LBO limit was found by gradually decreasing the equivalence ratio from $\Phi = \Phi_{\text{init}}$ until LBO occurred at $\Phi = \Phi_{\text{LBO}}$.

For the $S = 0.53$ swirl case, in ideal conditions, fuel and steam would be mixed separately in the axial and the swirl flow to get fully premixed air and the same steam ratio as described in the previous subsection. Due to control issues, it was not possible to maintain a constant steam and fuel flow rate. Therefore, I decided to inject the steam and fuel in the swirl flow (largest fraction).

All tests were performed at atmospheric pressure. The inlet air temperature was kept constant and equal to 650 K in order to exclude the effect of inlet air temperature variations. Previous experiments indicated that changing the inlet temperature by 200 K will reduce the LBO equivalence ratio by 0.1 [254]. The inlet air temperature was controlled by adjusting the air heaters and measuring the temperature in the centre of the inlet before and after the experiments using a K-type thermocouple.

CO emissions measurements

CO emissions were captured for each swirl number at different equivalence ratios and steam injection ratios. A sample of the flue gases was taken above the metal liner (Figure 4.15). The sampling device consisted out of a metal tube with different openings along the burner radius, in order

[1]slpm = standard litre per minute (at 25 °C and 1.013 bar)

to get a representative sample of the total exhaust gas emissions. The water in the flue gases was condensed before entering the CO measuring device. The device was calibrated on a daily basis and compensated for the changing atmospheric pressure. The maximal CO concentration that could be measured was 950 ppm. Finally, the CO emissions were measured and averaged over a period of 3 minutes in which steam flow rate and equivalence ratio were kept constant.

4.2.2 Results of combustion experiments

In this section, I will discuss the effect of steam dilution on methane combustion, with special focus on LBO and CO emissions.

The steam fraction is defined as follows:

$$\Omega = \frac{\dot{m}_{\text{steam}}}{\dot{m}_{\text{air,dry}}}. \tag{4.24}$$

The equivalent fuel-air ratio Φ is defined in dry air:

$$\Phi = \left(\frac{\dot{m}_{\text{fuel}}}{\dot{m}_{\text{air,dry}}}\right) \Big/ \left(\frac{\dot{m}_{\text{fuel}}}{\dot{m}_{\text{air,dry}}}\right)_{\text{Stoichiometric}} \tag{4.25}$$

In following subsections, I will first discuss the effect of steam dilution on the LBO limit. In the next subsection, the effect of steam addition on the CO emissions is discussed.

Effect of steam on the LBO limit

Increasing the steam fraction will increase the LBO equivalence ratio for methane combustion (Figure 4.17). For both swirl numbers ($S = 0.66$ and $S = 0.53$) and mass flow rates (200 slpm and 125 slpm), the increase in LBO equivalence ratio is linear. For the same mass flow rate, the difference between the swirl numbers $S = 0.66$ and $S = 0.53$ is rather small. This is in accordance with previous experiments, where Sayad et al. indicated that the differences in LBO equivalence ratio between high swirl numbers are rather small [254]. Lowering the swirl number will lead to an increasing LBO equivalence ratio. The deviations in the measurements can be explained by the uncertainty on the steam flow rate and fuel flow rate. Decreasing the air mass flow rate slightly increases the LBO limit, which is also in accordance

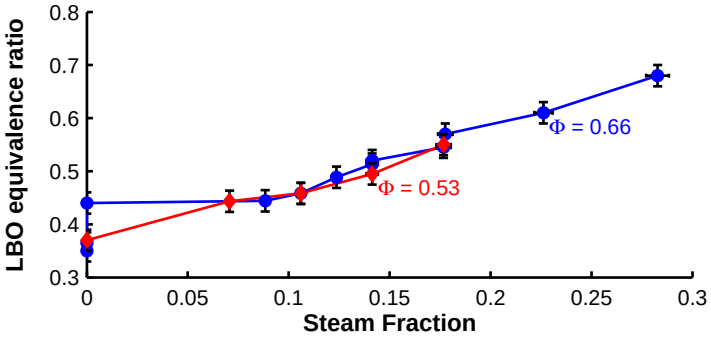

Figure 4.17: The LBO equivalence ratio increases linearly with increasing steam fraction in the combustion air.

with previous experiments. Sayad et al. indicated that for air flow rates lower than 200 slpm, the LBO limit increases with decreasing mass flow rate [254].

The increasing LBO equivalence ratio from Figure 4.17, is a result of the increasing steam fraction. The presence of the steam in the combustion air will absorb heat of the combustion. This results in lower flame temperature, explaining the increasing LBO equivalence ratio.

Figure 4.18 and 4.19 give broadband luminosity photographs of the changing flame due to decreasing equivalence ratio under dry conditions (Figure 4.18) and wet conditions (Figure 4.19) during LBO experiments. During previous experiments studying the LBO limit at various swirl numbers, three distinct categories of blowout were observed. These could be classified as low swirl ($S \approx 0.03$), moderate swirl ($S \approx 0.28$) and high swirl ($S \approx 0.60$) cases [255]. LDA measurements of these previous experiments indicated an inner and outer recirculation zone at high swirl numbers in the flow.

At ignition equivalence ratio, the dry flame is very short, attached to the inlet (Figure 4.18(a)). The flame is concentrated around the inner recirculation zone, resulting in a heart-like shape. When the equivalence ratio is reduced, the flame starts to oscillate between the initial position around the inner recirculation zone and the outer recirculation zone. This behaviour is the result of the existence of the two circulation zones. At the transition zone between these two positions, the combustion becomes very unstable. This gives rise to very hard vibrations and noise. These instabilities even lead to flameout. For the determination of the LBO limit, the equivalence

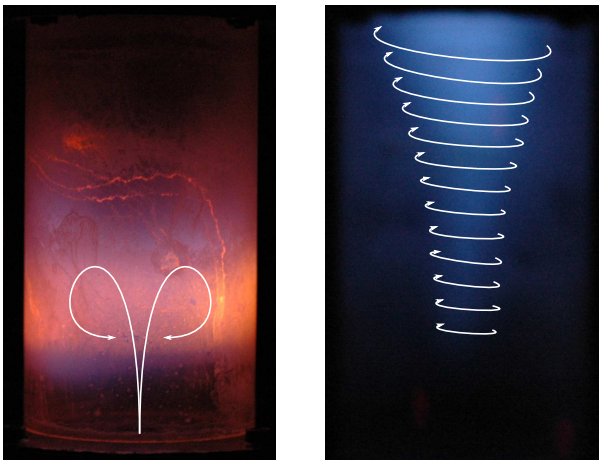

(a) **(b)**

Figure 4.18: Broadband luminosity photographs of a methane flame at $S = 0.53$, no steam injection and $\Phi = 0.5$ (a) and $\Phi = 0.38$ (b).

ratio needed to be lowered faster, in order to quickly transit through this transition zone, lacking the time to take a photograph. When the fuel flow rate is further reduced (reducing the equivalence ratio), the flame becomes detached from the burner and moves to a stable lifted position (Figure 4.18(b)). Further reducing the equivalence ratio will keep the flame in its lifted position, but will make the flame progressively thinner and elongated until blowout occurs very smoothly.

The same phases as seen in the methane flame under dry conditions, could be distinguished during experiments with steam injection, although there is a shift in equivalence ratio. At ignition equivalence ratio ($\Phi = 0.8$, Figure 4.19(a)), the flame is located around the inner recirculation zone. Light emissions in the visible spectrum are shifted from blue to yellow. The flame is also slightly stretched, which was also noticed by Göke et al. [252]. Reducing the equivalence ratio results again in an oscillating flame ($\Phi = 0.65$). The flame oscillates between the inner and the outer recirculation zone (Figure 4.19(b)). Oscillations are however less violent than in the dry case, allowing fairly stable combustion. Steam has clearly a stabilizing effect on the methane combustion. This stabilizing effect is possibly due to the presence of additional OH or due to higher mass flow rate, which will affect the flame speed [255]. Finally, reducing the equivalence ratio more

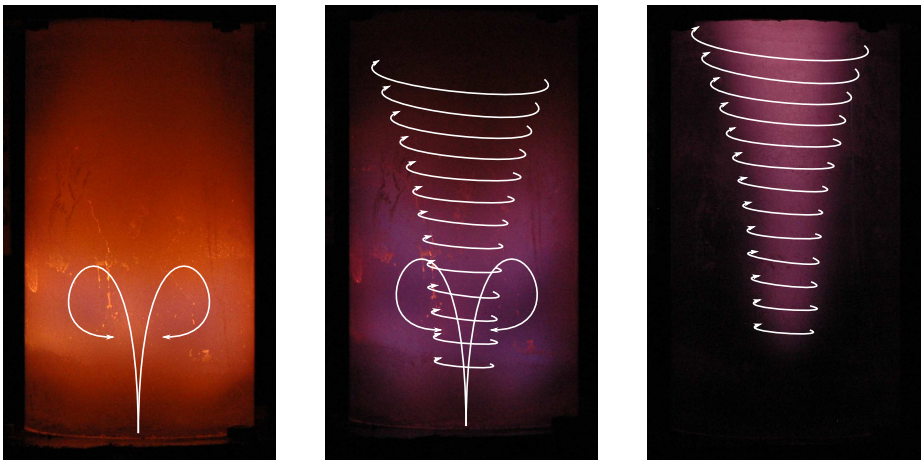

(a) **(b)** **(c)**

Figure 4.19: Broadband luminosity photographs of a methane flame at $S = 0.53$, with steam injection of 2.5 kg/h ($\Omega = 18\,\%$) and $\Phi = 0.8$ (a), $\Phi = 0.65$ (b) and $\Phi = 0.57$ (c).

($\Phi = 0.57$) results in a stable detached flame (Figure 4.19(c)). Reducing Φ further will finally lead to blowout.

As a final remark, steam has a very corrosive effect on the quartz tube of the burner. The steam affects the glass, by making it rough, resulting in a milky shine, which effects the photographs.

Effect of steam dilution on CO emissions

CO levels in the exhaust gases start to rise for both swirl numbers ($S = 0.66$ and $S = 0.53$) at higher equivalence ratios with increasing steam fraction (Figure 4.20). This is a result of the higher LBO equivalence ratio. Measuring CO levels for decreasing equivalence ratios for pure methane combustion (no steam addition) was not possible. As mentioned before, at the transition zone from a flame concentrated around the inner recirculation zone to a flame concentrated around the outer recirculated zone, the combustion became too unstable, resulting in blowout due to these instabilities. Therefore it was not possible to measure the exhaust gas emissions over a 3 minutes time period. For the determination of the LBO limit, the equivalence ratio was lowered faster, in order to go faster through this transition zone. After this transition zone, combustion was again stable, however CO levels were

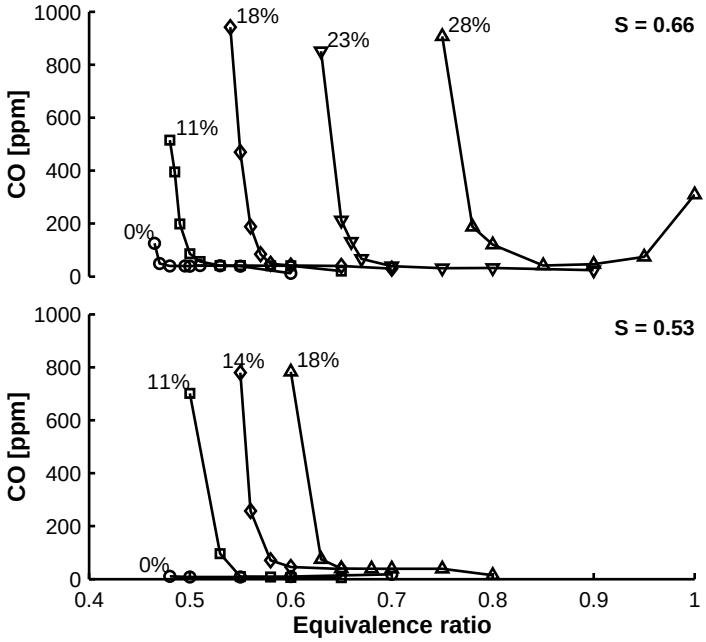

Figure 4.20: CO levels increase with decreasing equivalence ratio. At high steam fraction, CO levels are still low which indicate that the combustion efficiency remains high.

above the scale of the measuring device ($\geq 950\,\text{ppm}$). The instabilities at decreased equivalence ratio for methane combustion were less aggressive during steam injection. Therefore it was possible to capture CO levels at the transition zone.

At full combustion with a flame concentrated around the inner recirculation zone, CO levels are for all steam fractions of the same order of magnitude as the pure methane combustion (Table 4.4). This indicates that the combustion is complete, which will result in a high combustion efficiency. $\Phi_{\text{transition}}$ from Table 4.4 is defined as the lowest equivalence ratio at which the flame is still concentrated around the inner recirculation zone. With increasing steam fraction, this $\Phi_{\text{transition}}$ shifts towards higher equivalence ratios. This shift is comparable to the shift in Φ_{LBO}. Therefore, full combustion occurs at higher equivalence ratio. This indicates that more fuel needs to be added to the combustion chamber under steam injection conditions.

Table 4.4: CO levels are constant and independent of the steam flow rate in full combustion conditions.

$\Omega(\%)$	$\Phi_{\text{transition}}$	CO (ppm)
0	0.48	40
10.6	0.53	41
17.7	0.65	40
22.6	0.75	31
28.3	0.85	41

Full, stable combustion was still achieved at steam fraction of 28 % ($\Phi = 0.66$) and 18 % ($\Phi = 0.53$). Higher steam fractions were not possible due to the limited power of the steam generator. Hermann et al. indicated that the maximum humidity level is dependent on inlet air temperature and aerodynamic load. In their experiments, the maximum achieved humidity level was 33 %. Above 33 %, CO levels become too high [242]. Belokon et al. measured a high combustion efficiency at 20 % steam injection [246].

4.2.3 Conclusion of combustion experiments

Steam dilution experiments have been conducted on an atmospheric, variable-swirl premixed combustor to study the effect of humidified combustion air on CO emissions and LBO limit for methane combustion. Major conclusions from these experiments were:

- The LBO equivalence ratio increases linearly with increasing steam fraction;
- The CO levels start to rise at higher equivalence ratios when injecting more steam;
- CO levels at complete, stable combustion are constant and equal to dry combustion;
- Steam has a stabilizing effect on methane combustion when lowering the equivalence ratio.

Summarizing for mGT applications, it is possible to maintain a stable and complete combustion under steam injection conditions. Fuel flow rate however needs to be increased in order to stay away from LBO limit and to keep CO emissions low.

Chapter 5

Humidified mGT development

Water injection in the compressor exhaust, to recuperate waste heat, is considered a possible route to improve the electric efficiency and overall performance of the mGT. In this chapter, I will discuss the different steps towards the development of a humidified mGT cycle. First, the optimal route for waste heat recovery through water injection is determined. Therefore, I have performed simulations using a two-step method. In a first step, the thermodynamic limit for water injection is sought using a black box method. In a second step, the cycle layout is designed by means of composite curve theory. Once the optimal route was defined, I performed a sensitivity analysis on the heat exchanger network of the selected optimal humidified mGT cycle. The sensitivity analysis showed the effect of the boundary conditions on the cycle performance. In addition, the effect of the non-idealities of the heat exchanger network and the operation mode of the mGT on the global cycle performance, when transforming the ideal cycle design into a final design for a humidified T100 mGT layout, are discussed. In the final section of this chapter, the developing process of the humidification system is discussed. This process includes a two-phase flow model development and a sensitivity analysis to select the final saturation tower design.

5.1 Optimal route for waste heat recovery in the mGT through water injection

A way to improve the electric efficiency of the mGT is to introduce water (vapour/liquid) in the cycle. Water injection is considered a successful way to increase electric efficiency of GT and mGT cycles [30]. In periods with a low heat demand, the lost thermal power can be recovered by introducing auto-raised steam/heated water inside the mGT cycle, resulting in a more profitable investment [25]. As mentioned in the literature review (section 1.2), several studies focus on the beneficial effect of water introduction in the mGT cycle. None of the previous mentioned studies however identified the optimal route for water introduction in a mGT cycle to recuperate the lost thermal power. Bram and De Ruyck developed in the past a general two-step approach for optimal humidified GT cycle development [258]. In this procedure, the thermodynamic potential of water injection is first determined using an adiabatic black box method. In a second step, the final cycle layout is designed, using composite curve theory. This two-step approach showed its potential by identifying the HAT cycle, as proposed by Rao [74], as the optimal layout for a humidified cycle. This two-step approach also led to the development of a new humidified GT, without using a saturation tower, the REVAP® cycle [73]. This cycle has about the same net efficiency as the HAT cycle (54 %) [30]. In addition, this approach also helped developing an alternative route for biomass use in GTs, the so-called: co-utilization of biomass and natural gas through primary steam reforming of natural gas [259]. I apply here this two-step method to the mGT cycle to identify the optimal way for water introduction in a mGT cycle for waste heat recovery.

In this section, I consider two different scenarios of the water injection in a mGT. In the first scenario [Scenario 1 (S1)], the black box is considered as adiabatic and no fixed stack temperature is imposed (thus allowing condensation of the exhaust gases). In the second scenario [Scenario 2 (S2)], the cycle is made self-sufficient with water, since water consumption is a major issue for mixed air/water GTs. In the first scenario S1, I did not control the amount of condensed water. In the second scenario S2, I added a new constraint to condense exactly the amount of water injected in the mGT cycle (not all water present in the flue gases which is partly due to the combustion of natural gas). The main goal of S1 and S2 is to identify the thermodynamic limit for water introduction in a mGT under

these considered boundary conditions. By using composite curve theory, different ways for water introduction in a mGT cycle for waste heat recovery could be developed. The performance of each cycle is then compared with the black box results in order to check if the full potential for waste heat recovery is exploited. The cycle that best approaches the black box results is then identified as the optimal way for waste heat recovery through water injection in the mGT. Both selection procedure and final cycle layout will be presented in this section.

5.1.1 Approach for optimal humidified mGT cycle development

The current section summarizes the results of two series of water injection simulations, performed on the Turbec T100 mGT. The study is intended to be general on waste heat recovery in mGT cycles, similar to the cycle depicted in Figure 3.1. This includes all recuperated Brayton cycles, using single-stage radial compressor, operating at variable shaft speed. This is the major difference between the study presented in this thesis and the study previously presented by De Ruyck et al., where a constant pressure ratio was used [73]. For the simulations, I preferred to use real data from the Turbec T100 mGT, since it is very important to consider the behaviour of the compressor at variable shaft speed. The Turbec T100 mGT was selected since it is representative for recuperated mGT cycles operating at variable shaft speed. Moreover the off-design behaviour is well known due to previous dry (chapter 3) and wet experiments (chapter 4).

The adopted analysis method was a two-step procedure for the design of mixed air/water power cycles, developed by Bram and De Ruyck [258]. In this procedure, the thermodynamic potential of water injection is first studied, using a black box method. As mentioned in the introduction, in the first scenario (S1), the black box is considered adiabatic and no fixed stack temperature is imposed (thus allowing condensation of the exhaust gases), while in the second scenario (S2), the cycle is made self-sufficient with water. In the second step, the final cycle layout is designed, using composite curve theory. In this step, the black box is realized by developing a heat exchanger network. Although black box results of S1 and S2 ensure theoretical feasibility due to the overall positive exergy destruction, the final heat exchanger network design corresponding to this potential will probably be too complex and too costly for mGT applications. Therefore,

an additional constraint was added to the second step: maximum two heat exchangers in the heat exchanger network. To make the waste heat recovery through water injection in the mGT attractive for small-scale CHP users, the cycle must remain simple, easy to operate and the additional capital cost should remain low. By limiting the amount of heat exchangers to two, the final cycle design remains simple and easy to operate by non-specialists and additional capital costs are limited. The final result of this second step will then be the design of the optimal mGT cycle layout for waste heat recuperation using water injection under the given constraints.

5.1.2 Selection method for humidified mGT cycle development

All simulations, presented in this section, were again performed using the Aspen® software package. Simulations were performed at constant nominal power of the T100 mGT (100 kW_e). In this subsection, first the modelling of the water introduction in the T100 mGT in Aspen® will be discussed. Next to the modelling of the mGT components, the black box simulation method and exergy analysis of scenarios S1 and S2 are discussed. Finally, additional information about the composite curve theory, used to design the heat exchanger network, is given.

mGT components modelling

For the modelling of the mGT in the Aspen® plus simulation package, an adapted version of the previously developed model of the dry and wet mGT is used (subsection 3.1.1 and 4.1.1).

For the modelling of the compressor, the same Turbec compressor map – as used for the dry and steam injection simulations – was used (Figure 3.2). When water is injected in the cycle, the total mass flow rate through the turbine will increase, like in the steam injection case, resulting in a higher turbine/electric power. To keep the produced electric power constant, rotational speed is decreased, resulting in a lower compressor mass flow rate (off-design). Since it is the goal of this section to find the limit for water injection in the mGT, the operating point of the compressor will move further away from its optimal dry point compared to the steam injection case, resulting in a lower isentropic compressor efficiency. For this reason,

areas of constant compressor efficiency were implemented in the Aspen® compressor map.

Water injection in the mGT requires a modified model of the turbine in Aspen® to predict the off-design behaviour. For the wet simulations, the turbine is still assumed to be choked (Equation 3.1). Due to the injection of water, the heat capacity ratio (k_{turb}) in Equation 3.1 will change (0.1 % per 0.01 $\text{kg}_{\text{steam}}/\text{kg}_{\text{air}}$), resulting in a different choking value. Next to the choking condition, the isentropic efficiency of the turbine will also change due to water injection. The dry turbine efficiency of 0.85 can again be compensated using the following formula (same as Equation 4.1):

$$\frac{\eta_{\text{is}}}{\eta^*_{\text{is}}} = \frac{k-1}{k^*-1}\sqrt{\frac{k^*+1}{k+1}\frac{1-1/\pi^{\gamma^*}}{1-1/\pi^{\gamma}}}. \tag{5.1}$$

For the water injection simulations, unlike for the steam injection simulations, both the choking condition and the turbine efficiency were corrected, since the amount of injected water is much higher than in the steam injection experiments.

The heat exchangers were modelled with generic heat exchanger models. Pressure loss over the cold side of the heat exchange network was set to 3 % of the total pressure (160 to 197 mbar), for the hot side, a pressure drop of 40 mbar or 3.8 % was imposed. These losses correspond to the actual losses in the dry cycle of the T100 mGT. The pressure loss is considered as a design specification and it is kept constant to allow for a systematic comparison of all simulation results. The imposed 3 % pressure loss is a trade-off between the cost of the heat exchangers (which is related to their size) and the efficiency of the installation (which is related to the imposed pressure drop). Dry simulations using the Aspen® model showed that increasing pressure loss between compressor outlet and turbine inlet from 3 to 4 % will result in a 0.32 % absolute efficiency loss. This is comparable to the 0.33 % absolute efficiency loss mentioned by Lagerström and Xie [48]. Each final cycle design will thus require the development of specific heat exchangers to meet the design conditions for heat transfer and pressure drop. For a gas/gas recuperator, typically a primary-surface counter-flow heat exchanger with cross corrugated duct configuration is used [65], while for an economizer (gas/liquid), a typical cross-flow shell-tube heat exchanger

can be used as in the T100 [158]. For the saturation tower, the *V-DRUM1* block from Aspen® has been used. This block will saturate the air in case sufficient water is injected. Over the saturation tower, a pressure loss of 0.5 % is assumed due to the water injection.

The existing controller of the T100 mGT – implemented in the dry and steam injection model (subsection 3.1.1 and 4.1.1) – was slightly modified for the Aspen® simulations to identify the optimal humidified mGT cycle. In these simulations, I still assume that the mGT control system will keep the produced electric power constant. However, for the wet simulations in this section, TIT was kept constant by changing the fuel flow rate, rather than keeping TOT constant. As noticed in the steam injection simulations (Table 4.1), keeping TOT constant in wet conditions results in a reduction in TIT due to the changing properties of the working fluid. Lower TIT results in lower electric efficiency. To find the potential for water injection in the mGT system, the control scheme in the Aspen® simulations of Figure 3.4 is slightly changed by setting TIT as a design specification instead of TOT.

Finally, for the simulations of the humidified mGT in Aspen®, a more elaborated model to calculate the thermodynamic properties of the different streams was used: the UNIFAC property method implemented in Aspen® instead of the RKS-BM property method. This model was also used by Queiroz et al. to calculate a cooling tower in Aspen® [260]. Careful selection of the used thermodynamic property model is crucial for the design of cycles, especially at low temperatures and high pressures [261]. The major difference between the new used property method and the old method is the way it handles water. The RKS-BM property method does not consider the polarity of the different elements, while in the UNIFAC property method, the polarity of elements is used. This changes the results of the condensing water. In the RKS-BM method, the maximal possible relative humidity that could be reached was 83 %, while with UNIFAC full saturation is reached. The different property model however has no effect on the mGT simulations without humidification, since all other used elements (O_2, CO_2, N_2 and CH_4) are non-polar. An alternative for the the UNIFAC property method is the IDEAL property method that uses the ideal gas properties. Dry and wet simulations show differences below 0.1 % for the simulated electric efficiency between the IDEAL and UNIFAC property method. This is in line with the findings from Yan et al., who indicated that for high temperatures and low pressures (below 5 bar), the difference between the results of the different methods is small [261].

Black box analysis

For the simulations performed in the first step of the two-step method, all heat exchangers in the mGT layout from Figure 3.1 were removed and replaced by a black box. For the first scenario (S1), an adiabatic black box was used, for the second scenario (S2), heat exchange with the environment (heat sink) was allowed, since the flue gases needed to be cooled in order to make the cycle self-sufficient with water. In Aspen®, a straightforward implementation of a black box does not exist. Bram and De Ruyck [258] proposed an alternative, by generating a network of generic heaters and coolers, that would act as a black box system. A modified version of the proposed black box network in [258] is used for the simulations performed for my thesis. The T100 mGT has only one compressor stage, so there is no intercooling, which reduces the number of heaters and coolers in the black box network to two.

For S1, the black box network design as depicted in Figure 5.1 has been used. The water is first injected in the compressed air. Before entering the combustion chamber, the air/water mixture is preheated in the HEATER. The flue gases coming from the turbine are then cooled in the COOLER before they are ejected through the stack. When expressing conservation of the energy over the black box, the correlation between the thermal power of the heater and cooler can be expressed as:

$$\dot{Q}_{\text{cooler}} + \dot{Q}_{\text{heater}} = 0. \tag{5.2}$$

In the black box, there are three parameters that can be controlled (injected water mass flow rate, stack temperature and hot pinch temperature), but only two degrees of freedom, since the compressor outlet mass flow rate, pressure and temperature and the TOT are controlled by the adapted mGT control system (power output and TIT control). If the temperature difference between the cold side outlet and hot side inlet of the black box is imposed (hot pinch), together with the stack temperature, and taking into account the energy balance in Equation 5.2, the amount of water that must be injected is determined.

The goal of S2 is to check the possibility to make the cycle self-sufficient for water. The major disadvantage of mixed air/water GTs is the large water consumption [262]. By introducing a condenser in the cycle, it is possible to recover all the injected water [263]. For this scenario, the black box layout is thus slightly adjusted (additional grey parts in Figure 5.1). The flue gases

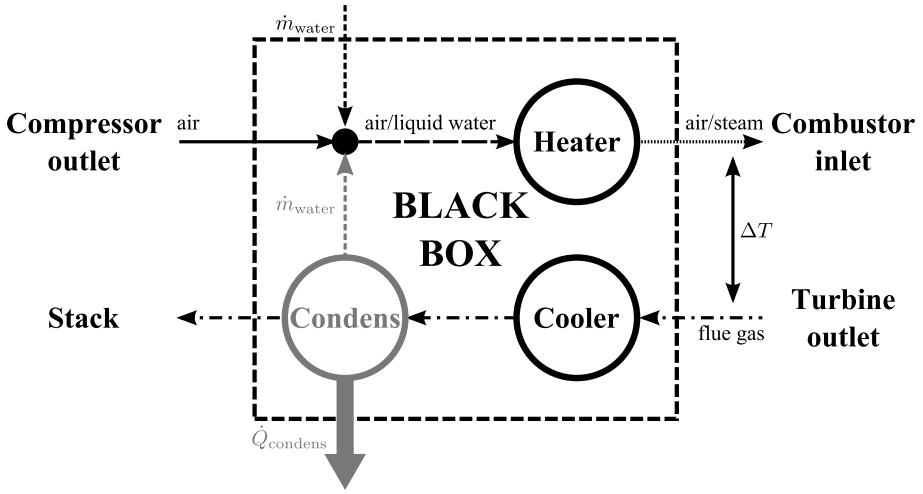

Figure 5.1: Black box layout used for simulating Scenario 1 (S1) and Scenario 2 (S2, grey parts).

coming from COOLER in Figure 5.1 are cooled further in CONDENS to get condensation of the water present in the flue gases. The excess heat of the CONDENS cooler ($\dot{Q}_{\text{condens}}$) is rejected to the environment. Again, three parameters can be controlled in the black box, while there are only two degrees of freedom. In this case, if the hot pinch and the heat disposal to the environment are imposed, the stack temperature and the amount of circulating water are set, due to the closed loop.

The boundary conditions used for the black box simulations of S1 and S2 are shown in Table 5.1. The stack temperature during simulations is variable. Rather than applying a specific stack temperature to the black box system, it was decided to control the amount of injected water. Simulations showed that controlling the amount of injected water allows Aspen® to reduce the convergence time, especially when condensation appears in the flue gases. I used methane as fuel, since natural gas composition can vary, depending on the source of the gas. This has a slight effect on the total turbine mass flow rate (0.2 %).

Exergy analysis of the black box systems

The exergy destruction in the Black Box (BB) as a fraction of the total exergy content of the fuel is defined as follows:

$$\text{BB}^{\text{dest}} = \frac{\sum_{\text{in}} \dot{E}x - \sum_{\text{out}} \dot{E}x}{\dot{E}x_{\text{fuel}}}. \tag{5.3}$$

Exergy efficiency is defined as the ratio between the sum of the exergy of the streams that gain exergy, and the sum of the exergy of the streams that lose exergy:

$$\text{BB}^{\text{eff}} = \frac{\sum_{\text{gain}} \Delta\dot{E}x}{\sum_{\text{lose}} \Delta\dot{E}x}. \tag{5.4}$$

By defining the exergy efficiency as the ratio of the exergy gained over the exergy lost by the streams in the black box, it is possible to express how efficient the exergy is used in the black box. Equation 5.4 expresses how efficient the exergy is transferred between the different streams in the black box. For both S1 and S2, the exergy efficiency is thus reduced to the ratio between the exergy gain of the compressed air and the exergy loss of the flue

Table 5.1: Boundary conditions used in the black box simulations of Scenario 1 (S1) and Scenario 2 (S2).

Compressor	
Pressure ratio	3.16 to 3.89 [1]
Isentropic efficiency	0.76 to 0.79 % [1]
Inlet air temperature	15 °C
Turbine	
Turbine back pressure	50 mbar
Isentropic efficiency	85 to 86 % [2]
Turbine Inlet Temperature (TIT)	950 °C
Combustion chamber	
Combustor pressure loss	5 %
Heat recovery system	
Cold side pressure loss	3 %
Hot side pressure loss	40 mbar
Water injection pressure loss	0.5 %
Hot inlet/cold outlet temperature difference	50 °C
Stack temperature	53 to 253 °C [3]
Feedwater inlet temperature	15 °C
Fuel (methane)	
Fuel temperature	30 °C
Fuel pressure	6 bar
Lower Heating Value (LHV)	50 MJ/kg
General	
Produced electric power	100 kW_e

[1]The manufacturer compressor map was used in the simulations (Figure 3.2).

[2]The isentropic efficiency depends on the water content of the working fluid, but TIT is constant.

[3]The final stack temperature depends on the amount of injected water in scenario S1 and in S2 on the cooling load of the condensor.

gases. Since the water injection system is designed to recover waste heat, the condensation heat, which is exposed to the environment, is seen as a loss and is therefore not introduced in the exergy balance. For the calculation of the exergy of the different streams, an in-house Fortran procedure has been used [258].

For each amount of injected water, exergy destruction and efficiency were calculated. In literature, values of a global exergy destruction of minimal 5 % and a black box exergy efficiency as high as 93 % are used as limits for the heat transfer systems [264]. Crossing these limits will lead, in practice, to very large heat exchanger designs which are too expensive.

Heat exchanger network design

After the black box analysis, the final design of the heat exchanger network is based on composite curve theory [265]. For the composite curves, a minimum pinch of 10 °C was set as design condition. Altered networks of evaporators and heaters and coolers were proposed until a positive minimum approach temperature of 10 °C was obtained between the composite curves. For all simulations, the same boundary conditions as given in Table 5.1 and used for the black box simulations were used. Furthermore, generic heat exchanger models were used, since the actual design of the heat exchangers is beyond the scope of this thesis.

Possible heat exchanger network designs for waste heat recovery in a mGT were taken from large scale humidified GTs. As mentioned in the introduction, Jonsson and Yan divided these humidified GTs into three categories [30]:

- GTs with injection of water that evaporates completely;
- GTs with injection of steam;
- GTs with injection of water in a humidification tower, with a recirculation water loop.

The first category includes not only systems with water injection behind the compressor with recuperation, but also water injection at the compressor inlet for power augmentation on hot days and water injection in the compressor for intercooling. In this thesis, water injection in the compressor or

compressor inlet is not taken into account and neither is water (steam/liquid) injection in the combustion chamber. Water is always introduced behind the compressor and before the combustion chamber (Figure 5.1). Both inlet and intercooling techniques can be applied on a mGT to increase the power production or efficiency by decreasing the compressor work. These techniques are however not suited for the recovery of available waste heat in the hot exhaust gases and are therefore not included in this study. Water injection in the combustion chamber will increase the power production and decrease NO_x emission. The waste heat recovery is however limited, since the water is introduced after the regenerator. Finally, to keep the cycle layout simple, easy to operate and reduce the capital cost, it was decided to limit the amount of heat exchangers to maximum two.

5.1.3 Results of black box analysis

In this section, first three possible problems related to water injection in a mGT are discussed: surge margin reduction, combustion stability and water condensation from the flue gases. In the second part, black box simulation results of S1 and S2 are discussed. Finally, the optimal heat exchanger network design is proposed.

Water injection related issues

Adding water to the mGT cycle will, like during the steam injection experiments, reduce the compressor surge margin and affect the combustion stability. The Turbec T100 mGT operates at constant electric power output condition. During the steam injection experiments, no problems were encountered, however humidifying the mGT cycle will result in a higher amount of injected water, shifting the compressor operating point towards the surge limit and possibly leading to an unstable, incomplete combustion. When analysing the different cycles, it is highly important to take these two possible issues into account.

Besides the possible surge and combustion stability issues, experimental results of full water recovery in a steam injection GT [266] and a HAT cycle [97] also showed that the condensed water contained several contaminants (ions) and had a certain level of acidity due to the presence of dissolved CO_2. Water treatment is thus necessary before the water can be recycled. In addition, once the temperature of the flue gases drops below the dew point

temperature, an acidic environment is created due to the water condensation. The heat exchangers and stack need to be protected against corrosion. The water condensation will only happen at low temperature, therefore standard treatments or materials used in condensing boilers can be used in this application.

Black box

For both S1 and S2, water and compressed air are mixed before entering the HEATER (Figure 5.1). Depending on the amount of water, the mixture entering the HEATER is either humidified air, fully saturated air or saturated air that still contains liquid water droplets. All remaining droplets however will be evaporated in the HEATER. Final Combustor Inlet Temperature (CIT) varies from 629 °C (no water injection) till 675 °C (maximum 0.09 kg/s water injection). CIT is higher when injecting water, because TIT is kept constant and TOT will increase. TOT increases due to higher heat capacity and lower pressure ratio.

With increasing injected water flow rate, the stack temperature in S1 decreases linearly (Figure 5.2). The more water is injected, the more heat needs to be exchanged between the flue gases and the wet compressed air in order to reach a combustor inlet temperature such that the hot pinch temperature is 50 °C (Table 5.1). The stack temperature reduces continuously until 53 °C is reached. At this point, the water inside the flue gases starts to condensate, resulting in an extra release of heat. The total amount of water condensed is also shown on Figure 5.2. For this reason, it was decided to use the injected water mass flow rate as variable in the black box calculations and to calculate the stack temperature, which allowed simulating beyond the point of condensation. If the stack temperature was set to 53 °C, no convergence in Aspen® was reached, since a 0.1 °C difference in stack temperature results in a much higher heat release and thus higher injected water flow rate, diverging the final solution.

The stack temperature in S2 slightly increases with increasing water mass flow rate (from 24 °C at 5 g/s to 28 °C at 90 g/s) (Figure 5.2). The increasing stack temperature is a result of the decreasing air mass flow rate. The higher the water injection mass flow rate, the more the mGT controller will reduce the rotational speed and thus the air mass flow rate. The lower the air mass flow rate, the less water can be evaporated in the saturated air, which results in a higher stack temperature when all necessary water is condensed. The

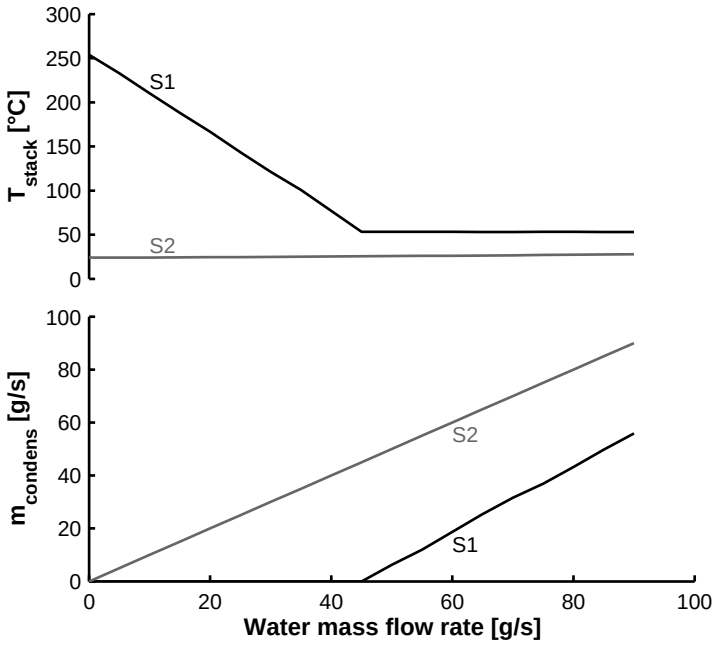

Figure 5.2: In Scenario 1 (S1), stack temperature reduces linearly with increasing injected water mass flow rate till 53 °C, when water condensation releases extra heat, resulting in a nearly constant stack temperature. Stack temperature slightly increases for Scenario 2 (S2) with increasing water injection.

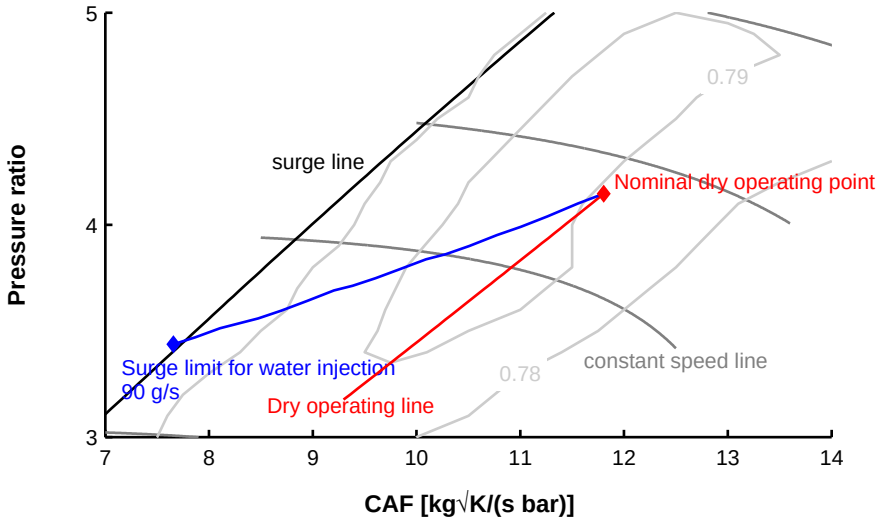

Figure 5.3: Compressor map showing the shift of the wet operating point towards the surge limit due to water injection.

temperature rise is however slightly slowed down since less fuel is burned. The amount of condensed water in S2 corresponds to the amount of injected water, since it was the goal to make the cycle self-sufficient for water in S2.

Simulations of S1 and S2 were stopped at an injection of 90 g/s of water for both scenarios (Figure 5.2). At this point, the compressor had reached its surge limit (Figure 5.3). The impact of the water injection on the compressor performance is shown on Figure 5.3. As mentioned before, the operating point shifts towards the surge margin. Surge margin is reached when 90 g/s of water is injected in the cycle, corresponding to a water fraction of 17 wt%, which is still below the limit set by Hermann et al. for combustion stability [242]. In order to reach this 90 g/s of water injection, the compressor needs to be redesigned in order to obtain a sufficient surge margin of 15 to 20 % [162].

For all applied water mass flow rates, the exergy destruction and efficiency are below the limits from literature for exergy destruction (minimum 5 %) and efficiency (maximum 93 %) [264] (Figure 5.4). For increasing injected water mass flow rates, the exergy efficiency of the black box from S1 decreases first, while destruction increases. Afterwards, exergy destruction starts to

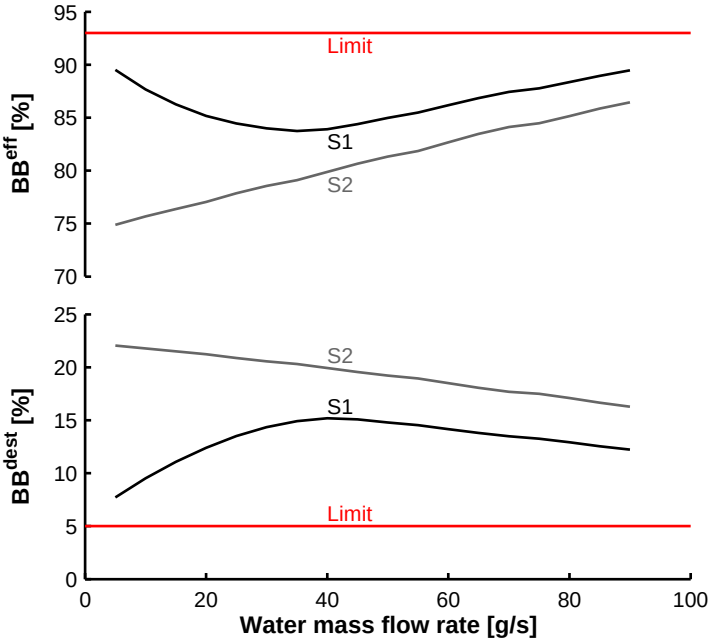

Figure 5.4: Exergy efficiency and destruction in the black box remain below the limit from literature for all different amounts of injected water.

decrease while exergy efficiency increases again. Exergy efficiency of S2 increases with increasing water mass flow rate, while exergy destruction decreases. The higher the amount of injected water, the more energy is recuperated in the HEATER-COOLER system and less is lost in the cooling process to condensate the flue gases. This explains the increasing efficiency and decreasing destruction. One can also see that the exergy efficiency of the black box in S2 is lower than the exergy efficiency of the black box in S1, which is due to the lower stack temperatures in S2 (Figure 5.4). Flue gases are cooled to get condensation of the water; however, the exergy of this cooling process is not used, resulting in an extra loss, explaining the lower exergy efficiency. In the case where the exergy from the stack flow is not considered in the black box results, both black box efficiency and destruction will be the same.

The behaviour of exergy efficiency and destruction in S1 can be explained by looking at the exergy fluxes entering and leaving the black box (Figure 5.5).

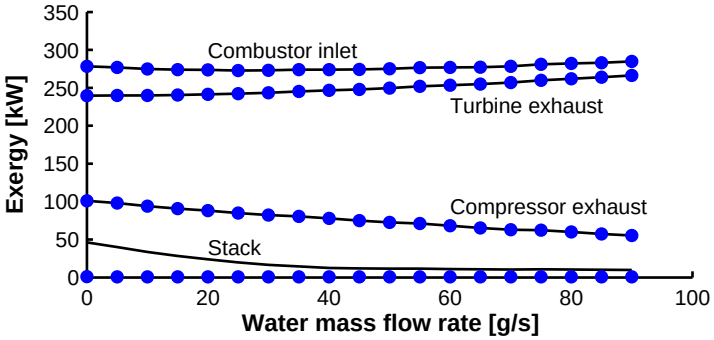

Figure 5.5: The different exergy flows of the black box system explain the difference in exergy efficiency and destruction between S1 and S2. Results of S1 are shown using lines, while the corresponding results of S2 are shown using symbols.

The exergy flow of the feedwater from S1 is not shown on Figure 5.5, since the water is introduced in the black box in its standard state (15 °C, 1 bar, liquid phase) and has therefore no exergy.

The different behaviour of the different exergy flows from Figure 5.5 can be explained as follows:

- With increasing water injection, the exergy flow through the turbine exhaust increases, due to the higher water content of the flow. Because of the higher water content, the TOT is also slightly higher, since TIT is kept constant by the mGT control system. The control system however also reduces the mass flow rate, which limits the exergy flow increase.
- Exergy flow at the combustor inlet however remains more or less constant. The increasing exergy flow because of the higher temperature and water content is compensated by the lower pressure and mass flow rate, resulting from the lower rotational speed set by the mGT controller.
- The lower pressure ratio, mass flow rate and compressor outlet temperature result in a decreasing exergy flow entering the black box from the compressor outlet.
- Since the stack temperature is gradually reduced with increasing water

injection, the outgoing exergy flow through the stack is also reduced. From the injection of 45 g/s of water on, the stack temperature remains nearly constant due to the condensation of water, resulting in a stabilisation of the exergy flow.

Using previous information, exergy efficiency and destruction of S1 of Figure 5.4 can be explained. The exergy flow of the stack decreases faster than the exergy flow of the compressor outlet. The exergy flow increase of the turbine exhaust is larger than the one at the combustor inlet. This results in decreasing exergy efficiency, while the exergy destruction of the black box increases. When reaching a stack temperature of 53 °C, the exergy loss through the stack remains constant, resulting in increasing exergy efficiency and decreasing exergy destruction.

Comparing the exergy flow of S1 with S2 shows only one difference. Exergy flows of the combustor inlet, turbine exhaust and compressor outlet remain constant at the same injected water fraction, while the exergy flow of the stack is much smaller in S2 than S1. The stack temperature of S2 is low compared to the stack temperature of S1 (Figure 5.2). On top of this lower temperature, the amount of water vapour present in the flue gases is much lower, due to the condensation of the necessary water, resulting in a very low exergy flow.

The electric efficiency of the mGT will increase, as expected, with increasing injected water mass flow rate (Figure 5.6). Although the exergy efficiency first decreases and then increases; this has no effect on the global efficiency of the mGT. The absolute efficiency rise depends on the amount of injected water. The non-linear efficiency increase is a result of the transformation of the compressor map into working lines. The efficiency slightly decreases between 70 and 75 g/s water injection by 0.01 %. Due to the increasing water mass flow rate, the mGT control system will reduce the compressor rotational speed to keep the produced power constant. By doing so, the compressor shifts further away from its design operating point, resulting in a decreasing compressor efficiency. Between 70 and 75 g/s, compressor efficiency drops from 77.4 to 76.0 %. In this case, the positive effect of extra water addition is fully cancelled by the lower compressor efficiency.

At an injection rate of 90 g/s, the absolute efficiency rise amounts to 9 %. Comparing results of S1 (squares) with S2 (triangles) shows that there is no difference between the electric efficiency increase, as could be expected. In the black box system of S2, the feedwater flow is replaced by a condenser

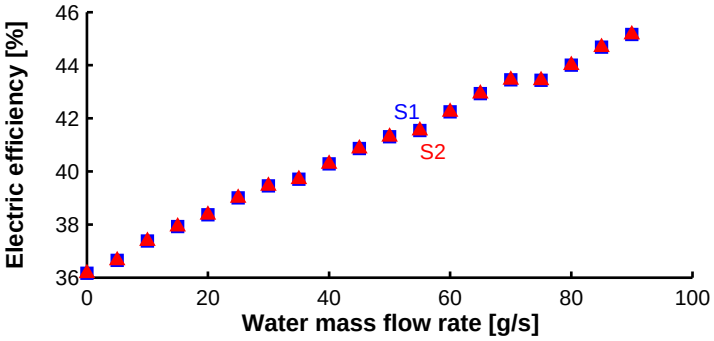

Figure 5.6: Electric efficiency increases with increasing injected water mass flow rate for S1 (squares) and showing good accordance with efficiency increase from S2 (triangles).

that will provide the necessary water. The heat output of this condenser is not used in the system; so finally, there is no difference between S1 and S2 for the mGT performance. In the actual power plant, when the losses of the auxiliaries need to be taken into account, there will be a difference, since energy is needed for the water treatments or for the cooling of the flue gases to get condensation (and possible also condensed water treatment).

From the results of the electric and exergy efficiency, one can conclude that condensing the exhaust gases needs to be accomplished with an external heat sink. None of the transferred exergy can be used in the system. The final design of the heat exchanger network is the same as for S1, with an additional cooler on the flue gas flow to cool the flue gases to get condensation of the required water.

Heat exchanger network design

For the heat exchanger network design of S1, three possible layouts were simulated (Figure 5.7). A first possibility is the direct injection of the water in the compressor outlet (A), the second possibility is the injection of preheated water in the compressor outlet (B) and the final test case was the use of a saturation tower (the mHAT approach (C)). Next to these three proposed layouts (Figure 5.7), several additional layouts are possible, using additional heat exchangers (for instance an aftercooler and a second economizer to preheat the feedwater, as proposed by Parente et al. in the mHAT Plus cycle [34]). These layouts were however excluded from this study, since the maximum amount of heat exchangers was set to two in order to keep the cycle layout simple.

The simulations of case B are divided into two subcases. In a first subcase, water was heated, but the final injection temperature remained below the boiling point. In the second subcase, liquid water was heated, boiled and the raised steam was superheated (5 °C). For this subcase, where temperature at the boiling point remains constant, a different approach needed to be applied; the water heater has been split up in three parts: a water heater, a boiler and a super heater. Finally, injection of a liquid-vapour mixture was not considered.

Even though exergy analysis of the black box showed that injection up to 90 g/s of water (surge limit of the compressor) still results in a global exergy efficiency and destruction below limits that can be found in literature [264],

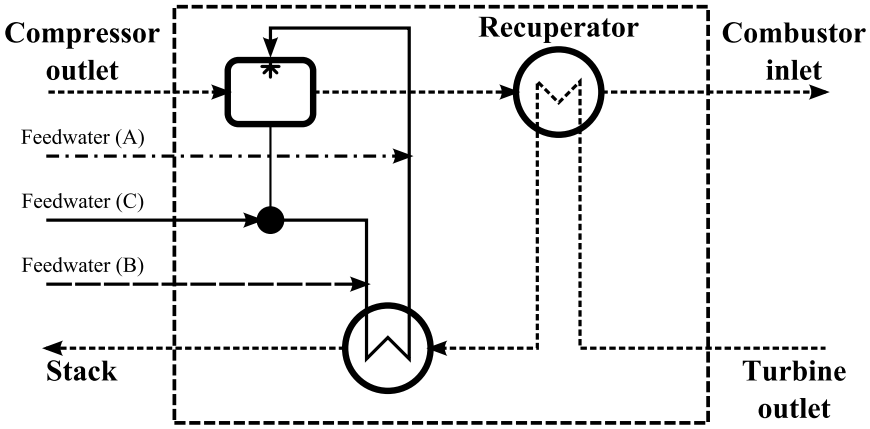

Figure 5.7: Heat exchanger network designs, using direct water injection (Case A), preheated water injection (Case B) and the use of a saturation tower (Case C).

Table 5.2: Results of heat exchanger network design, using different injection types, indicate that direct injection of heated water (Case B liquid) increases electric efficiency the most.

	Case A	**Case B**		**Case C**
		liquid	**steam**	
T_{stack}	76 °C	62 °C	132 °C	82 °C
T_{mix}	63 °C	65 °C	172 °C	74 °C
$\dot{m}_{\text{water}}$	40 g/s	43 g/s	29 g/s	40 g/s
η_{el}	40.5 %	40.8 %	39.5 %	40.0 %
$\dot{Q}_{\text{condens}}$	129 kW_{th}	127 kW_{th}	136 kW_{th}	134 kW_{th}
T_{condens}	25.7 °C	25.7 °C	25.0 °C	25.4 °C

this potential cannot fully be explored with the three considered networks in Figure 5.7. The optimal network, corresponding to the limit found in the black box simulations, requires more heat exchangers, which will make the cycle too complex for mGT applications. The black box maximal water injection of 90 g/s of water is never reached, because the simulated stack temperature of 53 °C can never be reached (Table 5.2) in any of the three considered networks. The limitation for the stack temperature is the temperature of the working fluid mixture after water injection in Case A and C, and the low amount of water that can be heated in Case B. For direct injection (Case A), the mixing temperature of the compressed air and the liquid water is still quite high (around 63 °C). The stack temperature cannot be lowered further than this mixing temperature, otherwise the composite curves will cross, which is prohibited. The same explanation as for Case A can be given for Case C, the mHAT. The temperature of the excess water leaving the saturation tower, which is rerouted to the water heater, will determine the lowest possible stack temperature. Hot flue gases cannot be cooled below this temperature, which corresponds to the saturation temperature of the compressed air.

The reason why the simulated black box potential cannot be reached with the simple heat exchanger networks considered in this section (Figure 5.7), is illustrated by the hot composite curve of the black box (Figure 5.8). When injecting 90 g/s of water in the mGT cycle, water starts to condense from the exhaust gases once the temperature gets below 67.3 °C. From this point, the temperature changes little, even though a large amount of heat is available due to the condensing water. To use this heat without violating the second law – without crossing composite curves – a lot of

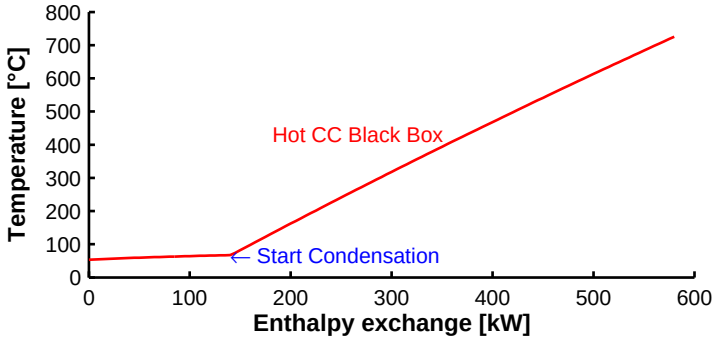

Figure 5.8: The very flat hot composite curve at low temperature, due to water condensation, makes that simple heat exchanger networks are not capable of reaching the black box potential, since not enough heat can be recovered at low temperature.

heat needs to be absorbed in the cold stream at low temperature. Since the 90 g/s of feedwater at 15 °C is the only available incoming stream of the network at low temperature, this cannot be accomplished with simple heat exchanger networks. To be able to recover this energy, more complex networks, using multiple-phase flow heat exchangers are necessary. These networks are however too complex and too expensive and thus not in line with the mGT usage objective.

Final composite curves are shown in Figure 5.9. For all composite curves, only the heat transfer inside the actual heat exchangers is considered. The mixing is not taken into account, since mixing does not require a minimal pinch. For both the direct injection (Case A, Figure 5.9 (a)) and the mHAT case (Case C, Figure 5.9 (b)), the minimal pinch (10 °C) can be seen at the lowest temperature of the composite curves, meaning the difference between the stack and mixing temperature, which proves that the stack temperature is determined by the mixing temperature. For the indirect injection of steam (Case B steam), the minimal pinch depends on the boiling point of the water (Figure 5.9 (c)). If the stack temperature would be lowered, hot and cold composite curve would cross, which is prohibited. For the indirect injection of heated water (Case B water), the minimal stack temperature depends on the amount of water injected, since one should avoid the production of steam (Figure 5.9 (d)).

The lower the stack temperature, the more water can be injected, resulting in

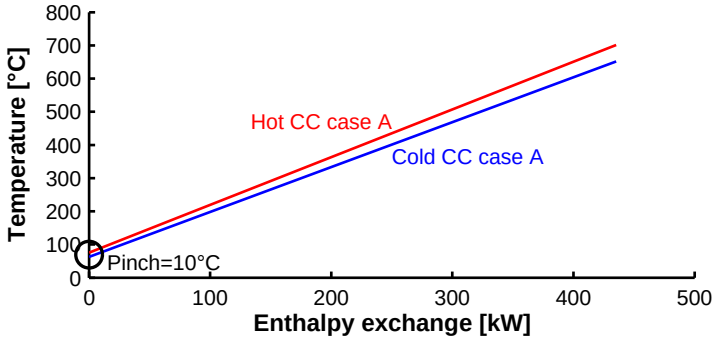

(a)

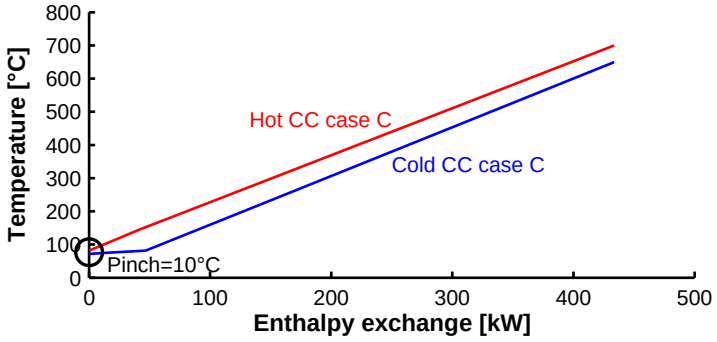

(b)

Figure 5.9: Composite curves of direct water injection (Case A), the injection of heated water (Case B Water) and auto-raised steam (Case B Steam) and the mHAT case (Case C).

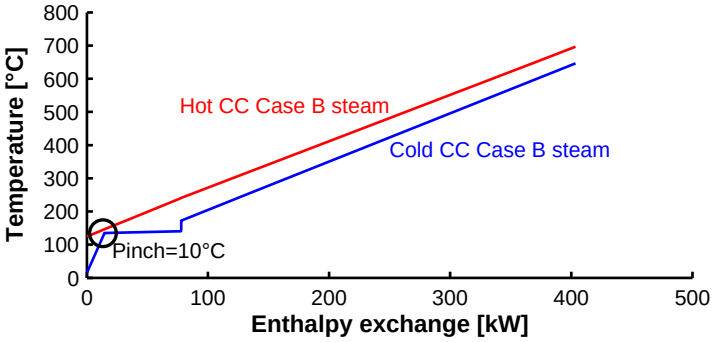

(c)

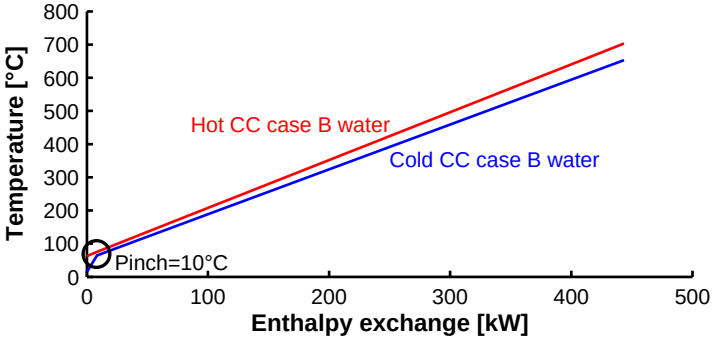

(d)

Figure 5.9: (continued)

a higher electric efficiency (Table 5.2). Additionally, results of condensation simulations show that the lower the injected amount of water, the more the stack temperature needs to be lowered and the more heat needs to be disposed to the environment in order to make the cycle self-sufficient with water.

State of the art HRSGs allow a minimal pinch of 5 °C rather than 10 °C. Reducing this minimum pinch has however a limited effect on the final electric efficiency. Reducing the pinch by 5 °C will increase electric efficiency from 40.5, 40.8, 39.5 and 40.0 % to 40.6, 40.9, 39.6 and 40.1 % for respectively direct water injection, injection of preheated liquid water, steam injection and the mHAT case, which indicates that the minimum pinch set for the heat exchangers has little effect on the final efficiency. Reducing the hot inlet/cold outlet temperature difference of the recuperator by 5 °C has a much larger effect on the electric efficiency. Reducing this temperature difference from 50 to 45 °C in the mHAT case will increase the efficiency from 40.0 to 40.9 °C (as will be show in following section). The electric efficiency is thus more sensitive to changes in the hot inlet/cold outlet temperature difference of the recuperator than the pinch set for the heat exchangers.

Injection of heated water is the most efficient way of water injection for waste heat recovery; however, differences between the different cases are rather small (Table 5.2). As mentioned before, electric efficiency is very sensitive to changing pressure losses. Increasing the pressure drop on the hot side by 1 % will lower the electric efficiency by 0.37 % for case A, 0.37 % (liquid hot water injection) and 0.44 % (steam injection) for case B and 0.31 % for case C. These changes are the same order of magnitude as the difference in efficiency (Table 5.2). Therefore the results from Table 5.2 are only valid when heat exchangers with a cold and hot side pressure drop of 3 % and 3.8 % (160 to 197 mbar and 40 mbar) are implemented in the cycle. This maximal pressure drop will determine the final size of the heat exchanger, along with the necessary heat transfer surface. Regenerator investment cost is approximately 30 % of the total installation cost [28]. Traverso and Massardo showed that specific capital costs ranged from 125 to 190 $/kW$_e$ [50]. This indicates that a different regenerator design will have a significant influence on the final total investment cost. Due to the small difference in efficiency, it might be possible that from an economic point of view, heated water injection is not the optimal route for waste heat recovery in a mGT cycle.

When the maximal amount of water is injected, by means of injection of heated water, the surge margin is reduced from 25 % to 16 %, which is still within the limits for power generation [162]. Similar surge behaviour was observed during the steam injection experiments (Figure 4.8) and by Ferrari et al. during steam injection experiments in their T100 mGT [38]. This is due to a good design surge margin performance. The water fraction is limited to 6.7 wt%, which should still allow for a stable combustion [242]. Final stack temperature is 62 °C (Table 5.2), which is above the dew point temperature of 52 °C (Figure 5.2).

Finally, as a proof of concept, the mHAT Plus, designed by Parente et al. [34], has been simulated in Aspen®. The cycle layout is depicted in Figure 5.10. The saturation tower was simulated using the *RADFRAC* block from Aspen®, according tot the simulations of Queiroz et al., in case of a counter-flow saturation tower [260]. In essence, the saturation tower is a pressurized counter flow cooling tower. Depending on the ratio between the water flow rate sent to the Aftercooler and the Economizer 1, a maximum electric efficiency of 40.9 % can be reached. The major gain compared to the classic mHAT design (electric efficiency of 40.0 %) is that additional heat is recovered from the exhaust gases, using the Economizer 2 to preheat the feedwater. In the mHAT Plus case, the exhaust gases are cooled till 56.6 °C, which is significantly lower than the 82 °C of the classic mHAT case. The difference in efficiency between both cycles is however again very small. Therefore it is essential to perform an economic analysis to see if the additional efficiency increase justifies the higher investment costs due to the necessary installation of two heat exchangers (Economizer 2 and the Aftercooler) compared to the classic mHAT cycle.

5.1.4 Conclusion of the optimal humidified mGT development

In this section, I presented the results of a series of simulations of water injection in the compressor outlet of a mGT. Water injection in the compressor outlet is a possible route for waste heat recovery in the mGT. The additional water will enhance the performance of the mGT, especially the electric efficiency. This will make the mGT as CHP more attractive for applications with a non-continuous heat demand. A two-step method was used, to find the thermodynamic optimal of the water injection. In the first step, the heat exchanger network of the mGT has been replaced by a black

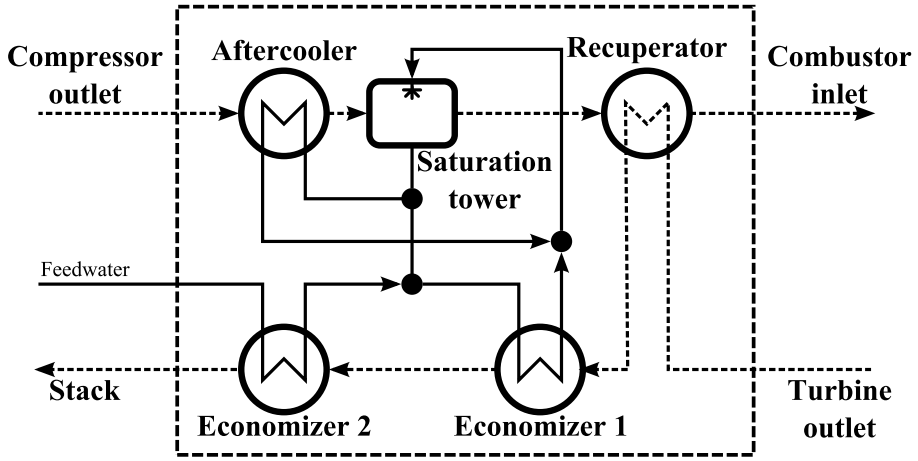

Figure 5.10: Heat exchanger network of the mHAT Plus design [34]. Part of the circulating water is used to cool the hot compressed air. The other part is heated in the economizer. Finally, both streams are mixed and injected in the saturation tower. The feedwater is preheated by the exhaust gases to recuperate more heat.

box system. Two different scenarios were studied during this first step. In the first scenario, I investigated the maximal potential for water injection, by lowering the stack temperature, without violation of the second law of thermodynamics. In the second scenario, the cycle was made self-sufficient with water by condensing the water in the exhaust gases; since the cost of the water consumption and treatment is a major drawback of humidified gas turbines. The final heat exchanger network was designed during step two of the two-step procedure by using composite curve theory.

Simulation performed on a Turbec T100 mGT, representative for mGTs, resulted in following results:

- Black box simulations indicated that 9 % absolute efficiency increase can be achieved by injecting 17 %wt of water (90 g/s) in the compressor exhaust without global violation of the second law of thermodynamics. By doing so, the remaining waste heat in the flue gases is recovered, resulting in a final stack temperature of 53 °C.
- Composite curve theory and pinch analysis however showed that this theoretic potential cannot be achieved with a limited amount of heat exchangers (two). Lowering stack temperature until 53 °C is not possible in this case, which limits the recovery of waste heat.
- The lowest possible stack temperature, depending on the injection type is 76 °C (direct injection of water), 62 °C (direct injection of heated water) and 82 °C (mHAT). These stack temperature respectively corresponded to an injection of 40, 43 and 40 g/s of water, which resulted in absolute efficiency increases of 4.3, 4.6 and 3.8 %.
- To make the cycle fully self-sufficient for water, the flue gases need to be cooled to lower the stack temperature below 26 °C. Below this temperature, enough water will condensate from the flue gases to compensate for the injected water.

From a thermodynamic point of view, direct injection of heated water is identified as the optimal cycle layout for waste heat recovery through water injection in a mGT. The most waste heat can be recovered in this injection scheme, resulting in the lowest stack temperature. The difference in efficiency increase between the different injection schemes is however rather limited. Taking into account economic parameters, like investment costs and electricity and natural gas prices, might lead to a different optimal design.

5.2 Humidified Turbec T100 mGT development

The final goal of this thesis is to develop a mGT layout that can work as a CHP unit when there is heat demand, but that can also switch to water injection mode – for waste heat recovery – with higher electric efficiency when the heat demand drops. By doing so, forced shutdown is avoided, resulting in a more profitable investment.

In the previous section, injection of preheated water was identified as the optimal route for waste heat recovery in the mGT cycle. The difference between the possible injection schemes was however very limited. Therefore, the mHAT layout offers the best potential. Rather than redesigning the whole heat exchanger network inside the T100 mGT, it was decided to keep the existing gas/gas recuperator and economizer and use these components for water injection.

The main advantage of using this type of water introduction in the mGT cycle is that the original CHP installation remains unaffected. This allows the use of the mGT in CHP mode during periods with heat demand and in water injection mode when there is no demand for heat. Eventually, it should be possible to use both modes at the same time, resulting in a mGT that produces continuously the nominal electrical power, independent of the heat demand.

Another advantage of using a saturation tower instead of direct injection of water is the water quality. By letting a huge amount of water circulate through the system, only a small part of the circulated water will evaporate. In case of direct water injection, all water will evaporate, so all contaminants present in the water will enter the mGT and foul the recuperator and turbine. With the saturation tower, only a small part of the water evaporates, the contaminants remain in the water, so a lower feedwater quality is acceptable, resulting in a lower operational cost. For this reason, it was decided to use a saturation tower in combination with an economizer. When direct injection (Case A from Figure 5.7) or indirect injection of heated water (Case B from Figure 5.7) is used, the remaining liquid water in the air entering the recuperator will completely evaporate, leaving behind all contaminants, resulting in recuperator fouling.

In this section, the black box simulations of the previous section are extended, but rather than finding the optimal route for waste heat recovery, the effect of changing the boundary conditions on the mGT performance is searched.

In a second part, the Turbec T100 based mHAT cycle is developed and simulated. The effect of different non-idealities of the heat exchanger network and the operating procedure of the T100 mGT on the final performance is studied.

5.2.1 Simulations of the mHAT cycle

The simulations presented in this section were again performed with the Aspen® process simulator, using the previously developed wet model of the Turbec T100 mGT (subsection 5.1.1).

Black box analysis

For the black box simulations, the same layout as in previous section was used for the simulations (Figure 5.1). By setting the stack temperature and the pinch on the hot side of the black box, the injected mass flow rate of water is fully determined, since there are only two degrees of freedom in the black box system. With these boundaries set, the only remaining variables in the black box system are the heat flux between the heater (HEATER) and the cooler (COOLER) and the injected mass flow rate. The other variables: $\dot{m}_{\text{air}}$, π and the produced power are changed and controlled by the mGT control system in order to reach the requested power at maximum TIT with a choked turbine.

In this section, different hot pinches are imposed in combination with different stack temperatures. For the simulations performed for this section, stack temperature was imposed rather than injected water flow rate. The exergy destruction over the black box (BB^{dest}) is calculated (Equation 5.3) together with the exergy efficiency (BB^{eff}, Equation 5.4). Boundary conditions used for the simulations are summarized in Table 5.3.

Heat exchanger network design

Rather than redesigning the whole heat exchanger network inside the T100 mGT, it was decided to keep the existing gas/gas recuperator and economizer and use these components for water injection. This leads to the final mHAT cycle design as depicted in Figure 5.11.

Table 5.3: Boundary conditions used in the black box simulations. Both stack and hot pinch temperature were changed to study the effect on global performance.

Compressor		
	Pressure ratio	3.5 to 3.7 [1]
	Isentropic efficiency	0.79
	Inlet air temperature	15 °C
Turbine		
	Turbine back pressure	50 mbar
	Isentropic efficiency	0.85
	Turbine Inlet Temperature (TIT)	950 °C
Combustion chamber		
	Combustor pressure loss	5 %
Heat recovery system		
	Cold side pressure loss	3 % [2]
	Hot side pressure loss	40 mbar
	Water injection pressure loss	0.5 %
	Hot inlet/cold outlet temperature difference	30 to 70 °C [3]
	Stack temperature	80 to 120 °C [3]
	Feedwater inlet temperature	15 °C
Fuel (methane)		
	Fuel temperature	30 °C
	Fuel pressure	6 bar
	Lower Heating Value (LHV)	50 MJ/kg
General		
	Produced electric power	100 kW_e

[1] The manufacturer's compressor map was used in the simulations (Figure 3.2).

[2] The pressure losses on hot and cold side are taken constant and will be a design specification.

[3] For all simulations, the hot side temperature difference and final stack temperature are varied.

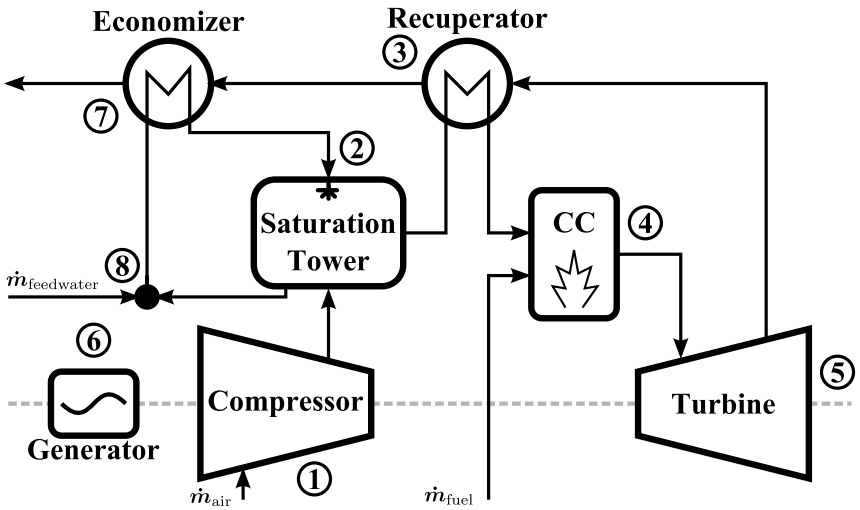

Figure 5.11: In the model of the mHAT cycle based on the Turbec T100 mGT, compressed air coming out of the compressor (1) is first humidified in the saturation tower, by means of an excess of water (2). The saturated air-water mixture is then preheated by the exhaust gases in the recuperator (3). Afterwards, the air-vapour mixture is heated till maximal TIT by burning natural gas in the combustor (4). Expansion over the turbine (5) provides the necessary power to drive the compressor and the high speed generator for electric power production (6). After preheating the compressed saturated air, exhaust gases are used to reheat the water returning from the saturation tower (7). Feedwater to replace the evaporated water is added to the water cycle (8).

A large amount of water is heated in the economizer ((7) Figure 5.11). After the water is heated, it is injected in a saturation tower where the compressed air is flowing in order to saturate it. Part of the water will evaporate till the compressor air is saturated. The saturated air is heated further by the hot exhaust gases of the turbine in the recuperator until the hot pinch temperature is reached, while the remaining water from the saturation tower is rerouted back to the heat exchanger, where extra feedwater is injected in order to keep the total mass flow rate of water going through this heat exchanger and the saturation tower constant. For the saturation tower, the *V-DRUM1* block from Aspen® has been used as in subsection 5.1.2. When the black box boundary conditions are applied (design calculations), the exergy destruction and efficiency of the system are equal to the results the black box simulations. In addition, the performance of the heat exchanger network is independent of the amount of circulating hot water. No additional exergy is added, since the circulating water does not leave the control volume. The water only transports the energy.

With fixed heat exchange areas for the recuperator and economizer (off-design calculations), the exergy efficiency will change because of the changing boundary conditions. The question is whether the amount of circulating water will have an influence on the global exergy efficiency and exergy destruction. One should also take into account the control system of the mGT itself. As mentioned before, the maximal TIT of the T100 mGT is around 950 °C; however the controller will set this temperature by keeping the TOT constant at 645 °C. Once water is added to the cycle, the thermodynamic properties of the gas/vapour mixture in the turbine will change. The controller however uses fixed correlations to estimate TIT out of the measurements of TOT. During water injection, the controller will underestimate TIT, resulting in a remarkable electric efficiency loss. For the final simulation, instead of controlling TIT, TOT is kept constant in order to be able to simulate the injection of water in the T100 mGT as precisely as possible.

By letting water recirculate inside the heat exchanger network, an extra degree of freedom is added to the system. For the simulations, either the boundary conditions of the black box are applied to the heat exchanger network or the existing specifications of the heat exchangers are used. Even though an extra degree of freedom is added to the system, it is still not possible to set the injected amount of water. This amount of injected water is controlled by the saturation of the hot compressor exhaust air, while the amount of recirculation water can be chosen. This corresponds to reality,

where only the power of the pump (not included in Figure 5.11) – necessary for recirculating the hot water – can be controlled. Depending on the amount of water that evaporates in the saturation tower, a controller will add more or less water to the water circuit in order to maintain a constant circulating water flow rate.

Finally, during simulations of the heat exchanger network, using the existing heat exchangers, constant pressure drops were assumed, however due to water injection, flow specification will change. Due to the injection of water, the mass flow rate reduces. In combination with this mass flow rate reduction, volume flow rate and density will also change, resulting in lower pressure losses (29 % on cold side of the recuperator, 10 % on turbine exhaust). By keeping the pressure losses constant, the final performance and electric efficiency of the mGT is underestimated by 0.4 %. It was chosen not to adapt the pressure losses, since it is difficult to predict pressure loss in the saturation tower. By keeping the pressure loss constant, efficiency increase is determined in a conservative way.

5.2.2 Results of the sensitivity analysis for the humidified Turbec T100 mGT development

In this subsection, I first discuss the sensitivity analysis results, indicating the effect of changing boundary conditions on the global performance of the mGT. Second, I present the effect on the performance of the non-idealities of the heat exchanger network and the mGT operating strategy, when converting the ideal humidified mGT cycle into the humidified Turbec T100 mGT. All simulations for black box and mHAT simulations were performed at nominal power of the T100 mGT (100 kW_e).

Black box sensitivity analysis

In this subsection, the water fraction is defined as:

$$\Omega_{\text{water}} = \frac{\dot{m}_{\text{water}}}{\dot{m}_{\text{air}} + \dot{m}_{\text{water}}} \tag{5.5}$$

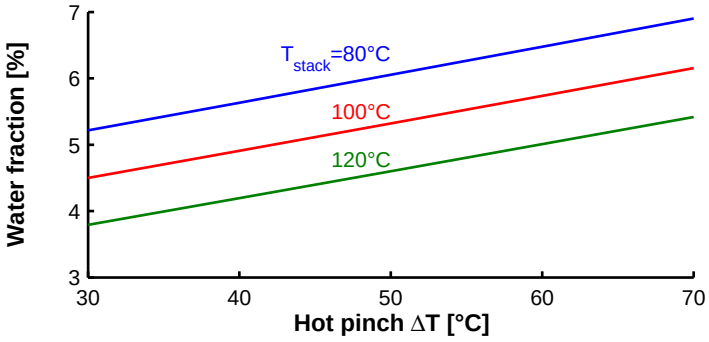

Figure 5.12: The highest water fraction in the working fluid is obtained at the lowest stack temperature and highest pinch temperature.

Lowering the stack temperature or increasing the hot pinch temperature will increase the injected water fraction (Figure 5.12). A higher stack temperature leads to a reduced water fraction at constant pinch temperature on the hot side, since less energy is extracted from the exhaust gases for evaporating the water. The bigger the temperature difference between the inlet of the combustion chamber and the outlet of the turbine at constant stack temperature, the more the injected water fraction will increase. At constant stack temperature, the heat absorbed in the heater (HEATER) does not vary much. Although TIT is kept constant, the limited water fraction has little effect on TOT. In addition, the changes in heat capacity of the exhaust air are limited. This means that the same amount of heat needs to be absorbed in the Heater. In order to meet the boundary condition of a certain hot pinch, more water needs to be injected and evaporated with increasing pinch, since a lower combustor inlet temperature is required. The highest water fraction is obtained at the lowest stack temperature and highest pinch temperature.

Due to the action of the control system under water injection condition to keep the power output constant, rotational speed, compressor pressure ratio and air mass flow rate will reduce. The more water will be added, the more the rotational speed, and accordingly the pressure ratio and inlet air mass flow rate will reduce. Figure 5.13 gives the results of this changing rotational speed, pressure ratio and compressor air mass flow rate. The results are reduced, using the dry operation parameter. At nominal power ($100\,\mathrm{kW_e}$), the mGT runs at 66 700 rpm, resulting in a mass flow rate $\dot{m}_{\mathrm{air}}$ of $0.70\,\mathrm{kg/s}$ and a pressure ratio π of 4.1.

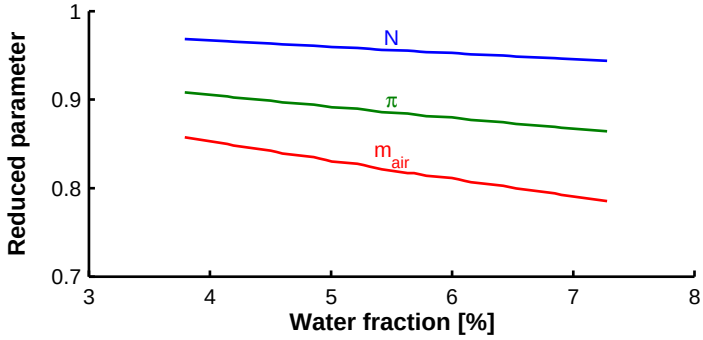

Figure 5.13: Due to the action of the control system, rotational speed, compressor mass flow rate and pressure ratio will reduce with higher water fractions.

The exergy efficiency of the black box decreases lineary with increasing hot pinch, while the influence of the stack temperature is more complex (Figure 5.14). The higher the pinch temperature on the hot side of the heat exchanger network, the lower the outgoing exergy flow of the cold stream. The lower temperature is partially compensated by the higher water content of the air-vapour mixture but, as mentioned before, the maximum water fraction in the exhaust air is limited, and is not high enough to compensate for the lower outlet temperature of the cold stream. For changing stack temperatures, the exergy efficiency only varies little (differences are smaller than 0.2 %). At high pinch temperatures, exergy efficiency is slightly higher for lower stack temperatures. At lower pinch temperatures, exergy efficiency at higher stack temperatures becomes slightly bigger than at lower stack temperatures. The complex behaviour of the exergy efficiency as function of the stack temperature is a result of the different parameters influencing the in- and outgoing streams of the black box, e.g. the changing water fraction. The black box system is part of a bigger system, the mGT, where the controller tries to keep the produced electrical power constant, by changing the fuel flow rate and the shaft speed, resulting in a different compressor mass flow rate, temperature and pressure. So finally, exergy efficiency is little affected by stack temperature.

The exergy destruction – which must be positive as required by the second law expressed over the black box – will increase with increasing hot pinch and decreasing stack temperature (Figure 5.14). The increasing exergy destruction with increasing hot pinch temperature corresponds well with the calculated exergy efficiencies. The higher the pinch temperature, the more exergy will be destructed in the heat exchanger, resulting in a lower efficiency. The stack temperature seems to have a bigger influence on exergy destruction. With increasing stack temperature, the exergy destruction will also decrease. The complex influence of the other parameters on the exergy efficiency seems to have disappeared by taking the difference between the in- and outgoing exergy flows (Equation 5.3), resulting in a straight-forward correlation between stack temperature and exergy destruction. Even though exergy efficiency varies little at constant hot pinch, exergy destruction changes due to the changing properties of the gases because of the changing water fraction. A remarkable difference exists between the decreasing exergy destruction from 80 to 100 °C and from 100 to 120 °C (Figure 5.14). This difference results from an altered working fluid composition, resulting in a non-linear decreasing exergy destruction.

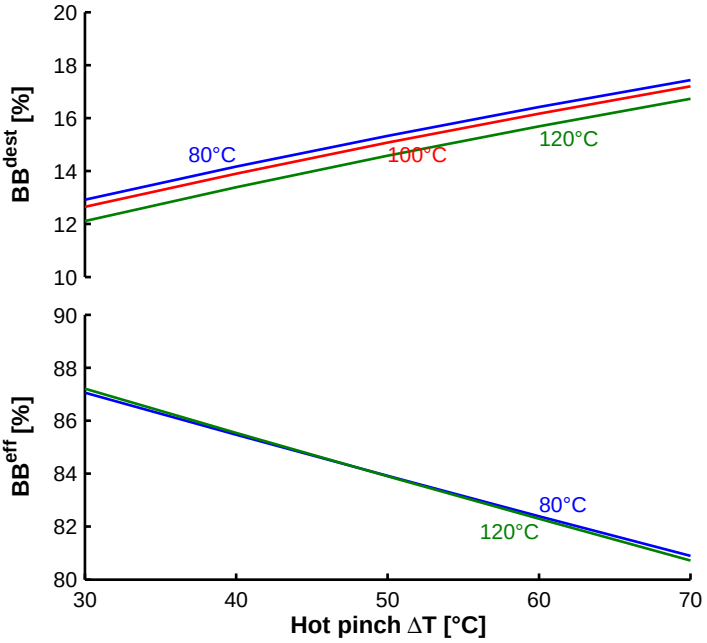

Figure 5.14: Exergy destruction is very sensitive for changing hot pinch and stack temperature, while exergy efficiency is rather unaffected by the stack temperature.

The black box exergy efficiency and exergy destruction are below the limits that can be found in literature [264] (Figure 5.14), so all scenarios should be feasible, as could be expected. The simulated stack temperature is much higher than the stack temperature obtained at the limit for water injection in section 5.1. For a gas/gas heat exchanger having acceptable pressure losses and size, a hot pinch of 50 °C is considered as economically viable. Stack temperatures lower than 90 °C should be avoided, in order to prevent condensation of the water in the heat exchanger, since in that case, special treatment/materials are necessary.

In order to gain an insight in which components are crucial in the black box, an analysis of the exergy destruction in the different components is made (Figure 5.15). For a small pinch, the destruction in the heat exchanger (heater (HEATER) and cooler (COOLER) combined together) is nearly twice as big as the destruction in the mixer. With increasing pinch temperature, the exergy destruction in the heat exchanger increases dramatically. On the other hand, the exergy destruction by mixing the water with the compressed air decreases with increasing hot pinch. The injected fraction of water increases with increasing hot pinch (Figure 5.14). Higher water fractions force the mGT control system to slow down the compressor to keep the produced power constant (Figure 5.3). Slowing down the compressor results in a decreasing air mass flow rate, pressure ratio and especially a lower air temperature. Through the decreasing compressed air outlet temperature, water and air temperature match better for mixing, resulting in a lower exergy destruction. The stack temperature has no influence on the mixing exergy loss, even though more water is injected at lower stack temperature. The mixing exergy loss remains constant through the increasing exergy input in the cycle because of the higher fuel flow rate, which results in a lower efficiency (Figure 5.16). By matching injection temperatures better, the exergy destruction in the final layout of the mGT heat exchanger network can be reduced in order to obtain a better performance. Finally, the exergy destruction in the heat exchanger network remains limited. As shown by Balli and Aras, the major exergy destruction takes place in the combustion chamber. The combustion chamber is responsible for 37.54 % of the exergy destruction in the dry cycle [267].

The electric efficiency will increase with decreasing stack temperature and hot pinch temperature, since more energy is recuperated with a lower stack temperature and less fuel is required to reach the maximal TIT when the hot pinch temperature difference is smaller (Figure 5.16). The corresponding dry case efficiency (with TIT equal to 950 °C) results in an electric efficiency

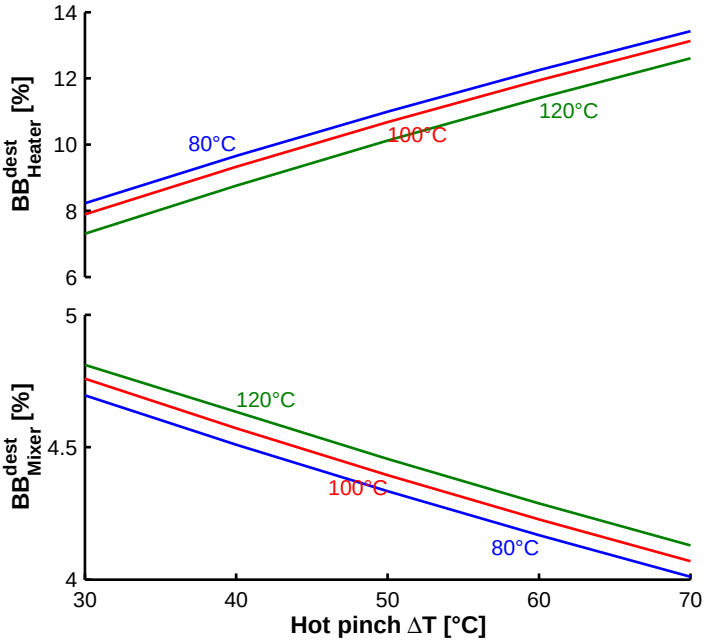

Figure 5.15: The heater is responsible for the largest part of the exergy destruction in the black box. This part increases with increasing pinch temperature.

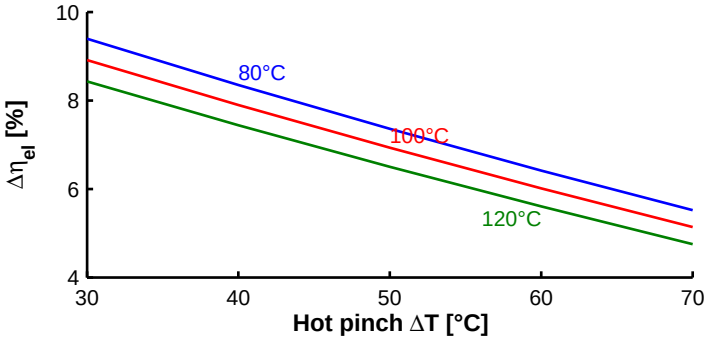

Figure 5.16: Electric efficiency of the mGT is positively influenced by decreasing pinch and stack temperature.

of 32.7 %, showing that with a hot pinch of 50 °C and a stack temperature of 90 °C, the efficiency could be increased by 7 % absolute compared to the dry-case mGT. Since the T100 mGT operates in constant electric power production mode, the injection of the water will lead to a reduction in fuel consumption. With 6 % of the total air mass flow rate replaced by water, the total fuel consumption can be decreased by 18 %. Compared to the injected water fraction, the resulting absolute electric efficiency increase seems to be a little bit contradictory (Figure 5.12). One should expect that the total electric efficiency will increase with increasing water fraction; however results from simulations show the opposite. The previous statement is only true when all other parameters are kept constant. In these simulations, the water mass flow rate is used to reach several boundary conditions and so the injected water mass flow rate is determined by the boundary conditions. So the boundary conditions (hot pinch and stack temperature) determine the final increase in electric efficiency of the mGT.

The minimal pinch between the hot and cold composite curve is 27 °C (Figure 5.17). The composite curves of the black box system are calculated using a temperature difference at the hot side of the heat exchanger system of 50 °C, which is an acceptable value for a gas/gas heat exchanger and a final stack temperature of 90 °C, in order to avoid problems with condensation of water inside the heat exchanger. The mixing of the air and water is introduced into the composite curves as a heat exchanger, where the cold stream corresponds to the injected water and the hot stream to the compressed air.

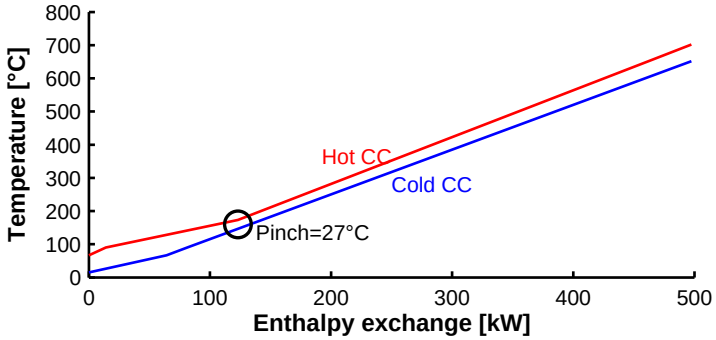

Figure 5.17: Composite curves of the black box heat exchangers system.

Heat exchanger network design

For all simulations performed in this part of the study, a hot pinch temperature of 50 °C has been used in combination with a stack temperature of 90 °C. As mentioned before, gas/gas heat exchangers with acceptable pressure losses and a hot pinch of 50 °C are considered as economically viable.

The circulating water mass flow rate in the mHAT cycle has no effect on exergy destruction and efficiency for all the different simulation cases (Figure 5.18). The exergy destruction and efficiency in the mHAT case are the same as for the black box case when the same boundary conditions are used and TIT is kept constant. When taking into account the limitations of the installed heat exchangers in the T100 mGT (the limited surface for heat exchange), the exergy efficiency will decrease. The use of existing heat exchangers results in a higher stack temperature (Figure 5.19). This has however only a little effect on exergy efficiency. The limited heat exchange surface also leads to a higher hot pinch temperature, which has a severe negative effect on the exergy efficiency. Although exergy efficiency is reduced, the circulating water flow rate has still no effect on the global exergy destruction and efficiency. The recirculation flow rate has a minor effect on the final stack temperature, but has a huge effect on its injection temperature in the saturation tower (Figure 5.19). The higher stack temperature will lead to a higher exergy loss through the stack, what should result in lower exergy efficiency, however the water fraction in the exhaust gases is very low and this in combination with a very small stack temperature increase, leads to an insignificant difference (Figure 5.18).

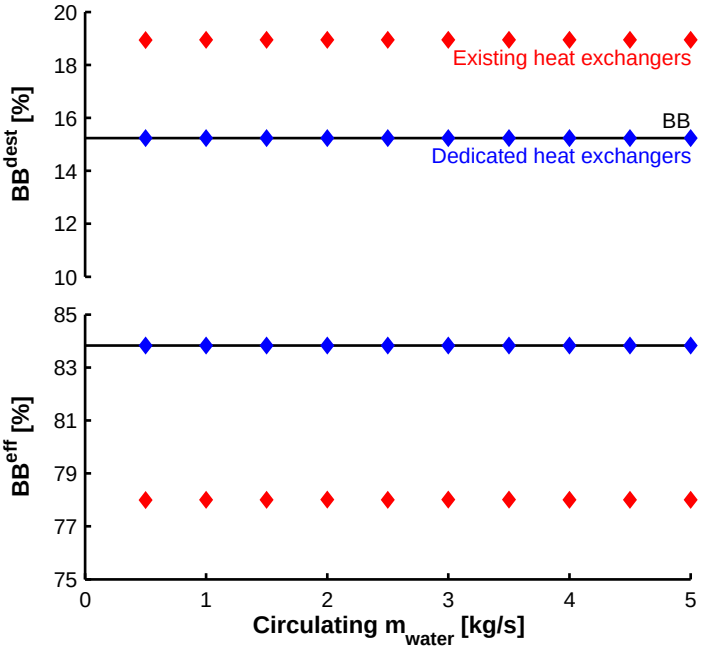

Figure 5.18: Exergy efficiency and destruction of the heat exchanger network, using dedicated heat exchangers and using the existing ones, compared to the black box efficiency and destruction.

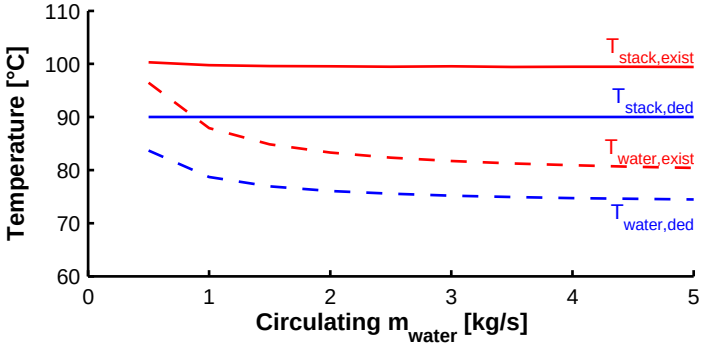

Figure 5.19: A limited heat exchange surface will lower the stack temperature and increase the temperature of the injected water. The amount of circulating water has no effect on the stack temperature, but will determine the injected water temperature.

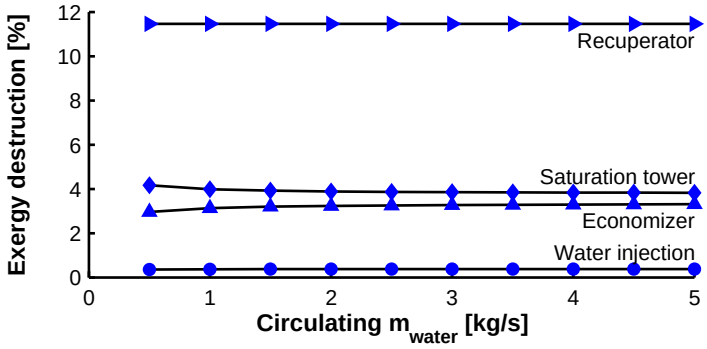

Figure 5.20: The recuperator is responsible for the largest exergy destruction in the heat exchanger network. Circulating water mass flow rate has only a minor effect on the exergy destruction in the saturation tower and the economizer.

The recuperator is responsible for the largest exergy destruction in the heat exchanger network (Figure 5.20). The exergy destruction inside the recuperator remains constant, since the same amount of water is evaporated in the compressed air. The exergy destruction in the economizer is lower at lower water mass flow rates, because of the higher outlet water temperature (Figure 5.19). The mixing exergy destruction is higher at lower mass flow rates, even though the water temperature is higher and matches better the air temperature. However in this case, both water and air will cool down, due to evaporation, so the mixing temperature is lower than water temperature (79 °C), so at lower flow rates, the temperature difference between in- and outlet will be higher, resulting in a higher exergy destruction. Both phenomena counteract, resulting in a network exergy destruction independent of the water flow rate.

Although the circulating water mass flow rate has no direct impact on the global performance of the mHAT, it has a huge impact on the final size of the saturation tower and the losses to the auxiliaries. The water mass flow rate will determine the total volume of the saturation tower required to saturate the compressed air. Another parameter to take into account is the pump power, necessary to increase the water pressure to compensate the head losses in the water circuit. The higher the water flow rate, the more produced electric power is needed for the auxiliaries, the lower the electric efficiency will be. The necessary pump power to compensate the head losses is rather low with maximal 0.11 kW_e at a circulating water mass flow rate

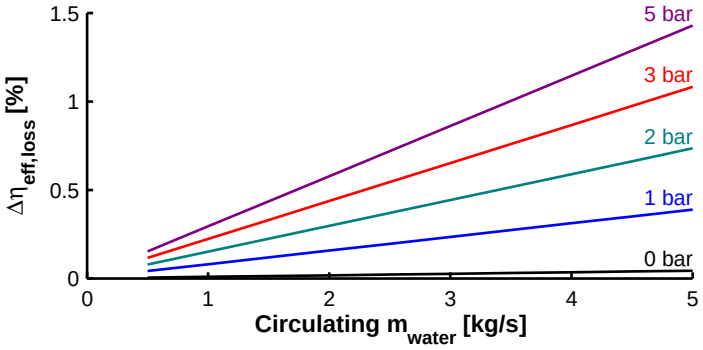

Figure 5.21: Final selection of the amount of circulating water and the injection nozzles has a huge impact on electric efficiency. The friction losses in the water network should remain low to limit the loss in efficiency to the auxiliaries.

of 5 kg/s. This pump power results in a minimal effect on global efficiency with an absolute loss in efficiency of 0.04 % (Figure 5.21). Commonly, the water is introduced in the saturation tower by means of injection nozzles. For these nozzles, a certain pressure difference is necessary to obtain a minimal sauter mean droplet diameter. Increasing the injection pressure (up to 5 bar) and the circulating mass flow rate (maximal 5 kg/s) has a huge effect on cycle efficiency (absolute loss in efficiency of 1.5 % to the auxiliary pump, Figure 5.20). For the final design of the saturation tower, a trade-off between size and pumping power needs to be found.

The non-idealities in combination with the modus operandi of the T100 mGT have a negative effect on the exergy efficiency of and destruction in the heat exchanger network (Figure 5.22). Due to the limitations of the heat exchangers (limited heat exchange area), the temperature difference between the inlet of the combustion chamber and the TOT will increase with increasing stack temperature. Using the existing heat exchangers (Case Ex) instead of newly designed dedicated ones (Case Ded) the exergy efficiency will decrease. When taking into account the modus operandi of the control system – meaning keeping TOT constant (Case TOT) instead of TIT (Case TIT) – exergy efficiency will drop even more. Lowering TOT results in a lower exergetic efficiency.

The total electric efficiency of the mGT cycle is negatively affected by the decreasing exergetic efficiency and increasing exergy destruction resulting

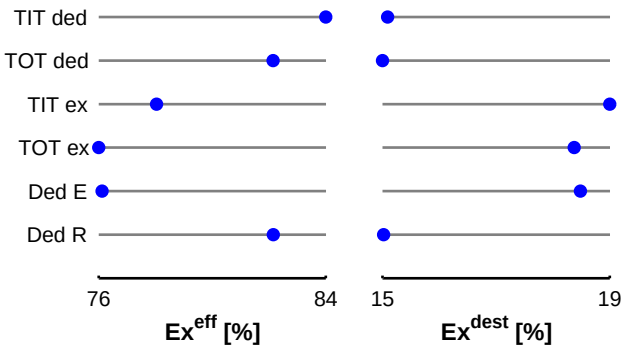

Figure 5.22: The non-idealities – using the existing heat exchangers (Case Ex) instead of newly designed dedicated ones (Case Ded) – in combination with the modus operandi of the T100 mGT – keeping TOT constant (case TOT) instead of TIT (Case TIT – have a negative effect on the exergy efficiency of and destruction in the heat exchanger network. Redesigning only the recuperator (Case Ded R) increases the performance significantly, while only changing the economizer has a minor effect (Case Ded E).

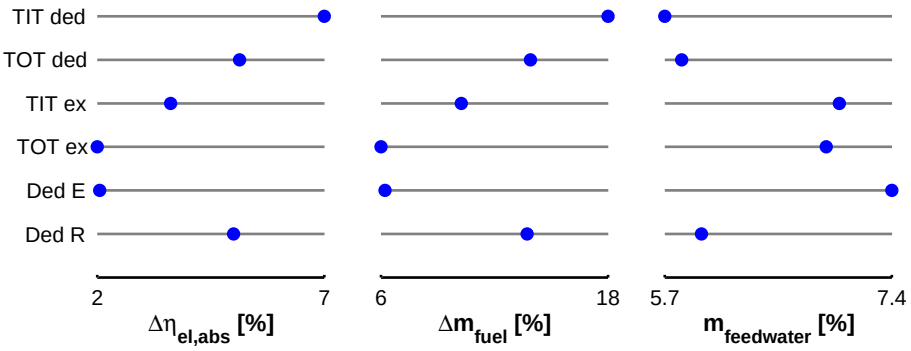

Figure 5.23: Higher exergy efficiencies results in higher electric efficiency increases and fuel savings while less water needs to be introduced in the cycle.

from non-idealities and the mGT operating mode (Figure 5.23). Since the water flow rate has no effect on global energy and exergy efficiency (Figure 5.18), Figure 5.22 and 5.23 only show the results of simulations performed using 2.5 kg/s circulating water. The difference between the exergy efficiency and destruction at constant TIT or TOT are limited, however the energetic efficiency is more influenced by keeping TOT constant instead of TIT, because a constant TOT results in a lower TIT and higher exergy destruction in the combustion chamber, which results in a lower global electric efficiency. The final simulation results of the T100 based mHAT, using the existing heat exchanger and control system, show that the electric efficiency increase is limited to 2 % absolute (Figure 5.23). The low efficiency gain is in line with the findings of Nikpey et al. and Zhang and Xiao. In their papers, Zhang and Xiao predicted a 3.7 % efficiency increase when converting a mGT into a HAT cycle [36], while Nikpey et al. predicted a 1.7 % absolute efficiency increase when converting a Turbec T100 into a HAT cycle [40]. Finally, Zhang and Xiao indicated that the absence of intercoolers and the limited amount of available waste exergy not fully display the advantages of the HAT cycle [36].

A higher electric efficiency of the mHAT can be reached by adapting the control system of the mGT. As mentioned before, fuel flow rate is controlled to keep TIT below a certain limit (950 °C). Exceeding this limit is dangerous for the turbine inlet. Measuring TIT is not possible due to technical limitations; instead TOT is measured and controlled. By using the fixed lookup tables, TIT is estimated out of this TOT measurement. During

steam or water injection, these lookup tables however are no longer valid, since the heat capacity of the medium has increased, due to the addition of water. Using the measured TOT in combination with the original Turbec lookup tables will result in a TIT underestimation. This means there is still margin to increase TIT without damaging the turbine inlet. This lower TIT has a direct negative impact on turbine efficiency. Adapting the TOT controller to a TIT control mechanism in Aspen® is rather simple, since TIT values are directly available in simulations, however adapting the control system of the T100 would require an additional measurement of the water content in the flue gases. In order to reach optimal steam injection, the following adapted control mechanism for the T100 mGT is proposed. An additional sensor to measure water content in the flue gases gives additional information to the control system about the composition of the flue gases. Based upon this composition, in combination with the measurement of TOT, using a new composition dependent lookup table, TIT can be estimated. This allows a more precise TIT control and allows the T100 mGT to fully perform at its maximal possible TIT, independent of possible steam/water injection. Increasing TOT can however have a negative effect on the recuperator. Like the turbine, the mGT recuperator has a maximum temperature, which should not be exceeded [268]. Before adapting the control system, it is very important to check the maximum material temperature of the recuperator. Exceeding this temperature will require the development of a new recuperator, using more advanced/expensive materials, like alumina-forming austenitic steels. Alumina-forming austenitic steels show good creep and oxidation results at 600 to 800 °C [268] and are a candidate for next generation recuperators.

As a small case study, the influence of redesigning only one of the two existing heat exchangers has been examined (Figure 5.22 and 5.23). Redesigning the recuperator can increase the performance of the heat exchanger network significantly (Case Ded R), while changing the economizer only has a minor effect on global performance of the T100 mGT (Case Ded E). Even with only an adapted recuperator, a stack temperature of 88 °C can be reached. The lower stack temperature explains the very high exergy efficiency and low exergy destruction (as low as the black box) from Figure 5.22. The final energetic efficiency is however still lower than the black box efficiency (Figure 5.23), due to the higher exergy destruction in the combustion chamber when operating at constant TOT instead of constant TIT.

The minimal pinch for the heat exchange system in the mHAT is 22.6 °C at water heater (Figure 5.24). For the construction of these composite curves,

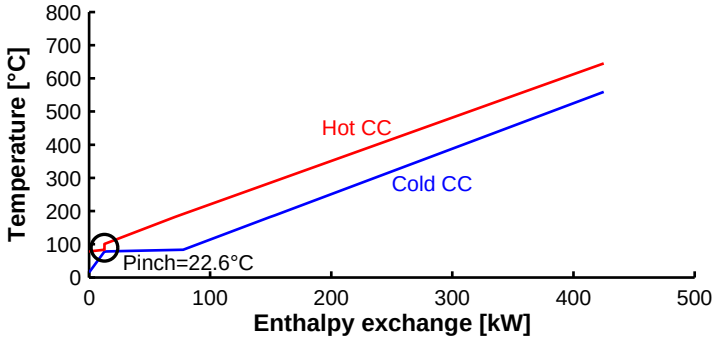

Figure 5.24: Composite curves of the final layout of the heat exchanger network.

the saturation tower has been excluded, since it is not possible to split the different streams into hot and cold streams. Both, water and air inlet stream cool down inside the saturation tower, because a small amount of the water will evaporate and extract sensible heat from both the water and air stream. The removal of the saturation tower from the composite curves results into a jump in the hot curve. At 12 kW_{th}, the pinch amounts only 1.1 °C, which does not cause any problems, because it is the result of the mixing process between the hot water, coming back from the saturation tower and the cold feedwater. The injected mass flow rate of feedwater is very low compared to the recirculating water flow rate, so equilibrium should be reach without problems.

Finally, Table 5.4 gives an overview of the thermodynamic conditions of the mHAT design of the Turbec T100 mGT using the existing economizer and recuperator. In addition, simulations are performed using natural gas, similar to the natural gas available in the lab of the VUB. At nominal electric power production and full humidification, the total water fraction in the combustion air is limited to 5 wt%. This is again far below the values of 10 wt% and 33 wt% of Chen et al. and Hermann et al. [242, 245] and in the same range as the steam fraction during steam injection experiments (subsection 4.1.3), so no problems with combustion stability could be expected. In addition, the surge margin is reduced to 20.8 % (Table 5.4), which is similar to the surge margin reduction in the steam injection experiments (subsection 4.1.2). This surge margin should be sufficient to operate the T100 mGT safely without risking any possible surge.

Table 5.4: Thermodynamic conditions of the T100 mGT at each stage of the dry mGT and wet mHAT cycle using the Aspen® simulation model.

	Dry mode[1]	Wet mode[2]
Compressor		
T_{in}	15 °C	15 °C
p_{in}	1.013 bar	1.013 bar
T_{out}	195.7 °C	177.6 °C
p_{out}	4.194 bar	3.718 bar
$\dot{m}_{\text{comp}}$	0.704 kg/s	0.605 kg/s
P_{comp}	129.6 kW	100.1 kW
SM	22.1 %	20.8 %
Saturation tower		
$T_{\text{in,air}}$	–	177.6 °C
$T_{\text{in,water}}$	–	82.4 °C
$T_{\text{out,air/water}}$	–	77.8 °C [3]
$p_{\text{in,air}}$	–	3.718 bar
$p_{\text{in,water}}$	–	4.218 bar
$p_{\text{out,air/water}}$	–	3.700 bar[3]
$\dot{m}_{\text{in,air}}$	–	0.605 kg/s
$\dot{m}_{\text{in,water}}$	–	2.550 kg/s
$\dot{m}_{\text{water,evap}}$	–	50.0 g/s
Relative Humidity	–	101.5 %
Recuperator		
$T_{\text{in,cold}}$	195.7 °C	77.8 °C
$T_{\text{in,hot}}$	645 °C	645 °C
$T_{\text{out,cold}}$	574.9 °C	559.6 °C
$T_{\text{out,hot}}$	283.3 °C	186.2 °C
$\dot{Q}_{\text{comp}}$	286.5 kW	352.1 kW
Combustion chamber		
fuel	Natural gas	Natural gas
LHV	40.19 MJ/kg	40.19 MJ/kg
T_{out}	917.1 °C	886.6 °C

[1] *Dry mode* corresponds to the normal CHP mode of the mGT, running at nominal electric power.

[2] *Wet mode* corresponds to the mHAT case. The thermodynamic conditions given in the table correspond to the maximal water injection possible (water fraction of 7 %).

[3] Both circulating water and air stream are in thermal equilibrium after leaving the saturation tower.

Table 5.4: (continued)

	Dry mode	Wet mode
p_{out}	3.775 bar	3.409 bar
$\dot{m}_{\text{fuel}}$	7.69 g/s	7.21 g/s
Turbine		
T_{out}	645 °C	645 °C
p_{out}	1.05 bar	1.05 bar
$\dot{m}_{\text{turb}}$	0.711 kg/s	0.651 kg/s
P_{turb}	229.6 kW	200.1 kW
Economizer		
$T_{\text{in,air}}$	283.3 °C	186.2 °C
$T_{\text{in,water}}$	50.0 °C	76.6 °C
$T_{\text{out,air}}$	102.9 °C	100.6 °C
$T_{\text{out,water}}$	61.2 °C	82.4 °C
$\dot{m}_{\text{water}}$	2.5 kg/s	2.550 kg/s
$\dot{Q}_{\text{comp}}$	134.8 kW	61.9 kW
Global		
P_{el}	100.0 kW_{e}	100.0 kW_{e}
η_{el}	32.35 %	34.51 %
N	67 312 rpm	63 526 rpm
T_{stack}	102.9 °C	100.6 °C

5.2.3 Conclusion of the humidified Turbec T100 mGT development

In this section, the black box simulations of the previous section were extended. The effect of changing the boundary conditions on the mGT performance was searched, rather than aiming at optimal waste heat recovery. In a second part, the Turbec T100 based mHAT cycle is developed and simulated. The effect of different non-idealities of the heat exchanger network and the modus operandi of the T100 mGT on the final performance is studied.

- The stack temperature and hot pinch, imposed as boundary conditions on the heat exchange network, have a direct influence on the exergy destruction in and efficiency of the black box heat exchanger network and also on the electric efficiency increase.

- Black box off-design simulations showed that exergy destruction and efficiency of the heat exchanger network are only affected by the applied boundary conditions. On top of that, for a fixed set of boundary conditions, the efficiency of the network does not depend on the circulating water mass flow rate. The circulating water mass flow rate will however determine the losses to the auxiliaries and the size of the final saturation tower.

- A final series of simulations, taking into account the operation of the control system of the T100 mGT and based on the existing heat exchangers installed in the T100, showed that the maximal achievable final exergy and energy efficiency is lower than the black box simulations indicated, with only 2 % absolute increase in efficiency, when 2.5 kg/s of water is circulated.

5.3 Saturation tower development

The saturation tower for HAT or mHAT applications has been the subject of many studies performed by different researchers [85, 104, 269–275]. Enick et al. developed an algorithm for high-pressure gas humidification by dividing the column in different sections [269]. Lindquist et al. developed a physical model of the saturation tower and validated this model experimentally on the saturation tower constructed for the EvGT project in Lund [270]. Ågren and Westermark investigated the possibility of a part-flow EvGT [85]. Parente et al. developed a code to simulate the evaporation in the saturation tower, using the hypothesis of a semi-ideal gas mixture. Simulation results were validated against experimental results of the EvGT in Lund [271]. Pedemonte et al. and Traverso investigated both experimentally the saturation tower performance on a specially designed test rig [272, 274]. Afterwards Pedemonte et al. used their results to develop empirical correlations to predict the humidification process in a pressurized saturation tower with packing [273]. More recently, Hui et al. designed and tested experimentally a new type of packing saturation tower [276]. Finally, Araki et al. designed, simulated and validated experimentally the saturation tower of the 4 MW-class AHAT power plant built in Japan [104, 275].

All of the previously discussed saturation towers use packing material to increase the contact area between the compressed air and the water, which will speed up the humidification process. Packing material however induces

a pressure drop (approximate 400 Pa/m of packing [34]). Pressure losses in mGT have a large negative effect on mGT performance [48, 136]. For this reason, a new type of saturation tower has been developed using two-phase flow theory. Instead of increasing the contact area by using packing material, nozzles were used. The idea is that dividing the water in a large amount of small droplets will result in a large contact area between the liquid and the compressed air, which will provide the necessary surface for heat and mass transfer.

The final goal of this section is to design the saturation tower for the mHAT version of the Turbec T100 mGT. During the design process, the main parameters of interest are saturation tower size and pressure drop. It is of great importance that both are lower than in a classical saturation tower with packing material. The secondary goal was to study the sensitivity of the humidification process to possible variations of the saturation tower inlet conditions. Eventually, a saturation tower will be constructed based upon the obtained recommendations.

In the first part of this section, the modelling of the internal two-phase flow of the spray saturation tower is discussed. For every injection direction of the droplets, the considered assumptions are discussed. In the second part of this section, the results of the different two-phase flow simulations for the different injection strategies are presented and discussed. Sensitivity analysis is performed to indicate the crucial parameters. In the final part of the section, a conservative design for the saturation tower is proposed based on results of the sensitivity analysis.

5.3.1 Modelling of the saturation tower

In the literature, some experimental studies exist on compressed air humidification using water spray [277–279]. Wang et al. performed experiments on a counter-flow spray saturation tower for the HAT cycle [277, 278], while Xu et al. studied the air humidification by a water spray at elevated pressure [279]. A generic method to develop a spray saturation tower for mHAT applications however does not exist. Therefore a literature survey was conducted to find a model suitable for spray saturation tower modelling and development.

The saturation tower can be seen as a cooling tower. Although the function of a cooling tower is different, the thermodynamics, driving forces (low relative

humidity) and operating principle are the same. In literature, several studies exist on the modelling of cooling towers. Below is a non-limited summary of existing simulation models.

- Kachhwaha et al. modelled horizontal parallel and counter-flow air evaporative cooling [280, 281].
- Kloppers and Kröger investigated the heat and mass transfer of counter-flow wet cooling towers, using the Poppe, Merkel en e-NTU method [282, 283]. In addition, they studied the effect of the Lewis number (Le) on the performance prediction [284].
- Heidarinejad et al. studied numerically the counter-flow wet cooling towers by dividing the tower in three zones: spray, packing and rain zone [285]. Khan et al. used a similar approach to calculate the performance of counter-flow wet cooling towers [286], while Terblanche et al. studied the droplet distribution below the tower fill [287].
- Fisenko et al. studied the evaporative cooling in a natural draft cooling tower [288], while Petruchik et al. focused on simulating the cooling of water droplets and film flow in these natural draft wet cooling towers [289].
- Gan and Riffat modelled the closed wet cooling towers [290].
- Mohiuddin and Kant proposed a systematic method to design wet cooling towers [291, 292].
- Fossa and Niksiar and Rahimi both modelled co-current gas spray cooling [293, 294], while Makkinejad calculated the temperature profiles for co- and counter current spray towers [295];
- Fisenko et al. modelled a mechanical draft counter-current cooling tower [296];
- Fisenko and Brin made a model for a cross-flow cooling tower [297].
- Niksiar and Rahimi and Saravanan et al. both analysed the energy and exergy of spray cooling, indicating that the exergy of the water is not completely absorbed by the gas and a remarkable portion of exergy is destroyed [294, 298].

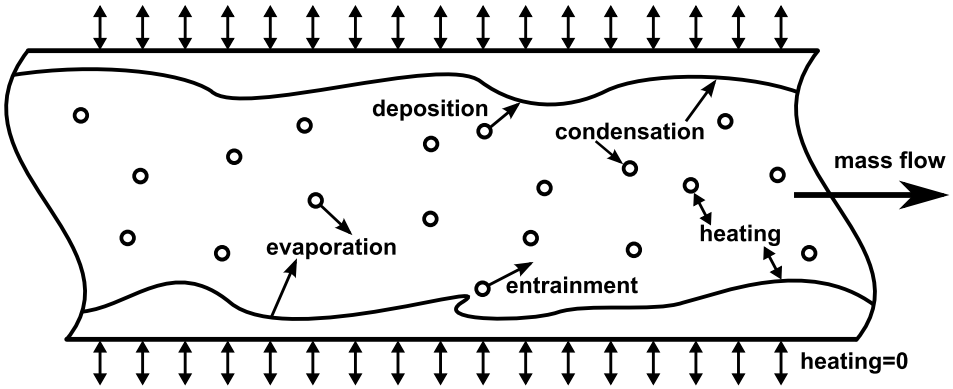

Figure 5.25: Annular dispersed two-phase flow phenomena covering heat exchange and mass transfer between the different phases; through evaporation, condensation, entrainment and deposition of droplets.

In addition to these cooling tower models, Bram presented in his thesis a review on more fundamental, annular two-phase flow models [299]. Nevertheless, none of these models can completely simulate the humidification process in the considered spray tower. Therefore, I developed my own model based on existing correlations for specific phenomena, like droplet deposition, film entrainment and heat and mass transfers [299].

To model the saturation tower, a 1D Non-Adiabatic Annular Two-Phase Model has been modified [299]. Rather than fully calculating the behaviour of the droplets by means of 3D-computational fluid dynamics, a simplified 1D-model is used to predict the optimal size of the saturation tower for full saturation of the hot compressed air. The model was constructed in the scope of the REVAP® project [92]. The goal of this project was the development of a humidified GT without saturation tower.

The model distinguishes three different components in the flow: gas core, liquid film and dispersed droplets. Each component is seen as a separated phase, which has a specific mass, momentum and energy. Different types of interaction exist between the different components of the flow (Figure 5.25). In this case, the saturation tower is considered adiabatic and perfectly insulated from the environment, so the heat exchange with the surrounding can be neglected.

In the case where nozzles are used to generate the droplets, there will be no uniform droplet diameter. Each different type of nozzle produces a specific distribution of droplets. A possible way to describe this, is using a discrete distribution of droplets with several representative diameters. All categories of droplet are thus seen as separated fractions, with own conservation equations. This would however make the model too complex. The final goal is to give a conservative design of the saturation tower and not to describe the exact internal behaviour of the droplets. Another possible solution is using the Sauter mean diameter d_s of the droplets. This diameter has the same ratio of surface to mass as the total droplet population. Mathematically:

$$d_s = \frac{\sum_{j=1}^{k} n_j d_j^3}{\sum_{j=1}^{k} n_j d_j^2}, \tag{5.6}$$

where n is equal to the amount of droplets with diameter d and k is equal to the total number of droplets categories.

For all simulations in this section, the same boundary conditions were used (Table 5.5). The boundary conditions were taken from the simulations of previous section (Table 5.4). The amount of evaporated water is rather low compared to the amount of injected water (2 %). The large amount of water is however necessary to provide the contact area for evaporation. This large amount of circulating water has an influence on the mHAT global performance. As indicated in the previous section, the loss in efficiency, resulting from the auxiliary pump power for water injection, depends on the total amount of circulating water, but also on the used injection pressure. For a total injected amount of water of 2.5 kg/s at 0.5 bar pressure difference, losses are equal to 0.1 % absolute efficiency decrease, which is low compared to the 2 % absolute efficiency increase due to the water injection.

The next subsections present the models made to describe the three possible injection strategies: co-, counter- and cross-current. In the co-current injection, the droplets are injected in the direction of the moving gas flow. In counter-current injection, the droplets are injected in the opposite direction of the moving gas core. In the cross-flow, the droplets are injected perpendicular to the moving gas flow.

Table 5.5: Inlet conditions of the saturation tower determined by the Aspen® simulations (Table 5.4).

	Air		**Water**	
	in	out	in	out
$\dot{m}$	0.605	0.655	2.550	2.500
T	177	78	82	78
p	3.7	$p_{\text{air}}^{\text{out}}$ [1]	$p_{\text{water}}^{\text{in}}$ [2]	$p_{\text{water}}^{\text{in}} = p_{\text{air}}^{\text{out}}$ [3]

[1]The pressure of the outgoing air depends on the total loss of pressure, which will be determined when designing the saturation tower.

[2]The pressure of the incoming water depends on the used nozzle to introduce the water.

[3]The pressure of the outgoing water is equal to the pressure of the outgoing air.

Co-current model

Mass conservation applies over each different cross section for each component, so one can write:

$$\frac{\mathrm{d}\dot{m}_i}{\mathrm{d}x} = \dot{m}_{\mathrm{s},i} - \dot{m}_{\mathrm{loss},i}, \tag{5.7}$$

where i indicates the different component (gas, film or droplets). The source term $\dot{m}_{\mathrm{s},i}$ combines all possible sources to the specific phase. For the droplets, for example, this combines the amount of water condensation from the gas core back to the droplets together with the amount of entrained droplets in the considered section of the saturation tower. The loss term $\dot{m}_{\mathrm{loss},i}$ combines all possible mass losses of the considered phase in the considered section. For the droplets, $\dot{m}_{\mathrm{loss},i}$ is equal to the sum of the amount of water that evaporates from the droplets into the gas core and the amount of droplets that are deposited in the film.

Conservation of momentum gives

$$\frac{\mathrm{d}\left(\dot{m}_i C_i\right)}{\mathrm{d}x} + A_i \frac{\mathrm{d}p}{\mathrm{d}x} = F'_i + \dot{m}_{\mathrm{s},i} C_i - \dot{m}_{\mathrm{loss},i} C_i, \tag{5.8}$$

where F'_i is the combined force, like friction between the different components, applied on the different components. A_i is the part of the cross section occupied by different flow components. Since only one dimension is considered, the effect of gravity is only taken into account when a vertical

flow is considered. Results indicated that the fraction of gravity in the momentum change is generally smaller than 12 % during the evaporation process.

Finally, the energy equations are

$$\frac{\mathrm{d}\left(\dot{m}_i h_i\right)}{\mathrm{d}x} = \dot{m}_{\mathrm{s},i} h_i - \dot{m}_{\mathrm{loss},i} h_i + \dot{Q}'_i + F'_i C_i, \tag{5.9}$$

where $\dot{Q}'_i$ is the heat exchange between the different phases.

Equation 5.7, (5.8) and (5.9) result into a set of 9 Ordinary Differential Equations (ODEs) with 10 unknown parameters ($\dot{m}_i$, C_i, h_i and p). By differentiating the following equations, the system of ODEs can be closed [299]:

- the ideal gas law;
- the relations between mass flow rate and velocity;
- the sum of all flow sections must be equal to the saturation tower cross section;
- the change in molecular weight of the gas core;
- the enthalpy-temperature relation of the gas core;
- the evolution of the droplet mass.

In the case of co-current injection of the droplets, the ODEs can be solved directly, using a variable step size ODE-solver, `ode15s`, implemented in Matlab [300]. The stability in this application of the solver was tested in the past by Bram [299].

In the simulations, all different injection positions (Figure 5.26) were investigated. This means that depending on the direction of movement of the gas and droplets, gravity is excluded (Figure 5.26(b)) from Equation 5.8 and (5.9) or included (Figure 5.26, (a) and (c)).

Counter-current model

The equations described in the previous paragraph (Equation 5.7 to 5.9) were also used for counter-current simulations. The conservation equations

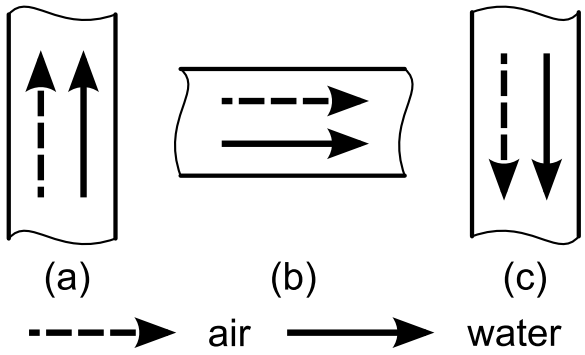

Figure 5.26: I evaluated these layouts of a co-current saturation tower: upwards (a), horizontal (b) and downwards (c) injection, to investigate the importance of gravity.

will not change, only the direction of the velocity and forces has changed. Different effects inherent to annular dispersed flow, like droplet entrainment and deposition will however change. Different empirical formulas need to be found in literature. Little studies on this subject however exist. Therefore in the counter-current model, the interaction with the film is neglected. The fraction of heat and mass exchange between film and gas core is very small compared to the exchange between droplets and gas. For typical values of the inlet parameters, the mass transfer from the droplets to the gas is four order of magnitude bigger than the mass transfer from the film to the gas. Even though exchange with the film is neglected, the film flow rate is still considered as a loss of water to preserve mass conservation.

Unlike in the co-current case, in the counter-current case, the inlet conditions of the water are defined on the opposite side of the saturation tower than the air inlet conditions (Figure 5.27). This has some implications for solving the problem. Here the ODEs need to be solved in an iterative way. The major difficulty in this case is the tower length. In the co-current case, the set of ODEs can be solved over a long tower. Results of relative humidity will indicate the point of full saturation of the compressed air. This point indicates the minimal necessary saturation tower length. Making the saturation tower longer will have no effect on the outlet conditions of the stream, since thermodynamic equilibrium is achieved. In the counter-current case, a different length will result in a different final solution, meaning different outlet conditions. An additional problem is that not every combination of parameters will lead to a solution. The initial velocity

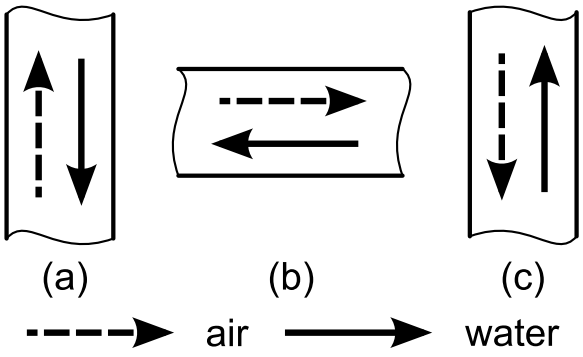

Figure 5.27: Evaluated layouts of a counter-current saturation tower, based on gas flow direction: upwards (a), horizontal gas flow (b) and downwards (c).

of the droplets needs to be higher than in the co-current case, since the droplets have to travel against the air flow and are exposed to higher friction forces. Especially the small droplets will encounter difficulties in reaching the bottom of the saturation tower and will most likely turn, which changes the counter-flow into a co-current flow. Higher injection velocity requires however higher pressure difference over the nozzle.

Cross-current model

For simulating the cross-current, at least 2D-simulations are required, since the droplets will move in a direction perpendicular to the gas flow. However, by applying some conservative simplifications to the model, a 1D-model can be used to simulate cross-current:

- the heat and mass transfer with the film is neglected and the film flow rate is considered as a loss of water;
- the droplet temperature, as a conservative choice, is taken equal to the temperature of the outgoing water (78 °C). Calculating the temperature profile of the droplets is not possible since 1D-simulations are performed, so the temperature is kept constant along the droplet trajectory. Thermodynamic simulations of the saturation tower have shown that the water temperature does not change much (4 °C from Table 5.5);

- droplets are homogeneous distributed over the length and width of the saturation tower. The total amount of droplets per cross section depends on the height and the initial velocity. Based upon these parameters, the residence time can be calculated. Thus in the cross flow case, the tower length also needs to be predefined, as in the counter-current model;

- droplet diameters are also considered constant along the droplet trajectory. Only 2 % of the total water flow rate will evaporate (Table 5.5) along the full length of the tower. The droplet diameter is mostly reduced within the first 15% of the saturation tower tower length, where most of the mass transfer occurs (Figure 5.33). This reduction in droplet diameter is still rather limited;

- droplets are considered to have zero velocity in the compressed air flow direction. Correct relative velocity (vector sum of droplet and gas velocity) is however used to calculate the heat and mass transfer coefficients.

The assumption of zero velocity of the droplets in the compressed air flow direction is justified by simulating the droplets trajectories. The possible cross-current injection schemes are indicated in Figure 5.28. Figure 5.29 shows the different droplet trajectories in the saturation tower, using the different injection schemes from Figure 5.28. Simulations are conducted using the same inlet conditions as used in cross-current saturation tower simulations (section 5.3.2) and neglecting the heat and mass transfer. The x-axis is defined as the gas flow direction, while the y-axis is the injection direction. In case (b), where the gas is moving downward and droplets are injected horizontally, droplets do not reach the other side of the saturation tower, but are dragged along the tower, which results thus in a co-current flow. In this case, the hypothesis of zero velocity in the compressed air flow direction is no longer valid. Case (b) was not considered during simulation. In case (d), droplets are just falling back down. This results in coalescence between the upgoing and falling droplets, resulting in larger droplets and thus less contact area. In addition, there is no contact between the droplets and the compressed air in the upper section of the saturation tower. This will result in not fully saturated air. This case is thus also not considered in the simulations. Finally, for cases (a) and (c), droplets will move along the cross section in the direction of the gas flow. The displacement of droplets (which is the movement of the droplets in the flow direction of the

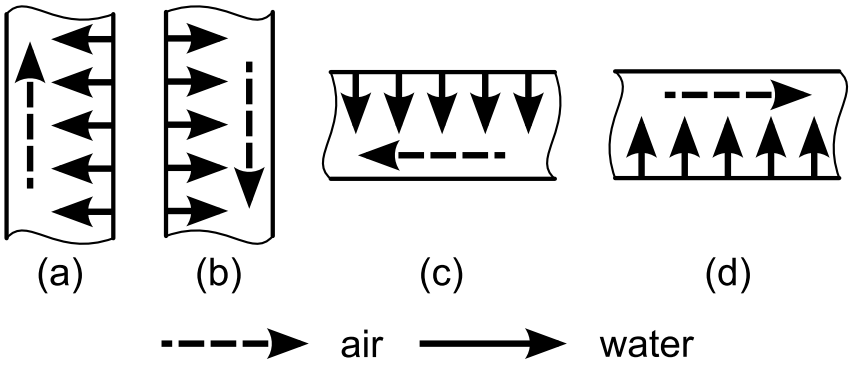

Figure 5.28: Evaluated layouts of a cross-current saturation tower, based on gas flow direction: upwards (a), downwards (b), horizontal – droplets injected downwards (c) and horizontal – droplets injected upwards (d).

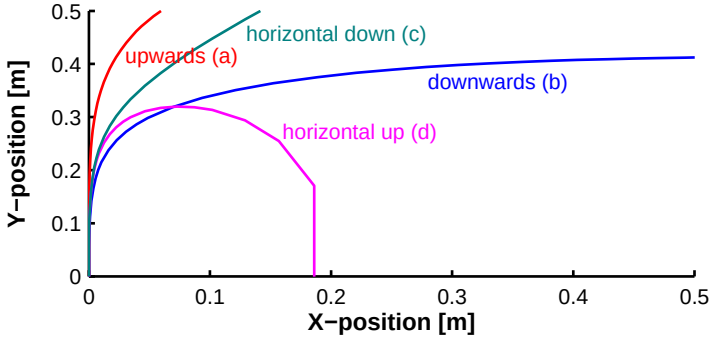

Figure 5.29: Droplet flow trajectory simulations indicating droplet displacements in the x-direction (compressed air flow direction) are limited (respectively 0.06 m and 0.14 m) for injection scheme (a) and (c) for a cross-current saturation tower, which confirms the hypothesis of droplets standing still.

compressed air) is however limited (0.06 m in case (a) and 0.14 m in case (c)) compared to the total length of the tower (0.50 m). The limited movement justifies the assumption of zero droplet velocity in the compressed air flow direction. In addition, there will be also no droplet coalescence. All droplets follow the same trajectory, since the gas velocity does not change much as shown in Figure 5.33, resulting in constant friction forces on the droplets along the saturation tower.

5.3.2 Results of two-phase flow simulations

In this subsection, the results of the simulations of the saturation tower using the different injection principles (co-, counter- and cross-current) are presented. The focus is on the evaporation process, so only the main thermodynamic parameters are discussed.

Co-current

Co-current spray saturation tower is simulated using inlet conditions from Table 5.5 (Figure 5.30). Further inlet conditions, using common nozzles and saturation tower size, are:

- $d_{\text{droplet}} = 0.1\,\text{mm}$;
- $D_{\text{sat}} = 0.5\,\text{m}$;
- $C_{\text{droplet}} = 20\,\text{m/s}$.

In the co-current case, a cylindrical saturation tower is assumed, since the circular cross section matches best the nozzle spray cone. In this case, to exclude the effect of gravity on the performance, a horizontal saturation tower, with horizontal gas and droplet flow is assumed (case (b) from Figure 5.26).

Most of the heat and mass transfer happens just after the injection point (Figure 5.30). At this point, the driving force – low relative humidity, thus low vapour pressure in the gas – is very high. The higher the relative humidity becomes, the more the mass transfer process is slowed down. Due to this high evaporation rate, droplet, film and gas temperature all decrease, because all energy is necessary to evaporate the water. Final equilibrium temperature for droplets, film and gas is below their initial temperature.

The droplets continuously slow down, due to the friction with the gas (Figure 5.30). In the first 5 cm of the saturation tower, the gas will speed up due to the friction with the droplets and the evaporation (increasing gas volume). After this 5 cm, the friction with the wall and film starts to become more important, resulting in a decreasing gas velocity. Film velocity remains almost constant and very low.

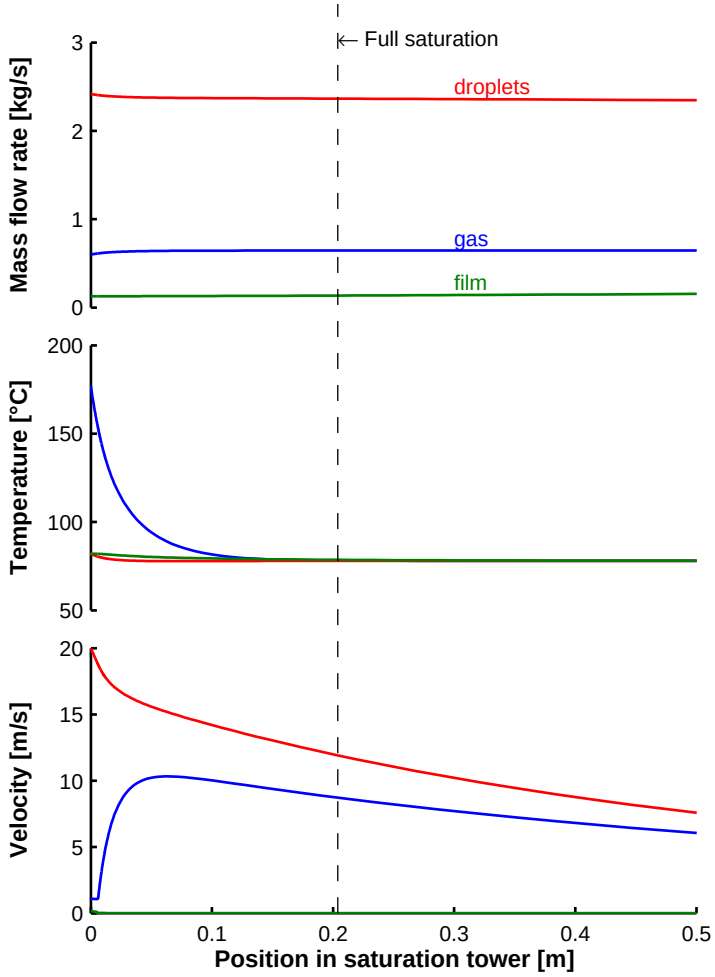

Figure 5.30: Simulation results of a co-current saturation tower, indicating tower length required for full saturation is 0.20 m.

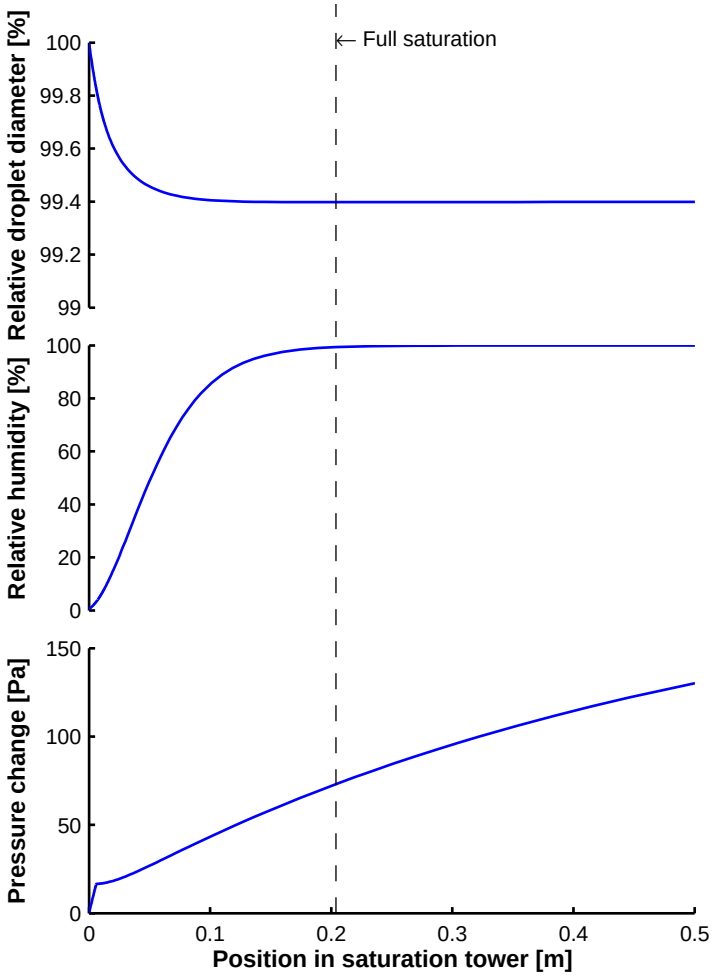

Figure 5.30: (continued)

The droplet diameter does not vary significantly during the evaporation process (Figure 5.30). The small droplet diameter variation (max. 0.6 %) is a result of the large amount of injected water. Only 2 % or 0.045 kg of the total amount of injected water will evaporate. After 0.20 m, the compressed air reaches full saturation (100 % relative humidity, see Figure 5.30). Once this point is reached, the gas mass flow rate remains constant, but the droplet mass flow rate is continuously decreasing, due to the deposition of droplets in the film.

Pressure increases during the evaporation process due to deceleration of the droplets, as indicated on Figure 5.30. The behaviour of the pressure is rather complex and needs some additional study. For this reason, the saturation tower has been elongated (5 m total length) to better show the effect of water injection on the pressure.

The pressure is a complex parameter, whose behaviour is influenced by several effects that counteract. On the one hand, pressure will increase due to the evaporation of the water. On the other hand, pressure will decrease due to the friction between the gas core and the wall (or film) and the lower temperature. Finally, there is also the effect of the presence of the droplets. Pressure simulations show the effect of the droplets injection and the evaporation process on velocity and pressure (Figure 5.31). In case $C_{\text{droplet,init}} > C_{\text{gas,init}}$, pressure will first increase. Finally, after the pressure has reached a maximum, it starts to decrease. In this phase, droplets, film and gas are in thermal equilibrium (same temperature and relative humidity of 100 %, so that there is no more heat and mass transfer). There is no more friction between the droplets and the gas core since $C_{\text{droplet}} = C_{\text{gas}}$. The only remaining effect is the friction between the gas core and the film/wall, which will decrease the pressure. Since the velocity difference between gas core and film is low, pressure losses are limited in this region (0.06 Pa/m). In the case where $C_{\text{droplet,init}} < C_{\text{gas,init}}$, pressure decreases first largely, until the equilibrium is reached. In the second phase, as mentioned before, pressure losses are limited, explaining the change in pressure loss gradient.

Counter-Current

Like in the co-current case, the inlet conditions of Table 5.5 are used to simulate the counter-current saturation tower (Figure 5.32). Further inlet conditions are:

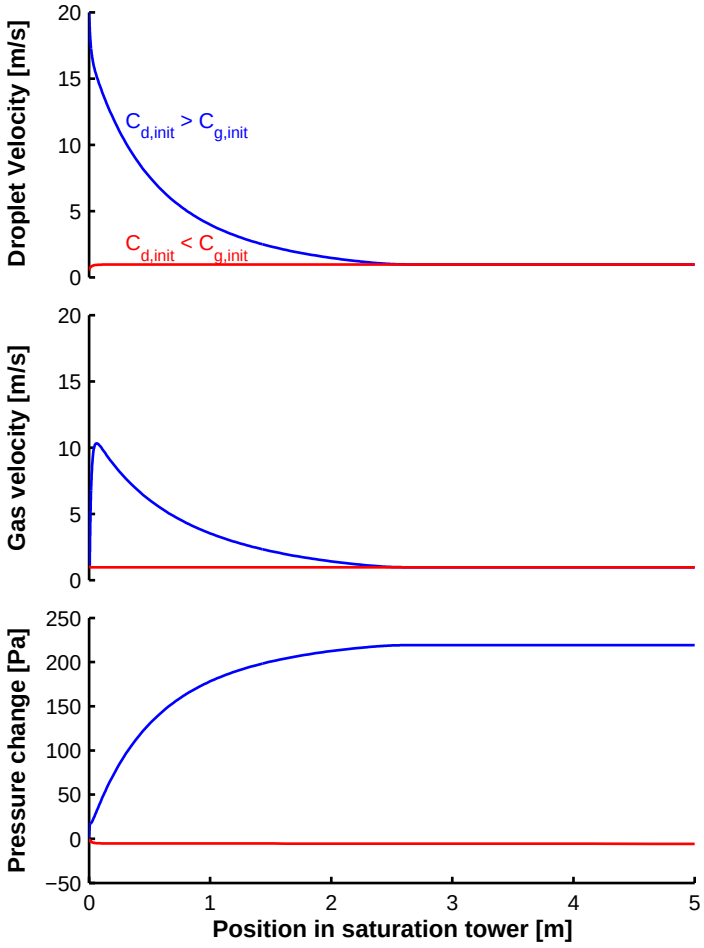

Figure 5.31: Velocity and pressure results in extended (5 m) saturation tower where initial droplet velocity is larger than the initial gas velocity (case $C_{\text{droplet,init}} > C_{\text{gas,init}}$) and where initial droplet velocity is lower than the initial gas velocity (case $C_{\text{droplet,init}} < C_{\text{gas,init}}$).

- $d_{\text{droplet}} = 0.5\,\text{mm}$;
- $D_{\text{sat}} = 0.5\,\text{m}$;
- $L_{\text{sat}} = 0.5\,\text{m}$;
- $C_{\text{droplet}} = 8\,\text{m/s}$.

Finally, injection scheme (a) from Figure 5.27 is used to generate the results of Figure 5.32.

Most of the mass and heat transfer occurs at the compressed air inlet, due to the large driving force (low relative humidity and big temperature difference (Figure 5.32)). The temperature of the outgoing saturated compressed air is 82 °C. Both gas and droplet velocity decrease continuously due to friction. Droplet diameter reduces 0.8 % along the saturation tower axis. This is more than in the co-current case (0.6 %), but since the outgoing air temperature is higher, more water is evaporated to reach full saturation after 0.5 m. Pressure loss is larger than in the co-current case, since the gas and droplets are moving in the opposite direction, resulting in larger friction forces (119 Pa).

Cross-current

The inlet conditions as described in Table 5.5 are used for cross current flow simulations, except for the droplet temperature (Figure 5.33). As mentioned before, the droplet temperature is kept constant and equal to the outlet temperature ($T_{\text{droplet}} = 78\,°\text{C}$). For the simulations, shown in Figure 5.33, injection scheme (c) from Figure 5.28 is used. Further inlet conditions are:

- $d_{\text{droplet}} = 0.5\,\text{mm}$,
- $H_{\text{sat}} = 0.5\,\text{m}$,
- $W_{\text{sat}} = 0.3\,\text{m}$,
- $L_{\text{sat}} = 0.5\,\text{m}$,
- $C_{\text{droplet}} = 20\,\text{m/s}$.

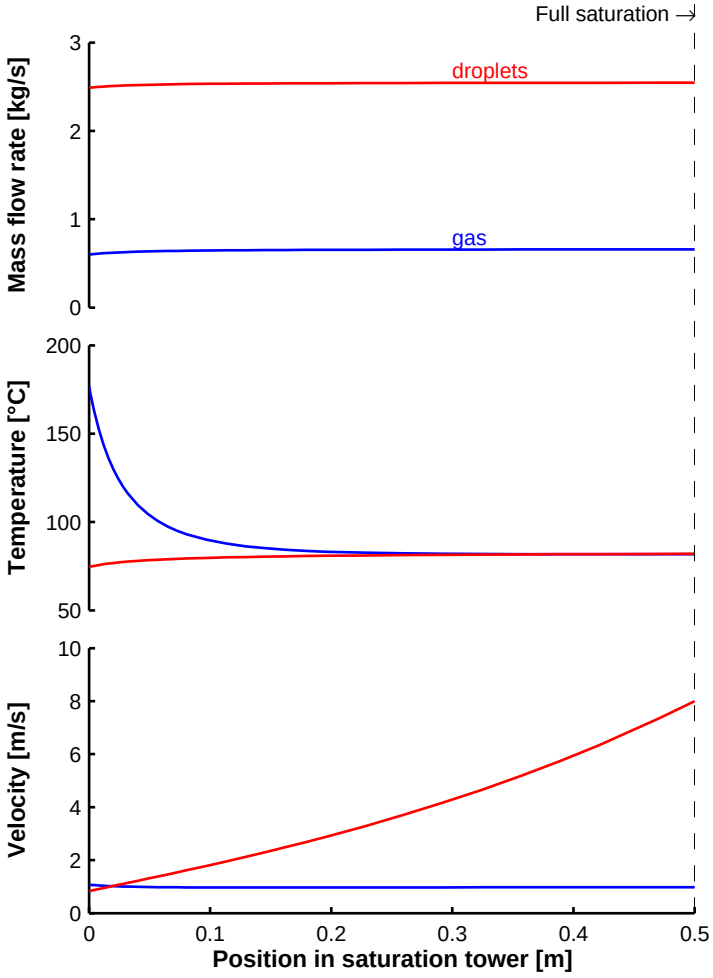

Figure 5.32: Simulation results of a counter-current saturation tower, indicating necessary tower length for full saturation is 0.50 m.

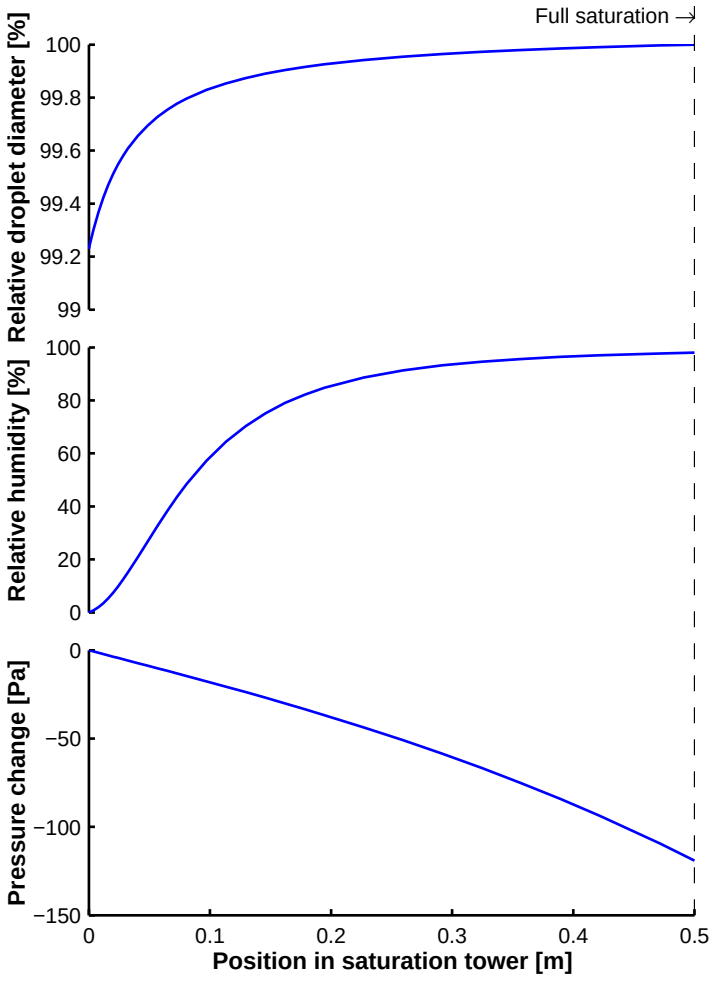

Figure 5.32: (continued)

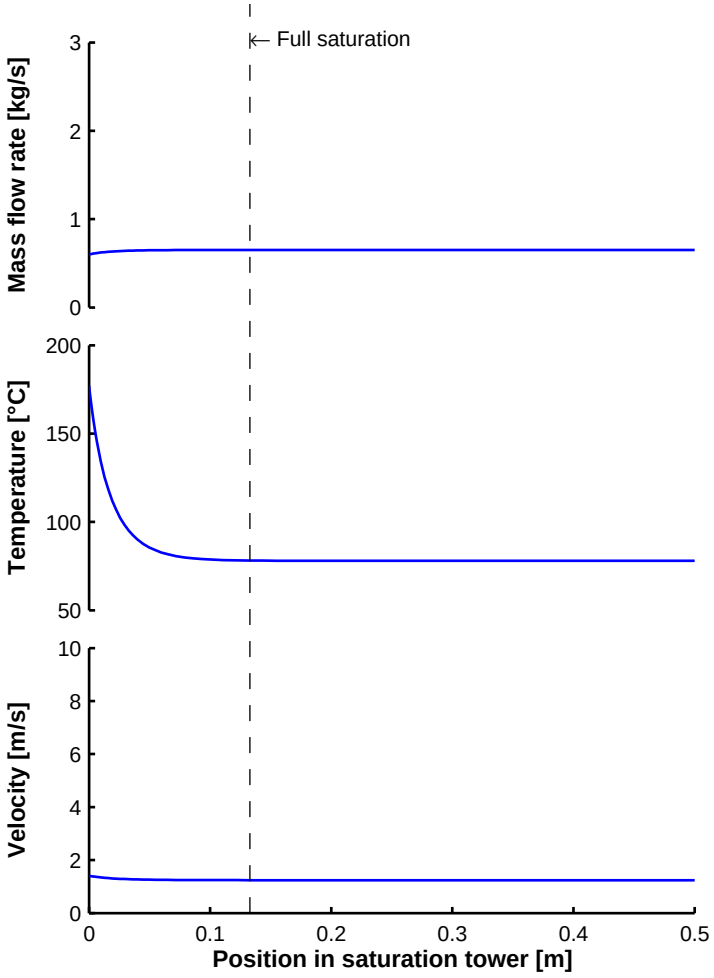

Figure 5.33: Simulation results of a cross-current saturation tower, indicating necessary tower length for fully saturated air is 0.13 m.

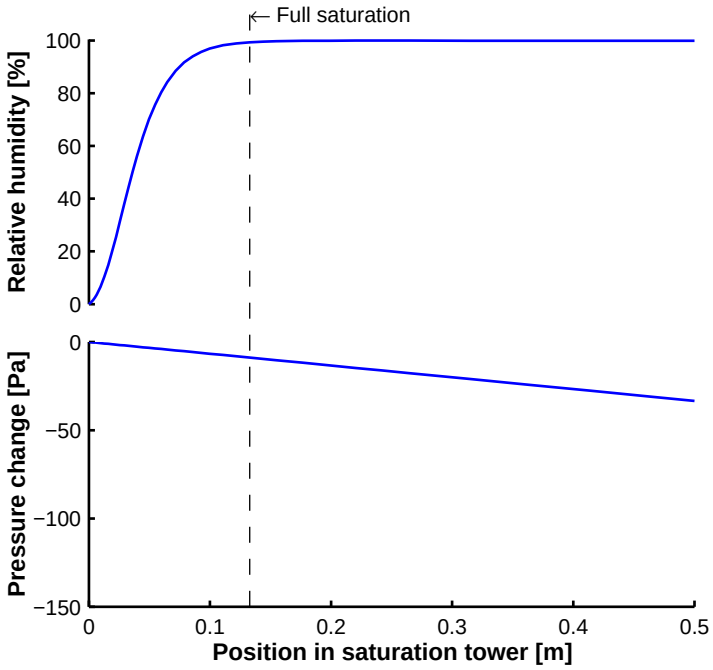

Figure 5.33: (continued)

In the cross-current flow, a rectangular cross section has been used, for the ease of simulations. The final cross section design will depend on the spray cone of the nozzle. The cross section should match the spray cone, in order to obtain an optimal contact between the air flow and injected droplets.

Since the droplet temperature is kept constant and droplets move in a direction perpendicular to the gas flow, droplet temperature, mass flow rate and velocity are not shown on Figure 5.33.

The mass transfer occurs again in the first 10 cm of the saturation tower (Figure 5.33), due to the large driving force (low relative humidity, Figure 5.33). The compressed air cools down, till the equilibrium temperature of 78 °C is reached (Figure 5.33). According to Figure 5.33, saturation is already reached after 0.13 m. Shortening the tower is however not possible. If the tower length is changed, the amount of injected water also needs to be changed, since a homogeneous distribution of the droplets is assumed. Changing this amount however, will affect the performance of the water heater of the mHAT, and will result in a lower mHAT performance.

The gas is slowed down by the friction between the gas core and wall and droplets, since the droplets are moving perpendicular to the gas flow (Figure 5.33). Pressure simulations indicate that the pressure decreases over the length of the saturation tower due to the friction with the wall and the droplet (Figure 5.33). Total pressure losses are however very low (less than 40 Pa or 0.01 % of the total pressure).

5.3.3 Results of the sensitivity analysis

For the sensitivity analysis, all different input variables have been varied over a specific range. The parameters are droplet diameter (d_{droplet}) and velocity (C_{droplet}), saturation tower cross section (A_{sat}), water and air mass flow rate ($\dot{m}_{\text{water}}$ and $\dot{m}_{\text{air}}$), water and air temperature (T_{water} and T_{air}) and pressure (p). The range was chosen based on the possible physical variations of the parameters.

One can divide the parameters into two main groups: the design parameters and the thermodynamic parameters. The design parameters – d_{droplet}, A_{sat}, $\dot{m}_{\text{water}}$, T_{water} and C_{droplet} – can be chosen in order to minimize the size of the saturation tower and to minimize the pressure drop. In the sensitivity analysis, these parameters are varied in order to gain insight in the effect of these parameters on the saturation tower length. The thermodynamic

properties of the compressed air on the other hand are controlled by the mGT control system. The control of these parameters is thus not within reach of the designer of the saturation tower; however variation of these parameters is likely. Depending on the inlet air conditions and the operator chosen set points (produced electrical power), the mGT control system will change the rotational speed of the compressor, which will of course have an effect on compressor outlet condition and thus on the saturation tower inlet conditions (T_{air}, p and $\dot{m}_{\text{air}}$) as well. In case there is a small variation on these parameters, compressed air leaving the saturation tower still needs to be saturated. In the sensitivity analysis, these parameters are thus varied over their operational range, to verify if the compressed air is fully saturated when leaving the saturation tower.

The main goal of the sensitivity analysis was to determine the effect of each parameter on the minimal length of the saturation tower and on the total pressure change. Saturation length is defined as the necessary tower length to achieve the full saturation. Results of parameter variation on relative humidity and pressure change for the different injection strategies – co-, counter- and cross-current injection – are presented in following subsections.

Co-current

The saturation length for co-current droplet injection is most sensitive to variations in the droplet diameter and water mass flow rate (Figure 5.34), while droplet velocity, saturation tower diameter and water mass flow rate variations have a major effect on pressure drop (Figure 5.35). For this sensitivity analysis of the co-current model, the inlet conditions of Table 5.5 are used in combination with the geometric conditions given in section 5.3.2. Every time, the indicated parameter is varied over the specified range while all other parameters were kept constant to really focus on the influence of the considered parameter. In addition, interaction with the film flow has been neglected to save calculation time.

Droplet diameter (d_{droplet}) has a huge impact on saturation length (Figure 5.34) and on pressure changes (Figure 5.35). The droplet diameter determines the contact area for heat exchange and mass transfer. A droplet diameter twice as large results in a reduction of contact area by four. This has a severe negative effect on heat and mass transfer, since these two phenomena take place at the contact surface of both phases. Since smaller

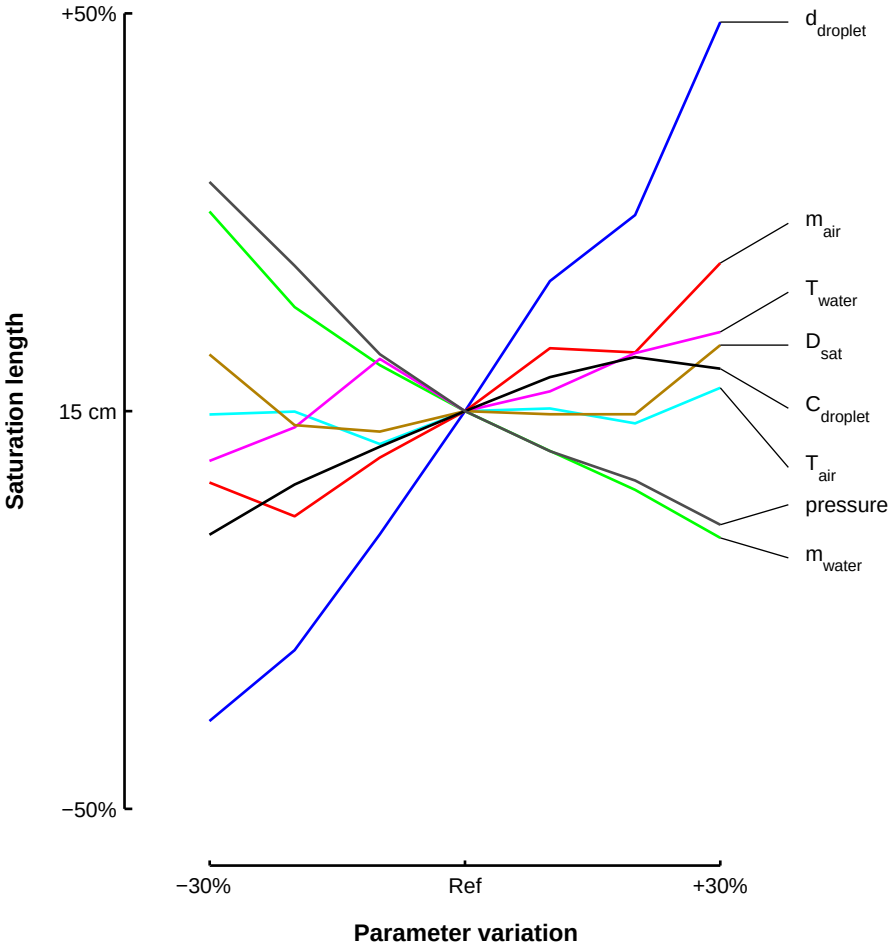

Figure 5.34: Droplet diameter and water mass flow rate are the most crucial parameters for saturation length in co-current injection.

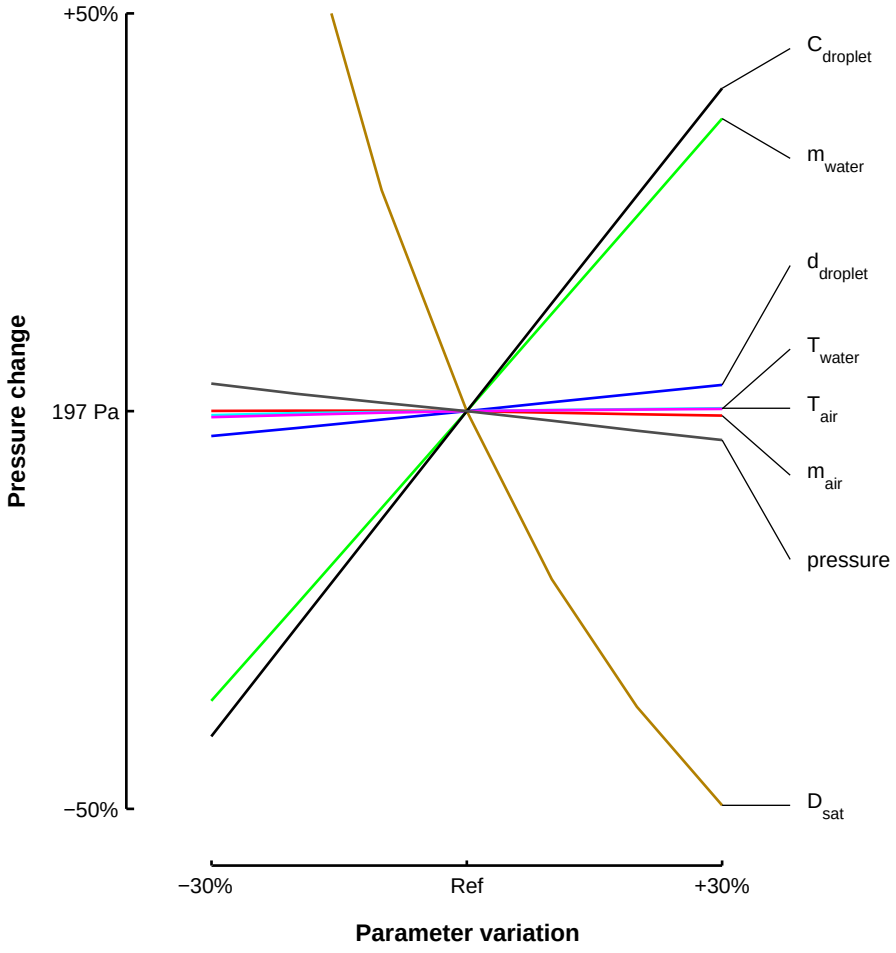

Figure 5.35: Water mass flow rate and saturation tower diameter have the largest effect on total pressure change in co-current injection.

droplets result in more contact surface, there will be more friction, which explains the increasing pressure changes for smaller droplet diameters.

Both droplet velocity (C_{droplet}) and cross section size (here in the form of the saturation tower diameter, D_{sat}) have a rather small influence on the saturation length (Figure 5.34), but a large effect on pressure variations (Figure 5.35). The cross section determines the gas velocity. Heat and mass transfer are positively influenced by a larger velocity difference. On the other hand, this effect is not strong enough to compensate the faster moving gas core, which results in a larger saturation length. Since the saturation tower diameter affects the gas velocity, it has the largest effect on pressure change. A higher gas velocity results in a higher pressure increase due to the interaction with the droplets. The bigger the difference between droplet and gas velocity, the more the pressure will increase, due to higher friction forces between both. Pressure will increase since $C_{\text{droplet}} > C_{\text{gas}}$ (see section 5.3.2).

The water mass flow rate ($\dot{m}_{\text{water}}$) has a positive effect on the saturation length (Figure 5.34) and on pressure variations (Figure 5.35). More water will result in more droplets and thus more contact area, which will enhance the heat and mass transfer. The larger the injected amount of water is, the more droplets there are. All these droplets are slowed down by the gas, which will increase the pressure.

The influence of the air (T_{air}) and water temperature (T_{water}) on the saturation tower length and pressure variations is low (Figure 5.34 and 5.35). A higher temperature has a positive effect on the heat and mass transfer, which should speed up the evaporation process. However it requires more water evaporation to achieve full saturation. So even though the evaporation process is enhanced, saturation length remains more or less constant since more water needs to evaporate to achieve the saturation condition.

The inlet air mass flow rate ($\dot{m}_{\text{air}}$) has only a minor effect on the saturation length (Figure 5.34). A lower mass flow rate results in a lower amount of water that needs to be evaporated for saturation. The air mass flow rate has also no effect on pressure loss, since the gas velocity is rather low (1 m/s).

The pressure (p) has a large effect on the saturation length (Figure 5.34), however variations of 30 % on the total pressure are rather large. A different saturation tower inlet pressure has only a minor effect on pressure changes (Figure 5.35).

Finally, simulations showed that the orientation of the saturation tower has

no effect at all on the saturation length. The orientation of the tower has also no effect on the pressure in the entrance region, but after this region, the effect of gravity is visible on the pressure change, however rather small (300 Pa for case (a) from Figure 5.26, 250 Pa for case (b) and finally 200 Pa for case (c)).

Counter-current

The saturation length of the counter-current water injection is more sensitive to parameter variations (Figure 5.36) compared to co-current injection (Figure 5.34), while the pressure variations are less sensitive (Figure 5.37 versus Figure 5.35). For some variations of several parameters, no saturation was reached within the tower length or droplets did not even reach the end of the tower, resulting in no depicted results. This clearly highlights the narrow margin for counter-current droplet injection. For the sensitivity analysis of the counter-current model, the same inlet and boundary conditions as in Table 5.5 and section 5.3.2 are used.

The droplet diameter, velocity, water mass flow rate and saturation tower length have the largest effect on the humidification process (Figure 5.36). If the droplets are too large, saturation is not reached inside the saturation tower. But on the other hand, too small droplets with a low velocity, will not reach the end of the tower, due to friction with the gas. In this case, droplets are stopped, will coalesce and fall down, depending on the orientation of the tower. The higher the velocity, the faster the droplets will move through the saturation tower. So the compressed air has no time to saturate. With a too low velocity, however, it is possible that the droplets will not reach the saturation tower exhaust. The saturation tower diameter has the same effect as the droplet velocity, since the saturation tower diameter will change the gas velocity. A too large section will make the droplets pass too fast, while a too small section results in too high gas velocity and coupled friction, which augments the risk for droplet stagnation. The water mass flow rate determines the contact area between gas and water and it has a direct effect on saturation length. The saturation tower length is also of great importance. If the saturation tower is too short, the residence time of the droplets is not long enough to saturate the air. A too long tower however increases the risk of droplet stagnation. The effect of water and air temperature and air mass flow rate are limited. Finally, orientation has a minor effect on the saturation process.

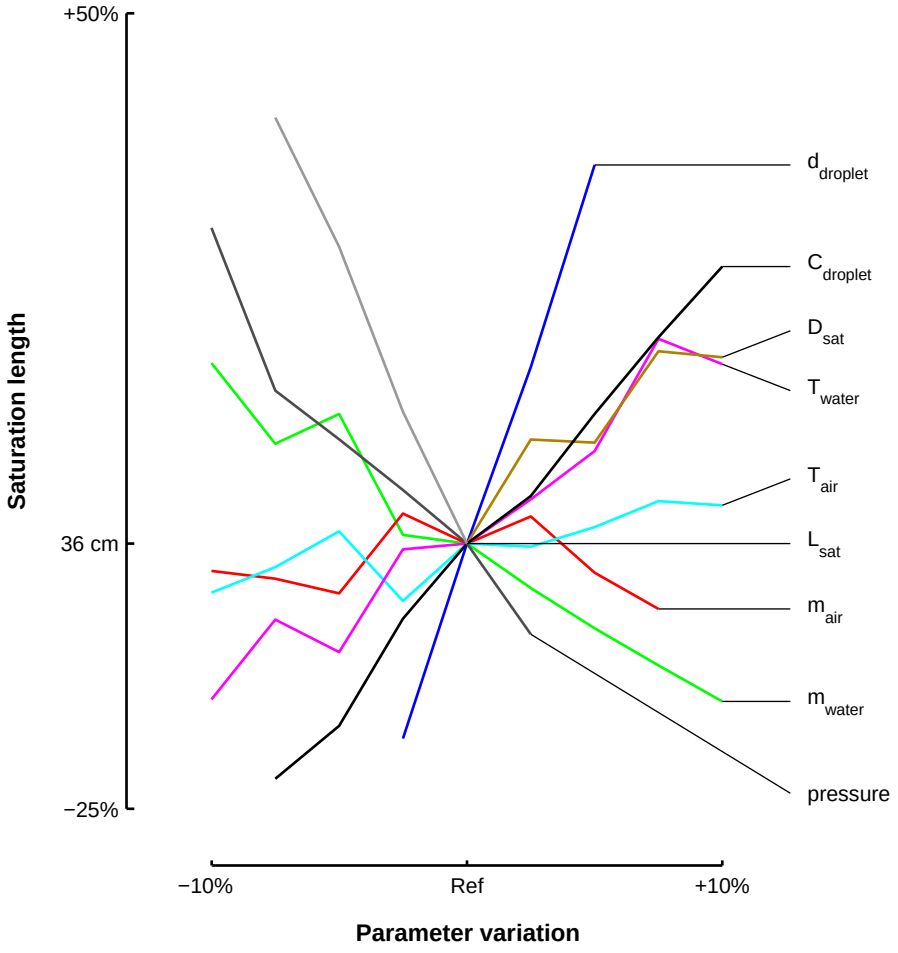

Figure 5.36: Droplet diameter, velocity, water mass flow rate and tower length are the most crucial parameters for saturation length in counter-current injection.

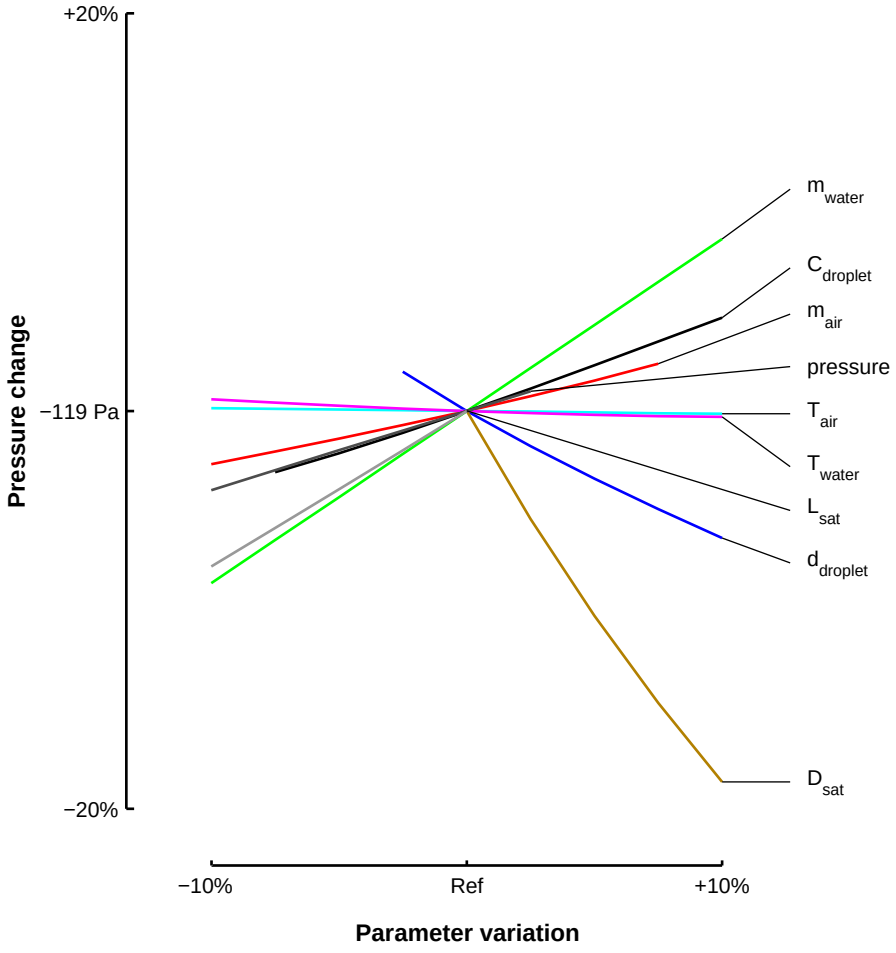

Figure 5.37: In cross-current injection droplet diameter, cross section and tower length and width are the most crucial parameters for total pressure change.

All parameters that influence the contact area (like droplet diameter and water mass flow rate) and the velocity difference between the gas and water phase (droplet velocity, saturation tower diameter and tower orientation), have a large influence on pressure drop, since the pressure drop is a function of these two parameters (Figure 5.37). Finally, in the counter-current injection case, the gas temperature and mass flow rate have little influence on the saturation process.

Cross-current

Saturation length in the cross-current water injection is very sensitive to saturation tower height and droplet diameter variations (Figure 5.38), while droplet diameter and saturation tower width variations have the largest effect on pressure losses (Figure 5.39). In the cross-current case, inlet conditions of Table 5.5 and section 5.3.2 have been used.

Since a larger droplet diameter results in less contact area, compressed air will never reach saturation when too large droplets are injected. Making the saturation tower longer as in the co-current case is in the cross-current case no option. A small droplet diameter on the other hand provides a large contact area between both the gas and the droplets. This is positive for the heat exchange and mass transfer, but has however a negative effect on the pressure loss (Figure 5.39).

The droplet velocity has a large effect on saturation length (Figure 5.38) and on pressure change (Figure 5.39). The velocity will determine the residence time of the droplets in the saturation tower and thus the available droplets in the saturation tower. A larger amount of droplets is beneficial for the heat and mass transfer, but result also in more friction and thus a higher pressure drop.

Changing the saturation tower width (W_{sat}) has almost no effect on the saturation length in the cross-current case, while the height of the saturation tower (H_{sat}) is on the other hand of great importance (Figure 5.38). Changing the width will only influence the gas velocity. Since the gas velocity is rather low (approximate 1 m/s), gas velocity does not change much with increasing width. The heat and mass transfer coefficient will thus vary little, resulting in no visible effect on the saturation length. The higher the saturation tower on the other hand, the faster full saturation is reached. A

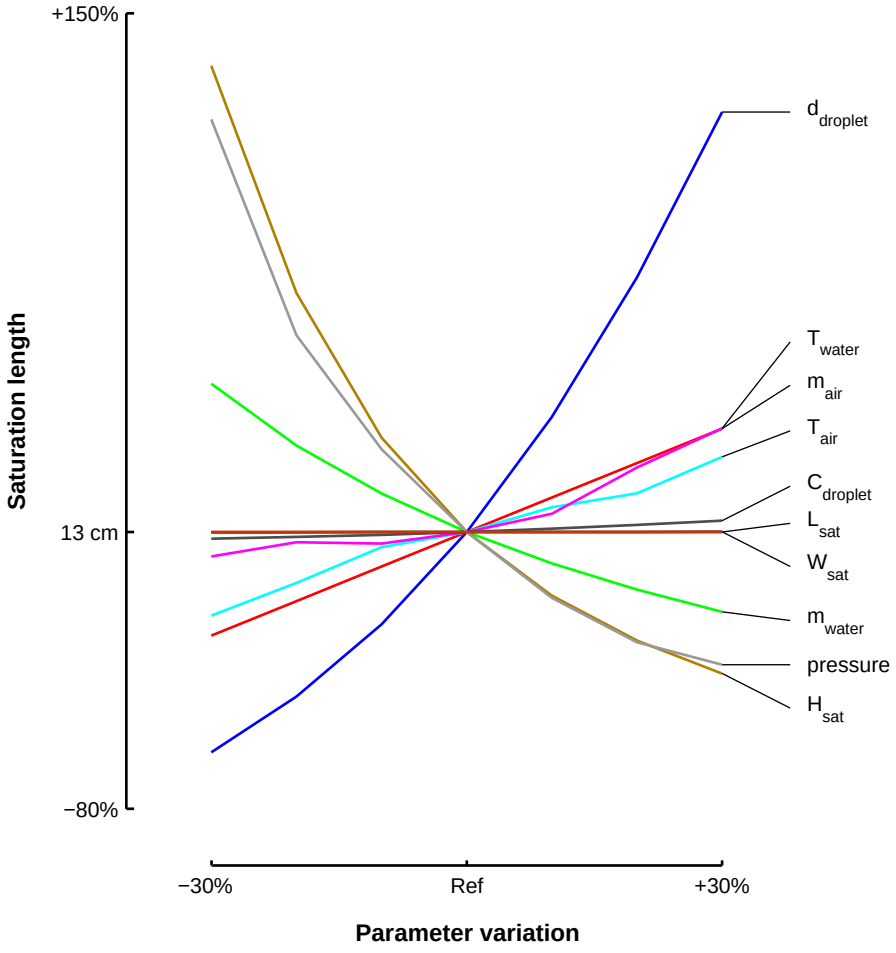

Figure 5.38: Droplet diameter, tower height and water mass flow rate are the most crucial parameters for saturation length in cross-current injection.

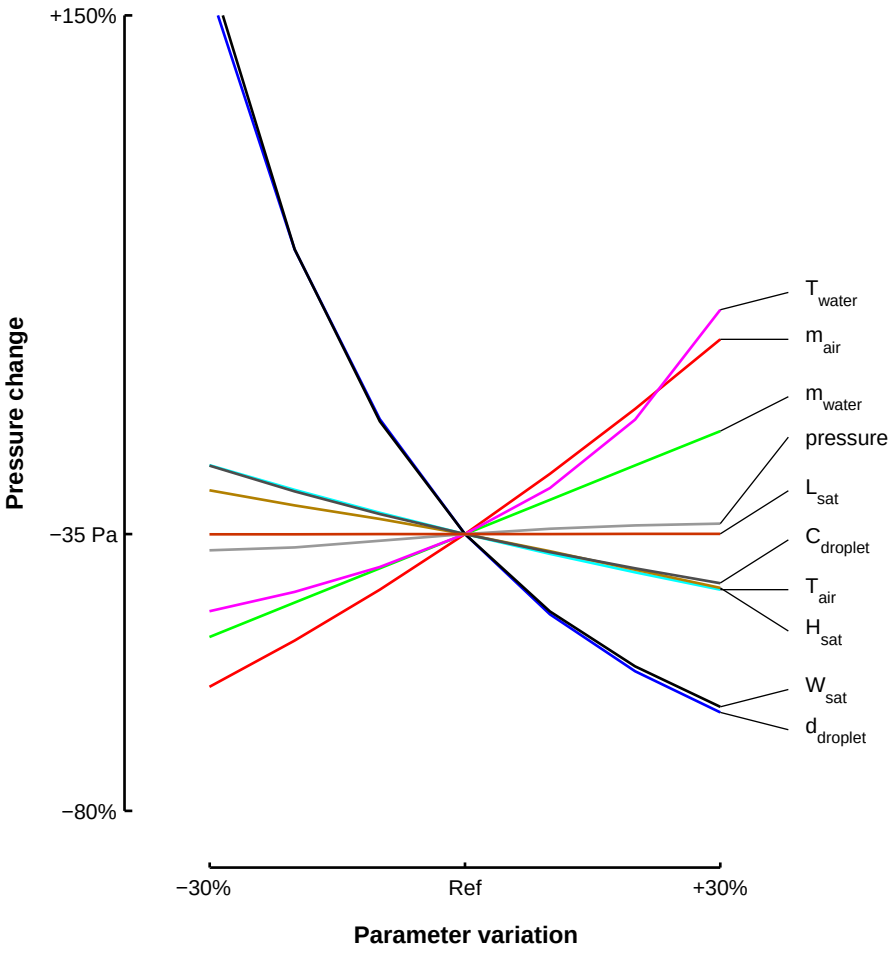

Figure 5.39: In cross-current injection droplet diameter and tower width are the most crucial parameters for total pressure change.

higher saturation tower contains more water than a lower one, since the residence time of the droplets is larger. This provides a larger surface for heat exchange. Width and height of the saturation tower determine the gas velocity. The higher the velocity, the higher the pressure loss will be (Figure 5.39).

Water mass flow rate has a large effect on saturation length (Figure 5.38). The higher the water mass flow rate is, the more droplets there are, so the more contact area. A higher water mass flow rate results in more droplets and higher friction forces with the gas (Figure 5.39).

The length of the saturation tower (L_{sat}) has a minor effect on the saturation length (Figure 5.38) and on the pressure drop (Figure 5.39). The droplets are distributed homogeneously along the longitudinal axis of the saturation tower. Making the saturation tower longer results in a lower droplet density per cross section and thus a smaller contact area per cross section, which explains the longer saturation length. Relative saturation length – saturation length normalized by the total tower length – remains the same.

As in the co- and counter-current case, both air and water temperature have a minor effect on the saturation length (Figure 5.38). Air and water temperature also have a minor effect on pressure loss (Figure 5.39). Higher air and water temperatures result in more evaporation, which has an effect on the gas velocity. In addition, the air temperature will influence the density, which has also an effect on the velocity.

The air mass flow rate has, as in the co-current case, a small effect on the saturation length (Figure 5.38). Increasing the air mass flow rate will increase the gas velocity and thus the friction, explaining the large effect of air mass flow rate on pressure drop.

Finally changing the pressure has only a minor effect on the saturation length (Figure 5.38). Using injection scheme (a) from Figure 5.28 results in a shorter saturation length (0.09 m), since in this case; the movement of the droplets through the gas core is not influenced by gravity, resulting in a longer residence time than in injection type (c) from Figure 5.28 (0.13 m). In addition, pressure has no effect on pressure changes as indicated in Figure 5.39. Orientation has a small influence on the pressure loss (less than 4 Pa).

5.3.4 Saturation tower design for Turbec T100 mGT

The final goal of this section is to design a novel spray saturation tower that could be applied on the Turbec T100 mGT. By using a spray tower, the aim is to get a lower pressure loss than in a classical tower with packing material, while not exceeding the size of a classical saturation tower.

In their research paper, Parente et al. performed simulations of a Turbec T100 mGT converted to a mHAT operations [34] to obtain the necessary saturation tower volume. Final simulations indicated that a total packing volume of $0.08\,\mathrm{m}^3$ is necessary to fully humidify the compressed air of the $100\,\mathrm{kW_e}$ mGT with a pressure drop of $400\,\mathrm{Pa/m}$ of packing height. The total expected pressure drop over the packing can be calculated out of the simulation results for the saturation tower size, using empirical correlation to estimate pressure drop over cooling tower fills [301]. This pressure drop is in the order of magnitude of 100 Pa, which corresponds to Parente's assumption [34].

The pressure loss can be lower than for a classic packed saturation tower, by choosing carefully the dimensions of the saturation tower, the nozzles (who will determine droplet velocity and diameter) and the amount of circulating water. Simulations of cross-current injection of droplets have shown that the pressure drop is very limited (33 Pa). In the co-current case, depending on the droplet velocity (C_{droplet}), the pressure drop is low (5 Pa, $C_{\mathrm{droplet,init}} < C_{\mathrm{air,init}}$) or total pressure even slightly increases (130 Pa, $C_{\mathrm{droplet,init}} > C_{\mathrm{air,init}}$).

The impact of the pressure loss due to the introduction of the saturation tower in the mHAT cycle on the electric efficiency is limited. The effect of this additional pressure loss on the efficiency can be calculated using the Aspen® simulations. Adding 100 Pa additional pressure loss to the mHAT cycle results in a relative efficiency loss of 0.2 %. However, due to the accuracy of natural gas flow rate meters (1 % for typical vortex flow meters), relative changes in efficiency smaller than 1 % cannot be measured (section 3.1). According to this limitation and since calculations have shown that the pressure drop differences between a packed and a spray saturation tower are limited, I can conclude that as long as the pressure drop is within an order of magnitude of 100 Pa, the impact on the efficiency is far below the increase of efficiency (7 %).

I decided not to use co-current injection of the droplets, to avoid supplemental auxiliary power necessary to generate the smaller droplets. Simulations

have shown that for both the co- and cross-current case, using the dimensions as mentioned in 5.3.2 and 5.3.2, fully saturated air is reached after 0.20 m and 0.13 m. In the co-current case, droplets of 0.1 mm need to be used, while in the cross-current case, droplets of 0.5 mm could be used. In order to get smaller droplets, the injection pressure of the water over the nozzles needs to be higher. Sauter mean diameter (d_s) of a nozzle at a specific pressure can only be determined experimentally. Each different nozzle has its own specification. For a standard industrial nozzles (Nozzle type: CAY2970 [302]), to reduce the droplet diameter by a factor two, the pressure needs to be increased by a factor two (according to measurements of the manufacturer). This implies that in the co-current case, more power is lost to the auxiliary circulation pump for water injection, 1.5 kW compared to 150 W in the cross-current case. The smaller droplet diameter is penalized by a relative efficiency loss of 1.5 % compared to the 0.15 % loss in the cross-current case due to the higher necessary auxiliary power. The loss through the auxiliaries to provide smaller droplet diameter is of greater importance than pressure drop. Therefore, if was decided not to use co-current injection of the droplets.

Counter-current was excluded as a possible injection scheme for the saturation tower due to the high sensitivity of the saturation length to inlet parameter variations. Comparing simulations of counter- (Figure 5.32 and 5.32) and cross-current (Figure 5.33 and 5.33) flow shows that in both cases saturation can be reached in a 0.5 m long saturation tower. Sensitivity analysis results of counter-current flow however showed that saturation can only be reached in a small window of boundary conditions variation. For example in case the velocity is too low, droplets will turn around, in case the velocity is too high, no saturation is reached. In the cross-current flow simulations, the final saturation length is less sensitive to variations of these inlet conditions. Since the goal is to obtain a robust design, cross-current injection is preferred.

The final design is therefore a cross-current saturation tower, with the following dimensions:

- $H_{\text{sat}} = 0.5\,\text{m}$,
- $W_{\text{sat}} = 0.3\,\text{m}$,
- $L_{\text{sat}} = 0.5\,\text{m}$.

For the ease of implementation, the horizontal gas flow (Figure 5.28, case (c)) will be used, since according to sensitivity analysis, there is little difference between case (a) and (c) from Figure 5.28. The evacuation of the remaining water is moreover easier. In case (a), the water will first move downwards through the saturation tower wall, before it can be removed. Total pressure loss over the saturation tower (33 Pa) is in the same order of magnitude as the packed saturation tower (100 Pa). The total size is equal to 0.075 m^3, which is in the same order as the packed saturation tower proposed by Parente et al. (0.08 m^3) [34].

5.3.5 Conclusion of the saturation tower development

A two-phase flow model is developed for designing a novel saturation tower for a Turbec T100 mGT based mHAT application. A spray saturation tower has been chosen to reduce pressure losses. The two major boundary conditions were pressure drop and saturation tower volume. The aim of this study was to develop a saturation tower with better performance than the classical saturation tower with packing. The two-phase flow model is also used to perform a sensitivity analysis to identify the parameter which variation will have the largest influence on global performance.

Simulation of co-, counter- and cross-current two-phase flow calculations for a spray saturation tower gave rise to the following conclusions:

- It is possible to fully saturate the compressed air within acceptable dimensions for the mHAT application.
- Sensitivity analysis indicated droplet diameter and water flow rate as the most crucial parameters for all different flow configurations. Halving the droplet diameter results in twice the required auxiliary pump power, while doubling the water mass flow rate, also results in twice the required auxiliary power. Per 100 W required auxiliary power, electric efficiency is reduced by 0.1 %.
- Pressure drop is in the same order of magnitude as the pressure drop of a classic saturation tower with packing material.

Based upon these results, a suggestion for a saturation tower design for the Turbec T100 mGT has been proposed.

5.4 Conclusion

In this chapter, the different steps for the development of a humidified mGT cycle were discussed.

First, the optimal route for waste heat recovery through water injection was determined by using a two-step method. By using a black box method, it was found that the surge margin reduction was the limit for water injection, rather than the thermodynamic limit (violation of the second law). The surge limit was reached by injection 17 %wt of water in the compressor exhaust, resulting in an absolute efficiency increase of 9 % and a final stack temperature of 53 °C. In the second step, the cycle layout was designed by means of composite curve theory. Direct injection of heated water was identified as the cycle that approached best the black box potential, resulting in an absolute efficiency increase of 4.6 %. The differences between the different cycles were however rather limited. Therefore it was decided to use the mHAT cycle layout for humidification of the mGT, since the mHAT cycle layout still allows to operate the mGT in both dry and wet mode without major modification to the engine. In that configuration, the absolute increase of efficiency is limited to 3.8 %.

Once the mHAT was defined as optimal route, a sensitivity analysis on the heat exchanger network of the mHAT cycle was performed. The sensitivity analysis showed that the choice of the boundary conditions: hot pinch and final stack temperature, has a huge impact on the cycle performance. Increasing hot pinch and stack temperature has a severe negative effect on final mHAT performance. In addition, I discussed the effect of the non-idealities of the heat exchanger network (absolute efficiency drop of 3.2 %) and the operation mode of the mGT (absolute efficiency drop of 1.9 %) on the global cycle performance when transforming the ideal cycle design into a final design for a humidified T100 mGT layout. The limited surface for heat exchange in combination with a lower TIT negatively influences the potential for water injection. The final increase in efficiency when transforming the Turbec T100 mGT into a mHAT is 2 % absolute efficiency increase.

In the final section of this chapter, the developing process of the humidification system was discussed. This process included a two-phase flow model development and a sensitivity analysis to select the final saturation tower design. The two-phase flow simulations indicated that it is possible to fully humidify the compressed air within acceptable dimensions for the saturation

tower and keeping the pressure drop in the same order of magnitude as the pressure drop of a classic saturation tower with packing material. Water flow rate and droplet diameter were identified as the most crucial parameter. Finally, based upon these results, a suggestion for a cross-flow injection saturation tower design for the mHAT version of the Turbec T100 mGT was done.

Chapter 6

Experimental mHAT characterization

In this chapter, I will discuss the results of the experiments performed on the modified Turbec T100 mGT. As a proof of concept, the mGT has been equipped with a spray saturation tower to humidify the compressed air. Experiments were performed to validate the mHAT simulations. In a first section, the converted Turbec T100 mHAT test rig is discussed. A short description of the cycle layout and the installed sensors is given as well as a more elaborated discussion on the installed spray saturation tower and the used injection nozzles. Secondly, the mHAT operation procedures are discussed. Starting the humidification requires a specific procedure due to the additional water in the working fluid. Both dry and wet start-up are discussed and experimentally tested. Introducing a saturation tower in the mGT cycle has also an impact on the transient behaviour of the mGT during shutdown. Therefore, the surge margin reduction and surge avoidance during shutdown are discussed. In the final section, the actual humidification experiments are discussed. The experiments are conducted at different power levels and with different water injection rates. The effect of the humidification on the mGT performance and the different parameters is discussed.

6.1 mHAT test rig development

In this section, the installed mHAT test rig in the lab of the Department of Mechanical Engineering at the VUB is discussed. In a first subsection, the mHAT and the global installation are described. Special focus is placed on the installed measurement equipment to capture the effect of the water introduction on the mGT performance. In the second subsection, the surge margin control is presented. The third subsection gives more insight in the spray saturation tower and the injection system. Finally, the selection of appropriate nozzles is discussed, as this is critical to limit the losses to the auxiliaries.

6.1.1 mHAT cycle

The Turbec T100 mGT has been modified to transform the recuperated mGT into a mHAT (Figure 6.1). After being compressed to 4 bar in the radial compressor (1), the hot compressed air (200 °C) is saturated in the saturation tower (2), where hot water around 82 °C is sprayed in the compressed air. The fully saturated air is then preheated by the exhaust gases in the recuperator up till around 595 °C (3). Inside the combustion chamber (4), natural gas is burned till a TIT of ∼890 °C is reached, which corresponds to a maximum TOT of 645 °C. The hot gases expand over the turbine (5), which is connected through a single shaft to the compressor. The turbine delivers the necessary power to drive the compressor. The remaining shaft power is transformed into electric power by a high-speed generator (6). After having preheated the saturated compressed air, the hot exhaust gases (180 °C) are used to heat the water in the economizer (7). This hot water is routed towards the saturation tower, where the water is atomized in the compressed air. A total amount of 2.5 kg/s (10 m^3/h) of water is circulating in the water circuit. Since water will evaporate in the saturation tower, feedwater needs to be added to the circuit (8) to keep the total amount of circulating water constant.

To control the mHAT cycle, several valves and two pumps were installed (Figure 6.2). Feedwater is added to the circuit by means of a *Wanner WANH0006* multi-membrane pump. By changing the pump speed, the feedwater flow rate can be controlled. A variable speed *Etaline inline pump* is installed to keep the water circulating and to control the injection pressure of the nozzles in the saturation tower. All installed valves are

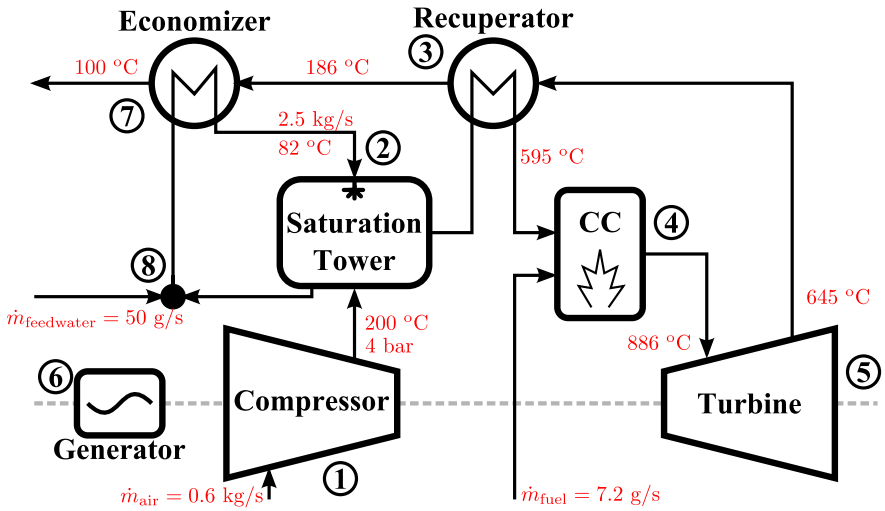

Figure 6.1: The recuperated mGT cycle is turned into a mHAT by adding a spray saturation tower between the compressor outlet and recuperator inlet to saturate the compressed air to the cycle.

manually controlled ball or butterfly valves for the water circuit and manually controlled globe valves for the compressed air circuit. A saturation tower bypass valve is added to the compressed air piping network. Opening this valve will bypass the saturation tower, allowing the operator to run the mGT in the original recuperated Brayton cycle layout. A saturation tower bypass line is also installed in the water circuit. Bypassing the saturation tower with the water results in the original heating cycle. The bypass can be controlled gradually, which allows the control of the amount of injected water in the saturation tower, while still keeping the total amount of circulating water constant.

Two 90 kW_{th} air heaters are installed in the water circuit outside the lab (Figure 6.2). The air heaters dump the thermal energy of the T100 mGT into the environment. In wet mode, the heat exchangers are disconnected from the circuit by opening the bypass valve. In case the rerouted water from the saturation tower still contains too much energy, due to a too low energy transfer from the water to the compressor air, the remaining energy can be removed from the water with these air heaters. One air heater is equipped with a variable speed ventilator, allowing the control of the total heat load from 0 to 180 kW_{th}

To measure the effect of the water injection on the mHAT test rig, several sensors have been installed on the test rig (Figure 6.2), additionally to the previously installed sensors on the mGT test rig (subsection 3.1.2). Class-A Pt100 *Yokogawa* temperature sensors (accuracy ±0.55 °C) are installed to monitor the water and compressed air temperature. TOT, CIT and the recuperator outlet temperature are measured each two times by K-type, class-1 thermocouples (accuracy ±0.004 times the measured value). A second *Yokogawa* differential pressure sensor (0 to 10 bar, accuracy ±0.015 % of the full range) is installed behind the saturation tower, allowing the measurement of the the pressure loss over this saturation tower. A *RAMC* rotameter measures the injected amount of feedwater (0 to 3.60 L/min, accuracy ±1.6 % of the measured value), while a *Woltman* water flow rate meter (0.25 to 10 m^3/h, accuracy ±1.0 % of the full scale) monitors the circulating water mass flow rate. Additionally, a second *RAMC* rotameter (0.35 to 16 m^3/h, accuracy ±1.0 % of the measured value) is installed to measure the exact amount of injected water in the saturation tower. Finally, a temperature and pressure compensated *Honeywell* vortex flow meter (0.10 to 2.13 kg/s, accuracy 1.0 % of the measured value) was installed in between the compressor outlet and the saturation tower inlet to measure the compressor mass flow rate. On the test rig, no humidity sensor has been

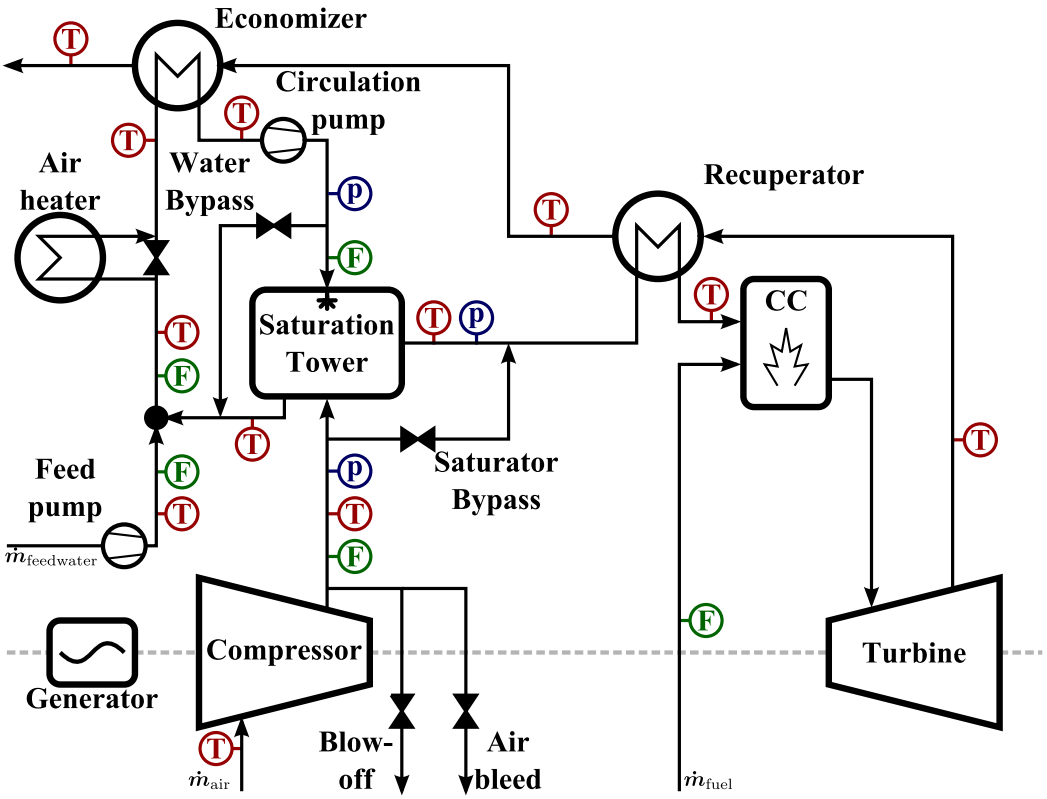

Figure 6.2: The mHAT test rig was equipped with several sensors to capture the effect of air saturation on mGT performance.

installed, since these sensors are only operated at atmospheric pressure, have a maximum operating temperature that is lower than the dry operating temperature or are too expensive. Therefore, I decided to use the pressure, temperature and mass flow rate of the compressed air, in combination with the amount of feedwater added, to calculate the relative humidity.

6.1.2 Surge margin control

To assess the surge margin, simulations of the mHAT cycle were performed in the Aspen® plus model of subsection 5.2.1.

Initial water injection simulations (subsection 5.2.2) and steam injection experiments in the T100 mGT (subsection 4.1.3) indicated that surge would not be an issue (point 'Ideal Wet' Figure 6.3). The Aspen® simulations predicted a reduction of 20 % in surge margin (Table 5.4). Analysing initial dry measurement data at 80 kW_e electric power output however showed a 4.33 % pressure drop between the compressor outlet and the recuperator inlet. This pressure drop is introduced by the saturation tower and the additional piping network. Detailed analysis of this pressure drop showed that the pressure drop over the saturation tower itself was limited to 0.95 %, as expected. The major reason for the pressure drop is the piping network, connecting the compressor outlet with the saturation tower inlet. Due to a lack of space, the saturation tower needed to be placed relatively far away from the compressor outlet, making the piping network too long and containing several curves. This piping network caused a 3.37 % pressure drop. Simulations indicated that the total 4.33 % additional pressure drop severely reduces the surge margin. Taking the constructor's surge line, surge margin is reduced by 44 % compared to the dry operation of the mGT (point 'p_{loss}=5 %', Figure 6.3).

A manually controlled globe bleed valve was installed to increase compressor surge margin during wet experiments (Figure 6.2). According to Aspen® simulations bleeding 5 % of the compressor air, would limit the surge margin reduction to 28 % (compared to the constructor's surge line, point 'p_{loss}=5 %, $\dot{m}_{bleed}$=5 %', Figure 6.3). Parallel to the bleed valve, a pneumatic controlled *Dafram* blow-off ball valve is installed to protect the compressor against surge during shutdown. As mentioned by Pezzini et al., the additional volume between compressor and turbine causes surge problems during normal and emergency shutdowns [303]. By opening the blow-off valve during mGT

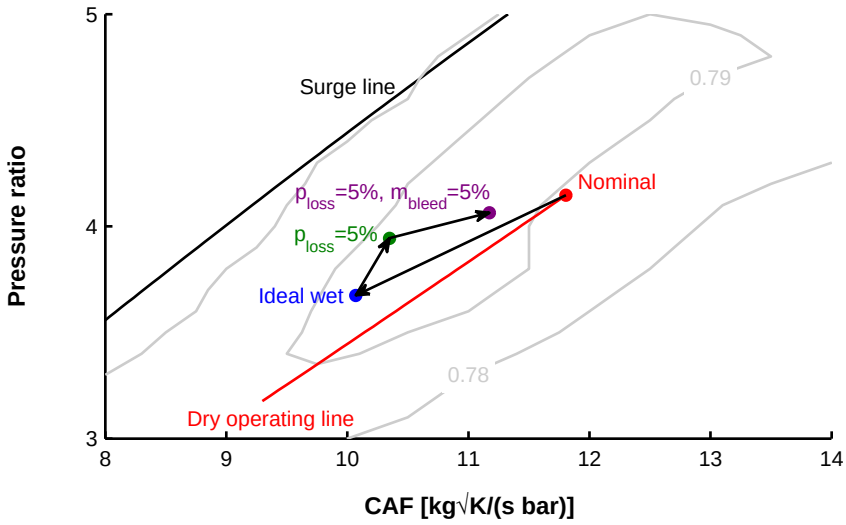

Figure 6.3: The compressor surge margin is reduced due to an additional pressure drop caused by the humidification unit. Water injection reduces the surge margin by 20 % ('Ideal wet') compared to the dry operation ('Nominal'). The additional pressure drop results in an even larger reduction of 44 % ('p_{loss}=5 %'). Bleeding air increases the surge margin again ('p_{loss}=5 %, $\dot{m}_{\mathrm{bleed}}$=5 %').

shutdown, the compressor was kept away from its surge limit. A more elaborated discussion on the shutdown procedure is presented in section 6.2.

6.1.3 Spray saturation tower and injection system

The function of the saturation tower is the saturation of the compressed air. The saturation process can be enhanced by increasing the contact area between the water and the compressed air, since heat and mass transfer occurs at the contact surface between the liquid and gas phase. I designed the saturation tower based on the results from a two-phase flow analysis (section 5.3). From the insights obtained from these simulations, a cross-current spray saturation tower has been developed (Figure 6.4). The compressed air in- and outlet duct of the vessel are connected to the compressor exhaust and the recuperator inlet through a piping network (Figure 6.4(a)). On this piping network, pressure, temperature and flow rate sensors are installed. As mentioned before, a bypass network is placed parallel over the saturation tower (Figure 6.2). This allows the operator to bypass the saturation tower and run the T100 mGT in its classical configuration (recuperated Brayton cycle). The air flows horizontally through the saturation tower.

The compressed air is saturated by spraying hot water in the saturation tower. In total seven injection nozzles are installed on top of the saturation tower, placed in staggered position (Figure 6.4(a)). The nozzles are fed with pressurized water from two collectors (not included in Figure 6.4(a)). The collectors keep the injection pressure constant, which will result in a constant injection flow rate. On each connection between the nozzles and the collector, a manually controlled ball valve is installed. This allows the control of the amount of active injection nozzles in order to be able to control the injection water flow rate. The specific staggered way of nozzle placement is selected to avoid interference of the sprays from different nozzles. In case two spray cones interfere, droplets will coalesce, resulting in thicker droplets. The droplet diameter is a crucial parameter determining the contact area and thus has a direct impact on the saturation process. Droplet coalescences must be avoided at any time. By placing the nozzles in a staggered position, the saturation tower length could be reduced by a factor two. Inside the vessel, air guidance plates are installed to force the air through the water spray (Figure 6.4(b)). The guidance plates are under the same angle as the opening angle of the spray cone of the installed nozzles. Finally, two loopholes are installed to check the behaviour of the spray nozzles inside

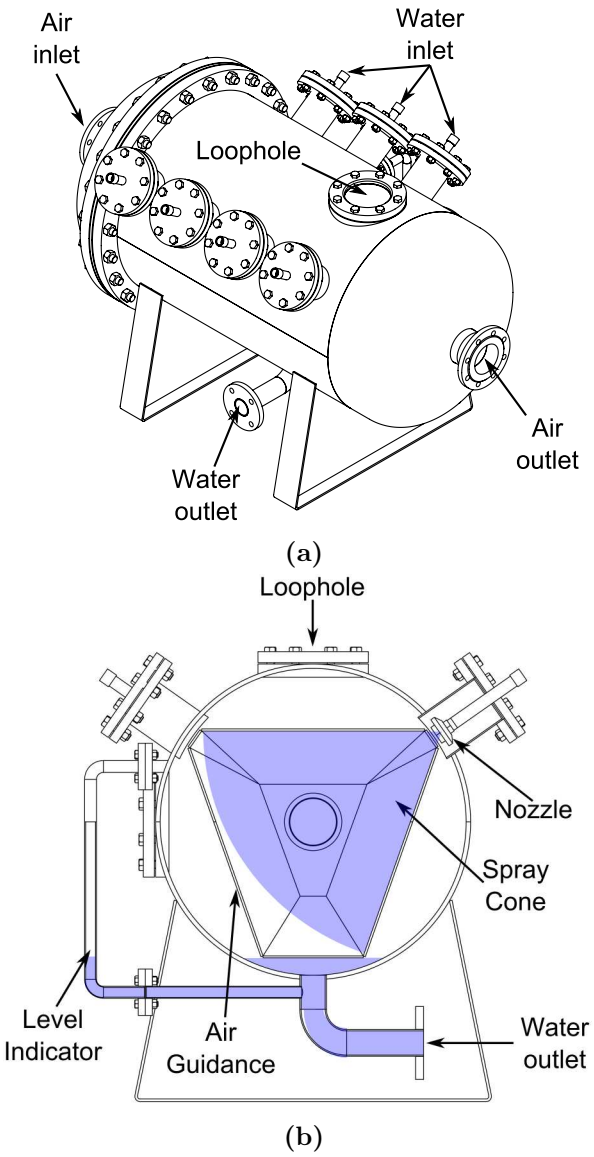

Figure 6.4: The spray saturation tower is specially designed and constructed for the Turbec T100 mGT. The spray tower is equipped with seven nozzles to atomize the water to increase the contact surface between water and compressed air (a). Air guidance plates are installed to force the air through the water spray (b).

the saturation tower.

An accurate determination of the amount of evaporated water is necessary to control the feedwater pump and to give an estimation of the humidity level of the compressed air. One possibility is measuring the in- and outgoing water flow rate of the saturation tower. The required feedwater rate is then equal to the difference between both measurements. The total amount of evaporated water is however very low (50 g/s), compared to the total amount of circulating water (2.5 kg/s, Table 5.4). Standard volumetric water flow rate measuring techniques have an accuracy of 1 %, which is too low to accurately detect the 2 % water loss through evaporation. At the bottom of the saturation tower, there is a water layer. The level of this water can be seen by the level indicator. The feedwater pump is controlled so that the water level inside the saturation tower, and thus the amount of water in the circuit, is kept constant.

Behind the saturation tower outlet, a droplet separator is installed (not indicated on Figure 6.4). Initial tests showed that a considerable amount of droplets travelled along with the saturated air towards the recuperator inlet. These droplets would evaporate in the recuperator, leading to deposit of contaminants, resulting in recuperator fouling. This should be avoided at any time, since one of the advantages of the mHAT is the lower water quality requirement. The droplet separator would eliminate any remaining droplets from the compressed air flow. In a further design of the saturation tower, this droplet separator should be integrated in the saturation tower.

6.1.4 Spray nozzle selection

On the saturation tower, seven *PNR* stainless steel full-cone nozzles, type CAS.2551.B3.SB with an angle of 70°, have been installed (Figure 6.5, [302, p.18]). From a geometric point of view, installing flat-cone nozzles would be favourable. These nozzles can be installed close to each other without risking droplet coalescence, resulting in a reduced saturation tower size. The flat-cone nozzles however require a higher injection pressure to reach the same droplet size as full-cone nozzles. Reducing the injection pressure is crucial to keep the energy consumption of the auxiliaries low. Hollow-cone nozzles need even lower injection pressures. The installation of hollow-cone nozzles would lead to a non-homogeneous droplet distribution in the saturation tower, which may result in not fully saturated outgoing compressed air. Each of the selected nozzles combines seven hollow-cone

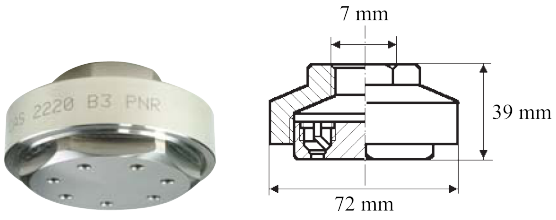

Figure 6.5: To inject the water in the saturation tower, seven CAS.2551 spray nozzles from *PNR* have been installed [302, p.18].

nozzles to obtain a final full-cone spray [302, p.18]. The beneficial effect of the lower injection pressure in the hollow-cone is combined with the homogene droplet distribution of the full-cone nozzle. The multi-orifice nozzles produce a finer spray than a standard full-cone single-orifice nozzle working at the same pressure and delivering the same quantity of liquid [302, p.18]. Each nozzle will deliver a flow rate of 26.6 L/min at a pressure difference of 0.7 bar.

An alternative for standard nozzles would be the use of ultrasonic spray nozzles [304]. The minimum amount of energy necessary to create droplets is the energy necessary to create the droplet surface (surface tension). To atomize 2.5 kg/s of water in droplets with a diameter of 0.5 mm, a total power of 1.9 W is necessary. This is very low compared to the 150 W, necessary to provide the atomization pressure for a standard nozzle. Most of the energy is transformed into kinetic energy or lost due to friction. This kinetic energy is necessary to create the vortex in the flow to achieve wave break-up into droplets. The classic nozzle is therefore very energy inefficient. Only 1 % of the total energy is used to create the droplet surface, while the rest is lost due to friction or transferred to the droplet as kinetic energy. In the application of the spray tower, a lower kinetic energy, thus lower droplet velocity is however more favourable, since it will increase the residence time. Ultrasonic nozzles on the other hand use a different technique to break a film into droplets. The film will break up into droplet due to the vibrations. Ultrasonic droplet generation has a much higher energy efficiency. For a typical droplet size production with a particular liquid flow rate, the energy consumed in an ultrasonic nozzle is 6 % of the total electrical energy required in a two-phase external-mix type nozzle [305]. Currently, many theoretical and experimental studies are conducted to predict the droplet size and distribution in ultrasonic nozzles depending on different parameters like flow rate, injector size, surface tension and

frequency [305–309]. Droplet size can easily be reduced by increasing the vibration frequency [310]. The major problem however is the very limited flow rate [311]. Today, ultrasonic droplets are mainly used in precision applications, like pharmaceutical industry, but may offer a solution in the future for a spray saturation tower.

6.2 mHAT operation

The mHAT converted Turbec T100 mGT cycle requires specific start-up and shutdown procedures. In this section, the selected start-up and shutdown procedures are discussed. During the selection of the procedures, the major focus was on the protection of the T100 mGT compressor. A faulty start-up or shutdown procedure can lead to possible compressor surge. Compressor surge should be avoided at all cost, since it can lead to the destruction of the compressor.

6.2.1 Start-up procedure

In this subsection, the used start-up procedures of the mHAT test rig are discussed. Two different start-up procedures were initially developed: *Dry start-up* and *Wet start-up*.

During a *Dry start-up*, the mGT is started without water injection in the saturation tower, thus without evaporation. The mGT is started and will go through its start-up procedure. The mGT connects then to the grid and will speed-up until the requested electric power output is reached. After the mGT is stabilized, water injection in the saturation tower is started. The amount of injected water will be steadily increased until the nominal water injection flow rate of 2.5 kg/s is reached. A higher water injection flow rate will result in more droplets, so a larger contact area and more heat and mass transfer. When the nominal amount of 2.5 kg/s of water is injected, the air will be fully saturated, resulting in optimal performance of the mHAT.

Using the *Wet start-up*, water injection in the saturation tower is started before the mGT. As the mGT starts up, the compressed air will be partially saturated, depending on the temperature of the water and the compressed air. To avoid start flameouts, as a result of a too low CIT due to the presence of water in the air, a dry mGT run – to heat up all mGT parts

and the water – is performed prior to a *Wet start-up*. Initially, the injected water amount is limited, however during the start-up, the water injection is gradually increased until full water injection is achieved. Once full injection of 2.5 kg/s of water is reached at the requested electric power output, the feedwater pump needs to be started to keep the circulating water mass flow rate constant. As mentioned before, this water flow rate is kept constant by keeping the water level inside the saturation tower constant. The amount of injected feedwater can manually be controlled by changing the rotational speed of the feedwater pump.

Both start-up procedures have been tested experimentally. Results of these experiments are summarized in the following subsections.

Dry start-up

The *Dry start-up* procedure has been tested unsuccessfully two times at 80 kW_e power production. The mGT had been running dry for approximately 1 h before the water injection was started. The total amount of injected water was below the minimal start flow rate (0.25 m^3/h) of the water flow meter. A few seconds after the water injection was started, a flameout occurred resulting in a compressor surge (Figure 6.6), due to a failure in the blow-off system. When the water injection is started (blue line on Figure 6.6), the rotational speed (N) starts to increase (620 rpm in 2 s). Water evaporation increases the turbine mass flow rate and thus the turbine power, which allows the turbine to speed up. The increasing rotational speed results in an increased compressor outlet pressure (p_{comp}, 80 mbar). The higher pressure will increase the electric power production (P_{el}). The TOT remains more or less constant (less than 2 °C reduction during the water injection). Due to the sudden injection of water, the composition of the combustor inlet air changes rapidly. The control system cannot anticipate this change, resulting in a flameout. Once the flameout occurs, rotational speed (19 %) as well as the compressor outlet pressure (37 %) drop severely, which results in a compressor surge (Figure 6.6). The produced electric power, P_{el}, follows this trend, however there is a slight delay, because of the power electronics. The beginning of the surge can be clearly seen by the measured pressure loss over the inlet air filter, Δp_{filt}. The pressure loss increases rapidly, because of the pressure build-up inside the mGT casing due to the reversed flow in the compressor. Due to the severe drop in rotational speed, the power electronics cannot sustain the voltage in

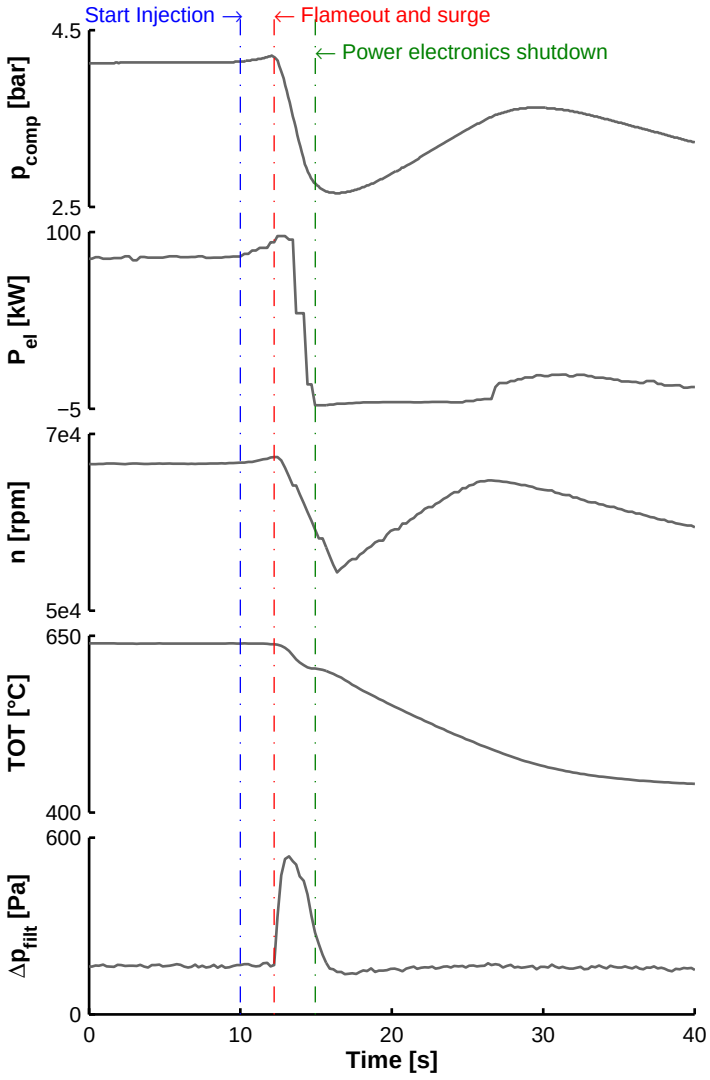

Figure 6.6: Time series of some key parameters during *Dry start-up*. The mGT compressor goes into surge 3 s after the water injection in the saturation tower is started, due to a flameout.

the required range, resulting in a too high DC voltage. The control system detects this high DC voltage and shuts down the power electronics. Once the power electronics are shut down, the shaft is no longer braked down, and since the recuperator still contains a lot of energy, the mGT speeds up again. This explains the rotational speed increase from 54 320 rpm till 64 740 rpm, approximately 5 s after the flameout and coupled compressor surge occured. After a few seconds, the compressor starts to slow down again, since all remaining energy in the recuperator has been consumed.

Although a very small amount of water was injected (less than 0.25 m^3/h), the existing control system of the T100 mGT was not capable of handling the sudden change. Starting with a lower amount of water injection is not possible. Therefore, to protect the compressor, it was decided to no longer use this *Dry start-up* procedure.

For future experiments, flameout at dry start-up might be avoided by increasing the fuel flow rate of the pilot flame to stabilize the flame. Increasing this pilot fuel flow rate too much will however result in a too high local combustor temperature with possible damage as a result. Measuring NO_x emissions helps monitoring the combustor temperature, since high NO_x levels indicate high temperature. The main objective of this thesis was the development of a humidified mGT cycle without major changes to the cycle layout and control system. Therefore the option of changing pilot fuel flow rate was not tested.

Wet start-up

The initial *Wet start-up* procedure did not lead to stable mGT operation with water injection (Figure 6.7, test 1 (t1)). The water injection was started before the mGT was started (blue line on Figure 6.7). The mGT successfully completed the start-up procedure and connected to the grid (green line, Figure 6.7). The mGT accelerated till 73 % of the nominal rotational speed was reached and an electric power output of 50 kW_e was produced. Once this electric power output was reached, the fuel flow rate to the combustor was steadily increased to reach maximal TOT. Increasing TOT results in higher power, so the control system could reduce the rotational speed and thus the compressor outlet pressure (Figure 6.7). During the whole test, air was bled to keep the compressor away from surge. After 900 s, a mGT flameout occurred, resulting in a sudden drop in rotational speed and compressor outlet pressure. As a result of the mGT failure, the produced

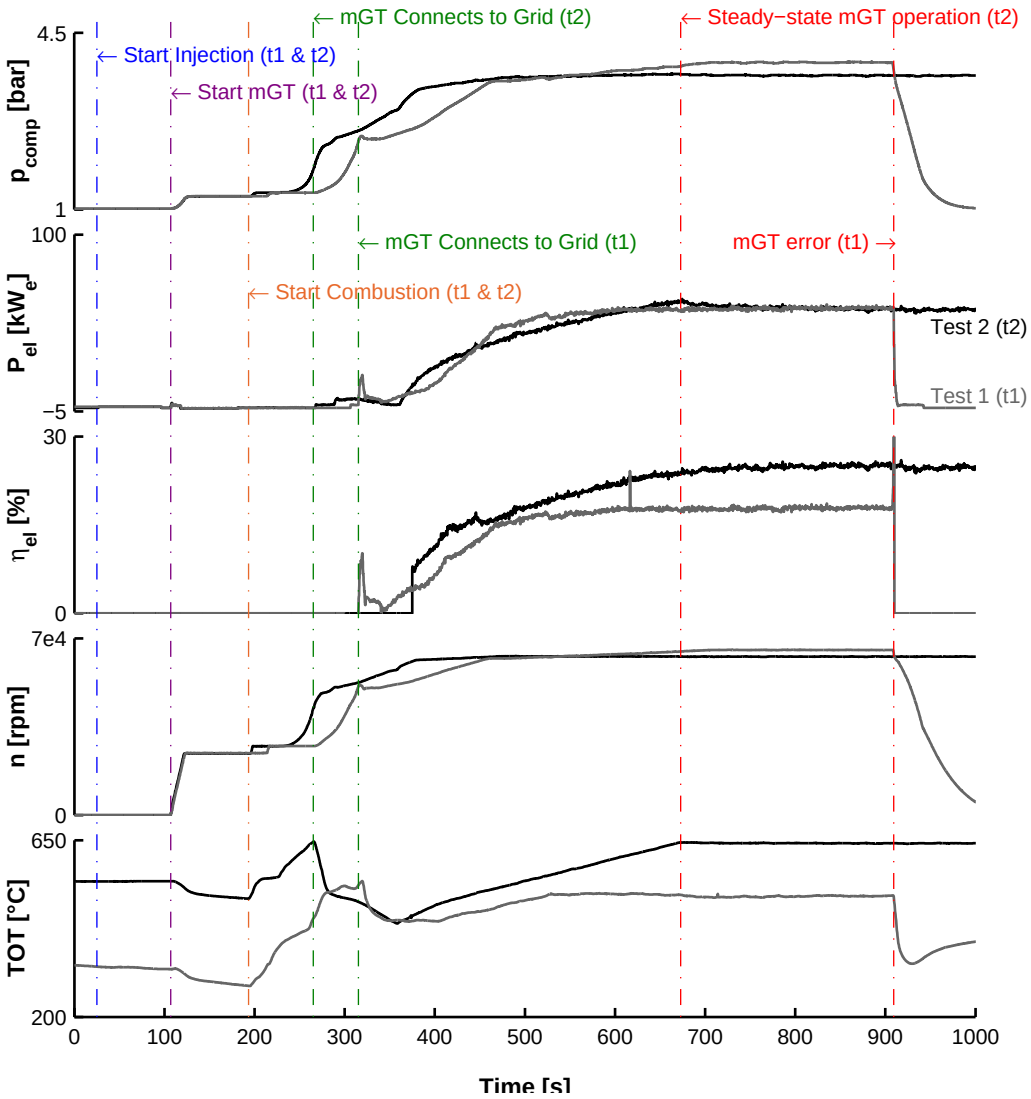

Figure 6.7: Time series of some key parameters after water injection using the *Wet start-up* procedure: by bleeding part of the compressor air, surge during *Wet start-up* could be avoided. After 900 s during the first test (t1), the mGT is stopped due to a flameout as a result of a failure in the natural gas supply due to a too high fuel demand. After 670 s during the second test (t2), the mGT has reached steady-state conditions, with A TOT of 645 °C and a rotational speed of 62 730 rpm.

power drops suddenly and the control system disconnects the mGT from the grid. During the test, 0.55 kg/s of water was injected in the saturation tower.

The flameout was caused by a failure in the fuel supply system. In contrast to the simulation results (Table 5.4), water injection did not result in a mGT run at reduced rotational speed, reduced compressor ratio and increased electric efficiency. Although turbine mass flow rate was increased due to water evaporation, the electric efficiency was lower compared to the efficiency measured during the dry run prior to the wet test (17.7 %, Figure 6.7, compared to 28.4 % dry efficiency). Accurate determination of the evaporated water mass flow rate was not possible due to the too short stable injection period. The mGT control system has problems with reaching the requested electric power of 60 kW_e, resulting in a reduced electric power production of 55.7 kW_e. The low electric efficiency of 17.7 % is a result of the low TOT and linked TIT. Reducing TIT has a negative effect on the electric efficiency of the T100 mGT. During water injection, TOT drops from 645 °C to 509 °C even though a large amount of fuel is injected in the combustion chamber (7.8 g/s), which is 27.8 % higher than in the dry case. Moreover, the fuel flow rate of 7.8 g/s is close to the nominal mass flow rate (9.9 g/s) of the *'Copeland'* scroll compressor used to pressurize the natural gas. The compressor is not capable of providing this natural gas flow rate for a long period, resulting in a flameout.

The high fuel demand is caused by a reversed heat transfer in the saturation tower. Although no temperature sensors were installed at the recuperator exhaust at the time of these first experiments and CIT could thus not be measured, reduced TOT and increased fuel mass flow rate indicate that CIT is reduced. The control system of the mGT tries to compensate this low CIT by injecting a large amount of fuel in order to increase TOT till 645 °C. Simulations of the mHAT cycle, indicated that the heat for water evaporation in the saturation tower needs to be extracted partially from the injected water. This means that the temperature of the water leaving the saturation tower should be lower than the inlet temperature (Table 5.4). In that case, waste heat from the water is transferred to the compressed air, resulting in an enhanced mGT performance. However, during this experiment, the outgoing water temperature was higher than the ingoing water temperature (60.7 °C compared to 58.8 °C ingoing temperature). This means that the necessary heat for the water evaporation is fully provided by the compressed air. In addition, an extra amount of heat is transferred to the circulating water, explaining the higher outgoing water temperature.

Instead of increasing the enthalpy of the compressed air by saturating the air with water vapour, the enthalpy of the compressed air is reduced during this experiment. The saturation tower acted like an aftercooler, where heat is extracted from the compressed air, rather than adding residual waste heat from the water. Due to the limited contact surface for heat transfer, the recuperator cannot compensate the heat losses, resulting in a lower CIT.

By reducing the amount of injected water in the saturation tower, the energy loss to the water during start-up will be lower, allowing the mGT control system to increase TOT. Reducing the water mass flow rate causes however a problem in the economizer. The exhaust gases leaving the recuperator are still hot. This heat needs to be evacuated. If the water flow rate is too low, the temperature of the water leaving the economizer will become too high, resulting in a forced mGT shutdown by the control system. By bypassing part of the water over the saturation tower (Figure 6.2) and only injecting a low amount of water, the mGT start-up sequence can be completed without any problems. The bypassed water is cooled by the two air heaters allowing to evacuate up to 180 kW_{th} thermal power to the environment.

Adapting slightly the *Wet start-up* procedure, by bypassing part of the water over the saturation tower, resulted in successful mGT start-up (Figure 6.7, test 2 (t2)). Bypassing the circulating water allowed to keep the injected water flow rate limited, while keeping the water temperature leaving the economizer below the limit of 95 °C. The start-up sequence was successfully terminated after 660 s when the mGT had reached a TOT of 645 °C and 54 kW_e electric power output, resulting in an electric efficiency of 24.9 %. Finally, the *Wet start-up* of test 2 (t2) resulted in 3 h of stable operation of the mGT at constant rotational speed and pressure ratio. The same *Wet start-up* procedure was tested again, in order to show the repeatability of the procedure. Later attempts always resulted in successful tests of over 1 h (see section 6.3).

The hot *Wet start-up* time of the mHAT test rig is equal to the hot dry start-up time with air bleed (Figure 6.8). The start-up process is not affected by the water injection. During both experiments, full stable operation has been reached after 660 s. Tests with cold *Wet start-up* have not been performed. The effect of the air bleed on dry start-up time is also limited. Closing the air bleed during dry start-up reduces start-up time by 60 s (Figure 6.8).

During *Wet start-up*, air was always bled to prevent compressor surge. *Wet start-up* without air bleed always leads to compressor surge. With the existing Turbec T100 mGT controller, it is difficult to identify the cause of

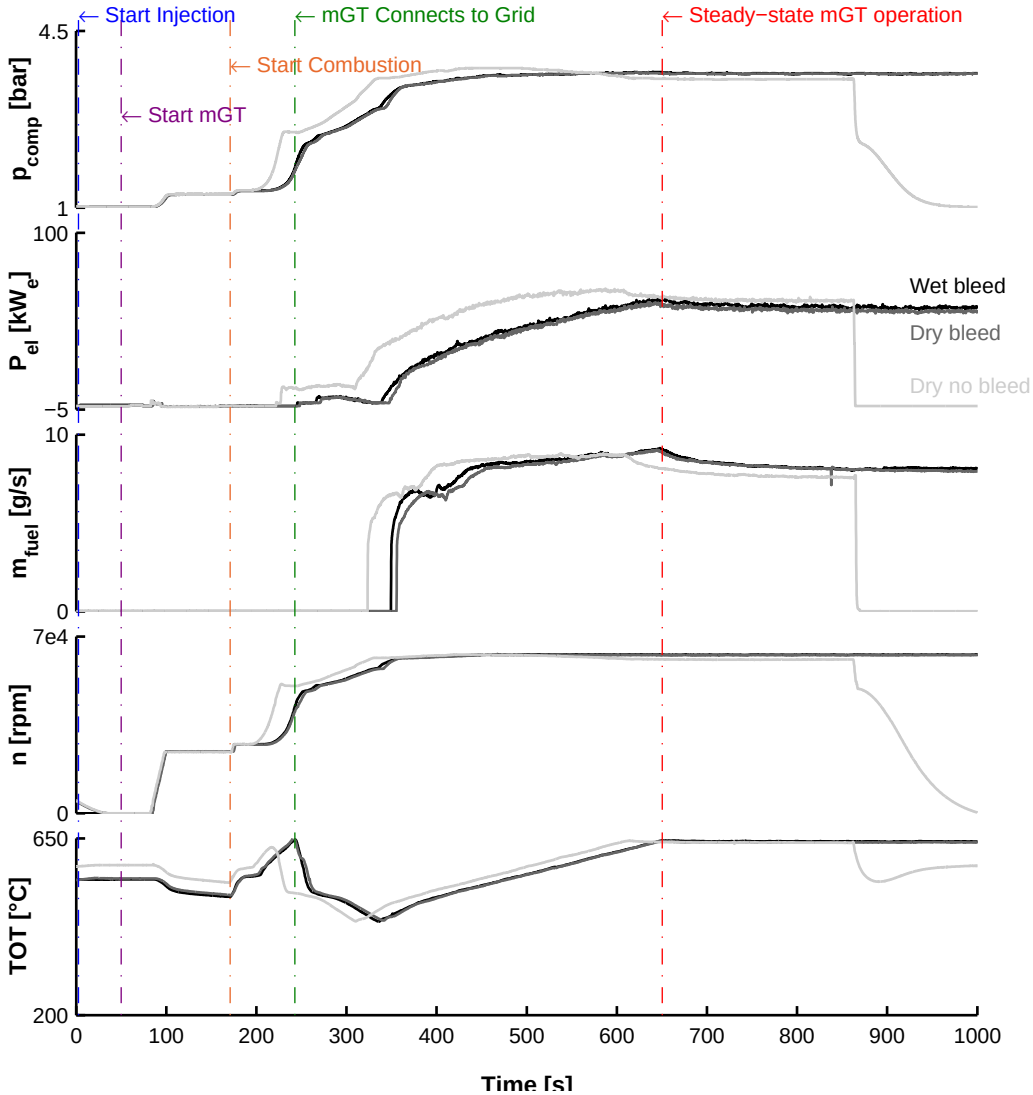

Figure 6.8: Time series of some key parameters during start-up for a dry and wet test run. Compressed air was bled to prevent the compressor going into surge. Both start-ups were finished after 660 s, when the mGT reached steady-state operating conditions. The injection of water has no effect on the start-up time.

Wet start-up failure, since the control system cannot detect a compressor surge. A drop in rotational speed and produced power is identified by the mGT control system as a flameout, since there is no actual flame detector in the T100 mGT combustor. The error message given by the mGT control system always indicated a flameout however it is not clear whether an actual flameout occurred, followed by a compressor surge or a compressor surge without flameout was wrongly interpreted by the control system as a flameout. Experimental data confirmed both hypothesises of flameout followed by surge and surge without flameout (Figure 6.9). In case the mGT is stopped due to a flameout, TOT drops immediately after the error occurred. Due to the flameout, pressure ratio and rotational speed decrease, leading to a compressor surge. In case the compressor goes into surge without flameout, TOT increases, since the surge results in a reduced air mass flow rate to the combustor, while the amount of injected fuel remains constant. Finally, fuel flow is cut by the mGT control system since the control system interprets the drop in rotational speed and power as a flameout.

6.2.2 Shutdown procedure

The addition of the saturation tower to the mGT cycle caused an additional problem as has been indicated in the previous subsection: surge at shutdown. The additional volume of the saturation tower results in a higher compressor back pressure during shutdown. The rotational speed of the compressor drops quickly after shutdown ($\sim$3500 rpm/s), since the control system keeps the mGT a few seconds longer connected to the grid. The relatively fast drop in rotational speed in combination with the high back pressure at the compressor exhaust results in a compressor instability. Depending on the operating point, the compressor will go into surge or rotating stall [312, 313]. To solve this problem, two shutdown procedures were developed for two different scenarios:

- Operator controlled shutdown;
- Error provoked shutdown.

Both procedures are briefly explained in the following subsections. Ideally, a complete surge control system, as described by Kurz and White [314, 315] should be installed. Developing such a system is however very time-consuming.

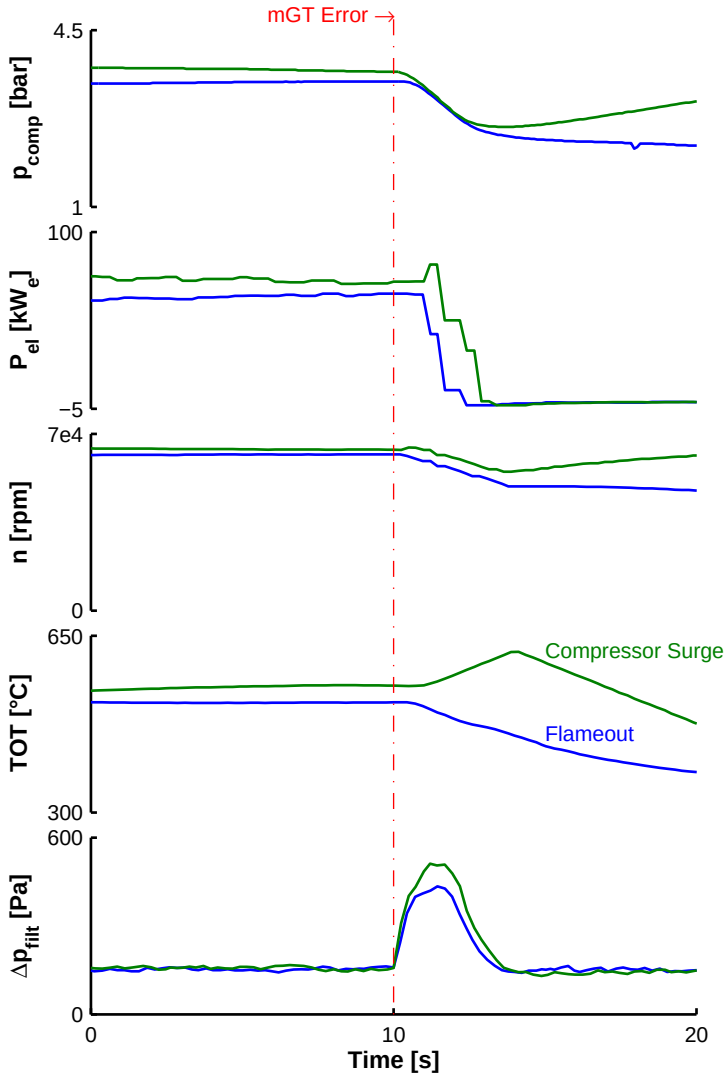

Figure 6.9: Two different mGT failures were identified during *Wet start-up* – flameout followed by compressor surge and compressor surge without flameout – based on measurements of the TOT.

Controlled shutdown

During a controlled shutdown, the operator decides to shut down the mGT. Since the operator gives the signal to shut down the mGT, the blow-off valve can be opened when the command is given to the mGT control system to shut down. The blow-off valve will keep the compressor operating point away from the surge limit, as observed during experiments (Figure 6.10).

To shut the mGT down, the control system stops the fuel flow to the combustion chamber. The control systems slows down the mGT compressor and turbine shaft slightly by keeping the mGT connected to the grid. Without the blow-off valve, similar mGT behaviour was also noticed during the tests with the *dry start-up* method after the flameout (Figure 6.6). The rotational speed and compressor outlet pressure reduction result in a compressor surge, since the back pressure in the saturation tower is too high. The surge can be seen, as previously mentioned, in the pressure loss over the inlet filter (Δp_{filt}). Once the compressor goes into surge, the electric power productions drops immediately to $0\,\text{kW}_\text{e}$. When the compressor recovers from the surge, the rotational speed increases again, as well as compressor outlet pressure.

The blow-off valve is opened when the fuel flow is cut (Figure 6.10). The blow-off valve limits the rotational speed reduction rate by reducing the back pressure of the compressor. This keeps the compressor away from its surge limit during shutdown. Rotational speed and compressor output pressure reduce steadily till the mGT is fully stopped.

This control can also be used during emergency shutdown, since it is known upfront that the mGT will be shut down, so the blow-off valve can be opened when the signal is given to the control system. Unlike hybrid mGT/fuel cell systems, where a surge during emergency shutdown must primarily be avoided to protect the fuel cell [303], in the mHAT case, surge must be avoided to protect the compressor.

Error provoked shutdown

In case the shutdown is provoked by an error (in most cases a flameout), the error signal of the mGT controller comes a few seconds after the event has happened. During this period, the compressor rotational speed has already decreased, resulting in a compressor surge, even before the blow-off

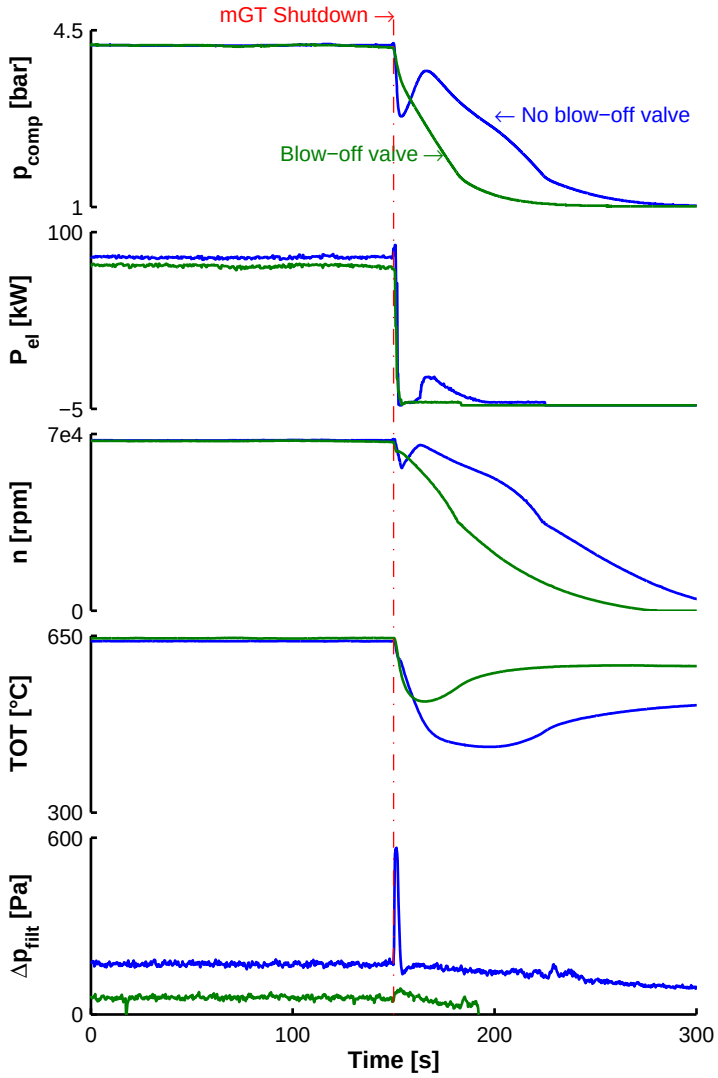

Figure 6.10: After installing a blow-off valve, compressor surge during shutdown of the mHAT could be avoided.

valve control system can open the valve after receiving the error signal (Figure 6.6).

To protect the mGT against surge in this case, initially an additional pressure controlled opening signal was sent to the blow-off valve. In case a sudden pressure drop was recorded, the blow-off valve needed to be opened. The whole system however reacted too slow, resulting in a compressor surge during shutdown. Since the reduction in pressure results from the decreasing rotational speed, there is a delay on this pressure decrease. To detect the flameout more quickly, the pressure control was replaced by a speed guard. When a highly negative slope in the rotational speed was detected, meaning a flameout had occurred, the blow-off valve was opened. The results of the speed guard were better, however the signal suffers from some noise, leading to unwanted blow-off valve openings. In addition, the detection of flameouts was not fast enough in some cases, still resulting in compressor surge. This indicates that an actual flame detection mechanism (UV or temperature sensor) should be installed in the combustion chamber to detect the flameouts directly.

The installation of a check valve is a more robust protection against surge. These check valves however cause an additional pressure drop over the compressed air network of 10 %. Since the pressure drop over this network is already considerably high, this would lead to further surge margin reduction and loss in electric efficiency (Figure 6.3). Rather than installing this check valve, I decided to perform the initial test while bleeding compressor air, to keep the operating point away from the surge limit.

6.3 mHAT experimental results

All experiments discussed in this section were performed using the *wet start-up* procedure. In addition, air was bled during start-up to increase the surge margin. Experiments were performed at different power levels. Maximum power level was 90 kW_e, since due to the additional pressure drop over the saturation tower and piping network, the nominal electric power output of the Turbec T100 mGT (100 kW_e) could no longer be reached. To compensate the pressure losses, a higher compressor mass flow rate and higher pressure ratio are necessary. Therefore the compressor has to speed up, however it had reached its maximum rotational speed of 70 000 rpm before 100 kW_e electric output was reached. For each water

injection experiment, a dry reference with or without air bleed (depending on the performed wet experiment) was taken before, in between or at the end of the injection experiments (depending on the test progress).

For all water injection experiments, the electric efficiency (average and instantaneous) is calculated using following formula:

$$\eta_{\mathrm{el}} = \frac{P_{\mathrm{el}}}{\dot{m}_{\mathrm{fuel}}\mathrm{LHV}} \tag{6.1}$$

(same as Equation 3.7). Using Equation 6.1, the error on the electric efficiency can be determined:

$$\left|\frac{\Delta\eta_{\mathrm{el}}}{\eta_{\mathrm{el}}}\right| \leq \left|\frac{\Delta P_{\mathrm{el}}}{P_{\mathrm{el}}}\right| + \left|\frac{\Delta\dot{m}_{\mathrm{fuel}}}{\dot{m}_{\mathrm{fuel}}}\right| + \left|\frac{\Delta\mathrm{LHV}}{\mathrm{LHV}}\right|. \tag{6.2}$$

The relative error on the electric efficiency is 3 % resulting in a 0.9 % absolute error (subsection 3.1.2). To calculate the effect of the water injection on the electric efficiency, the difference should be taken between wet and dry efficiency. This will lead to an absolute error of 1.8 % on the absolute efficiency increase.

An initial test at 60 $\mathrm{kW_e}$ power demand and with air bleed clearly shows that the electric efficiency increases due to the water injection (Figure 6.11). With an increasing water flow rate, the electric efficiency will increase more. The injected water flow rate was controlled by changing the injection pressure – by increasing the rotational speed of the circulation pump and by changing the position of the bypass valve – or by opening the valve of an additional nozzle, allowing a larger mass flow rate. Measurements of the exact injected water mass flow rate are however incorrect in this test. The *RAMC* rotameter is a variable area flow meter, using a float to measure the flow rate. Due to a crack in the water circuit just before the flow meter, the sensor could not give any reading. The amount of injected water was thus monitored visually through the loop holes (Figure 6.12).

Although the T100 mGT was operating in constant power mode, the generated power increases with increasing water flow rate (Figure 6.11). Due to the air bleed and additional air pressure drop over the piping network and the saturation tower, the compressor needs to speed up to reach the requested power output. For each power output, the control system has however a fixed set of inlet air temperatures linked to predefined rotational speeds. During start-up, the controller will aim for this point. Due to the air bleed and pressure loss, the controller will move the compressor away

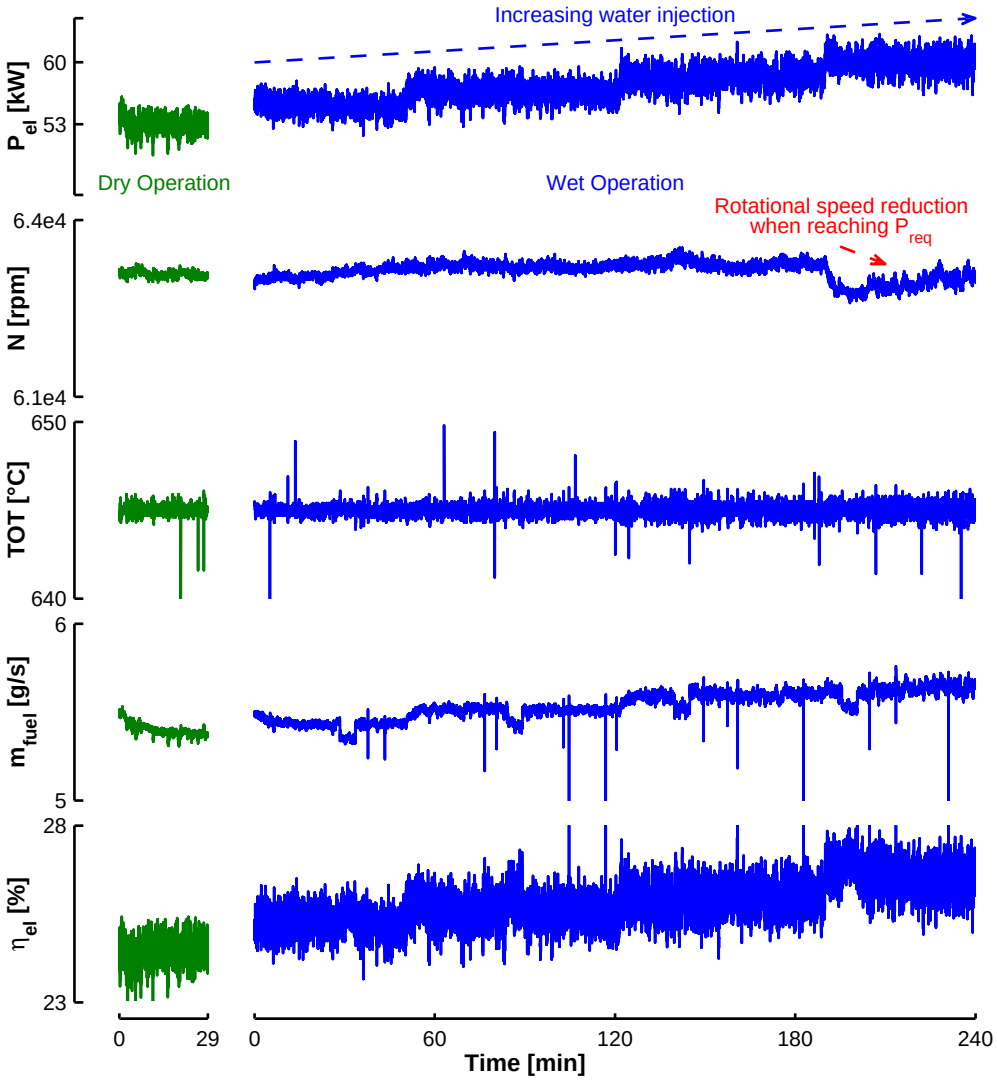

Figure 6.11: Increasing the injected water mass flow rate at part load ($60\,\mathrm{kW_e}$) results in higher power production and electric efficiency.

(a) **(b)**

Figure 6.12: The injected flow rate was monitored through the saturation tower loop holes. The injected water flow rate from (a) corresponds to the initial water flow rate, while (b) shows the water flow rate after increasing the injection pressure.

from this operating point (off-design). The deviation of this operating point is however limited. For each power output, a maximum allowed rotational speed is given. Once this speed is reached, the mGT will keep operating at constant maximum rotational speed, rather than at constant power production mode. Measurements of the rotational speed indicate that in dry mode and at low water injection flow rates, the rotational speed remains constant (Figure 6.11). By adding water to the mGT working fluid, the produced electric power P_{el} will increase due to the higher turbine mass flow rate. In normal operating conditions, the control system will reduce the rotational speed to keep the power output constant. Since $P_{\mathrm{el}} < P_{\mathrm{req}}$, the controller will keep the rotational speed constant at the limit. Once enough water is injected and evaporated so that the requested power output of $60\,\mathrm{kW_e}$ is reached, the control system will start to reduce the rotational speed to keep P_{el} constant.

The electric efficiency increases, although the consumed fuel flow rate increases (Figure 6.11), while Aspen® simulations (Table 5.4) predicted a reduction. The action of the controller is again responsible for this mGT behaviour. While Aspen® simulations used a constant power mode for the controller, the experiments from Figure 6.11 were actually performed at constant rotational speed due to the pressure loss and air bleed. A constant rotational speed leads to a constant compressor mass flow rate. Increasing the water injection will heighten the water fraction in the compressed air, changing the heat capacity considerably. Therefore more fuel needs to be burned to keep TOT constant during the test (Figure 6.11). The higher fuel flow rate is however compensated by the higher power production, explaining the efficiency increase. Due to the water injection, the electric efficiency increases from $23.3 \pm 0.9\,\%$ in the dry case to $25.5 \pm 0.9\,\%$ at the highest water injection rate.

Bleeding air has a huge impact on the mGT performance (Figure 6.13, Table 6.1). The tests with and without air bleed both were performed at $80\,\mathrm{kW_e}$ and injection of $10\,\mathrm{m^3/h}$ of heated water. In both bleeding and non-bleeding case, produced electric power P_{el} is constant and equal to the requested power output of $80\,\mathrm{kW_e}$. To reach the same P_{el} in the bleeding case, rotational speed needs to be increased by 2170 and 2665 rpm respectively for the dry and wet case. TOT is in all cases constant and equal to 645 °C. Fuel consumption is also strongly negatively affected by the air bleed. The fuel flow rate is 9 % higher in both cases, resulting in an absolute efficiency loss of $2.8 \pm 1.8\,\%$ and $2.9 \pm 1.8\,\%$ for dry and wet operation. The effect of water addition on the absolute efficiency increase is

somewhat independent of the air bleed ($1.4 \pm 1.8\,\%$ and $1.5 \pm 1.8\,\%$).

During mGT operation, the blow-off valve opened due to noise on the rotational speed signal (Figure 6.13). A blow-off valve opening leads to a sudden reduction in rotational speed, pressure ratio and produced electric power. The controller will try to compensate by increasing the rotational speed, however the blow-off flow rate is too high, so the controller cannot recover steady-state operation. Closing the valve manually within 10 s after the opening allows the mGT to recover the steady-state operation. Directly after closing the valve, mGT speeds up and power production increases, due to the action of the controller. After a few seconds, the mGT operates in the same state as before. If the blow-off valve is closed too late, the mGT will shut down, since the controller was not able to restore stable operation. Increasing the blow-off trigger value will prevent this problem, however a possible flameout and following compressor surge can be missed. Therefore, I decided not to adapt the blow-off control. Since the issue only takes a few seconds, it has no effect on the global performance after averaging over a period of 1 h.

Full water injection at 80, 85 and 90 $\mathrm{kW_e}$ and no air bleed resulted in stable mHAT operation at reduced rotational speed, pressure ratio and increased electric efficiency (Figure 6.14). The water injection has similar effects on the mGT performance in all cases: constant generated electric power, reduced rotational speed, maximum constant TOT of 645 °C, reduced fuel flow rate and increased electric efficiency. At 85 $\mathrm{kW_e}$ power production, the blow-off valve opened again unwanted several times. The spikes in the natural gas flow rate are a result of unsteady operation of the natural gas compressor. Due to the high temperature in the T100 mGT room, the heat from the natural gas compressor could not be evacuated, resulting in several gas pressure drops and followed sudden changes in natural gas flow rate. These changes influence the instantaneous calculated electric efficiency. The final average results of the experiments can be found in Table 6.1.

The electric efficiency increases for all experiments since the fuel flow rate reduces while the produced electric power remains constant (Table 6.1). In all cases, the produced electric power P_{el} is equal to the operator controlled requested power output P_{req}. The fuel flow rate $\dot{m}_{\mathrm{fuel}}$ reduces due to the additional water in the working fluid. Since the inlet air temperature of the compressor changed during the test (Figure 6.15), the dry electric efficiency however needs to be compensated. Values of the dry reference efficiencies were corrected using the data from Figure 3.7. Final average elec-

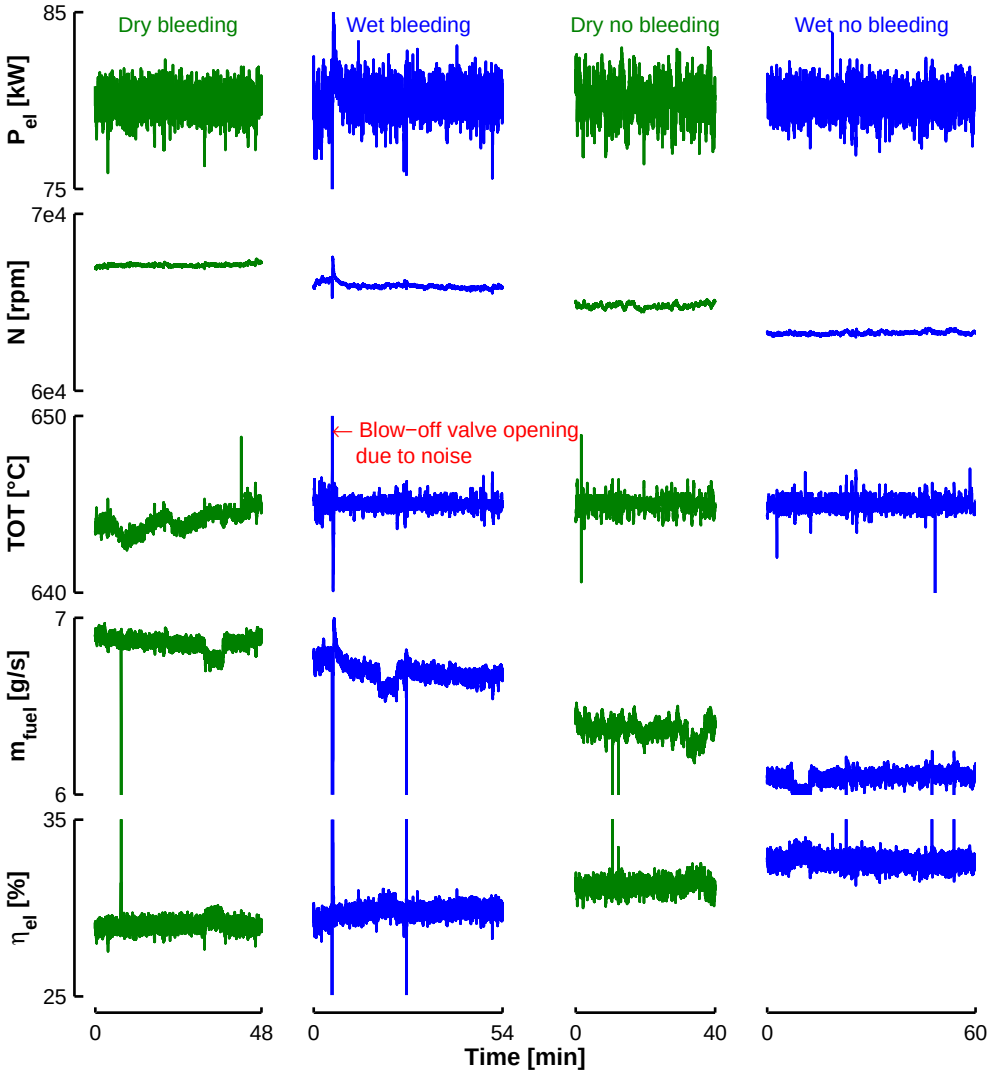

Figure 6.13: Bleeding air has a severe negative impact on the mGT performance in dry and wet operation (test performed at 80 kW_e power output).

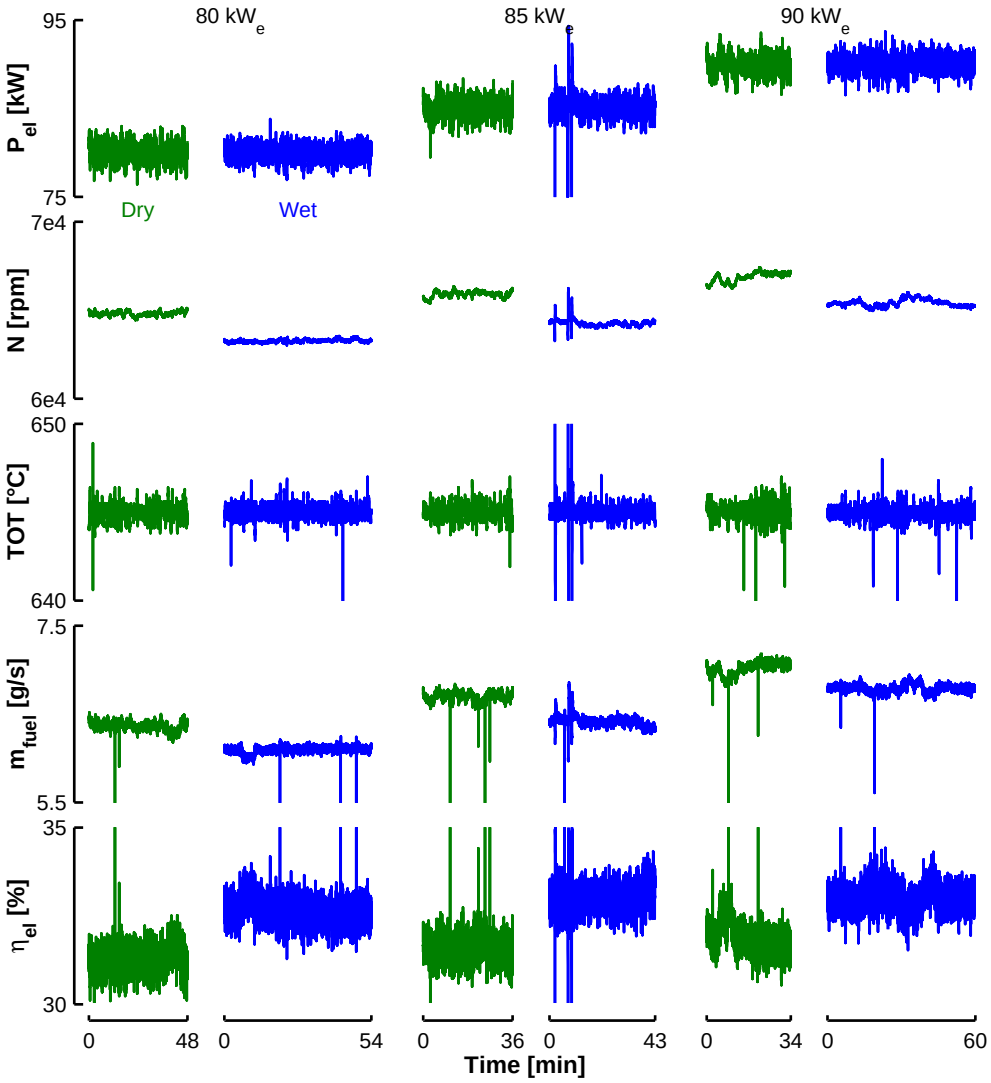

Figure 6.14: Experiments with water injection at different power outputs all result in stable mGT operation at constant power production, reduced rotational speed and fuel flow rate and increased electric efficiency.

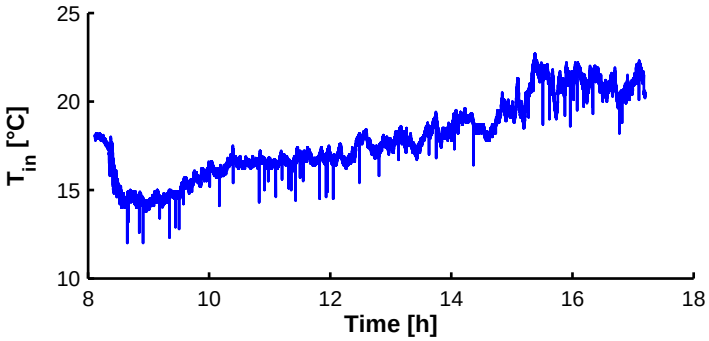

Figure 6.15: During the water injection test, inlet air temperature (T_{in}) increases due the changing atmospheric conditions and the slowly heating of the 100 mGT room, making it necessary to compensate the efficiency results.

tric efficiency increases amounted $1.0 \pm 1.8\,\%$, $1.1 \pm 1.8\,\%$ and $0.8 \pm 1.8\,\%$ respectively, which is below the simulations results of Aspen® (1.7, 1.6 and 1.5 %). In addition, these changes are in the range of the accuracy on the efficiency measurements.

Even though the nominal amount of water is injected in the cycle ($10\,\text{m}^3/\text{h}$), electric efficiency increase was below the simulated values. This indicates that the compressed air is most likely not fully saturated, as will be shown later on. A too low water injection temperature or a too large droplet diameter are two possible explanations for the lower humidity level. Due to control issues, it was not possible to increase the water temperature till the necessary 80 °C. Secondly, droplet diameter can be too large, resulting in a too low surface for heat exchange. Laser techniques should be used to determine the exact droplet size.

Unfortunately, the saturation level could not be determined, since the compressor air mass flow rate was not known. Although a temperature and pressure compensated *Honeywell* vortex flow meter was installed in-between the compressor outlet and the saturation tower inlet, the measurement values are not correct. The vortex flow meter requires a straight air flow, but due to a lack of space, the installation requirements of 20 diameter straight pipe in front of the sensor could not be respected. In addition, the radial compressor introduces vortices in the air flow, resulting in a too high measured value. To measure the air flow rate correctly, a flow straightener should be installed.

Table 6.1: Results of stable water injection tests.

	Bleed		**No Bleed**					
	Dry	**wet**	**Dry**	**wet**	**Dry**	**wet**	**Dry**	**wet**
General								
P_{ref} (kW_e)	80.0	80.0	80.0	80.0	85.0	85.0	90.0	90.0
P_{el} (kW_e)	79.2	80.0	80.0	80.0	85.0	85.0	90.1	90.2
$\dot{m}_{\text{fuel}}$ (g/s)	6.9	6.7	6.4	6.1	6.7	6.4	7.0	6.8
η_{electric} (%)	27.5	28.8	30.3	31.7	30.5	32.0	30.8	31.8
Compressor								
p_{out} (bar)	4.08	3.97	3.88	3.76	4.01	3.88	4.13	4.00
T_{in} (°C)	14.6	16.4	20.8	16.7	21.1	17.6	20.6	18.1
T_{out} (°C)	190	189	190	179	195	185	199	190
$\dot{m}_{\text{air}}$ (kg/s)[1]	0.85	0.82	0.78	0.74	0.81	0.77	0.84	0.80
N (krpm)	67.0	65.9	64.8	63.2	65.9	64.3	66.8	65.3
Saturation tower								
$p_{\text{air,out}}$ (bar)	4.03	3.92	3.83	3.71	3.96	3.82	4.08	3.95
$p_{\text{water,out}}$ (bar)	–	4.92	–	4.71	–	4.80	–	4.75
$T_{\text{air,in}}$ (°C)	108	183	186	175	191	179	192	182
$T_{\text{air,out}}$ (°C)	146	70.9	170	71.1	172	72.4	163	71.5
$T_{\text{water,in}}$ (°C)	–	71.0	–	71.3	–	72.6	–	72.0
$T_{\text{water,out}}$ (°C)	–	70.8	–	71.3	–	72.7	–	72.4
$\dot{m}_{\text{water,in}}$ (m^3/h)	0	10.3	0	10.4	0	10.3	0	9.2
Recuperator								
$T_{\text{cold,in}}$ (°C)	171	144	182	139	186	139	184	145
CIT (°C)	585	591	597	592	596	592	594	590
Turbine								
TOT (°C)	641	645	645	645	645	645	645	645
Economizer								
$T_{\text{air,in}}$ (°C)	213	197	228	193	231	193	228	196
$T_{\text{air,out}}$ (°C)	83.2	97.1	93.6	97.4	96.2	98.8	94.0	98.2
$T_{\text{water,in}}$ (°C)	45.8	63.8	55.5	64.8	57.6	66.0	55.4	64.7
$T_{\text{water,out}}$ (°C)	56.9	71.2	63.8	71.6	66.2	73.0	64.1	73.3
$\dot{m}_{\text{water}}$ (m^3/h)	9.2	10.0	10.0	10.0	10.0	10.0	10.0	9.4
$\dot{Q}$ (kW_th)	120	93.3	125	87.3	130	88.7	131	92.3

[1]The compressed air mass flow rate through the compressor is calculated using the compressor map, pressure ratio and rotational speed.

This flow straightener will however introduce an additional pressure drop, so I decided not to include this in the piping network.

For all conducted wet experiments (nominal water injection experiments from Table 6.1 and the preliminary experiments), electric efficiency increases, but the measured efficiency increase is below the predictions from Aspen® simulations (Figure 6.16). In addition, the error on the calculated efficiency is very large. Since the inlet air temperature changes between the wet test and the dry reference, values for electric efficiency of the dry reference were again corrected using the dry data of Figure 3.7. Since the injected water mass flow rate and/or temperature were too low, which results in an incomplete saturation of the compressed air, the measured efficiency increase is below the predictions from Aspen® simulations. Unfortunately, due to aforementioned reasons, this relative humidity or the exact amount of evaporated water could not be determined. In addition, due to the crack in the water system, the injected amount of water in the saturation tower is unknown for some of the tests (the water flow rate is only known for the tests shown in Table 6.1). Since the humidity level and injected amount of water are not known, it is not possible to compensate the Aspen® simulations. By reverse engineering in Aspen®, trying to link the measured efficiency increase with a certain humidity level, the evaporated amount of water could be determined for the experiments from Table 6.1. Simulations indicating 19, 21 and 17 g/s of water was evaporated during the experiments, which is below the necessary amount of water for full saturation simulated in Aspen® (42, 44 and 46 g/s). General results however show that water injection has a positive effect on electric efficiency, even at low injection rates and water temperature. In addition, stable mGT operation was successfully achieved during all experiments at different power outputs, showing the robustness of the Turbec T100 mGT control system.

Although the outgoing water and air of the saturation tower have the same temperature, indicating thermal equilibrium and fully saturated air, the recuperator cold stream inlet temperature is much higher than the saturated air temperature after the saturation tower (Table 6.1). Both temperature sensors are located on the same compressed air pipe, connecting the saturation tower outlet duct with the recuperator inlet duct. This difference cannot be explained by the measurement accuracy or possible heat losses, since the difference is too big. The sensor measuring the saturation tower outlet temperature is however located directly behind the droplet separator, while the temperature of the cold air entering the recuperator is measured further downstream at the recuperator inlet. The temperature

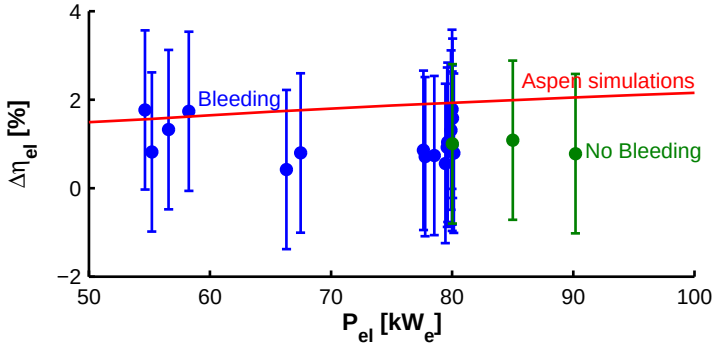

Figure 6.16: The measured increase in electric efficiency is below the prediction from the Aspen® simulations due to an incomplete saturation of the compressed air

of the outgoing air of the saturation tower is equal to the water outlet temperature which indicates droplets are still present in the air and deposit on the sensor. This results in a lower air temperature reading. The value given by the sensor is in-between the real air temperature and the wet bulb temperature. After travelling through the piping, all remaining droplets have been separated from the flow or evaporated, leading to a correct air temperature measurement. The air leaving the saturation tower is thus clearly not fully saturated. These measurements were used to estimate the amount of evaporated water. Assuming the measured temperature behind the saturation tower is equal to the wet bulb temperature, the absolute humidity could be calculated (27, 29 and 22 g/kg). Multiplying with the calculated air mass flow rate, gives an estimation of the amount of evaporated water (20, 22 and 18 g/s). These results correspond to the values found by reverse engineering in Aspen®. Similar observations were done during the preliminary experiments (Figure 6.17). The difference in measured temperatures $T_{\mathrm{rec,in}}$ and $T_{\mathrm{sat,out}}$ is a clear indication that the air is in these experiments also not fully saturated, explaining the limited efficiency increase (Figure 6.16).

No additional waste heat is recovered from the water during the final wet experiments. The outgoing water temperature is equal to the ingoing water temperature (Table 6.1). This indicates that the necessary evaporation heat is delivered by the air and not taken from the water. Also in most of the preliminary experiments – depending on the operating conditions: water injection temperature and mass flow rate – no waste heat is recovered, resulting in a negative water temperature difference (Figure 6.17). This indicates again that the evaporation heat is taken from the air, rather than from the water. In addition, heat was transferred from the air to the water, so that the saturation tower acted as an aftercooler.

Even though no waste heat is recovered in the saturation tower, electric efficiency still increases, since more heat is recovered in the recuperator. The higher heat recovery is illustrated by the lower recuperator inlet temperature ($T_{\mathrm{cold,in}}$) and the nearly constant CIT. Due to the humidification process, the recuperator inlet air temperature is lower while the heat capacity of the working fluid has increased. This requires a higher heat transfer to obtain the same CIT. The slight drop in CIT is a result of the limited area for heat transfer in the recuperator. Therefore, the 50 °C hot pinch could not be respected. Final hot pinch temperature however is still reasonable (∼53 °C). The nearly constant temperature difference between CIT and TOT (hot pinch), measured during the preliminary experiments, indicates that the

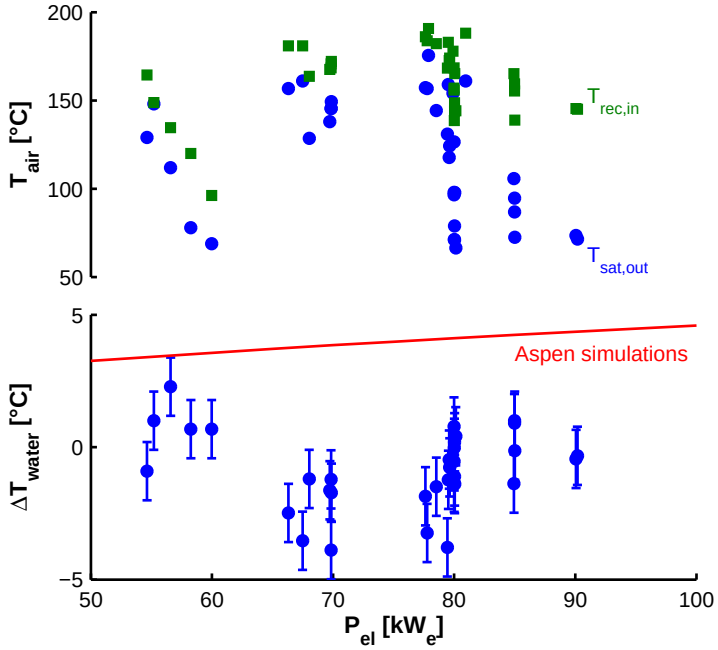

Figure 6.17: The temperature drop over the saturation tower of the compressed air and injected water is limited due to an incomplete saturation.

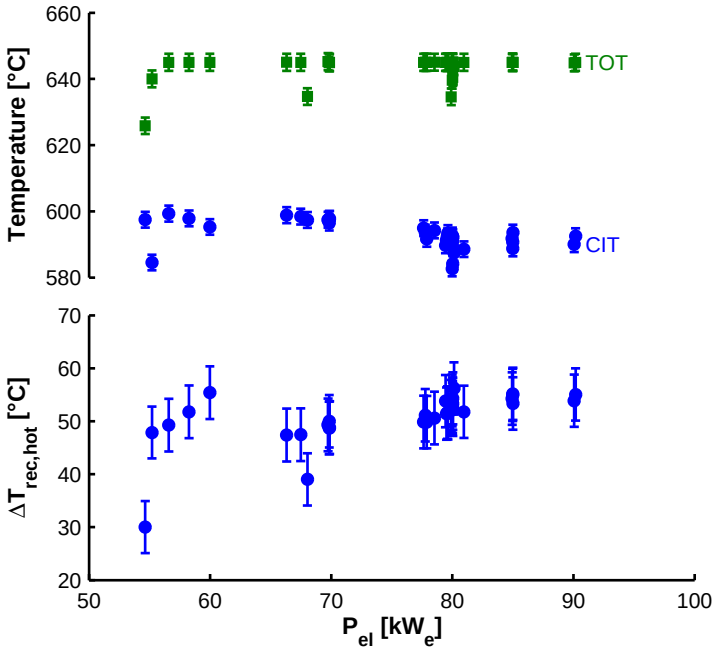

Figure 6.18: The constant hot pinch temperature indicates that the Turbec T100 mGT has a favourable off-design behaviour for the mHAT application.

off-design behaviour of the recuperator is very favourable (Figure 6.18). Independent of the produced electric power and the humidity level, hot pinch temperature remains constant and equal to 50 °C. The constant measured temperature difference indicates that the recuperator area for heat transfer is sufficient to handle the higher necessary heat flux and has thus a very favourable off-design behaviour. Finally, mGT control system succeeds in keeping TOT constant.

During the final experiments, the nominal amount of water is injected in the saturation tower (10 m^3/h) with an average injection pressure difference of 1 bar (Table 6.1). The injection nozzles were selected to deliver the nominal water flow rate at a pressure difference of 0.5 bar. A slightly higher injection pressure is however necessary to compensate the pressure losses over the collector and the valves controlling the feed of each nozzle. The slightly reduced injection rate at 90 kW_e is a result of a lower injection pressure.

Increasing the injection pressure over the saturation tower will increase

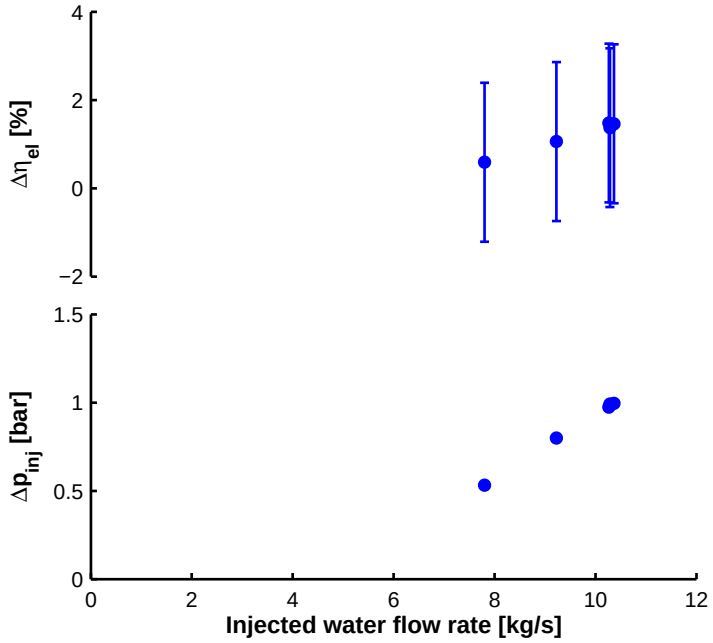

Figure 6.19: Increasing the water flow rate will increase the electric efficiency due to the higher energy transfer in the saturation tower. The water flow rate can be increased by heightening the injection pressure.

the water flow rate (Figure 6.19). By increasing the water flow rate, more contact area will be available for heat and mass transfer. Due to this higher heat and mass transfer, the electric efficiency increase will grow (Figure 6.19). Changing the rotational speed of the circulation pump will increase the injection pressure and thus the injected mass flow rate. In addition, a higher injection pressure results in smaller droplets.

During the different dry and wet experiments, a pressure drop below 0.05 bar was measured over the saturation tower and the compressed air network for most experiments (Table 6.1). There is no measurable difference between the pressure loss during dry and wet experiments. As simulated, the pressure drop due to water injection is 33 Pa (see section 5.3), which is below the minimal difference of 300 Pa that can be observed by the pressure sensors. Similar pressure drops of 0.05 bar were observed during the preliminary wet and dry experiments (Figure 6.20). During one particular experiment

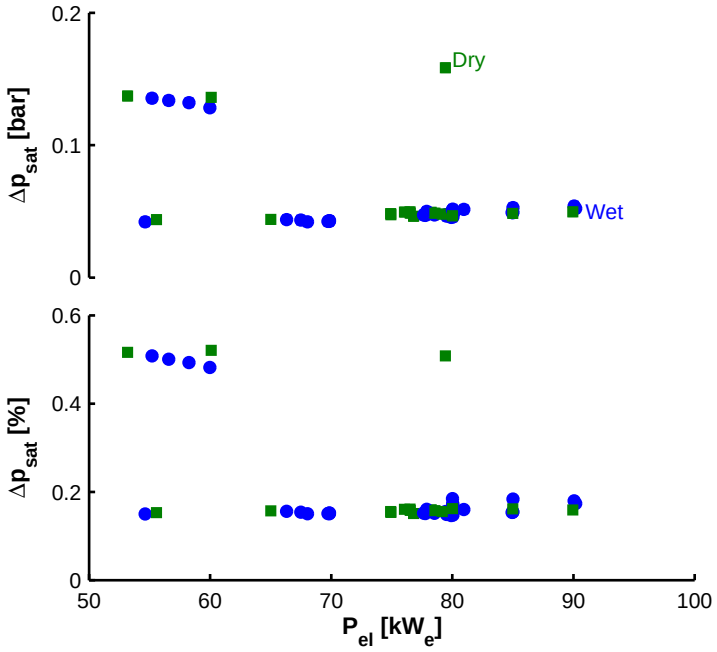

Figure 6.20: The additional pressure drop due to the water injection is very low.

however, an increased pressure drop of above 0.1 bar was measured. This is possibly due to an issue in the configuration like a not fully opened valve. The available measurement results cannot give an inclusive explanation for this sudden increased pressure drop. Later experiments no longer showed such behaviour. The relative pressure drop remains also constant with decreasing power output (Figure 6.20). Since the loss in pressure slightly reduces with reducing power output, the relative pressure loss remains constant, resulting in a similar effect on final electric efficiency.

6.4 Conclusion

A Turbec T100 mGT has been equipped with a saturation tower in order to show the beneficial effect of water addition to the mGT cycle. Results of the experiments on the mHAT test rig have been presented.

The spray saturation tower was added to the cycle between compressor

outlet and recuperator inlet. The water was injected in this saturation tower using specific nozzles that can provide the necessary droplet diameter while reducing the necessary pump energy. In addition, several sensors were installed to capture the effect of water injection on the mGT performance.

The integration of the saturation tower in the cycle required a special *Wet start-up* procedure and shutdown procedure. Both procedures were developed to protect the mGT compressor against surge. The mGT could successfully be started using the *Wet start-up* procedure under water injection conditions, resulting in stable runs. During start-up, air must be bled to keep the compressor operating point away from surge. Opening a blow-off valve during engine shutdown also keeps the compressor away from surge.

Final wet experiments at nominal water injection resulted in stable mHAT operation at reduced rotational speed, pressure ratio and fuel consumption. During these wet tests, an absolute electric efficiency increase of $1.0 \pm 1.8\,\%$, $1.1 \pm 1.8\,\%$ and $0.8 \pm 1.8\,\%$ was recorded at power levels of 80, 85 and $90\,\mathrm{kW_e}$. The electric efficiency increase is below the Aspen® simulation results, which indicates that the compressed air leaving the saturation tower is not fully saturated. Too large droplets or a too low water injection temperature are two possible explanations for the incomplete saturation.

Chapter 7

Conclusions and future work

In this final chapter, the main conclusions of this PhD thesis are summarised. Special focus is placed on the comparison between the main objective and the final results. This allows to see to what extent these goals have been achieved. Additionally, the perspectives for the mHAT are discussed. First a set of possible improvements for the developed mHAT test rig are formulated. Then, future opportunities for flexible heat production from a mGT are given.

7.1 Conclusions

mGTs were found very promising for small-scale CHP operation. Despite the huge market potential and advantages over the ICE, the mGT never fully penetrated the market. The major drawback was their heat-driven use. In periods with low or no heat demand, part of the produced heat should be discarded to keep the mGT running at high electric load. Depending on the economic conditions, this could even lead to a forced mGT shutdown which has a severe negative impact on the profitability. The relative low mGT electric efficiency of 30 % makes them less attractive compared to ICEs, explaining their low market share. Converting the mGT into a mHAT cycle was found a possible route for improving the overall economic performance of the mGT CHP. The injection of water in the cycle offers a route for waste heat recovery during periods with low heat demand. The evaporated water in the saturation tower will enhance the mGT performance, resulting in an increased electric efficiency, which allows the mGT to keep running. Converting the mGT into a mHAT cycle was found economically feasible, depending on the electricity and fuel prices.

The main goal of the thesis was the development of a humidified mGT cycle for flexible heat production. In literature, several studies exist on the effect of water (steam/liquid) injection on the mGT performance. A generic framework, identifying and designing the optimal cycle, however was missing. In this thesis, I developed such a framework for the optimal humidified mGT cycle development. This framework consists of four major steps: cycle identification, cycle development, cycle construction and validation. First, the dry and wet operation were simulated and experimentally validated to predict the correct mGT behaviour under humidified conditions. Afterwards, these models were used in the development phase to identify the optimal cycle layout using a two-step method. In the development process, this ideal model was later converted into a model for the considered Turbec T100 mGT. In addition, a proper water injection system for this cycle had to be developed. The next step was the conversion of the mGT into a mHAT. The developed water injection system was constructed and integrated in the cycle, converting the Turbec T100 mGT into a mHAT. Finally, experiments have been conducted on the constructed test rig. The experimental results have been used to evaluate the mHAT performance and validate the developed model of this mHAT cycle.

In chapter 2, the literature review on the mGT cycle showed that the attrac-

tiveness of the machine can only be improved by using ceramic materials in the cycle. Using ceramic materials allows mGTs to operate at higher TIT, resulting in electric efficiencies up to 40 %. Since low cost ceramic turbine parts are not yet available, other methods need to be exploited to improve the economic performance of the mGT. Converting the mGT into a mHAT cycle is one of them. The HAT cycle is identified in literature as the optimal humidified GT and a similar performance is expected for mGT cycles. The two HAT and AHAT demonstration plants were studied to get more insight in the technical problems inherent to humidified GT cycle construction and operation. Finally, different studies on the Turbec T100 mGT showed the capacity of the machine to operate at off-design conditions and even with a modified cycle layout.

For the development of a humidified mGT cycle, accurate dry performance data is necessary. A dry Aspen® model of the mGT cycle was developed and validated against measurements (chapter 3). The results indicated that both nominal and part-load performance predicted by the simulations corresponded to the measurement results. In addition, the dry operating line of the compressor could be verified.

Next to the dry mGT performance, the behaviour of the mGT in wet conditions needs to be determined prior to the humidified mGT development. The mGT behaviour under steam injection was studied by means of simulations and experiments in chapter 4. These experiments showed the capability of the Turbec T100 mGT to deal with the injected steam and demonstrated the beneficial effect of the injection on the performance. Steam injection experiments resulted in stable mGT operation at reduced rotational speed and in a higher electric efficiency. Pressure ratio and air mass flow rate measurements showed the effect of steam injection on the compressor operating point, indicating a surge margin reduction. The performance increase predicted with Aspen® could be validated using experiments by means of a perturbation analysis. Finally, additional experiments on an atmospheric, variable-swirl premixed combustor indicated that it is possible to maintain a stable and complete combustion under steam injection conditions.

The actual humidified mGT cycle was developed in chapter 5. First, direct injection of preheated water in the mGT cycle was identified as the optimal route for waste heat recovery through water injection by using a two-step method. The difference between the different considered cycle layouts was however limited. Therefore, the mHAT cycle layout was used for humidified mGT development, since this cycle still allowed to operate the mGT in CHP

mode. Simulations predicted a 3.8 % absolute electric efficiency increase. Secondly, a sensitivity analysis showed that the choice of hot pinch and stack temperature has a huge impact on the cycle performance. In addition, the non-idealities of the heat exchanger network and the mGT operation mode have a large impact on the final mHAT performance. The limited surface for heat exchange in combination with a lower TIT negatively influenced the potential for the water injection. The final increase in efficiency when transforming a Turbec T100 into a mHAT was 2 % absolute efficiency increase. Finally, the necessary saturation tower for compressed air humidification was developed using a two-phase flow model. This model indicated that it is possible to construct a spray saturation tower with similar pressure drop and size as the classic saturation tower with packing material, used in other applications. The final suggested design was a cross-flow injection saturation tower.

To test the concept of water evaporation in the mGT cycle, the Turbec T100 mGT was equipped with a spray saturation tower (chapter 6). The spray saturation tower was constructed based on the simulations of chapter 5 and integrated into the cycle. Additionally, several sensors were installed to capture the effect of humidification on the performance. Using a specific developed wet start-up and shutdown procedure, the effect of humidifying the compressed air on the mGT performances was studied experimentally. These tests resulted in stable operation at constant power output and reduced fuel flow rate, resulting in absolute electric efficiency of 1.0 ± 1.8, 1.1 ± 1.8 and 0.8 ± 1.8 % at power levels of 80, 85 and 90 kW_e. The electric efficiency was below the predictions from the Aspen® simulations results (2 %), which indicated that the compressed air was not yet fully saturated. These experiments however indicated the beneficial effect of compressed air humidification on the mGT performance. Further optimizing the mHAT test rig operation will increase the final electric efficiency increase.

7.2 Future work and perspective

In this section, first recommendations for the improvement of the mHAT test rig and the mHAT at full humidification in general are formulated. Although the final experiments were successful and showed an efficiency increase, this increase is still below simulation results. Further improvements of the test rig infrastructure and operation are necessary to fully exploit the potential of the rig. Secondly, possible further research on the mHAT

is given. Before the application can be introduced in the energy market, mixed-mode operation and transient behaviour should be studied.

7.2.1 Improving the current Turbec T100 mGT test rig

The final test results highlighted the shortcomings of the test rig: electric efficiency increase and injected water mass flow rate need to be determined accurately, the loss to the auxiliaries is still too high and a proper surge protection is needed.

For a more accurate efficiency increase determination, a perturbation analysis must be performed on the mHAT test rig. The final experiments indicated an electric efficiency increase of 1 % (Table 6.1). The uncertainty on these results is however very high. Developing an analytic perturbation model of the mHAT cycle, similar to the model developed for the steam injection experiment (subsection 4.1.2), allows a more accurate efficiency determination. The implementation of a perturbation analysis will however be more complicated than in the steam injection case, because of the introduction of the saturation tower in the cycle. Accurate determination of the amount of injected water is necessary for this analysis. Once the electric efficiency increase is determined, the economic analysis needs to be repeated with the correct efficiency increase to find the impact on economic performance.

Measuring the relative humidity of the compressed air leaving the saturation tower would give the evaporated water flow rate. For the validation of the Aspen® simulation model, accurate measurement of the relative humidity is necessary. This can be done directly, by installing/developing a relative humidity sensor that can also operate at high temperature when the mHAT test rig is operated without water injection.

The losses to the auxiliaries can be minimized by minimizing the water injection pressure for full humidification. Reducing the auxiliary losses results in better economics. A minimum pressure difference over the nozzles is necessary to make sure that the droplet size is small enough for full compressed air humidification. Reducing the injection pressure during wet experiments while measuring the relative humidity allows the determination of this pressure.

Finally, an adequate surge protection system needs to be installed. More specifically, the detection of flameouts needs to be done more quickly, since

the currently used rotational speed triggered system is not capable of detecting the flameout fast enough, with a compressor surge as a result. An actual flame detecting sensor (measuring the chemiluminescence, the combustion temperature or the presence of radicals) can detect flameout upon occurrence. Based on this information, the blow-off valve can be opened, protecting the compressor.

7.2.2 Future prospectives

Mixed mHAT mode – operation with partial humidification and partial heat production – is necessary to enable full flexible heat production from a mGT. The simulations and experiments presented in this thesis only take into account full dry or full wet mode. The actual heat demand profile (Figure 1.9) hardly allows the mHAT to run in one of these two modes. During most periods of the year, there is still a heat demand that needs to be covered. Part of the heat from the exhaust gases will be used to produce the hot water to fulfil this heat demand. This results in a lower available energy for the humidification process. It is essential for correct economic analysis that the effect of the heat extraction on the mHAT performance is quantified. By means of simulations and experiments, the optimal route for mixed mode electricity and heat production can be determined. Different strategies need to be developed and tested in order to determine the most economical solution.

Full transient characterisation is also needed before the mHAT can be introduced in the energy market. In this thesis, only steady-state simulations and experiments were presented. When the mHAT would operate in a specific heat grid, the operation is controlled to meet the electric and thermal power demand. This includes changes from dry to partial/fully wet mode and vice versa. The effect of compressed air humidification on the surge margin and combustion stability has been studied in steady-state conditions. These conditions however differ during transient operation. The transient behaviour of the mHAT needs to be identified in order to be able to define a minimum time step for the final mHAT control.

The minimum required water quality for the mHAT needs to be determined. The development of the mHAT cycle was chosen over other possible humidified mGT cycles because this cycle allows a lower water quality. A lower water quality reduces the water make-up costs, resulting in a positive effect on the economics. In the conducted experiments with steam (chapter 4) and

water (chapter 6), fully demineralized water has been used (conductivity below 10 µS/cm). In the final commercial mHAT, a lower water quality will be used. Additional experiments with different water qualities need to be performed. Analysing the quality of the circulating water and the contaminants in the compressed humidified air would allow the determination of the minimum necessary water quality.

Finally, the impact of the humidified air on the mGT components must be addressed. Adding water to the cycle changes the properties of the working fluid, which affects the heat characteristics of all components. Additional corrosion in the components (especially in the recuperator) may arise. After a few 100 h wet mGT operation, the different components need to be inspected for possible damage due to heat or corrosion.

Bibliography

[1] European Commission, The 2020 climate and energy package, 2011. Online available: http://ec.europa.eu/clima/policies/package/ (accessed: 25-08-2014).

[2] European Commission, 2030 framework for climate and energy policies, 2014. Online available: http://ec.europa.eu/clima/index_en.htm (accessed: 25-08-2014).

[3] European Commission, Roadmap for moving to a low-carbon economy in 2050, 2014. Online available: http://ec.europa.eu/clima/policies/roadmap/index_en.htm (accessed: 25-08-2014).

[4] European Commission, Energy efficiency plan 2011, 2011. Online available: http://ec.europa.eu/energy/efficiency/action_plan/action_plan_en.htm (accessed: 25-08-2014).

[5] European Commission, Energy efficiency directive, 2012. Online available: http://ec.europa.eu/energy/efficiency/eed/eed_en.htm (accessed: 25-08-2014).

[6] European Parliament and European Council, Directive 2004/8/EC of 11 february 2004 on the promotion of cogeneration based on a useful heat demand in the internal energy market, 2004.

[7] Internation Energy Agency (IEA), Global CHP/DHC data, 2007. Online available: http://www.iea.org/chp/data/globalchpdhcdata-currentbaseline/ (accessed: 26-08-2014).

[8] European Environment Agency (EEA), Combined Heat and Power (CHP) (ENER 020) - Assessment, 2013. Online available: http://www.eea.europa.eu/data-and-maps/indicators/combined-heat-and-power-chp-1/combined-heat-and-power-chp-2 (accessed: 19-08-2014).

[9] C. Kiss, Update on cogeneration in Europe – A view from the COGEN Europe National Associations, in: COGEN Europe Annual Conference, 2013, p. 29 pages.

[10] Vlaamse Regulator van de Electriciteits- en Gasmarkt (VREG), Geïnstalleerd vermogen en aantal warmtekrachtinstallaties per provincie, 2014. Online available: http://www.vreg.be/sites/default/files/uploads/statistieken/warmtekrachtkoppeling/20140618-wkc_-_vermogen_en_aantal_installaties_per_provincie.pdf (accessed: 18-08-2014).

[11] S. Gamou, K. Ito, R. Yokoyama, Optimal operational planning of cogeneration systems with microturbine and desiccant air conditioning units, Journal of Engineering for Gas Turbines and Power 127 (2005) 606–614.

[12] S. Gamou, R. Yokoyama, K. Ito, Parametric study on economic feasibility of microturbine cogeneration systems by an optimization approach, Journal of Engineering for Gas Turbines and Power 127 (2005) 389–396.

[13] J. Kaikko, J. Backman, Technical and economic performance analysis for a microturbine in combined heat and power generation, Energy 32 (2007) 378 – 387.

[14] U.S. Department of Energy, Office of Energy Efficiency & Renewable Energy, Office of Power Technologies, Advanced microturbine systems – Program plan for fiscal years 2000 through 2006, 2000. Online available: http://www.energetics.com/resourcecenter/products/plans/samples/Documents/advanced_microturbine_plan.pdf (accessed: 14-09-2014).

[15] S. Sanaye, M. R. Ardali, Estimating the power and number of microturbines in small-scale combined heat and power systems, Applied Energy 86 (2009) 895 – 903.

[16] S. Campanari, L. Boncompagni, E. Macchi, Microturbines and trigeneration: Optimization strategies and multiple engine configuration effects, Journal of Engineering for Gas Turbines and Power 126 (2004) 92–101.

[17] F. Sancho-Bastos, H. Perez-Blanco, Cogeneration system simulation and control to meet simultaneous power, heating and cooling demands, Journal of Engineering for Gas Turbines and Power 127 (2005) 404–409.

[18] P. Katsigiannis, D. Papadopoulos, A general technoeconomic and environmental procedure for assessment of small-scale cogeneration scheme installations: Application to a local industry operating in Thrace, Greece, using microturbines, Energy Conversion and Management 46 (2005) 3150 – 3174.

[19] E. Carpaneto, G. Chicco, P. Mancarella, A. Russo, Cogeneration planning under uncertainty. Part I: Multiple time frame approach, Applied Energy 88 (2011) 1059 – 1067.

[20] E. Carpaneto, G. Chicco, P. Mancarella, A. Russo, Cogeneration planning under uncertainty. Part II: Decision theory-based assessment of planning alternatives, Applied Energy 88 (2011) 1075 – 1083.

[21] Frost & Sullivan, Combined heat and power: Integrating biomass technologies in buildings for efficient energy consumption, 2011.

[22] P. A. Pilavachi, Mini- and micro-gas turbines for combined heat and power, Applied Thermal Engineering 22 (2002) 2003 – 2014.

[23] J. Ho, K. Chua, S. Chou, Performance study of a microturbine system for cogeneration application, Renewable Energy 29 (2004) 1121 – 1133.

[24] L. Galanti, A. F. Massardo, Micro gas turbine thermodynamic and economic analysis up to 500 kWe size, Applied Energy 88 (2011) 4795 – 4802.

[25] F. Delattin, S. Bram, S. Knoops, J. De Ruyck, Effects of steam injection on microturbine efficiency and performance, Energy 33 (2008) 241 – 247.

[26] F. Bozza, M. C. Cameretti, R. Tuccillo, Adapting the micro-gas turbine operation to variable thermal and electrical requirements, Journal of Engineering for Gas Turbines and Power 127 (2005) 514–524.

[27] H. Onovwiona, V. Ugursal, Residential cogeneration systems: Review of the current technology, Renewable and Sustainable Energy Reviews 10 (2006) 389 – 431.

[28] C. Rodgers, 25-5 kW_e microturbine design aspects, in: ASME Conference Proceedings, 2000, ASME paper 2000-GT-626, pp. 1–11.

[29] M. Montero Carrero, W. De Paepe, A. Parente, J. Blondeau, H. Laget, F. Contino, Economic analysis of a micro humid air turbine for combined heat and power based on experimental data, in: J. Yan (Ed.), Sixth International Conference on Applied Energy (ICAE 2014), 2014, p. 7 pages.

[30] M. Jonsson, J. Yan, Humidified gas turbines – A review of proposed and implemented cycles, Energy 30 (2005) 1013 – 1078.

[31] J. J. Lee, M. S. Jeon, T. S. Kim, The influence of water and steam injection on the performance of a recuperated cycle microturbine for combined heat and power application, Applied Energy 87 (2010) 1307 – 1316.

[32] S. Dodo, S. Nakano, T. Inoue, M. Ichinose, M. Yagi, K. Tsubouchi, K. Yamaguchi, Y. Hayasaka, Development of an advanced microturbine system using humid air turbine cycle, in: ASME Conference Proceedings, 2004, ASME paper GT2004-54337, pp. 167–174.

[33] K. Mochizuki, S. Shibata, U. Inoue, T. Tsuchiya, H. Sotouchi, M. Okamoto, New concept of a micro gas turbine based co-generation package for performance improvement in practical use, in: ASME Conference Proceedings, 2005, ASME Paper PWR2005-50364, pp. 1305–1310.

[34] J. Parente, A. Traverso, A. F. Massardo, Micro humid air cycle: Part A – Thermodynamic and technical aspects, in: ASME Conference Proceedings, 2003, ASME paper GT2003-38326, pp. 221–229.

[35] J. Parente, A. Traverso, A. F. Massardo, Micro humid air cycle: Part B – Thermoeconomic analysis, in: ASME Conference Proceedings, 2003, ASME paper GT2003-38328, pp. 231–239.

[36] S. Zhang, Y. Xiao, Steady-state off-design thermodynamic performance analysis of a humid air turbine based on a micro turbine, in: ASME Conference Proceedings, 2006, ASME Paper GT2006-90335, pp. 287–296.

[37] K. Wan, S. Zhang, J. Wang, Y. Xiao, Performance of humid air turbine with exhaust gas expanded to below ambient pressure based on microturbine, Energy Conversion and Management 51 (2010) 2127 – 2133.

[38] M. L. Ferrari, M. Pascenti, A. N. Traverso, A. F. Massardo, Hybrid system test rig: Chemical composition emulation with steam injection, Applied Energy 97 (2012) 809 – 815.

[39] C. Wei, S. Zang, Experimental investigation on the off-design performance of a small-sized humid air turbine cycle, Applied Thermal Engineering 51 (2013) 166 – 176.

[40] H. Nikpey, M. Mansouri Majoumerd, M. Assadi, P. Breuhaus, Thermodynamic analysis of innovative micro gas turbine cycles, in: ASME Conference Proceedings, 2014, ASME paper GT2014-26917, p. 9 pages.

[41] C. Rodgers, Microturbine cycle options, in: ASME Conference Proceedings, 2001, ASME paper 2001-GT-552, p. 10 pages.

[42] C. F. McDonald, Recuperator considerations for future higher efficiency microturbines, Applied Thermal Engineering 23 (2003) 1463 – 1487.

[43] L. Goldstein, B. Hedman, D. Knowles, S. I. Freedman, R. Woods, T. Schweizer, Gas-Fired Distributed Energy Resource Technology Characterizations, National Renewable Energy Laboratory, Oak ridge, Tennessee, U.S.A., 2003.

[44] C. F. McDonald, C. Rodgers, Ceramic recuperator and turbine: The key to achieving a 40 percent efficient microturbine, in: ASME Conference Proceedings, 2005, ASME paper GT2005-68644, pp. 963–971.

[45] C. F. McDonald, C. Rodgers, Small recuperated ceramic microturbine demonstrator concept, Applied Thermal Engineering 28 (2008) 60 – 74.

[46] S. Campanari, E. Macchi, Technical and tariff scenarios effect on microturbine trigenerative applications, Journal of Engineering for Gas Turbines and Power 126 (2004) 581–589.

[47] M. T. Kim, S. W. Lee, Application of in situ oxidation-resistant coating technology to a home-made 100 kW class gas turbine and its performance analysis, Applied Thermal Engineering 40 (2012) 304 – 310.

[48] G. Lagerström, M. Xie, High performance and cost effective recuperator for micro-gas turbines, in: ASME Conference Proceedings, 2002, ASME paper GT2002-30402, pp. 1003–1007.

[49] C. F. McDonald, Low-cost compact primary surface recuperator concept for microturbines, Applied Thermal Engineering 20 (2000) 471 – 497.

[50] A. Traverso, A. F. Massardo, Optimal design of compact recuperators for microturbine application, Applied Thermal Engineering 25 (2005) 2054 – 2071.

[51] J. D. Leeper, The hybrid cycle: Integration of a fuel cell with a gas turbine, in: ASME Conference Proceedings, 1999, ASME paper 99-GT-430, p. 5 pages.

[52] A. F. Massardo, C. F. McDonald, T. Korakianitis, Microturbine/fuel-cell coupling for high-efficiency electrical-power generation, Journal of Engineering for Gas Turbines and Power 124 (2002) 110–116.

[53] M. Pascenti, M. L. Ferrari, L. Magistri, A. F. Massardo, Micro gas turbine based test rig for hybrid system emulation, in: ASME Conference Proceedings, 2007, ASME paper GT2007-27075, pp. 7–15.

[54] M. Hohloch, J. Zanger, A. Widenhorn, M. Aigner, Experimental characterization of a micro gas turbine test rig, in: ASME Conference Proceedings, 2010, ASME paper GT2010-22799, pp. 671–681.

[55] N. Lymberopoulos, Microturbines and their application in Bio-energy (EESD Contract No: NNE5-PTA-2002-003/1), Technical Report, Centre for Renewable Energy Sources (CRES), 2001. Online Available: http://ec.europa.eu/energy/renewables/studies/doc/bioenergy/2004_microturbines_bioenergy.pdf (accessed: 25-08-2014).

[56] N. Mirzamohammad, O. Razbani, M. Assadi, Review of theoretical and experimental studies implemented on (CHP) micro turbine using natural gas and biogas fuels, in: J. Desideri, U. Yan (Ed.), Third International Conference on Applied Energy (ICAE 2011), 2011, Perugia, Italy, p. 8 pages.

[57] D. Marroyen, S. Bram, J. D. Ruyck, An externally fired evaporative gas turbine cycle for small scale biomass gasification, in: ASME Conference Proceedings, 1999, ASME paper 99-GT-322, p. 8 pages.

[58] A. Traverso, A. F. Massardo, R. Scarpellini, Externally fired micro-gas turbine: Modelling and experimental performance, Applied Thermal Engineering 26 (2006) 1935 – 1941.

[59] D. Chiaramonti, G. Riccio, F. Martelli, Preliminary design and economic analysis of a biomass fed micro-gas turbine plant for decentralised energy generation in Tuscany, in: ASME Conference Proceedings, 2004, ASME paper GT2004-53546, pp. 79–86.

[60] M. Prussi, D. Chiaramonti, G. Riccio, F. Martelli, L. Pari, Straight vegetable oil use in micro-gas turbines: System adaptation and testing, Applied Energy 89 (2012) 287 – 295.

[61] D. Chiaramonti, A. M. Rizzo, A. Spadi, M. Prussi, G. Riccio, F. Martelli, Exhaust emissions from liquid fuel micro gas turbine fed with diesel oil, biodiesel and vegetable oil, Applied Energy 101 (2013) 349–356.

[62] C. Invernizzi, P. Iora, P. Silva, Bottoming micro-rankine cycles for micro-gas turbines, Applied Thermal Engineering 27 (2007) 100 – 110.

[63] R. Buck, S. Friedmann, Solar-assisted small solar tower trigeneration systems, Journal of Solar Energy Engineering 129 (2007) 349–354.

[64] T. Nakagaki, T. Ogawa, H. Hirata, K. Kawamoto, Y. Ohashi, K. Tanaka, Development of chemically recuperated micro gas turbine, Journal of engineering for gas turbines and power 125 (2003) 391–397.

[65] T. Heppenstall, Advanced gas turbine cycles for power generation: A critical review, Applied Thermal Engineering 18 (1998) 837 – 846.

[66] M. Alhazmy, Y. Najjar, Augmentation of gas turbine performance using air coolers, Applied Thermal Engineering 24 (2004) 415 – 429.

[67] S. Kang, J. Kim, T. Kim, Influence of steam injection and hot gas bypass on the performance and operation of a combined heat and power system using a recuperative cycle gas turbine, Journal of Mechanical Science and Technology 27 (2013) 2547–2555.

[68] W. L. R. Gallo, A comparison between the HAT cycle and other gas-turbine based cycles: Efficiency, specific power and water consumption, Energy Conversion and Management 38 (1997) 1595 – 1604.

[69] A. Traverso, A. F. Massardo, Thermoeconomic analysis of mixed gas-steam cycles, Applied Thermal Engineering 22 (2002) 1 – 21.

[70] H. Haselbacher, Performance of water/steam injected gas turbine power plants consisting of standard gas turbines and turbo expanders, International Journal of Energy Technology and Policy 3 (2005) 12–23.

[71] K. Nishida, T. Takagi, S. Kinoshita, Regenerative steam-injection gas-turbine systems, Applied Energy 81 (2005) 231 – 246.

[72] I. Roumeliotis, K. Mathioudakis, Evaluation of water injection effect on compressor and engine performance and operability, Applied Energy 87 (2010) 1207 – 1216.

[73] J. De Ruyck, S. Bram, G. Allard, Humid air cycle development based on exergy analysis and composite curve theory, in: ASME Conference Proceedings, 1995, ASME paper 95-CTP-39, p. 10 pages.

[74] A. D. Rao, Process for producing power. US patent no. 4829763, 1989.

[75] A. D. Rao, W. H. Day, HAT cycle status report, in: Eleventh Conference on Gasification Power Plants, 1992, Sheraton Palace Hotel, San Francisco, California, p. 19 pages.

[76] T. S. Kim, C. H. Song, S. T. Ro, S. K. Kauh, Influence of ambient condition on thermodynamic performance of the humid air turbine cycle, Energy 25 (2000) 313 – 324.

[77] A. Lazzaretto, F. Segato, Thermodynamic optimization of the HAT cycle plant structure – Part I: Optimization of the "basic plant configuration", Journal of Engineering for Gas Turbines and Power 123 (2001) 1–7.

[78] A. Lazzaretto, F. Segato, Thermodynamic optimization of the HAT cycle plant structure – Part II: Structure of the heat exchanger network, Journal of Engineering for Gas Turbines and Power 123 (2001) 8–16.

[79] A. Lazzaretto, F. Segato, A thermodynamic approach to the definition of the HAT cycle plant structure, Energy Conversion and Management 43 (2002) 1377 – 1391.

[80] R. M. Kavanagh, G. T. Parks, M. Obana, Multi-objective optimisation of the humid air turbine, in: ASME Conference Proceedings, 2007, ASME paper GT2007-27456, pp. 211–221.

[81] B. Nyberg, M. Thern, Thermodynamic studies of a HAT cycle and its components, Applied Energy 89 (2012) 315 – 321.

[82] U. Desideri, F. Di Maria, Humid air turbine cycles with water recovery: how to dispose heat in an efficient way, in: ASME Conference Proceedings, 1998, ASME paper 98-GT-60, p. 7 pages.

[83] P. von Heiroth, J.-O. Gustafsson, T. Lindquist, A model of an evaporative cycle for heat and power production, Energy Conversion and Management 40 (1999) 1701 – 1711.

[84] M. C. Rydstrand, M. O. Westermark, M. A. Bartlett, An analysis of the efficiency and economy of humidified gas turbines in district heating applications, Energy 29 (2004) 1945 – 1961.

[85] N. D. Ågren, M. O. J. Westermark, Design study of part-flow evaporative gas turbine cycles: Performance and equipment sizing –

Part I: Aeroderivative core, Journal of Engineering for Gas Turbines and Power 125 (2003) 201–215.

[86] N. D. Ågren, M. O. J. Westermark, Design study of part-flow evaporative gas turbine cycles: Performance and equipment sizing – Part II: Industrial core, Journal of Engineering for Gas Turbines and Power 125 (2003) 216–227.

[87] M. A. Bartlett, M. O. Westermark, A study of humidified gas turbines for short-term realization in midsized power generation – Part I: Nonintercooled cycle analysis, Journal of Engineering for Gas Turbines and Power 127 (2005) 91–99.

[88] M. A. Bartlett, M. O. Westermark, A study of humidified gas turbines for short-term realization in midsized power generation – Part II: Intercooled cycle analysis and final economic evaluation, Journal of Engineering for Gas Turbines and Power 127 (2005) 100–108.

[89] Y. Hu, H. Li, J. Yan, Techno-economic evaluation of the evaporative gas turbine cycle with different CO_2 capture options, Applied Energy 89 (2012) 303 – 314.

[90] M. Nakhamkin, E. C. Swensen, J. M. Wilson, G. Gaul, M. Polsky, The Cascaded Humidified Advanced Turbine (CHAT), Journal of Engineering for Gas Turbines and Power 118 (1996) 565–571.

[91] J. Van Liere, G. Laagland, The TOPHAT® cycle, VDI-Berichte (2000) 161–175.

[92] J. De Ruyck, S. Bram, G. Allard, REVAP® cycle: A new evaporative cycle without saturation tower, Journal of Engineering for Gas Turbines and Power 119 (1997) 893–897.

[93] S. Hatamiya, Advanced humid air turbine system, in: The 7th national symposium on Power and Energy Systems of JSME, 2000, Tokyo, Japan, pp. 13–16. (in Japanese).

[94] R. M. Kavanagh, G. T. Parks, A systematic comparison and multi-objective optimization of humid power cycles – Part I: Thermodynamics, Journal of Engineering for Gas Turbines and Power 131 (2009) 041701 (10 pages).

[95] R. M. Kavanagh, G. T. Parks, A systematic comparison and multi-objective optimization of humid power cycles – Part II: Economics, Journal of Engineering for Gas Turbines and Power 131 (2009) 041702 (10 pages).

[96] T. Takahashi, E. Koda, T. Mimaki, A systematic analysis of the effect of air humidification to gas turbine systems, JSME International Journal Series B - Fluids and Thermal Engineering 45 (2002) 530–535.

[97] N. D. Ågren, M. O. Westermark, M. A. Bartlett, T. Lindquist, First experiments on an evaporative gas turbine pilot power plant: Water circuit chemistry and humidification evaluation, Journal of Engineering for Gas Turbines and Power 124 (2002) 96–102.

[98] J. Gotoh, K. Sato, H. Araki, S. Marushima, Efficient and flexible ahat gas turbine system, Hitachi Review 60 (2011) 372–376.

[99] R. Farmer, Gas Turbine World Handbook, Fairfield, 2010.

[100] S. Nakano, T. Kishibe, T. Inoue, H. Shiraiwa, An advanced microturbine system with water-lubricated bearings, International Journal of Rotating Machinery 2009 (2009) 1–12.

[101] S. Hatamiya, H. Araki, Y. Katagiri, S. Marushima, An experimental and analytical study on the advanced humid air turbine system, in: K. Cen, Y. Chi, F. Wang (Eds.), Challenges of Power Engineering and Environment, 2007, pp. 290–296.

[102] S. Higuchi, S. Hatamiya, H. Araki, S. Marushima, A study of performance on Advanced Humid Air Turbine systems, Journal of the Gas Turbine Society of Japan 34 (2006) 54–61.

[103] S. Higuchi, T. Koganezawa, Y. Horiuchi, H. Araki, T. Shibata, S. Marushima, Test results from the Advanced Humid Air Turbine system pilot plant: Part 1 – Overall performance, in: ASME Conference Proceedings, 2008, ASME paper GT2008-51072, pp. 691–700.

[104] H. Araki, S. Higuchi, T. Koganezawa, S. Marushima, S. Hatamiya, M. Tsukamoto, Test results from the Advanced Humid Air Turbine system pilot plant: Part 2 – Humidification, water recovery and water quality, in: ASME Conference Proceedings, 2008, ASME paper GT2008-51089, pp. 701–712.

[105] H. Araki, T. Koganezawa, C. Myouren, S. Higuchi, T. Takahashi, T. Eta, Experimental and analytical study on the operation characteristics of the AHAT system, Journal of Engineering for Gas Turbines and Power 134 (2012) 051701 (8 pages).

[106] M. Yagi, H. Araki, H. Tagawa, T. Koganezawa, C. Myoren, T. Takeda, Progress of the 40 MW-class advanced humid air turbine tests, Journal of Engineering for Gas Turbines and Power 135 (2013) 112002 (7 pages).

[107] T. Takeda, H. Araki, Y. Iwai, T. Morisaki, K. Sato, Test results of 40MW-class advanced humid air turbine and exhaust gas water recovery system, in: ASME Conference Proceedings, 2014, ASME paper GT2014-27281, p. 11 pages.

[108] D. Bohn, Micro gas turbine and fuel cell – A hybrid energy converion system with high potential, in: Micro Gas Turbines, 2005, pp. 13–1–13–46. Educational Notes RTO-EN-AVT-131, Paper 13. Neuilly-sur-Seine, France: RTO: Available from: `http://ftp.rta.nato.int/publiC/PubFullText/RTO/EN/RTO-EN-AVT-131/EN-AVT-131-13.pdf` (accessed 14-09-2014).

[109] T. Núñez, Classification of polygeneration systems – Review of technologies, in: PolySMART Public Workshop, 2010, Warszawa, p. 20 pages.

[110] B. Kolanowski, Guide to microturbines, Taylor and Francis, 2004.

[111] P. Grammelis, Solid Biofuels for Energy, Springer, 2010.

[112] L. P. Colombo, F. Armanasco, O. Perego, Experimentation on a cogenerative system based on a microturbine, Applied Thermal Engineering 27 (2007) 705 – 711.

[113] F. Caresana, G. Comodi, L. Pelagalli, M. Renzi, S. Vagni, Use of a test-bed to study the performance of micro gas turbines for cogeneration applications, Applied Thermal Engineering 31 (2011) 3552 – 3558.

[114] F. Caresana, L. Pelagalli, G. Comodi, M. Renzi, Microturbogas cogeneration systems for distributed generation: Effects of ambient temperature on global performance and components behavior, Applied Energy 124 (2014) 17 – 27.

[115] G. Ming, M. Onifri, Z. Lin, J. Ma, Experimental studies on a CCHP system based on a micro-turbine, in: Second International Conference on Mechanic Automation and Control Engineering (MACE), 2011, pp. 2159–2162.

[116] G. Ming, M. Onofri, J. Ma, Dynamic emission characteristics of micro-turbine startup, in: Asia-Pacific Power and Energy Engineering Conference (APPEEC), 2011, pp. 1–4.

[117] M. L. Ferrari, M. Pascenti, L. Magistri, A. F. Massardo, Micro gas turbine recuperator: steady-state and transient experimental investigation, Journal of Engineering for Gas Turbines and Power 132 (2010) 022301 (8 pages).

[118] M. L. Ferrari, A. Sorce, M. Pascenti, A. F. Massardo, Recuperator dynamic performance: Experimental investigation with a microgas turbine test rig, Applied Energy 88 (2011) 5090 – 5096.

[119] G. Caruso, L. De Santoli, F. Gianminuti, P. Sodani, A CHCP system constituted by a microturbine and an exhaust absorption chiller, 2006.

[120] A. Aguiar, M. L. M. Kimpara, J. O. P. Pinto, K. Al-Haddad, C. C. Merighi, Simulation of a distributed generation system using micro turbine at ceramic industry, in: Electrical Power Energy Conference (EPEC), 2009 IEEE, 2009, pp. 1–6.

[121] M. Costea, M. Feidt, G. Alexandry, D. Descieux, Optimization of gas turbine cogenration system for various heat exchanger configurations, Oil & Gas Science and Technology – Rev. IFP Energies nouvelles 67 (2012) 517–535.

[122] L. Martirano, S. Fornari, A. Di Giorgio, F. Liberati, A case study of a commercial/residential microgrid integrating cogeneration and electrical local users, in: 12th International Conference on Environment and Electrical Engineering (EEEIC), 2013, pp. 363–368.

[123] H. Nikpey, M. Assadi, P. Breuhaus, Development of an optimized artificial neural network model for combined heat and power micro gas turbines, Applied Energy 108 (2013) 137 – 148.

[124] H. Nikpey, M. Assadi, P. Breuhaus, Development of an artificial neural network model for combined heat and power micro gas

turbines, in: Innovations in Intelligent Systems and Applications (INISTA), 2012 International Symposium on, 2012, pp. 1–5.

[125] F. Orecchini, E. Bocci, A. D. Carlo, MCFC and microturbine power plant simulation, Journal of Power Sources 160 (2006) 835 – 841.

[126] L. Leto, C. Dispenza, A. Moreno, A. Calabrò, Simulation model of a molten carbonate fuel cell – Microturbine hybrid system, Applied Thermal Engineering 31 (2011) 1263 – 1271.

[127] D. P. Bakalis, A. G. Stamatis, Incorporating available micro gas turbines and fuel cell: Matching considerations and performance evaluation, Applied Energy 103 (2013) 607 – 617.

[128] A. Di Carlo, E. Bocci, A. Della'Era, Comparison by the use of numerical simulation of a MCFC-IR and a MCFC-ER when used with syngas obtained by atmospheric pressure biomass gasification, International Journal of Hydrogen Energy 36 (2011) 7976 – 7984. Hysydays.

[129] A. Di Carlo, D. Borello, E. Bocci, Process simulation of a hybrid SOFC/mGT and enriched air/steam fluidized bed gasifier power plant, International Journal of Hydrogen Energy 38 (2013) 5857 – 5874.

[130] M. L. Ferrari, M. Pascenti, Advances in Gas Turbine Technology, InTech, 2004.

[131] M. L. Ferrari, Solid oxide fuel cell hybrid system: Control strategy for stand-alone configurations, Journal of Power Sources 196 (2011) 2682 – 2690.

[132] L. Larosa, A. Traverso, M. L. Ferrari, V. Zaccaria, Pressurized SOFC hybrid systems: Control system study and experimental verification, in: ASME Conference Proceedings, 2014, ASME paper GT2014-25246, p. 10 pages.

[133] F. Caratozzolo, M. L. Ferrari, A. Traverso, A. F. Massardo, Emulator rig for sofc hybrid systems: Temperature and power control with a real-time software, Fuel Cells 13 (2013) 1123–1130.

[134] F. Lambruschini, M. L. Ferrari, A. Traverso, L. Larosa, Emergency shutdown management in fuel cell gas turbine hybrid systems, in:

ASME Conference Proceedings, 2014, ASME paper GT2014-25432, p. 10 pages.

[135] M. L. Ferrari, A. F. Massardo, Cathode–anode side interaction in SOFC hybrid systems, Applied Energy 105 (2013) 369 – 379.

[136] J. Zanger, A. Widenhorn, M. Aigner, Experimental investigations of pressure losses on the performance of a micro gas turbine system, Journal of Engineering for Gas Turbines and Power 133 (2011) 082302 (9 pages).

[137] M. Hohloch, A. Huber, M. Aigner, Experimental investigation of a SOFC/mGT hybrid power plant test rig – Impact and characterization of coupling elements, in: ASME Conference Proceedings, 2014, ASME paper GT2014-25918, p. 11 pages.

[138] H. Nikpey, M. Assadi, P. Breuhaus, Experimental investigation of the performance of a micro gas turbine fuelled with mixtures of natural gas and biogas, in: ASME Conference Proceedings, 2013, ASME paper IMECE2013-64299, p. 9 pages.

[139] M. C. Cameretti, R. Tuccillo, Combustion analysis in a micro-gas turbine supplied with bio-fuels, in: ASME Conference Proceedings, 2014, ASME paper GT2014-25560, p. 12 pages.

[140] A. Leach, Microturbines: The future for power generation from landfill gas, 2004. Online available: `http://warrr.org/963/1/Pa04018_-_Waste2004-Final.pdf` (accessed: 10-09-2014).

[141] A. Momo Atemkeng, Sustainable waste-to-energy production: Performance evaluation of distributed generation fuelled by landfill gas, Master's thesis, Faculty of Technology of Lappeenranta University, 2009.

[142] F. Delattin, G. D. Lorenzo, S. Rizzo, S. Bram, J. D. Ruyck, Comparison of natural gas and partially reformed natural gas combustion in a modified 100 kWe microturbine, in: The 2nd International Conference on Microgeneration and Related Technologies, 2011, Glasgow, UK, p. 7 pages.

[143] M. Cadorin, M. Pinelli, A. Vaccari, R. Calabria, F. Chiariello, P. Massoli, E. Bianchi, Analysis of a micro gas turbine fed by natural

gas and synthesis gas: MGT test bench and combustor CFD analysis, Journal of Engineering for Gas Turbines and Power 134 (2012) 071401 (11 pages).

[144] D. Cocco, P. Deiana, G. Cau, Performance evaluation of small size externally fired gas turbine (EFGT) power plants integrated with direct biomass dryers, Energy 31 (2006) 1459 – 1471.

[145] M. Kautz, U. Hansen, The externally-fired gas-turbine (EFGT-cycle) for decentralized use of biomass, Applied Energy 84 (2007) 795 – 805.

[146] G. Riccio, D. Chiaramonti, Design and simulation of a small polygeneration plant cofiring biomass and natural gas in a dual combustion micro gas turbine (BIO_MGT), Biomass and Bioenergy 33 (2009) 1520 – 1531.

[147] S. M. Camporeale, B. Fortunato, M. Torresi, F. Turbi, A. M. Pantoleo, Part load performance and operating strategies of a natural gas-biomass dual fuelled microturbine for CHP generation, in: ASME Conference Proceedings, 2014, ASME paper GT2014-27109, p. 15 pages.

[148] A. Pantaleo, S. Camporeale, N. Shah, Thermo-economic assessment of externally fired micro-gas turbine fired by natural gas and biomass: Applications in Italy, Energy Conversion and Management 75 (2013) 202 – 213.

[149] S. Luostarinen, A. Normak, M. Edström, Overview of biogas technology, in: Baltic Forum for Innovative Technologies for Sustainable Manure Management, 2011, p. 49 pages.

[150] A. Calabrò, P. Deiana, P. Fiorini, S. Stendardo, G. Girardi, An innovative test platform for hydrogen production and zero emission power generation from coal, in: 16th World Hydrogen Energy Conference (WHEC), 2006, Lyon, France, p. 7 pages.

[151] A. Calabrò, S. Stendardo, S. Cassani, L. Pagliari, Implementation of a CCS technology: the ZECOMIX experimental platform, in: Proceedings of the 25th interantional conference on Efficiency, Cost, Optimization, Simulation and environmental impact on energy systems (ECOS 2012), 2012, Perugia, Italy, pp. 222–1 – 222–5.

[152] S. Barsali, G. Ludovici, Externally fired micro gas turbine (75 kW_e) for combined heat and power generation from solid biomass: Concept, efficiency, cost and experience from pilot and commercial plants in Italy, in: Holzenergy-Symposium: Potenzial und Technik zur Holzenergie-Nutzung, 2010, ETH Zürich, p. 16 pages.

[153] S. Cordiner, V. Mulone, Experimental-numercial analysis of a biomass fuelled microgeneration power-plant based on microturbine, in: The 3rd International Conference on Microgeneration and Related Technologies, 2013, Naples, Italy, p. 10 pages.

[154] L. Amsbeck, R. Buck, P. Heller, J. Jedamski, R. Uhlig, Development of a tube receiver for a solar-hybrid microturbine system, in: Proc. 14th SolarPaces Symposium, Las Vegas, USA, 2008, p. 9 pages.

[155] L. Amsbeck, T. Denk, M. Ebert, C. Gertig, P. Heller, P. Herrmann, J. Jedamski, J. John, R. Pitz-Paal, T. Prosinečki, et al., Test of a solar-hybrid microturbine system and evaluation of storage deployment, in: Proceedings of the 16th SolarPACES Conference, Perpignan, France, 2010, p. 8 pages.

[156] S. Clemente, D. Micheli, M. Reini, R. Taccani, Bottoming organic rankine cycle for a small scale gas turbine: A comparison of different solutions, Applied Energy 106 (2013) 355 – 364.

[157] A. Passarrella, G. L. Arnulfi, Combined heat end power plants based on mirror heat exchange Brayton cycles, in: ASME Conference Proceedings, 2014, ASME paper GT2014-25377, p. 9 pages.

[158] Turbec AB, T100 microturbine CHP system: Technical description ver 4.0, 2000-2001.

[159] Aspen Technology Inc., Aspen plus version 2006.5, 2006. Online available: `www.aspentech.com` (accessed: 23-01-2014).

[160] S. Haugwitz, Modelling of microturbine systems, PhD thesis, Lund Institute of technology, 2002.

[161] Y. Çengel, M. Boles, Thermodynamics: an engineering approach, McGraw-Hill series in mechanical engineering, McGraw-Hill Higher Education, Boston, US, 2006.

[162] P. Walsh, P.P. Fletcher, Gas turbine performance, Blackwell Science Publications, Oxford, UK, 2004.

[163] K. Brun, M. G. Nored, GMRC Guideline – Release Version 4.3: Application guideline for centrifugal compressor surge control systems, Technical Report, Gas Machinery Research Council, Southwest Research Institute, 2008. Online available: https://www.gmrc.org/documents/GMRCSurgeGuideline_000.pdf (accessed: 12-09-2014).

[164] Aspen Technology Inc., Aspen physical property system: Physical property methods, 2009. Online available: http://chemelab.ucsd.edu/aspendocs/v7/AspenPhysPropMethodsV7_1-Ref.pdf (accessed: 2-03-2014).

[165] International Electrotechnical Commission (IEC), Electricity metering equipment (A.C.) – particular requirements – Part 21: Static meters for active energy (classes 1 and 2), 2003.

[166] S. Knoops, Performantie en evaluatie van de turbec T100 gasturbine op de VUB-campus, Predoctorale proef, Vrije Universiteit Brussel, 2007.

[167] O. Bolland, S. Sæther, New concepts for natural gas fired power plants which simplify the recovery of carbon dioxide, Energy Conversion and Management 33 (1992) 467 – 475.

[168] H. Li, M. Ditaranto, D. Berstad, Technologies for increasing CO_2 concentration in exhaust gas from natural gas-fired power production with post-combustion, amine-based CO_2 capture, Energy 36 (2011) 1124 – 1133.

[169] H. Li, G. Haugen, M. Ditaranto, D. Berstad, K. Jordal, Impacts of exhaust gas recirculation (EGR) on the natural gas combined cycle integrated with chemical absorption CO_2 capture technology, Energy Procedia 4 (2011) 1411 – 1418.

[170] O. Bolland, P. Mathieu, Comparison of two CO_2 removal options in combined cycle power plants, Energy Conversion and Management 39 (1998) 1653 – 1663.

[171] A. T. Evulet, A. M. ELKady, A. R. Branda, D. Chinn, On the performance and operability of GE's dry low NO_x combustors utilizing exhaust gas recirculation for postcombustion carbon capture, Energy Procedia 1 (2009) 3809 – 3816.

[172] A. M. ElKady, A. Evulet, A. Brand, T. P. Ursin, A. Lynghjem, Application of exhaust gas recirculation in a DLN F-class combustion system for postcombustion carbon capture, Journal of Engineering for Gas Turbines and Power 131 (2009) 034505 (6 pages).

[173] M. Ditaranto, J. Hals, T. Bjørge, Investigation on the in-flame no reburning in turbine exhaust gas, Proceedings of the Combustion Institute 32 (2009) 2659 – 2666.

[174] M. Finkenrath, T. P. Ursin, S. Hoffmann, M. Bartlett, A. Evulet, M. J. Bowman, A. Lynghjem, J. Jakobsen, Performance and cost analysis of a novel gas turbine cycle with CO_2 capture, in: ASME Conference Proceedings, 2007, ASME paper GT2007-27764, pp. 337–343.

[175] C. Botero, M. Finkenrath, M. Bartlett, R. Chu, G. Choi, D. Chinn, Redesign, optimization, and economic evaluation of a natural gas combined cycle with the best integrated technology CO_2 capture, Energy Procedia 1 (2009) 3835 – 3842.

[176] N. Sipöcz, M. Assadi, Combined cycles with CO_2 capture: Two alternatives for system integration, Journal of Engineering for Gas Turbines and Power 132 (2010) 061701 (6 pages).

[177] K. Jonshagen, N. Sipocz, M. Genrup, A novel approach of retrofitting a combined cycle with post combustion CO_2 capture, Journal of Engineering for Gas Turbines and Power 133 (2011) 011703 (7 pages).

[178] N. Sipöcz, A. Tobiesen, M. Assadi, Integrated modelling and simulation of a 400 MW NGCC power plant with CO_2 capture, Energy Procedia 4 (2011) 1941 – 1948.

[179] N. Sipöcz, K. Jonshagen, M. Assadi, M. Genrup, Novel high-performing single-pressure combined cycle with CO_2 capture, Journal of Engineering for Gas Turbines and Power 133 (2011) 041701 (8 pages).

[180] M. C. Cameretti, F. Reale, R. Tuccillo, Cycle optimization and combustion analysis in a low-NO_x micro-gas turbine, Journal of engineering for gas turbines and power 139 (2007) 996–1003.

[181] M. C. Cameretti, F. Reale, R. Tuccillo, NO_x suppression from a micro-gas turbine approaching the mild-combustion regime, in:

ASME conference Proceedings, 2007, ASME paper GT2007-27091, pp. 27–38.

[182] M. C. Cameretti, R. Piazzesi, F. Reale, R. Tuccillo, Combustion simulation of an exhaust gas recirculation operated micro-gas turbine, Journal of Engineering for Gas Turbines and Power 131 (2009) 051701 (10 pages).

[183] P. E. Røkke, J. E. Hustad, Exhaust gas recirculation in gas turbines for reduction of CO_2 emissions. Combustion testing with focus on stability and emissions, International Journal of Thermodynamics 8 (2005) 167–173.

[184] K. Hubin, Stoominjectie bij de microturbine, Master thesis, Vrije Universiteit Brussel, Vrije Universiteit Brussel, 2008.

[185] J. Gibbons, S. Chakraborti, E. Corporation, Nonparametric Statistical Inference, Textbooks and Monographs, Marcel Dekker, 2003.

[186] J. Counihan, An improved method of simulating an atmospheric boundary layer in a wind tunnel, Atmospheric Environment 3 (1969) 197 – 200.

[187] H. P. A. H. Irwin, The design of spires for wind simulation, Journal of wind engineering and industrial Aerodynamics 7 (1981) 361–366.

[188] N. Cook, On simulating the lower third of the urban adiabatic boundary layer in a wind tunnel, Atmospheric Environment 7 (1973) 691 – 705.

[189] N. Cook, Wind-tunnel simulation of the adiabatic atmospheric boundary layer by roughness, barrier and mixing-device methods, Journal of Wind Engineering and Industrial Aerodynamics 3 (1978) 157 – 176.

[190] M. Jensen, N. Franck, Model-scale test in turbulent wind – Part I: Phenomena dependent on the wind speed, The Danish Technical Press, Copenhagen, 1963.

[191] N. M. Standen, W. A. Dalgliesh, R. J. Templin, A wind tunnel and full-scale study of turbulent wind pressures on a tall building, Technical Report, National Research Council Canada, 1971.

[192] T. Lawson, Methods of producing velocity profiles in wind tunnels, Atmospheric Environment 2 (1968) 73 – 76.

[193] W. D. Lubitz, B. R. White, Atmospheric boundary layer wind tunnel applications in wind turbine siting, in: proceedings of World Wind Energy Conference, 2004, p. 6 pages.

[194] J. Schon, P. Mery, A preliminary study of the simulation of neutral atmospheric boundary layer using air injection in a wind tunnel, Atmospheric Environment 5 (1971) 299 – 311.

[195] T. J. Sluman, H. R. E. van Maanen, G. Ooms, Atmospheric boundary layer simulation in a wind tunnel, using air injection, Applied Scientific Research 36 (1980) 289–307.

[196] Y. Ohya, Wind-tunnel study of atmospheric stable boundary layers over a rough surface, Boundary-Layer Meteorology 98 (2001) 57–82.

[197] A. J. Bowen, D. Lindley, A wind-tunnel investigation of the wind speed and turbulence characteristics close to the ground over various escarpment shapes, Boundary-Layer Meteorology 12 (1977) 259–271.

[198] P. H. A. Barbosa, M. Cataldi, A. P. S. Freire, Wind tunnel simulation of atmospheric boundary layer flows, Journal of the Brazilian Society of Mechanical Sciences 24 (2002) 177–185.

[199] J. Armitt, J. Counihan, The simulation of the atmospheric boundary layer in a wind tunnel, Atmospheric Environment 2 (1968) 49 – 62.

[200] J. Counihan, Further measurements in a simulated atmospheric boundary layer, Atmospheric Environment 4 (1970) 259 – 275.

[201] J. Counihan, Wind tunnel determination of the roughness length as a function of the fetch and the roughness density of three-dimensional roughness elements, Atmospheric Environment 5 (1971) 637 – 642.

[202] J. Counihan, Simulation of an adiabatic urban boundary layer in a wind tunnel, Atmospheric Environment 7 (1973) 673 – 689.

[203] S. Rafailidis, Influence of building areal density and roof shape on the wind characteristics above a town, Boundary-Layer Meteorology 85 (1997) 255–271.

[204] C. Farell, A. K. S. Iyengar, Experiments on the wind tunnel simulation of atmospheric boundary layers, Journal of Wind Engineering and Industrial Aerodynamics 79 (1999) 11 – 35.

[205] M. Gu, Y. Quan, Across-wind loads of typical tall buildings, Journal of Wind Engineering and Industrial Aerodynamics 92 (2004) 1147 – 1165.

[206] T. Balendra, D. A. Shah, K. L. Tey, S. K. Kong, Evaluation of flow characteristics in the NUS-HDB wind tunnel, Journal of Wind Engineering and Industrial Aerodynamics 90 (2002) 675 – 688.

[207] M. E. De Bortoli, B. Natalini, M. J. Paluch, M. B. Natalini, Part-depth wind tunnel simulations of the atmospheric boundary layer, Journal of Wind Engineering and Industrial Aerodynamics 90 (2002) 281 – 291.

[208] K. Nagai, Wind tunnel modeling of hourly observed atmospheric diffusion by oscillating blade cascade, Journal of Wind Engineering and Industrial Aerodynamics 93 (2005) 99 – 113.

[209] J. Sanz Rodrigo, J. van Beeck, G. Dezsö-Weidinger, Wind tunnel simulation of the wind conditions inside bidimensional forest clear-cuts. Application to wind turbine siting, Journal of Wind Engineering and Industrial Aerodynamics 95 (2007) 609 – 634.

[210] R. Derdelinckx, C. Hirsch, Windtunnelstudie van het stadhuis te Brussel, Technical Report, Vrije Universiteit Brussel, Pleinlaan 2, 1050 Brussel, 1993.

[211] B. Birinchi, H. Vanbockryck, H. Hirsch, Windtunnelstudie van het stromingspatroon in het Koning Boudewijn Stadion, Technical Report, Vrije Universiteit Brussel, Pleinlaan 2, 1050 Brussel, 1996.

[212] J. Counihan, Adiabatic atmospheric boundary layers: A review and analysis of data from the period 1880-1972, Atmospheric Environment 9 (1975) 871 – 905.

[213] P. Jones, M. de Larrinaga, C. Wilson, The urban wind velocity profile, Atmospheric Environment 5 (1971) 89 – 90.

[214] Belgisch instituut voor normalisatie (BIN), Eurocode1: Belastingen op constructies – Deel 1-4: Algemene belastingen – windbelasting, 2005.

[215] Belgisch instituut voor normalisatie (BIN), Eurocode1: Actions on structures. Wind actions, 2002.

[216] R. H. Thuillier, U. O. Lappe, Wind and temperature profile characteristics from observations on a 1400 ft tower, Journal of Applied Meteorology 3 (1964) 299–306.

[217] A. K. S. Iyengar, C. Farell, Experimental issues in atmospheric boundary layer simulations: Roughness length and integral length scale determination, Journal of Wind Engineering and Industrial Aerodynamics 89 (2001) 1059 – 1080.

[218] N. Cook, Determination of the model scale factor in wind-tunnel simulations of the adiabatic atmospheric boundary layer, Journal of Wind Engineering and Industrial Aerodynamics 2 (1978) 311 – 321.

[219] Engineering Sciences Data Unit (ESDU), ESDU 74031: Characteristics of atmospheric turbulence near the ground. Part II: Single point data for strong winds (neutral atmosphere), 1974.

[220] Engineering Sciences Data Unit (ESDU), ESDU 85020: Characteristics of atmospheric turbulence near the ground. Part II: Single point data for strong winds (neutral atmosphere), 1985.

[221] H. Kozmar, Wind-tunnel simulations of the suburban ABL and comparison with international standards, Wind and Structures 14 (2011) 15–34.

[222] D. Lungu, P. van Gelder, Characteristics of wind turbulence with applications to wind codes, in: ESREL 2003 (European Safety and Reliability Conference), 2003, Maastricht, The Nederlands, pp. 1271–1277.

[223] J. C. Kaimal, J. C. Wyngaard, Y. Izumi, O. R. Cote, Spectral characteristics of surface-layer turbulence, Quartely Journal of the Royal Meteorological Society 98 (1972) 563–589.

[224] T. von Karman, Progress in the statistical theory of turbulence, Proceedings of the National Academy of Sciences of the United States of America 34 (1948) 530–539.

[225] H. Kozmar, Natural wind simulation in the TUM boundary layer wind tunnel, in: 5th European & African Conference on Wind Engineering, 2009, EACWE 5, Florence, Italy, p. 12 pages.

[226] H. Kozmar, An alternative approach to experimental simulation of wind characteristics in urban environments, Procedia Environmental Sciences 4 (2011) 43 – 50.

[227] H. Kozmar, Scale effects in wind tunnel modeling of an urban atmosphreci boundary layer, Theoretical and Applied Climatology 100 (2010) 153–162.

[228] H. Kozmar, Truncated vortex generators for part-depth wind-tunnel simulations of the atmospheric boundary layer flow, Journal of Wind Engineering and Industrial Aerodynamics 99 (2011) 130 – 136.

[229] I. S. Gartshore, K. A. D. Croos, Roughness element geometry required for wind tunnel simulations of the atmospheric wind, Journal of Fluids Engineering 99 (1977) 480–485.

[230] C. Fang, B. L. Sill, Aerodynamic roughness length: Correlation with roughness elements, Journal of Wind Engineering and Industrial Aerodynamics 41 (1992) 449 – 460.

[231] R. A. Wooding, E. F. Bradley, J. K. Marshall, Drag due to regular arrays of roughness elements of varying geometry, Boundary-Layer Meteorology 5 (1972) 285–308.

[232] P. F. P. Lopes, M. G. Gomes, J. G. Ferreira, Simulation of the atmospheric boundary layer for model testing in a short wind tunnel, Experimental Techniques 32 (2008) 1747–1567.

[233] F. E. Jørgensen, How to measure turbulence with hot-wire anemometers – A practical guide, Dantec Dunamics, Skovlunde, Denmark, 2002. Online available: `http://www.dantecdynamics.com/how-to-measure-turbulence-practical-guide` (accessed: 9-09-2014).

[234] Z. Y. Wang, E. J. Plate, M. Rau, R. Keiser, Scale effects in wind tunnel modelling, Journal of Wind Engineering and Industrial Aerodynamics 61 (1996) 113 – 130.

[235] G. Heinzel, A. Rüdiger, R. Schilling, T. Hannover, Spectrum and spectral density estimation by the Discrete Fourier Transform (DFT), including a comprehensive list of window functions and some new flat-top windows, Max Plank Institute 12 (2002) 122.

[236] A. N. Kolmogorov, The local structure of turbulence in incompressible viscous fluid for very large reynolds numbers, in: Dokl. Akad. Nauk SSSR, 1941, pp. 299–303.

[237] F. White, Fluid mechanics, McGraw-Hill series in mechanical engineering, WCB/McGraw-Hill, 1999.

[238] J. B. Barlow, W. H. Rae, A. Pope, Low-speed wind tunnel testing, third edition, John Wiley and Sons, 1999.

[239] Y. A. Çengel, Heat and mass transfer: A practical approach, McGraw-Hill series in mechanical engineering, McGraw-Hill Higher Education, Boston, US, 2006.

[240] A. Hahn, Modeling and control of solid oxide fuel cell – Gas turbine power plant systems, PhD thesis, University of Pittsburgh, 2004.

[241] K. Mathioudakis, Analysis of the effects of water injection on the performance of a gas turbine, Journal of Engineering for Gas Turbines and Power 124 (2002) 489–495.

[242] F. Hermann, J. Klingmann, R. Gabrielsson, Computational and experimental investigation of emissions in a highly humidified premixed flame, in: ASME Conference Proceedings, 2003, ASME paper GT2003-38337, pp. 819–827.

[243] A. Bhargava, M. Colket, W. Sowa, K. Casleton, D. Maloney, An experimental and modeling study of humid air premixed flames, Journal of Engineering for Gas Turbines and Power 122 (2000) 405–411.

[244] W. Day, B. kendrick, D knight, A. Bhargava, W. Sowa, M. Colket, K. Casleton, D. Maloney, HAT cycle technology development program, in: Advanced turbine systems annual program review meeting, 1999, pp. 2–8. Online available: `www.netl.doe.gov/publications/proceedings/99/99ats/2-8.pdf` (accessed: 23-01-2014).

[245] A. G. Chen, D. J. Maloney, W. H. Day, Humid air NO_x reduction effect on liquid fuel combustion, Journal of Engineering for Gas Turbines and Power 126 (2004) 69–74.

[246] A. A. Belokon, K. M. Khritov, L. A. Klyachko, S. A. Tschepin, V. M. Zakharov, J. George Opdyke, Prediction of combustion efficiency and NO_x levels for diffusion flame combustors in HAT cycles, in: ASME Conference Proceedings, 2002, ASME paper GT2002-30609, pp. 791–797.

[247] F. Dryer, Water addition to practical combustion systemsconcepts and applications, Symposium (International) on Combustion 16 (1977) 279 – 295.

[248] A. N. Mazas, D. A. Lacoste, T. Schuller, Experimental and numerical investigation on the laminar flame speed of CH_4/O_2 mixtures diluted with CO_2 and H_2O, in: ASME Conference Proceedings, 2010, ASME paper GT2010-22512, pp. 411–421.

[249] D. Zhao, H. Yamashita, K. Kitagawa, N. Arai, T. Furuhata, Behavior and effect on NO_x formation of OH radical in methane-air diffusion flame with steam addition, Combustion and Flame 130 (2002) 352 – 360.

[250] S. Göke, M. Füri, G. Bourque, B. Bobusch, K. Göckeler, O. Krüger, S. Schimek, S. Terhaar, C. O. Paschereit, Influence of steam dilution on the combustion of natural gas and hydrogen in premixed and rich-quench-lean combustors, Fuel Processing Technology 107 (2013) 14 – 22.

[251] H. Kobayashi, S. Yata, Y. Ichikawa, Y. Ogami, Dilution effects of superheated water vapor on turbulent premixed flames at high pressure and high temperature, Proceedings of the Combustion Institute 32 (2009) 2607 – 2614.

[252] S. Göke, S. Schimek, S. Terhaar, T. Reichel, K. Göckeler, O. Krger, J. Fleck, P. Griebel, C. O. Paschereit, Influence of pressure and steam dilution on NO_x and CO emissions in a premixed natural gas flame, in: ASME Conference Proceedings, 2012, ASME paper GT2013-94782, p. 11 pages.

[253] J. Park, S. I. Keel, J. H. Yun, Addition effects of H_2 and H_2O on flame structure and pollutant emissions in methane-air diffusion flame, Energy & Fuels 21 (2007) 3216–3224.

[254] P. Sayad, A. Schönborn, D. Clerini, J. Klingmann, Experimental investigation of methane lean blowout limit; effects of dilution, mass

flow rate and inlet temperature, in: ASME Conference Proceedings, 2012, ASME paper GTINDIA2012-9742, pp. 815–826.

[255] P. Sayad, A. Schönborn, J. Klingmann, Experimental investigations of the lean blowout limit of different syngas mixtures in an atmospheric, premixed, variable-swirl burner, Energy & Fuels 27 (2013) 2783–2793.

[256] P. Sayad, A. Schönborn, M. Li, J. Klingmann, Visualization of different flashback mechanisms for H_2/CH_4 mixtures in a variable-swirl burner, in: ASME Conference Proceedings, 2014, ASME paper GT2014-27090, p. 11 pages.

[257] N. Syred, J. Beér, Combustion in swirling flows: A review, Combustion and Flame 23 (1974) 143 – 201.

[258] S. Bram, J. De Ruyck, Exergy analysis tools for ASPEN applied to evaporative cycle design, Energy Conversion and Management 38 (1997) 1613 – 1624.

[259] J. D. Ruyck, F. Delattin, S. Bram, Co-utilization of biomass and natural gas in combined cycles through primary steam reforming of the natural gas, Energy 32 (2007) 371 – 377.

[260] J. A. Queiroz, V. M. Rodrigues, H. A. Matos, F. Martins, Modeling of existing cooling towers in ASPEN PLUS using an equilibrium stage method, Energy Conversion and Management 64 (2012) 473 – 481.

[261] J. Yan, X. Ji, M. Jonsson, Thermodynamic property models for the simulation of advanced wet cycles, in: ASME Conference Proceedings, 2003, ASME paper GT2003-38298, pp. 211–219.

[262] U. Desideri, F. Di Maria, Water recovery from HAT cycle exhaust gas: a possible solution for reducing stack temperature problems, International Journal of Energy Research 21 (1997) 809–822.

[263] M. De Paepe, E. Dick, Technological and economical analysis of water recovery in steam injected gas turbines, Applied Thermal Engineering 21 (2001) 135 – 156.

[264] M. A. El-Masri, A modified, high-efficiency, recuperated gas turbine cycle, Journal of Engineering for Gas Turbines and Power 110 (1988) 233–242.

[265] M. Ebrahim, A. Kawari, Pinch technology: An efficient tool for chemical-plant energy and capital-cost saving, Applied Energy 65 (2000) 45 – 49.

[266] E. Macchi, A. Poggio, A cogeneration plant based on a steam injection gas turbine with recovery of the water injected: Design criteria and initial operating experience, in: ASME Conference Proceedings, 1994, ASME paper 94-GT-17, pp. 1–10.

[267] O. Balli, H. Aras, Energetic and exergetic performance evaluation of a combined heat and power system with the micro gas turbine (MGTCHP), International Journal of Energy Research 31 (2007) 1425–1440.

[268] B. A. Pint, S. Dryepondt, M. P. Brady, Y. Yamamoto, Evaluation of commercial and next generation alumina-forming austenitic foil for advanced recuperators, in: ASME Conference Proceedings, 2013, ASME paper GT2013-94940, p. 8 pages.

[269] R. Enick, S. Klara, J. Marano, A robust algorithm for high-pressure gas humidification, Computers & Chemical Engineering 19 (1995) 1051 – 1061.

[270] T. Lindquist, M. Thern, T. Torisson, Experimental and theoretical results of a humidification tower in an evaporative gas turbine cycle pilot plant, in: ASME Conference proceedings, 2002, ASME paper GT2002-30127, pp. 475–484.

[271] J. O. Parente, A. Traverso, A. F. Massardo, Saturator analysis for an evaporative gas turbine cycle, Applied Thermal Engineering 23 (2003) 1275 – 1293.

[272] A. Pedemonte, A. Traverso, A. Massardo, Experimental analysis of pressurised humidification tower for humid air gas turbine cycles. Part A: Experimental campaign, Applied Thermal Engineering 28 (2008) 1711 – 1725.

[273] A. Pedemonte, A. Traverso, A. Massardo, Experimental analysis of pressurised humidification tower for humid air gas turbine cycles. Part B: Correlation of experimental data, Applied Thermal Engineering 28 (2008) 1623 – 1629.

[274] A. Traverso, Humidification tower for humid air gas turbine cycles: Experimental analysis, Energy 35 (2010) 894 – 901.

[275] H. Araki, S. Higuchi, S. Marushima, S. Hatamiya, Design study of a humidification tower for the Advanced Humid Air Turbine system, Journal of Engineering for Gas Turbines and Power 128 (2006) 543–550.

[276] Y. Hui, Y. Wang, S. Weng, Experimental investigation of pressurized packing saturator for humid air turbine cycle, Applied Thermal Engineering 62 (2014) 513–519.

[277] Y. Wang, Y. Li, S. Weng, Experimental investigation on inner two-phase flow in counter-flow spray saturator for HAT cycle, Applied Thermal Engineering 26 (2006) 2417 – 2424.

[278] Y. Wang, Y. Li, S. Weng, M. Su, Experimental investigation on humidifying performance of counter flow spray saturator for humid air turbine cycle, Energy Conversion and Management 48 (2007) 756 – 763.

[279] Z. Xu, Y. Xiao, Y. Wang, Experimental and theoretical studies on air humidification by a water spray at elevated pressure, Applied Thermal Engineering 27 (2007) 2549 – 2558.

[280] S. S. Kachhwaha, P. L. Dhar, S. R. Kale, Experimental studies and numerical simulation of evaporative cooling of air with a water spray – I. Horizontal parallel flow, International Journal of Heat and Mass Transfer 41 (1998) 447 – 464.

[281] S. S. Kachhwaha, P. L. Dhar, S. R. Kale, Experimental studies and numerical simulation of evaporative cooling of air with a water spray – II. Horizontal counter flow, International Journal of Heat and Mass Transfer 41 (1998) 465 – 474.

[282] J. C. Kloppers, D. G. Kröger, Cooling tower performance evaluation: Merkel, Poppe, and e-NTU methods of analysis, Journal of Engineering for Gas Turbines and Power 127 (2005) 1–7.

[283] J. Kloppers, D. Kröger, A critical investigation into the heat and mass transfer analysis of counterflow wet-cooling towers, International Journal of Heat and Mass Transfer 48 (2005) 765 – 777.

[284] J. C. Kloppers, D. G. Kröger, The lewis factor and its influence on the performance prediction of wet-cooling towers, International Journal of Thermal Sciences 44 (2005) 879 – 884.

[285] G. Heidarinejad, M. Karami, S. Delfani, Numerical simulation of counter-flow wet-cooling towers, International Journal of Refrigeration 32 (2009) 996 – 1002.

[286] J.-U.-R. Khan, M. Yaqub, S. M. Zubair, Performance characteristics of counter flow wet cooling towers, Energy Conversion and Management 44 (2003) 2073 – 2091.

[287] R. Terblanche, H. Reuter, D. Kröger, Drop size distribution below different wet-cooling tower fills, Applied Thermal Engineering 29 (2009) 1552 – 1560.

[288] S. Fisenko, A. Petruchik, A. Solodukhin, Evaporative cooling of water in a natural draft cooling tower, International Journal of Heat and Mass Transfer 45 (2002) 4683 – 4694.

[289] A. I. Petruchik, A. D. Solodukhin, S. P. Fisenko, Simulation of cooling of water droplet and film flows in large natural wet cooling towers, Journal of Engineering Physics and Thermophysics 74 (2001) 62–68.

[290] G. Gan, S. B. Riffat, Numerical simulation of closed wet cooling towers for chilled ceiling systems, Applied Thermal Engineering 19 (1999) 1279 – 1296.

[291] A. K. M. Mohiuddin, K. Kant, Knowledge base for the systematic design of wet cooling towers. Part I: Selection and tower characteristics, International Journal of Refrigeration 19 (1996) 43 – 51.

[292] A. K. M. Mohiuddin, K. Kant, Knowledge base for the systematic design of wet cooling towers. Part II: Fill and other design parameters, International Journal of Refrigeration 19 (1996) 52 – 60.

[293] M. Fossa, A simple model to evaluate direct contact heat transfer and flow characteristics in annular two-phase flow, International Journal of Heat and Fluid Flow 16 (1995) 272 – 279.

[294] A. Niksiar, A. Rahimi, Energy and exergy analysis for cocurrent gas spray cooling systems based on the results of mathematical modeling and simulation, Energy 34 (2009) 14 – 21.

[295] N. Makkinejad, Temperature profile in countercurrent/cocurrent spray towers, International Journal of Heat and Mass Transfer 44 (2001) 429 – 442.

[296] S. Fisenko, A. Brin, A. Petruchik, Evaporative cooling of water in a mechanical draft cooling tower, International Journal of Heat and Mass Transfer 47 (2004) 165 – 177.

[297] S. Fisenko, A. Brin, Simulation of a cross-flow cooling tower performance, International Journal of Heat and Mass Transfer 50 (2007) 3216 – 3223.

[298] M. Saravanan, R. Saravanan, S. Renganarayanan, Energy and exergy analysis of counter flow wet cooling towers, Thermal Science 12 (2008) 69–78.

[299] S. Bram, The thermodynamic Potential of evaporative regeneration in gas turbine cycles for power production, PhD thesis, Vrije Universiteit Brussel, Pleinlaan 2, 1050 Brussels, Belgium, 2002.

[300] Mathworks, Matlab R2012a, Natick, Massachusetts U.S.A., 2012. Online available: `http://www.mathworks.com/` (accessed: 28-02-2014).

[301] J. C. Kloppers, D. G. Kröger, Loss coefficient correlation for wet-cooling tower fills, Applied Thermal Engineering 23 (2003) 2201 – 2211.

[302] PNR, General purpose spray nozzles: CTG UG20 BR, PNR, Groot-Bijgaarden, Belgium, 2012. Online available: `http://www.pnr.eu/catalogo_sfoglia/general-purpose-nozzle/full_cone_nozzles.pdf` (accessed: 9-09-2014).

[303] P. Pezzini, D. Tucker, A. Traverso, Avoiding compressor surge during emergency shutdown hybrid turbine systems, Journal of Engineering for Gas Turbines and Power 135 (2013) 102602 (10 pages).

[304] R. J. Lang, Ultrasonic atomization of liquids, The Journal of the Acoustical Society of America 34 (1962) 6–8.

[305] R. Rajan, A. Pandit, Correlations to predict droplet size in ultrasonic atomisation, Ultrasonics 39 (2001) 235 – 255.

[306] D. Sindayihebura, J. Cousin, C. Dumouchel, Experimental and theoretical study of sprays produced by ultrasonic atomisers, Particle & Particle Systems Characterization 14 (1997) 93–101.

[307] D. Sindayihebura, L. Bolle, A. Cornet, L. Joannes, Theoretical and experimental study of transducers aimed at low-frequency ultrasonic atomization of liquids, The Journal of the Acoustical Society of America 103 (1998) 1442–1448.

[308] M. Dobre, L. Bolle, Theoretical prediction of ultrasonic spray characteristics using the maximum entropy formalism, in: ILASS-Europe '98, 1998, p. 6 pages.

[309] M. Tembely, C. Lecot, A. Soucemarianadin, Prediction and evolution of drop-size distribution for a new ultrasonic atomizer, Applied Thermal Engineering 31 (2011) 656 – 667.

[310] D. Sindayihebura, D. Dobre, L. Bolle, Experimental study of thin liquid film ultrasonic atomization, in: 4th World Conference on Experimental Heat Transfer, Fluid Mechanics and Thermodynamics, 1997, p. 7 pages.

[311] M. Dobre, L. Bolle, Practical design of ultrasonic spray devices: experimental testing of several atomizer geometries, Experimental Thermal and Fluid Science 26 (2002) 205 – 211.

[312] E. M. Greitzer, Surge and rotating stall in axial flow compressors – Part I: Theoretical compression system model, Journal of Engineering for Gas Turbines and Power 98 (1976) 190–198.

[313] E. M. Greitzer, Surge and rotating stall in axial flow compressors – Part II: Experimental results and comparison with theory, Journal of Engineering for Gas Turbines and Power 98 (1976) 199–211.

[314] R. Kurz, R. C. White, Surge avoidance in gas compression systems, Journal of Turbomachinery 126 (2004) 501–506.

[315] R. C. White, R. Kurz, Surge avoidance for compressor systems, in: Turbomachinery Symposium 2006, Houston, Texas, USA, 2006, pp. 123–134.

Flexible Heat Production from a micro Gas Turbine

Design and experimental analysis of humidified cycles

Ward De Paepe

Micro Gas Turbines (mGTs) offer several advantages for small-scale Combined Heat and Power (CHP) production compared to Internal Combustion Engines (ICEs) such as low vibration level, cleaner exhaust and lower maintenance costs. The major drawback is their heat-driven use. In periods with low or no heat demand, part of the heat must be discarded to keep the mGT operating at high electric load. Compared to ICEs, the lower electric efficiency of mGTs makes them less attractive when the heat demand is too low and economic constraints might even lead to complete shutdown. In addition, the specific capital cost of the mGT is still high, which makes that any shutdown has a severe negative effect on the economic performance of the mGT.

In order to increase the flexibility of the mGT and shift its use towards various heat and power demand profiles, the waste heat in the exhaust gases can be used to generate auto-raised steam or hot liquid water, which is then re-injected in the cycle. This so-called humidification of the mGT cycle will increase the electric performance, resulting in a higher profitability during periods with low or no heat demand.

The optimal route for waste heat recovery in a mGT through water injection was found to be the conversion of the mGT into a micro Humid Air Turbine (mHAT). The mHAT cycle was selected based on the high electric efficiency achievable, the relative low changes to the mGT CHP cycle – resulting in low additional capital cost – and the ability to operate with lower water quality. This thesis introduces a humidified mGT cycle for flexible heat production. It first describes the entire development process of a mHAT cycle based on a Turbec T100 mGT, including the dry and wet characterisation, the development of the optimal cycle layout and water injection. Then, it presents a final cycle layout that was constructed and experimentally tested. The experimental results confirm that waste heat recovery through water injection in a mGT cycle offers high potential for electric efficiency increase without major changes to the mGT cycle.